Warm Season Convective Storm Structures over the Northeastern U.S. and their Interaction with the Marine Environment.

A Dissertation Presented

by

Kelly Lombardo

to

The Graduate School

in Partial Fulfillment of the

Requirements

for the Degree of

Doctor of Philosophy

in

Marine and Atmospheric Science

Stony Brook University

August 2011

Stony Brook University

The Graduate School

Kelly Lombardo

We, the dissertation committee for the above candidate for the

Doctor of Philosophy degree, hereby recommend

acceptance of this dissertation.

Dr. Brian A. Colle – Dissertation Advisor
Professor
School of Marine and Atmospheric Sciences, Stony Brook University

Dr. Minghua Zhang - Chairperson of Defense
Professor, Dean of School of Marine and Atmospheric Sciences
School of Marine and Atmospheric Sciences, Stony Brook University

Dr. Marvin A. Geller
Professor
School of Marine and Atmospheric Sciences, Stony Brook University

Dr. Marat Khairoutdinov
Associate Professor
School of Marine and Atmospheric Sciences, Stony Brook University

Dr. Matthew D. Parker
Associate Professor
Marine, Earth, and Atmospheric Sciences, North Carolina State University

This dissertation is accepted by the Graduate School

Lawrence Martin
Dean of the Graduate School

Abstract of the Dissertation

Warm Season Convective Storm Structures over the Northeastern U.S. and their Interaction with the Marine Environment.

by

Kelly Lombardo

Doctor of Philosophy

in

Marine and Atmospheric Science

Stony Brook University

2011

The evolution of organized convective structures over the northeastern U.S. from initiation to decay is influenced by a variety of geographical features (elevated terrain, coastal boundary). Warm season convection over this region has been relatively unexplored, especially the interaction between quasi-linear convective structures (QLCSs) and the marine environment. This thesis is the first study to systematically explore the evolving convective structures over the Northeast, with particular emphasis on the coastal region from New Jersey northeastward to Rhode Island, through observational analysis as well as high-resolution simulations of 2 representative case studies.

Organized convective structures over the Northeast during the warm season (May-August) were identified and classified into 3 main groups, including cells, quasi-linear convection, and nonlinear structures. Across the Northeast, the occurrence of all convection decreases from the western Appalachian slopes eastward to the Atlantic coast. Composite analysis highlights the importance of terrain during the initiation of cellular convection, with a majority developing in orographically-favored upslope areas. Linear and nonlinear convection are dynamically supported with a weaker terrain influence.

Composite analyses reveal that QLCSs that decay upon encountering the Atlantic coastline organize along a surface pressure trough, collocated with a region of low-level frontogenesis. Those that maintain their intensity organize downstream of a surface trough within low-level warm air advection with higher saturation in the lowest 100 hPa compared to decaying events. Sensitivity studies of a representative decaying linear event illustrate that evaporative cooling causes the development of a strong a cold pool that overwhelms the weak ambient vertical wind shear downwind of the system causing the system to decay. During this event, the role of the marine layer appears secondary. For the maintaining event, the marine layer allows the magnitude of the surface winds to be larger compared to the land due to decreasing surface friction, which increases the vertical wind shear and helps to maintain the convection. Sensitivity tests show that by increasing the roughness length over the ocean to an equivalent land value, thus decreasing vertical wind shear, the maintaining event decays closer to the coastline compared to the control run.

Table of Contents

List of Tables

Chapter 2 **Page**

Chapter 4

List of Figures

Chapter 2 **Page**

Chapter 3

Chapter 4

Acknowledgements

I would like to thank my advisor Dr. Brian Colle for all of his guidance throughout this complex project. Under his supervision, I came to realize that there are many different angles through which a single scientific problem may be viewed and there are numerous ways to approach that problem. I would also like to thank my committee including Dr. Minghua Zhang, Dr. Marvin A. Geller, Dr. Marat Khairoutdinov, and Dr. Matthew D. Parker. They graciously carved out time within their busy schedules to serve on my committee. I appreciate all of their advice and feedback throughout my dissertation.

Thank you to the staff, not only for always helping me though the at times confusing bureaucratic university hoops, but also for being so thoughtful and caring to all of the students here. Your kindness never went unnoticed or unappreciated. To the students that I have been luckily enough to call my friends, I am very grateful that you were fighting along side me during this epic course at one time or another. To my friends outside of academia, thank you for reminding me that there is a world beyond academia that is worth embracing.

Finally, I would like to thank my beautiful daughter, Emily, for helping me keep what truly matters in perspective. She gave me the courage to begin this journey, helped me find my smile when the road became difficult, and gave me the strength to see this to the end when at times I felt that it was an impossibility. I am so incredibly proud to be her mother. I love you my babe.

Chapter 1:

Introduction

1.1 Background

Although the northeastern U.S. experiences fewer severe convective events compared the central U.S, it is still important we understand the evolving convective structures given the large population in the region as well as the high level of difficultly in predicting these storms over the area. Convective storms often organize and evolve into a variety of structures throughout their lifecycle. Over the northeastern U.S, convective storm evolution can be strongly modified by the Appalachians, land-water coastal boundaries, and various urban centers. The influence of these various surfaces across the northeastern U.S. on the initiation, evolution, and decay of convection makes forecasting warm season convection a challenge. Improved forecasts of these storms require a good understanding of the frequency of convective structures, their evolution spatially and temporally, as well as the environmental conditions that support such structures over this topographically complex region. The importance of an accurate forecast of these storms becomes even more crucial when these storms are associated with severe weather (i.e. high winds, hail, tornadoes). The Northeast can experience severe warm season (May-August) storms, which can pose a large threat to life and property, especially in the highly populated New York City (NYC) coastal zone (New Jersey, New York City, Long Island, Connecticut, and Rhode Island), where the population density (~493 people per km^2) is 24 times greater than Oklahoma. However, the examination of northeastern U.S. severe convective weather has received less attention than the central U.S. This is likely because of the fewer number of severe weather events over the Northeast as compared to the central Plains and Midwest (Brooks et al. 2003, Doswell et al. 2005).

This dissertation systematically examines the warm season convective organizational structures over the northeastern U.S, both non-severe and severe (i.e. severe wind, hail, tornadoes), with particular emphasis on the evolution of these structures over the coastal region. Through the use of high-resolution modeling, the processes involved in the modification of severe linear systems in a coastal environment are explored. The remaining sections of this chapter highlight the current state of the literature regarding northeastern U.S convection, as well as the influence of the coastal zone on evolving convective structures.

a. Convective Organizational Structures

Much of our understanding of convective storm structures has focused on the central U.S. (Maddox 1981; Smull and Houze 1985; Wakimoto et al. 1998), given the high frequency and severity of convection in this region during the warm season. For example, several studies have classified Mesoscale Convective Systems (MCSs) across the central U.S. according to structure using satellite or radar data, and noted their frequency of occurrence (Bluestein and Jain 1985; Blanchard 1990; Parker and Johnson 2000; Jirak et al. 2003; Gallus et al. 2008). Bluestein and Jain (1985) examined linear convective structures in Oklahoma and identified 4 organizational modes: broken line, back building, broken areal, and embedded areal. Parker and Johnson (2000) classified linear systems over the central U.S. according to the location of stratiform precipitation (i.e. trailing stratiform, leading stratiform, and parallel stratiform). Gallus et al. (2008; hereafter G08) divided warm season convection across the central U.S. into 9 morphologies: isolated cells (IC), clusters of cells (CC), broken lines (BL), squall lines with no stratiform rain (NS), squall lines with trailing stratiform rain (TS), squall lines with parallel stratiform rain (PS), squall lines with leading stratiform rain (LS), bow echoes (BE), and nonlinear systems (NL). No formal studies have looked at the climatology of these convective structures over the northeast U.S.

There have been a growing number of climatological studies describing convective storm frequency across the eastern U.S. Zajac and Rutledge (2001) showed that the diurnal cycle of lightning activity was more pronounced along the Atlantic coastal plain from Florida to the Delmarva than the Appalachian high terrain. Orville and Huffines (2001) highlighted the decrease of cloud-to-ground lightning frequency from Florida to the northeastern U.S. coast, with fewer flashes over the Appalachian high terrain compared to the Atlantic coastal plain. Parker and Ahijevych (2007) found that over the east-central U.S, the probability of convection (>40 dBZ) occurring at a point is maximized on either side of the Appalachian terrain, with a relative minimum over the crest. Using both radar and lightning data over the northeast U.S, Murray and Colle (2010) illustrated preferred regions of convection (>45 dBZ) over the windward and lee sides of the Appalachians and some of the major river valleys. During the peak in diurnal heating, the frequency of >45 dBZ convection maximizes over the Northeast inland areas. This convective maximum shifts to the coast and offshore over the Atlantic coastal waters during the evening and overnight. Wasula et al. (2002) found that on days with severe weather over interior eastern New York, cloud-to-ground lightning frequency was maximized within the Mohawk and Hudson River valleys, with twice as much lightning than the surrounding terrain.

Previous studies highlighted the frequency and spatial distribution of convective storms over the eastern U.S, but there is little knowledge of the spatial and temporal distribution of developing convective structures (e.g., isolated cells, cluster of cells, linear, etc.), across this region. The frequency of convective structures across the Northeast provides some information about the likelihood for the development of a particular type, while understanding the ambient conditions that favor the development of each convective structure will allow forecasters to better anticipate the type of organized convective structure on any particular day.

b. Severe weather associated with convective organizational structures

Severe weather has caused millions of dollars in damage as well as loss of life over the Northeast. For example, on 29 May 1995, the F3 Great Barrington, Massachusetts tornado killed 3 people, injured 29, and caused $35 million in damage (LaPenta et al. 2005, Bosart et al. 2006). On 21 May 1998, an F3 tornado passed through Mechanicville, New York injuring 68 people and causing $71 million in damage (LaPenta et al. 2005). More recently, on 8 August 2007, an EF1 tornado touched down on Staten Island, New York with no warning lead time, with a second touchdown (EF2) in Brooklyn, New York about 10 minutes later (National Weather Service, Upton, NY).

Several studies have investigated the synoptic conditions that support severe weather over the northeastern United States. Giordano and Fritsch (1991) examined the synoptic and thermodynamic conditions associated with strong tornadoes (≥F3) and flash flooding events over the Mid-Atlantic. A majority of strong convective events had 500 hPa southwest flow, cyclonic directional wind shear through the boundary layer, enhanced low-level moisture, and convective available potential energy (CAPE) exceeding 3000 J kg^{-1}. Strong tornadoes were shown to occur primarily on the warm side of frontal boundaries, while heavy rain events developed on either side of the boundary. Johns (1982) examined warm season severe weather outbreaks over the U.S, including the Northeast, which develop under 500-hPa northwesterly flow. These outbreaks occur with 850-hPa warm air advection, conditional instability, and a 500-hPa shortwave trough embedded within the northwesterly flow that can help provide mid-level ascent (Johns 1984). Over New England and eastern New York during the warm season, relatively strong (F2-F3) and violent (F4-F5) tornadoes form ahead of a surface cold front and occur more frequently under 500 hPa westerly and northwesterly flow than southwesterly flow (Johns and Dorr 1996).

The elevated mixed layer (EML), a layer of enhanced lapse rates above the surface that originates over the higher terrain of the western U.S. (Carlson and Ludlam 1968), is often associated with severe weather over the Northeast. The most violent Northeast tornadoes are often associated with an elevated mixed layer (Johns and Dorr 1996). Farrell and Carlson (1989) discussed the importance of elevated instability during the 31 May 1985 tornado outbreak that occurred over parts of Pennsylvania and New York. Banacos and Ekster (2010) showed that the horizontal advection of EMLs from the western U.S. toward the Northeast is the dominant reason for the existence of EMLs over the Northeast.

The complex topography of the Northeast has been shown to influence the development of severe weather. Wasula et al. (2002) linked the spatial distribution of severe events over New England to the influence of terrain under southwesterly and northwesterly 700 hPa flow. More specifically, it has been suggested that terrain channeling plays an important role in tornadogenesis for a number of events in New England by accelerating the surface flow and thus increasing shear in the lowest kilometer. On 29 May 1995 in Great Barrington, Massachusetts, tornadogenesis occurred due to the merger of flow channeled up the Hudson Valley with accelerated flow down the Catskill Creek (Bosart et al. 2006). The 31 May 1998 Mechanicville, New York tornado formed as a supercell interacted with southerly flow up the Hudson Valley (LaPenta et al. 2005).

The coastal marine environment may modify the distribution of severe convective storms over the Northeast (Murray and Colle 2011), but this has not been well studied from a convective structure and ambient condition perspective. Murray and Colle (2011) showed that severe weather over eastern Long Island, New York develops with a low-level trough positioned along the coastline, with low-level westerly flow advecting conditionally unstable air from the inland areas over the island. Presently, there is no work addressing the ambient conditions associated with severe weather from different convective structures along the densely populated coastal region of the Northeast.

Previous literature has highlighted the synoptic conditions that support severe weather over the Northeast as well as the influence of terrain on convection, though the focus was primarily on tornadoes. More understanding is needed of the organizational convective structures capable of producing the various severe weather types (strong wind, hail, and tornadoes) over the Northeast, as well as the associated synoptic patterns, instability, and vertical shear with each severe convective structure. For the central U.S, Gallus et al. (2008) identified 9 convective structures (i.e. cellular, linear, nonlinear) and discussed the risk of severe weather (wind, hail, tornadoes) posed by each. Duda and Gallus (2010) expanded the analysis to include the development of severe weather by supercells over the central U.S. Therefore, there has been no systematic study identifying the convective structures associated with severe weather over the northeastern U.S.

c. Influence of the coastal zone on quasi-linear convective systems

Previous literature has shown that the maintenance of quasi-linear convective systems (QLCS) is dependent on the ambient instability, the strength of the diabatically generated cold pool, as well as the ambient vertical wind shear (i.e. Rotunno et al. 1988, Coniglio and Stensrud 2001, Weisman 1992). Through a series of idealized numerical experiments, Rotunno et al. (1988) illustrated the importance of the balance between the horizontal vorticity generated by the horizontal density gradient at the leading edge of the cold pool and the horizontal vorticity induced by the low-level (0-2.5 km) line-perpendicular vertical wind shear in generating an upright convective core, and hence a long lived linear system. Coniglio and Stensrud (2001) challenged this low-level balance theory, showing though full physics 3-D simulations forced by a composite derecho atmospheric profile (12 events) that the maintenance of long-lived derechos depends more on tropospheric deep vertical wind shear rather than the low-level winds alone, with deep vertical wind shear providing a mechanism for tropospheric deep overturning and lifting of air parcels (e.g. Shapiro 1992, Moncrieff and Liu 1999). The processes leading to the maintenance of the convective line and the depth of the shear are currently under debate (Weisman and Rotunno 2004, Stensrud et al. 2005, Weisman and Rotunno 2005).

The initiation, evolution, and maintenance of an organized mesoscale convective system is also sensitive to the underlying surface variations, such as terrain (i.e. Carbone et. al 2002; Ahijevych et al. 2004, Frame and Markowski 2006; Reeves and Lin 2007; Parker and Ahijevych 2007; Letkewicz and Parker 2010; Letkewicz and Parker 2011, Miglietta and Rotunno 2009) and water bodies (i.e. Changnon 1980, Bosart and Sanders 1981, Lericos et al. 2007). Carbone et al. (2002) showed that organized convective systems (i.e. squall lines, mesoscale convective complexes) primarily form over elevated terrain, such as the Rocky and Appalachian Mountains, and subsequently propagate eastward. Consistent with the work of Carbone et al. (2002), Parker and Ahijevych (2007) found that many convective systems over the east-central U.S. develop over the Appalachians during the afternoon, though there are also convective systems that move eastward from the central U.S. toward the Appalachian terrain. Parker and Ahijevych (2007) showed that eastward moving systems have the greatest chance of survival crossing over the Appalachians if they traverse the terrain during the hours of peak heating (1700-2200 UTC). Letkewicz and Parker (2010) explored the maintenance of mesoscale convective systems crossing the Appalachians in further detail, showing that those events that successfully traversed the terrain were associated with greater instability east of the Appalachians, in part due to the diurnal cycle, smaller convective inhibition, as well as weaker wind shear compared to those that decay.

Several studies have examined the processes behind terrain forced fluctuations in the intensity of a QLCS as the system traverses a mountain range (Frame and Markowski 2006, Reeves and Lin 2007, Miglietta and Rotunno 2009). As a squall line ascends a mountain ridge, the cold pool becomes partially blocked by the terrain, causing the density current to become shallow and transition to a supercritical flow as it descends the ridge (Frame and Markowski 2006). The reduced lift at the leading edge of the more shallow cold pool weakens the convection in the lee. Once at the bottom of the ridge, the cold pool deepens causing the flow to become subcritical inducing a hydraulic jump, enhanced lift along the cold pool, and the generation of a new convective line at the base of the ridge. This evolution is dependent on a number of parameters, including the wind impinging on the mountain (Miglietta and Rotunno 2009). This behavior was observed during the 1987 Taiwan Area Mesoscale Experiment (TAMEX; Kuo and Chen 1990). A squall line that developed during an intense observation period moved noticeably slower over the mountains ridges compared to the valleys, causing the orientation of the line to become parallel to the terrain (Teng et al. 2000).

Comparatively less work has explored the modification of QLCS crossing over large water bodies. Moving from a land surface to a water surface, a QLCS encounters changes in the boundary layer thermodynamic profile (i.e. marine inversion), as well as variations in wind shear, in part due to reduced surface friction over the water surface. Mapes et al. (2003) found that over northwestern South America, a strong nighttime/morning maximum in rainfall exists over the coastal ocean, with the convective systems moving offshore (westward) with time. Murray and Colle (2011) found a similar trend over the northeastern U.S, with convective systems moving eastward towards the coast creating a nocturnal (0600-1200 UTC) maximum in convective activity over the coastal waters.

Several studies have highlighted the modification of convection by the Great Lakes (Bosart and Sanders 1981, Bosart and Galarneau 2005, Workoff 2010). In a study examining the urban and lake influences on precipitation over Chicago, IL and the surrounding areas, Changnon (1980) noted the suppression of convection over the Great Lakes. While there was an enhancement of precipitation over central Chicago compared to the adjacent rural areas, the enhancement was less than for the land-locked city of St. Louis, MO, due to the influence of the lake over Chicago (Changnon 1980). However, this lake influence was negligible for heavy rain events associated with squall lines and cold fronts (Changnon 1980). In contrast, the large mesoscale convective complex that produced the 1977 Johnstown PA floods moved over the Great Lakes before reaching PA, temporarily weakening due to a decrease in instability over the lake waters, and subsequently reintensified over PA due to the increase in instability over the land (Bosart and Sanders 1981).

During the 2003 Bow Echo and MCV Experiment (BAMEX) Experiment (Davis et al. 2004), a squall line crossing over Lake Michigan intensified at the western shore of the lake, weakened over the eastern portion of the lake, and then reintensified as it crossed the eastern shore of the lake (Bosart and Galarneau 2005). The authors hypothesize that while the surface winds over southern Michigan were southwesterly, southerly surface winds over lower Lake Michigan may have contributed to enhanced low-level convergence along the western shore of Lake Michigan, a greater veering wind profile, and thus the intensification of the squall line (Bosart and Galarneau 2005). Later in the lifecycle, as the squall line encountered Lake Erie, it decayed more quickly over the lake as compared to the part of the squall line over the land (Bosart and Galarneau 2005).

Workoff (2010) performed a climatological study to explore the effect of Lake Erie on organized convective systems. To determine the impact of the lake surface on the evolving convection, a number of parameters were examined, including the difference between the temperature of the lake surface and air temperature above the lake surface to assess the stability of the marine inversion, the strength of the cold pool produced by the convective system, 0-3 km vertical wind shear, and 0-6 km vertical wind shear. While no one parameter predicted the maintenance or decay of a system, a high correlation (r = 0.53) existed between weakening linear systems and weak (<15 m s^{-1}) ambient (not line-perpendicular) 0-3 km vertical wind shear. Furthermore, examination of one particular event from the climatology suggested that the reduced friction over the waters played a more important influence on the evolution of a squall line than variations in surface-based instability.

Lericos et al. (2007) used idealized 2-D simulations to investigate the modification of long lived-squall lines moving from an ocean to a land surface by varying the strength/depth of the vertical wind shear and the temperature of the land surface. While the thermodynamic properties over the land ahead of the squall line did not influence the overall structure of the squall line, the changes in wind shear over the land modified the orientation of the squall line's updraft (Lericos et al. 2007). The land surface reduces the speed of the low level winds over the land areas, causing the systems to tilt upshear when moving from the land to the ocean. However, the authors note that this behavior is not always observed in nature, which may be in part due to the fact that observed squall lines evolve 3 dimensionally while this study only studies the phenomena using 2-D simulations.

There has been work addressing the evolution of a squall line in response to a gradual diurnal cooling, rather than an abrupt change in the underlying surface conditions, such as moving from a land to water surface. Parker (2008) isolated the effects of variations in boundary layer thermodynamics using idealized simulations to examine the response of simulated squall lines to low-level cooling, representing nocturnal cooling over the central U.S. If the boundary layer air is sufficiently cooled (cooling >10K), a linear system will become elevated, ingesting air above the nocturnal inversion, and forced by a bore atop the stable layer.

Over the northeastern U.S, much of the research examining the influence of varying surface types on evolving convection has focused on the influence of terrain (e.g. Wasula et al. 2002), especially the impact of terrain channeling on tornadogenesis (i.e. Riley and Bosart 1987, LaPenta et al. 2005, Bosart et al. 2006). A limited amount of work has focused on the evolution of organized convective systems within a coastal environment. Murray and Colle (2011) found that convective activity over the coastal region of the northeastern U.S. increases through the warm season as the influence of the marine layer diminishes. Furthermore, there is a greater chance of severe convection over NYC and Long Island during a west-southwesterly low-level flow as opposed to a southerly flow during which the relatively cooler air over the cool ocean waters are advected over the coastal region (Murray and Colle 2011). While Murray and Colle (2011) illustrates that there is coastal influence on warm season convection over the Northeast, we do not understand the processes that cause the modification or lack of modification of a QLCS moving from land to over a marine layer.

1.2 Study goals and approach

The northeastern U.S. remains a relatively unexplored region concerning evolving warm season convective structures and severe weather. Compared to other areas of the country that experience severe weather (i.e. central plains, mid-west), the geography of the Northeast is unique (Fig.2.1). Not only does it contain both complex terrain (e.g. Appalachian Mountains, Catskill Mountains) as well as the Atlantic coastal boundary, the distance between the terrain and the coast can be very small, as little as ~20 km over southern NY and CT. This suggests that there may be an influence on the initiation of convection (elevated terrain, sea-breeze convergence boundary), as well as fairly rapid modification on the subsequent evolution and decay of convective organizational structures due to the highly varying topography.

Our current understanding of the influence of the marine environment on convection, both non-severe and severe, is limited. Much of the focus has been on convection moving over the Great Lakes either though a case-by-case basis (Bosart and Sanders 1981, Bosart and Galarneau 2005) or through climatological studies (Changnon 1980, Workoff 2010). Even less is known regarding the influence of much larger water bodies, such at the Atlantic Ocean, on warm season convection. Previous work has illustrated that the northeastern U.S. terrain influences severe convection (e.g. Riley and Bosart 1987, LaPenta et al. 2005, Bosart et al. 2006), though we do not know if or how the marine environment influences severe convection over the coastal zone. Furthermore, while studies have shown that there is a relationship between low-level flow regime and severe weather over the northeastern U.S. coastal zone (Murray and Colle 2011), we do not know the processes that are responsible for the decay or maintenance of a convection moving over the coastal environment. Therefore, this dissertation will address the following motivational questions:

- What are the temporal and spatial distributions of the various convective structures (cellular, linear, nonlinear) over the northeastern U.S. during the warm season and how does the initiation of these structures vary with respect to the diurnal cycle, the underlying complex terrain, and coastal boundaries?
- What type of severe weather (severe wind, hail, tornadoes) is produced by the various convective organizational structures over the entire northeastern U.S; how does this distribution compare with that over the northeastern U.S. southern coastal region as well as the central U.S
- What are the dynamic and thermodynamic conditions associated with severe convective organizational structures over coastal northeastern U.S?
- What environmental differences (e.g. synoptic and mesoscale forcing mechanisms, instability, moisture, shear) exist between a convective linear case that decays at the northeastern U.S. coastline and one that maintains its intensity over the coastal Atlantic waters?
- What are the physical processes that lead to the maintenance or decay of quasi-linear convective systems encountering the northeastern U.S. coastal boundary?

These questions will be addressed using a combination of observational analyses, a climatological approach, as well as high-resolution, full-physics simulations. Chapter 2 describes the different organizational structures of convection over the Northeast, exploring the development and evolution of these elements. Chapter 3 focuses on the severe weather events associated with these organizational structures, with particular emphases on the coastal region from New Jersey northeastward to Rhode Island. Chapter 4 examines the influence of the Atlantic coastal boundary on evolving quasi-linear convective systems, focusing on 2 particular events that impact the New York City-Long Island region. Chapter 5 provides a summary of the results and discusses potential future work ideas.

Chapter 2:

The Spatial and Temporal Distribution of Organized Convective Structures over the Northeast U.S. and their Ambient Condition

2.1 Introduction

Previous literature concerning warm season convective storms over the eastern U.S, including the northeastern U.S, has highlighted the spatial distribution of convection across the region (i.e. Orville and Huffines 2001, Wasula et al. 2002, Parker and Ahijevych 2007, Murray and Colle 2011). However, the details describing the organizational structures (cellular, linear, nonlinear) have gone unexplored. Each of these structures poses a different concern. For example, there is a greater chance for widespread precipitation associated with a linear or nonlinear system compared to a day with primarily cellular convection, due to the areal coverage of the storm types. The duration of the precipitation, especially intense precipitation, will vary with organizational structure. Furthermore, each type of convection is associated with a different type of severe weather, the details of which are addressed in chapter 3. Understanding the frequency of these convective structures as well as the environments in which they develop can help forecasters to more accurately predict the type of convective structure that is most likely to develop as well as where and when it will initiate. Section 2.2 describes the data and methods used in this chapter. The climatological results and the ambient conditions are presented in sections 2.3 and 2.4. Northeast and Midwest convective structures are compared in section 2.5.

2.2 Data and methods

Convective structures were identified and classified across the northeast U.S. (see Fig. 2.1 for region) for two warms seasons: 1 May – 31 August 2007 and a second warm season of days randomly selected from 1 May – 31 August 2002-2006. After completing the analysis for the 2007 season, it was determined that an aggregate season was needed, since there are relatively large (30-40%) interannual variations in storm frequency across the Northeast (Murray and Colle 2011). For example, for the season using multiple years, the authors chose 1 May data randomly from the five May 1st times available from 2002-2006. Starting on 1 May, each convective event over the Northeast was tracked from initiation to decay. A subsequent day from a different year was not selected until all convection across the Northeast decayed (e.g, if convection is observed continuously from 1 May – 3 May 2002, a new year will be selected starting 4 May). The subsequent day was manually selected to be sure that there was no ongoing convection at 0000 UTC of the new day. This ensures that the initiation and decay times and locations were documented for all convective elements included in the dataset. The number of days selected from each warm season from 2002-2006 was comparable.

The northeast U.S. was subdivided into 4 geographical domains (Fig. 2.1): upslope (UP), high terrain (HT), east slope/coastal plain (CP), and coastal ocean (CO) in order to relate each convective structure to changes in surface properties. The western boundary of the upslope (UP) domain is the U.S-Canadian border. The western boundary of the coastal ocean (CO) domain is the Atlantic coastline. The boundaries for the UP, HT, and CP sub-regions do not match the surface terrain exactly; rather, the geometry was simplified to more easily bin the convective structures manually into a particular domain. The 4 domains are not equivalent in size, thus the number of convective structures in each of the 4 regions was normalized by the fractional area that each domain covered relative to total of all 4 regions.

The convective structures were classified using the approach of G08. All convective structures were identified manually using Weather Services International (WSI) National Operational Weather Radar (NOWrad) images available every 15 minutes at 2 km grid spacing. This manual approach has been applied to identify convective organizational structures in previous studies (Parker and Johnson 2000; Parker et al. 2001; Jirak et al. 2003; G08). G08 used a ≥30 dBZ threshold for central Plains convection, but this relatively low threshold included too many frontal stratiform events over the Northeast. For this study, each convective element must reach a radar reflectivity ≥35 dBZ to be included in the climatology. The first occurrence and the decay times were also documented. The first occurrence time includes initiation (a convective element first reaches 35 dBZ), when one convective type converts to another type (and ≥35 dBZ), or when a convective type moves into the Northeast domain (e.g. north, south, west, and east boundaries of Fig. 2.1). The decay time occurs when the convection is <35 dBZ.

Figure 2.2 illustrates examples of these structures, including (a) clusters of cells (CC) and a bow echo (BE), (b) a linear system with trailing stratiform precipitation (TS) and isolated cells (IC), (c) a linear system with parallel stratiform precipitation (PS), (d) a linear system with leading stratiform precipitation (LS), (e) a linear system with no stratiform precipitation (NS) and a nonlinear system (NL), (f) a broken line (BL). Isolated cells have only one radar reflectivity maximum over a 20 km x 20 km area surrounded by clear air, while a cluster of cells contain at least two radar reflectivity maxima within a minimum of a 20 km x 20 km area, with weaker precipitation (<35 dBZ) connecting these more intense cores. Linear systems must be at least 50 km in length and exhibit a continuous line of ≥35 dBZ radar reflectivity with a length to width ratio of 5:1. Nonlinear systems have connected reflectivity maxima of ≥35 dBZ, with a length to width ratio of less than 5:1. For all convective organizational modes, each individual convective structure must be separated by 50 km from an adjacent convective structure by clear air (i.e, 0 dBZ radar reflectivity) and maintain its structure for a minimum of 30 minutes. As noted above, each time a convective group (i.e. clusters of cells) or element (i.e. linear system) organizes into a different structure, the formation of that new structure is catalogued as a new convective type with a new initiation location and time. For example, if clusters of cells initiate over the high terrain, move eastward and evolve into a linear system over the coastal plain, it is documented that a linear system developed over the coastal plain with the appropriate time.

To highlight the environments associated with the 3 main structural types (cellular, linear, and nonlinear), feature-based composites were constructed using the North American Regional Reanalysis (NARR) at 32 km grid spacing (Mesinger et al. 2006). The evolution of the most-unstable CAPE (MUCAPE) and 1000 hPa θ_e is presented to highlight the differing thermodynamic conditions between the 3 main structural types. For this study, the MUCAPE uses a parcel with the maximum θ_e in each 30 hPa layer from 0 to 180 hPa above the ground. Dynamical support for these structures is examined using 900 hPa Miller (1948) frontogenesis, 850 hPa temperature advection, as well as the evolving mid- and upper-level mass fields. Frontogenesis and temperature advection are examined at the levels at which the values are maximized.

The composite times include only those events during which at least 90% of the convection over the Northeast exhibits one particular organizational type (cellular, linear, or nonlinear). Composites included 47 cellular events, 38 linear events, and 42 nonlinear events during the 2007 and aggregate 2002-2006 warm seasons (Table 2.1). Composites were centered on the location of the initiating convection (feature-based), which allowed for more robust synoptic and thermodynamic signals compared to geographically fixed composites. For linear and nonlinear convection, a point was selected ~0.75° (~85 km) ahead of the moving convection at the closest 3-h time prior to the most intense (in dBZ) convection. Choosing a point ahead of the moving convection limits convective contamination in the composites. Ongoing convection can alter the ambient environment immediately adjacent to the convection by (1) reducing the local CAPE, (2) decreasing the surface θ_e due to convective outflow, (3) modifying the wind profile by local storm circulations. Cellular convection often does not move much horizontally, so choosing a point out ahead may not be representative of the conditions in which the cells are developing. Thus, for cellular events, the compositing point was the center of the initiating convection at the closest 3-h time prior to convective initiation. For all feature-based composite images, the center point of the feature-based composite is denoted as a star.

2.3 Distribution of convective structures and initiation

a. Warm season distribution

Figure 2.3 shows the percentage distribution of the 9 convective structures across the northeast U.S. for the 1071 convective elements included in this analysis. Of the 3 main organizational structures (i.e. cellular, linear, nonlinear), cellular convection is the most common type, comprising nearly half of all warm season convection. Within the cellular group, it is more common for cellular convection to organize into clusters (CC) compared to isolated cells (IC). Supercells are categorized as ICs, suggesting that supercells are not common over the Northeast. Nonlinear (NL) systems make up one third of all convective storms, while linear systems, the least common organizational type, develop only one fifth of the time. Over the Northeast, half of the linear systems that develop have no associated stratiform precipitation, while about 30% are trailing stratiform systems.

The monthly distribution of each structure was also examined (Fig. 2.4). Broken lines (BL) and isolated cells (IC) develop more often during the early warm season months of May and June, respectively. The remaining organizational structures preferentially develop later in the warm season from mid- to late-summer. Clusters of cells (CC) are equally as common from June through August. Nonlinear (NL) and two types of linear convection (NS, BE) develop more frequently during the late summer months, especially August. The remaining linear systems (TS, PS, LS,) do not show a preference for development during any part of the warm season, perhaps due to the more limited sample size.

b. Spatial variations and initiation

A Hovmöller plot shows the frequency of occurrence for isolated cells, cluster of cells, linear and nonlinear types as a function of time of day across the 4 regions of the northeast U.S. (Fig. 2.5). For the results presented herein, occurrence or development of a convective type is defined as the time it initiates, organizes into that type from a different convective structure, or enters into a region in Fig. 2.1, from outside the Northeast domain. All linear systems are grouped into one category (including broken lines, BL) in order to increase sample size.

Two-thirds of all isolated cells (ICs) occur from the morning into the late afternoon (1200-2100 UTC) over the land areas, with maximum development over the high terrain (Fig 2.5a). The formation of cellular clusters (CC) is maximized during approximately the same time frame (1200-0000 UTC) as ICs and occurs mainly over the upslope and high terrain regions (48% of all CC initiation, Fig. 2.5b). Unlike ICs, there is a small secondary maximum in CC development over the coastal plain in the early morning hours (0600-1200 UTC). Over the upslope and high terrain regions, the CCs may form during any time of the day, with their development decreasing from the high terrain region eastward to the coastal ocean.

Approximately two-thirds of all linear systems initiate between the late afternoon and early evening (1800-0000 UTC) over the land areas (Fig. 2.5c), about 6 h later than cellular development (IC, CC). There is almost no linear development during the early morning hours (0600-1200 UTC). Nonlinear systems primarily (61%) organize during the afternoon into the overnight hours (1800-0600 UTC) over all domains (Fig. 2.5d), which is ~3-6 hours later than the linear systems. There is a secondary peak in nonlinear organization at 1200 UTC near the coastline. Similar to linear systems and cellular clusters, NL initiation is maximized over the Appalachian upslope and declines eastward toward the coastal ocean.

Figure 2.6 compares the number of developing convective structures within each of the 4 domains throughout the diurnal cycle. About 41% of all Northeast convective structures (596 of 1451 events) develop over the upslope domain (Fig. 2.6a). This percentage decreases over the high terrain (27%) and coastal plain (24%), decreasing dramatically over the coastal ocean (7%). The peak in the frequency of occurrence over the upslope region is partially a reflection of upstream convection moving into the domain from the west. Manual inspection of all convective events entering the boundaries of the 4 domains in June 2007 suggests that approximately the same number of convective systems move into the high terrain domain as the upslope domain. Thus, the upslope domain is the most active of the 4 domains for convection developing in situ.

Over the upslope region (Fig. 2.6a), during the morning and early afternoon hours (1200-1800 UTC), clusters of cells (CC) and nonlinear convection (NL) are the most common convective structures. By the late afternoon and early evening (1800-0000 UTC), linear and nonlinear systems develop most often. The frequency of initiation declines slightly into the early nighttime (0000-0600 UTC), with linear and nonlinear systems remaining the most common. The total storm initiation declines into the nighttime and early morning hours (0600-1200 UTC), and nonlinear convection becomes the dominant organizational structure (41% of the total structures). Throughout the day over this region, there is a progression of the dominant initiating type from cellular and nonlinear in the morning, to linear and nonlinear in the afternoon/evening, to primarily nonlinear during the nighttime. This evolution from cellular clusters to more linear and nonlinear systems is also apparent over the high terrain and coastal plain regions (Figs. 2.6b,c). However, in the morning, there is less developing nonlinear convection over these two regions, with more isolated cells (IC) over the high terrain domain rather than CCs. The high terrain and coastal plain are also dominated by nonlinear systems in the evening (0000-0600 UTC).

The diurnal evolution of convection is much different over the coastal ocean. Nonlinear convection is the most common organizational structure during the day, with the exception of the late afternoon and early evening hours (1800-0000 UTC). During this time, all convective structures develop at approximately the same frequency.

2.4 Synoptic patterns and thermodynamic environments associated with convective structures

a. Cellular convective events

Figure 2.7 shows a series of spatial composites centered on the developing convection, illustrating the synoptic evolution for cellular (IC and CC) events, from 24-h before a cellular structure develops (t-24h) to the time of cell development (t-0h). At t-24h (Fig. 2.7a), a westward extension of the Bermuda anticyclone is located ~1200 km to the southwest of the cellular point, with a weak surface trough immediately east of this location. Southwesterly flow around the anticyclone advects warm and moist air (equivalent potential temperature or θ_e of ~336 K) air towards where the cell(s) first forms, with MUCAPE between 600-1000 J kg^{-1}. The core of the 20 m s^{-1} 300 hPa jet is ~1200 km poleward of the initiation point (Fig. 2.7b). A weak 500 hPa trough is located ~300 km to the west of the initiation point and the mid-level flow is nearly westerly. Inspection of many cases revealed that this nearly zonal flow in the composite is partially the result of the cancellation of the exact position of the short-wave troughs, as well as the variety of flow regimes (northwesterly, southwesterly, westerly) during these events. About 34% of cellular events develop in association with a mid-level short-wave trough.

By t-12h (Fig. 2.7c), there is little change in the surface pressure field (Fig. 2.7c), while MUCAPE decreases to <500 J kg^{-1} over the initiation point and the θ_e decreases to ~334 K. This composite time occurs during a diurnal minimum for many events, since 92% of cellular events develop between 1500-2100 UTC (Table 1). The 500 hPa trough is still ~300 km upstream of the initiation point, although it remains broad and weak (Fig. 2.7d).

At t-0h, the instability increases at the initiation point through daytime heating (MUCAPE >1000 J kg^{-1}), and the θ_e increases to 340 K (Fig. 2.7e). The precipitable water (32 mm) has increased little (~2 mm) over the previous 24-h (not shown). The surface trough to the east of the developing convection is more robust at this time (Fig. 2.7e). There is a weak 500 hPa trough axis centered where the cells first develop, so there is no vorticity advection, and the 300 hPa jet is displaced well to the north (Fig. 2.7f). As a result, there is little or no mid-level quasi-geostrophic (Q-vector) forcing (not shown). There is also little to no 850 hPa temperature advection where the cellular convection develops (Fig. 2.8a), and little frontogenetical forcing at 900 hPa (Fig. 2.8b).

Because there is limited synoptic forcing for ascent for these cellular events, it was hypothesized that upslope terrain forcing may provide a lifting mechanism. Figure 2.9 illustrates where the 47 cellular (IC and CC) convective events occurred over the northeast U.S. with respect to 4 flow regimes at 900 hPa (045-135^{o}, 135-225^{o}, 225-315^{o}, 315-045^{o}) obtained from the NARR dataset. From this analysis as well as the inspection of the individual events, ~60% of these cellular events develop along the terrain slopes in association with an upslope flow component. For example, westerly flow at 900 hPa (triangles) yields cellular initiation along western slopes and crest of the Pennsylvania Appalachians. Southerly flow (diamonds) favors cellular initiation on the southern and eastern slopes of the Catskill Mountains in south central NY. Thus, orographic lift is an important lifting mechanism during a majority of the cellular events. The remainder of the cellular storms forms along or near a surface baroclinic zone (~25% of all cellular events, not shown), as well as along sea breeze convergence zones over coastal NJ (~3 events).

b. Linear convective events

Figure 2.10 illustrates the composite synoptic evolution of all linear events from t-24h to the time of the most intense linear convection (t-0h) over the Northeast. At t-24h (Fig. 2.10a), a surface cyclone and trailing cold front is located ~1500 km to the northwest of where the linear system develops. There is enhanced MUCAPE (600-1000 J kg^{-1}) to the east of the surface front, which is associated with the northward advection of a surface θ_e ridge (~338 K) by southwesterly flow around an anticyclone off the southeast U.S. coast (Fig. 2.10a). The 500 hPa flow over the linear convection point is west-northwesterly at 10 m s^{-1} as a result of a broad 500 hPa ridge ~600 km to the west (Fig. 2.10b). The 30 m s^{-1} 300 hPa jet core is centered ~1000 km poleward of the convection.

At t-12h (Fig. 2.10c), the surface cyclone and associated upper-level trough advance eastward to within ~1000 km of the linear convection point, while the 300 hPa jet gains a larger meridional flow component over the Great Lakes (Fig. 2.10d). Since 86% of the linear events included in the composites occur during the day (1500-0000 UTC, Table 1), the instability within the warm sector east of the surface front has decreased to ~600 J kg^{-1} (Fig. 2.10c) through nocturnal cooling. Warm advection shifts the θ_e gradient poleward of the linear convection point, while a surface trough begins to develop with a north-south oriented axis over the convection location. This newly developing surface trough forms ~1000 km east of the surface cold front.

At t-0h (Fig. 2.10e), the trough to the east of the surface cold front has amplified (Fig. 2.10e), with linear convection organizing near the surface trough axis. It appears that linear events develop in association with a prefrontal surface trough ahead of a cold front. Examination of the individual events revealed that these prefrontal troughs are almost always located in the lee of the Appalachians. Manual inspection of these linear events suggests that the prefrontal troughs in the Appalachian lee develop from: (1) adiabatic compressional (downslope) warming, (2) synoptic-scale ascent as the mid-level trough advances ahead of the surface cold front, or (3) a forward tilting frontal structure, with the warmest mean tropospheric air and associated surface pressure trough located ahead of the surface front (Schultz and Steenburgh 1999, Schultz 2005).

Although linear systems can develop along prefrontal troughs, it is not as common as the composites might suggest, given the event averaging. During 40% of all linear events, there is a prefrontal/lee trough present, although the convection does not always organize within this trough. Manual inspection of the surface pressure maps revealed that ~22% of linear systems form within the axis of a prefrontal surface trough, while ~39% develop ahead of and within 300 km of a surface cold front, not within a surface trough. Furthermore, ~11% of the linear events form along a surface cold front within the associated surface trough, while ~17 % form within the warm sector in the absence of any surface baroclinic zones in close proximity.

At t-0h (Fig. 2.10e), moist, unstable air advects to the northeast creating a wedge of relatively large MUCAPE (1000-1400 J kg^{-1}) and a θ_e ridge near the linear development. Meanwhile, the precipitable water values over the organizing convection have increased from 33 to 38 mm during the previous 24-h (not shown). A broad 500 hPa trough axis northwest of the convection trails the surface cyclone by ~600 km, while the amplifying 300 hPa jet remains ~1000 km poleward of the linear convection (Fig. 2.10f). Given the locations of the 500 hPa trough and 300 hPa jet (Fig. 2.10f), there is weak Q-vector convergence (large-scale lift) from 700-500 hPa associated with the linear convection (not shown).

At 850 hPa for t-0h (Fig. 2.8c), the temperature advection is near zero over the developing convection, while there are relatively large warm and cold advections (+/- 5.4x10^{-1}

^{o}C hr^{-1}) to the northeast and northwest of this point, respectively. Meanwhile, there is 900 hPa frontogenesis (>10x10^{-2} K 100 km^{-1} 3 hr^{-1}, Fig. 2.8d) located immediately northwest of the linear convection (Fig. 2.8d), suggesting that linear systems organize on the warm side of a 900 hPa frontogenesis maximum.

c. Nonlinear convective events

At t-24h prior to nonlinear convective events (Fig. 2.11a), a surface pressure ridge is located over the nonlinear convection development point, with a broad surface trough ~1500 km to the west. The lack of a well-defined surface trough is the product of compositing a variety of surface cyclone locations relative to the convection. The environment over the development location is weakly unstable (MUCAPE ~200 J kg^{-1}), with most of the instability >400 km equatorward. A meridionally-orientated θ_e gradient extends from the Midwest to the East Coast. There is ~10 m s^{-1} of 500 hPa west-northwesterly flow and a 20 m s^{-1} 300 hPa jet over the nonlinear development location (Fig. 2.11b).

By t-12h, the broad surface trough advances eastward and is located over the Great Lakes, although there is little change in the ambient instability and thermal gradient as compared to 12-h earlier (Fig. 2.11c). The 500 hPa geopotential height field amplifies, as a mid-level trough deepens advancing towards the nonlinear composite point and the 25 m s^{-1} 300 hPa jet core broadens (Fig. 2.11d).

By t-0h, a more defined surface trough is located immediately west of the developing nonlinear convection, and the surface winds have veered to southerly ahead of this trough (Fig. 2.11e). Regardless, the instability remains equatorward, with MUCAPE of ~200 J kg^{-1} over the developing convection. The destabilizing of the atmosphere through diurnal heating is not required for nonlinear convection, since 57% of all nonlinear cases included in the composite develop between 0600-1200 UTC and the other 43% occur evenly between 1200-0600 UTC (Table 2.1). The precipitable water values have increased from 27 to 34 mm over the previous 12-h (not shown). The nonlinear system organizes along the surface baroclinic zone, with ~60% of the individual events included in this composite developing along a surface warm front (not shown). The 500 hPa trough continues to amplify as it approaches the developing convection (Fig. 2.11f). The 25 m s^{-1} 300 hPa jet shifts equatorward, placing the nonlinear convection in the right entrance region of the jet core, an area favorable for ascent and Q-vector forcing (not shown). Furthermore, 0-6 km shear over the developing NL convection has increased over the previous 12-h, with 1000 hPa winds rotating to from westerly to southerly as the surface trough encroaches on the developing convection in conjunction with a strengthening 500 hPa westerly flow (Figs. 2.11c-f).

At t-0h, 850 hPa temperature advection maximizes over the nonlinear convection, with values >45x10^{-6} ^{o}C s^{-1} (>1.6 ^{o}C hr^{-1}, Fig. 2.8e). Furthermore, the convection develops within a region of 900 hPa frontogenesis (6x10^{-2} K 100 km^{-1} 3 h^{-1}) associated with a strengthening warm front to the east of the surface trough (Fig. 2.8f). Overall, nonlinear systems develop in association with strong forcing by an active baroclinic system and limited instability. The large areal coverage of nonlinear systems developing under strong dynamical forcing is consistent with Schumann and Roebber (2010). Examining the relationship between convective morphology and forcing by potential vorticity features on the dynamic tropopause, they found that the stronger the forcing, the more widespread the convection. Recall, the development of nonlinear systems is more evenly distributed over all 4 domains (UP, HT, CP, CO) as compared to the other organizational structures (cellular, linear, Fig. 2.5), indicating that these systems are the least influenced by the underlying topography.

2.5 Discussion

a. Comparison between organizational structures

In order to more quantitatively compare the physical processes among the convective structures (cellular, linear, nonlinear), 1.5^{o} latitude-longitude area-averaged values are calculated for a variety of variables centered on the compositing point, for each of the individual events included in the composites (Table 1). A bootstrap method (Zwiers 1990) was applied to the area-averaged variables to test for statistical significance between the 3 groups (i.e. cellular, linear, nonlinear). For each variable, a new sample of the same size was generated 1000 times by randomly selecting from the original sample. The 95% confidence intervals around the mean were determined by finding the 2.5th and 97.5th percentile of the means of the 1000 resamples. The thermodynamic and dynamic quantities that support northeast U.S. convective structures are also compared to Midwest and central Plains convective environments (Weisman and Klemp 1982; Parker and Johnson 2000; Coniglio et al. 2007).

Figure 2.12a illustrates the distribution of 900 hPa frontogenesis for the cellular, linear, and nonlinear events. The mean 900 hPa frontogenesis values for linear (11.6x10^{-2} K 100 km^{-1} 3 h^{-1}) and nonlinear (13.1x10^{-2} K 100 km^{-1} 3 h^{-1}) systems are significantly greater than cellular events (1.6x10^{-2} K 100 km^{-1} 3h^{-1}) at the 95% level (not shown). A majority (~77%) of the cellular events that develop under frontolytical situations are forced by orographic lift over the Appalachian terrain, while the remaining events were supported by Q-vector forcing at mid-levels (not shown). The tail in the distribution for nonlinear events is skewed toward stronger frontogenetical forcing, with values as high as 63.1x10^{-2} K 100 km^{-1} 3 h^{-1}. Also, the mean 850 hPa warm air advection for nonlinear convective events (3.3x10^{-5} ^{o}C s^{-1} or 0.2 ^{o}C hr^{-1}) is significantly (95% level) larger than the near-neutral temperature advection during cellular (-0.5x10^{-5} ^{o}C s^{-1}) and linear (-0.6x10^{-5} ^{o}C s^{-1}) events (Fig. 2.12b).

The mean precipitable water value for linear convection (37.9 mm) is significantly greater than cellular (32.5 mm) and nonlinear (33.4 mm) convection at the 95% level (Fig. 2.13a). Furthermore, the spread of values is smaller for linear events, with values ranging from 27.4-48.7 mm, compared to cellular (9.3-45.7 mm) and nonlinear (14.19-46.43 mm) events. The middle 50% of precipitable water values (35.2-40.7 mm) for Northeast linear convection is greater than the average values for linear systems in the U.S. Plains (24.3-33.5 mm, Parker and Johnson 2000).

Both cellular and linear convection develop in moderate MUCAPE environments, (Fig. 2.13b). The interquartile range for cellular convection is between 516-1124 J kg^{-1} and 754-1322 J kg^{-1} for linear convection (Fig. 2.13b). The MUCAPE values are similar to the central U.S. Plains during May, with mean values ranging from ~800 J kg^{-1} for the PS type to ~1600 J kg^{-1} for the TS system (Parker and Johnson 2000). However, there is a large spread in MUCAPE that support Northeast linear convection (196-2737 J kg^{-1}, Fig. 2.13b). In contrast, the interquartile CAPE range for nonlinear convection is 21-301 J kg^{-1}, while the mean (207 J kg^{-1}) is significantly (95% level) less than both cellular (973 J kg^{-1}) and linear (1112 J kg^{-1}) values. Furthermore, the maximum MUCAPE value associated with nonlinear events is only 1706 J kg^{-1}, which is substantially less that the maximum MUCAPE for linear (2737 J kg^{-1}) and cellular convection (3413 J kg^{-1}, Fig. 2.13b). Two events included in the nonlinear composites had an MUCAPE value of 0, one of which was strongly and continuously forced by 850 hPa warm air advection and 900 hPa frontogenesis. This is consistent with the derecho work of Evans and Doswell (2001), who found that over the eastern two-thirds of the U.S, strongly synoptically forced derechos associated with a deep mid-level trough and surface cold front can occur in environments with little to no CAPE. The other no MUCAPE event developed in association with relatively weak dynamical forcing (not shown), although there was potential instability present (1000-800 hPa).

It has been shown that the relationship between CAPE and shear is important for determining the structure of convection (Weisman and Klemp 1982, 1984; Rotunno et al. 1988; Weisman et al. 1988; Parker and Johnson 2000). Ambient shear over several depths was compared between the 3 convective types, with shear calculated as the magnitude of the vector difference over the layer. For 0-1 km shear, cellular convection forms in the smallest shear environments, with the middle 50% of cellular events forming in 1-3 m s^{-1} of ambient shear (Fig. 2.14a). The interquartile range increases for linear convection (2.5-5.2 m s^{-1}) and more so for nonlinear convection (3.1-6.8 m s^{-1}). The mean values of 0-1 km shear for linear (3.9 m s^{-1}) and nonlinear systems (5.3 m s^{-1}) are significantly (95% level) greater than for the cellular convection (2.1 m s^{-1}). Furthermore, the mean 0-1 km shear for nonlinear systems is greater than for linear systems at the 90% significance level. The 0-3 km shear for linear and nonlinear convection is significantly (95% level) greater than cellular convection as well (not shown).

Mean values of 0-6 km shear for all 3 convective types are significantly different from each other at the 90% level, with a mean 0-6 km shear for cellular storms of 9.5 m s^{-1}, 12.3 m s^{-1} for linear systems, and 16.9 m s^{-1} for nonlinear events (Fig. 2.14b). The relatively weak deep layer shear during cellular events, with an interquartile range of 5.6-13.1 m s^{-1}, suggests that most northeastern U.S. cellular events are not supercellular (Fig. 2.14b). Through the use of proximity soundings, Thompson et al. (2003) found that the probability of supercells over the Midwest increases as the 0-6 km shear increases from 15 to 20 m s^{-1}. Though numerical simulations, Weisman and Klemp (1982) showed that for splitting cells to develop, the ambient 0-6 km shear must be a minimum of 20 m s^{-1}.

The middle 50% of linear events have 0-6 km shear values ranging from 8.6-14.8 m s^{-1}. There is little difference between the 0-3 km and 0-6 km shear values for linear systems (not shown), indicating that the greatest contribution to the ambient shear comes from winds below 3 km, consistent with Rotunno et al. (1988). About three-fourths of Northeast linear events included in this dataset have smaller 0-6 km shear values compared to all types of linear convective structures over the eastern half of the U.S. (Evans and Doswell 2001; Cohen et al. 2007; Coniglio et al. 2007), which ranged from 12-20 m s^{-1}.

In contrast, Northeast nonlinear systems have the greatest deep layer shear, with an interquartile range of 12.7-21.1 m s^{-1}, consistent with a well-defined baroclinic trough from the surface to mid-levels (Figs. 2.11e,f). The 0-6 km shear vector during Northeast nonlinear events more closely resembles the shear values that support central U.S. quasi-linear systems (Evans and Doswell 2001, Cohen et al. 2007).

b. Comparison between Northeast and Midwest convective types

There are large differences in terrain between the northeast U.S. and the central Plains, and the Atlantic coastal boundary adds another degree of complexity for the Northeast. These surface variations and associated ambient conditions (moisture, instability, and lift) will influence convective organizational structures over each region uniquely. To evaluate these differences, the structural distribution of convection over the Northeast (Fig. 2.3) is compared to the distribution over the Midwest highlighted by G08.

Although the Northeast convective structures were classified according to the 9 morphologies of G08, the results can not be compared directly since the analysis was completed manually by two separate research groups. Therefore, to compare our Northeast results with the G08 analysis, first, we first classified the convective structures over the G08 region of interest (i.e. Midwest) from 1-30 June 2002 using the same reflectivity data and approach described in section 2. We identified nearly twice as many convective structures across the Midwest compared to the G08 analysis for that month. There are two reasons for this discrepancy (W. Gallus, personal communication, 2010): (1) we classified all convective elements across the domain, while G08 identified the dominant morphology over the Midwest during a particular time and (2) we identified convective structures every 15-min, while G08 identified them every 1-h. Since a goal is to obtain a qualtitative comparison of the different structures between the Midwest and Northeast, the G08 percentages of the various convective types were adjusted to account for these differences in classification. Two convective distributions for June 2002 were calculated, one using the classification of G08 and the other using the our approach. The percentage difference between these two June 2002 distributions was calculated (adjustment factor) and added to the total warm season structural distribution of G08. This approach only provides a rough adjustment, so any differences noted between the 2 regions must be relatively large to be discussed.

Figure 2.15 illustrates the full warm season (April-August 2002) G08 distrubution modified by the adjustment factor noted above. The greatest variations between the original G08 distribution (G08 Fig. 6) and Fig. 2.15 are the adjusted distribution has 8% fewer NLs and 12% more CCs. Thus, the difference between the original G08 distribution and the adjusted G08 distribution are relatively small, giving us additional confidence in comparing the adjusted G08 distribution with our Northeast results.

The main structural differences between Northeast (Fig. 2.3) and Midwest (Fig. 2.15) convection exist in the percentage of NL and IC convection. During the warm season, there is a greater percentage of NL systems over the Northeast (33%) than the Midwest (20%). There is likely a larger number of baroclinic systems over the Northeast during the warm season compared to the central Plains. A smaller percentage of convection organizes into ICs over the Northeast (14%) compared to the Midwest (24%). This difference may reflect the more frequent supercell development over the Midwest compared to the Northeast.

Table 2.1 List of dates used in the NARR composite for the cellular, linear, and nonlinear convective storm events. These include only those events with at least 90% of the convection over the Northeast exhibiting one particular organizational type (cellular, linear, or nonlinear).

cellular events	linear events	Nonlinear events
1500 UTC 21 May 2002	1800 UTC 12 May 2002	0900 UTC 14 Jun 2002
1800 UTC 27 May 2002	2100 UTC 31 May 2002	1200 UTC 9 May 2003
1500 UTC 9 Jun 2002	1800 UTC 12 Jun 2002	0600 UTC 24 May 2003
1800 UTC 25 Jun 2002	2100 UTC 21 Jun 2002	0600 UTC 26 May 2003
1800 UTC 2 Jul 2002	2100 UTC 27 Jun 2002	1200 UTC 11 Jun 2003
2100 UTC 3 Jul 2002	1800 UTC 23 Jul 2002	1800 UTC 20 Jun 2003
1500 UTC 18 Jul 2002	0600 UTC 28 Jul 2002	0600 UTC 3 Jul 2003
1800 UTC 31 Jul 2002	1800 UTC 2 Aug 2002	0000 UTC 11 Jul 2003
2100 UTC 1 Aug 2002	2100 UTC 21 Jul 2003	0000 UTC 16 Jul 2003
1800 UTC 3 Aug 2002	1800 UTC 16 Aug 2003	0300 UTC 29 Jul 2003
1800 UTC 13 Aug 2002	1800 UTC 26 Aug 2003	0600 UTC 1 Aug 2003
1800 UTC 17 Aug 2002	1500 UTC 14 May 2004	1200 UTC 28 May 2004
1500 UTC 18 Aug 2002	2100 UTC 18 May 2004	0900 UTC 5 Jun 2004
1800 UTC 9 Jun 2003	0300 UTC 23 May 2004	1800 UTC 13 Jun 2004
1800 UTC 27 Jun 2003	1500 UTC 24 May 2004	0900 UTC 22 Jun 2004
1800 UTC 29 Jun 2003	2100 UTC 9 Jun 2004	0900 UTC 12 Jul 2004
1800 UTC 8 Jul 2003	0900 UTC 14 Jul 2004	0900 UTC 26 Jul 2004
1500 UTC 25 Jul 2003	2100 UTC 29 Aug 2004	0000 UTC 15 Aug 2004
1500 UTC 12 Aug 2003	1500 UTC 5 Aug 2005	0900 UTC 8 Aug 2005
1500 UTC 13 Aug 2003	2100 UTC 30 May 2006	0900 UTC 16 Aug 2005
1800 UTC 11 May 2004	1800 UTC 2 Jul 2006	0600 UTC 18 Aug 2005
1800 UTC 17 May 2004	0000 UTC 11 Jul 2006	0000 UTC 20 Aug 2005
1800 UTC 30 Jun 2004	1800 UTC 28 Jul 2006	0600 UTC 28 Aug 2005
1500 UTC 1 Jul 2004	0600 UTC 30 Jul 2006	0000 UTC 5 May 2006
0000 UTC 18 Aug 2004	1800 UTC 3 Aug 2006	1500 UTC 6 May 2006
1500 UTC 18 Jul 2005	1500 UTC 10 May 2007	0900 UTC 21 May 2006
1800 UTC 4 Aug 2005	1500 UTC 16 May 2007	0600 UTC 4 Jul 2006
1500 UTC 10 Aug 2005	2100 UTC 8 Jun 2007	0600 UTC 12 Jul 2006
1500 UTC 11 Aug 2005	1800 UTC 13 Jun 2007	1500 UTC 22 Jul 2006
1500 UTC 22 Aug 2005	2100 UTC 19 Jun 2007	2100 UTC 14 Aug 2006
1500 UTC 3 Jul 2006	1500 UTC 27 Jun 2007	1800 UTC 19 Aug 2006

1500 UTC 26 Jul 2006	1800 UTC 28 Jun 2007	2100 UTC 1 May 2007
1500 UTC 31 Jul 2006	1500 UTC 5 Jul 2007	0600 UTC 15 May 2007
1500 UTC 1 Aug 2006	0900 UTC 9 Jul 2007	0900 UTC 6 Jun 2007
1800 UTC 23 May 2007	1500 UTC 11 Jul 2007	2100 UTC 30 Jun 2007
1800 UTC 24 May 2007	1800 UTC 15 Jul 2007	0900 UTC 4 Jul 2007
1500 UTC 25 May 2007	1800 UTC 27 Jul 2007	0600 UTC 18 Jul 2007
1800 UTC 10 Jun 2007	1500 UTC 9 Aug 2007	0900 UTC 19 Jul 2007
1800 UTC 17 Jun 2007		0600 UTC 23 Jul 2007
1800 UTC 25 Jun 2007		1500 UTC 7 Aug 2007
1500 UTC 26 Jun 2007		0600 UTC 13 Aug 2007
1500 UTC 10 Jul 2007		1200 UTC 19 Aug 2007
1500 UTC 16 Jul 2007		
1500 UTC 25 Jul 2007		
1800 UTC 28 Jul 2007		
1500 UTC 30 Jul 2007		
1800 UTC 8 Aug 2007		

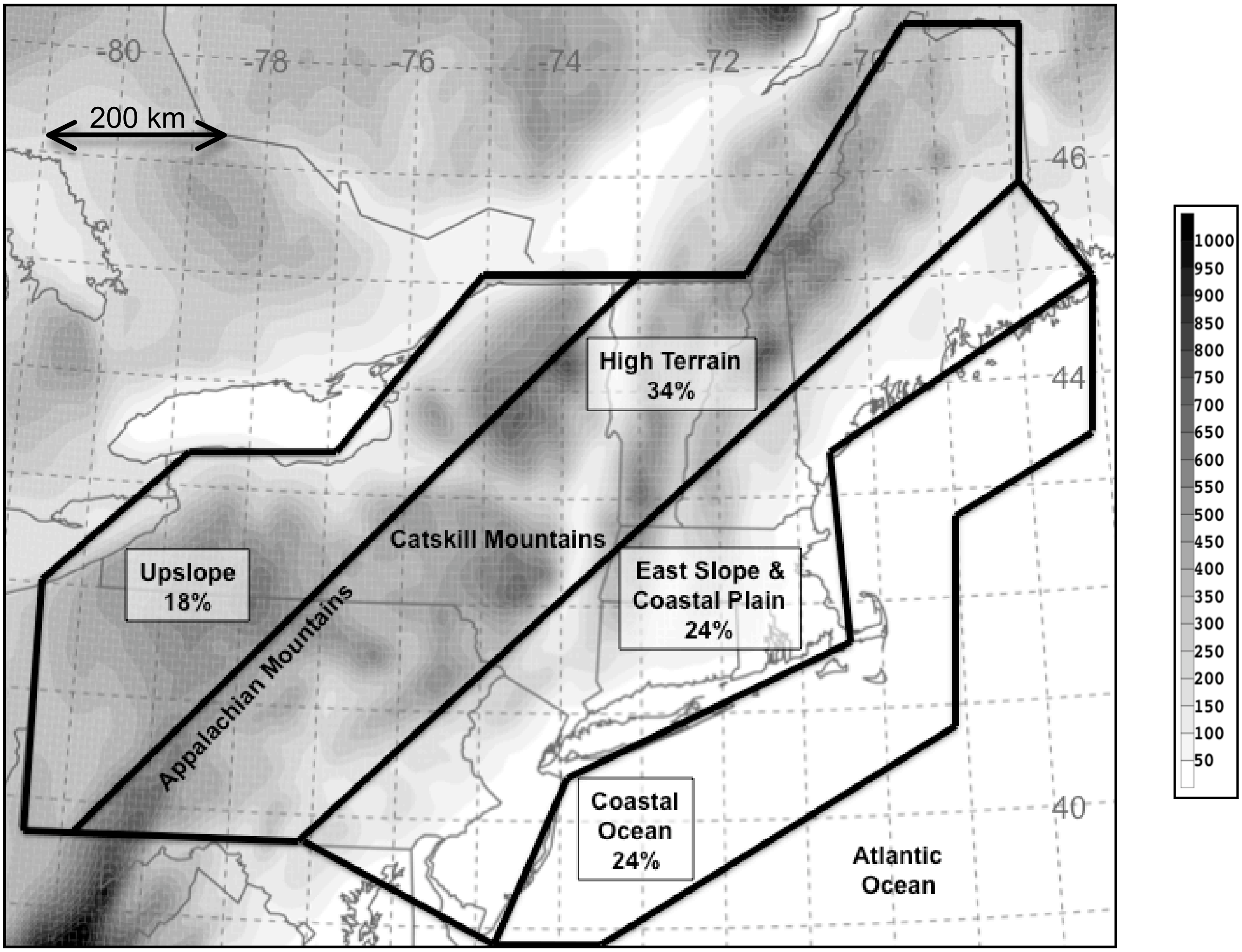

Figure 2.1 The northeast U.S. domain subdivided into 4 regions for the convective storm climatology. The fractional area of each subdomain with respect to the total Northeast area is indicated in percentage values. The terrain is shaded in meters.

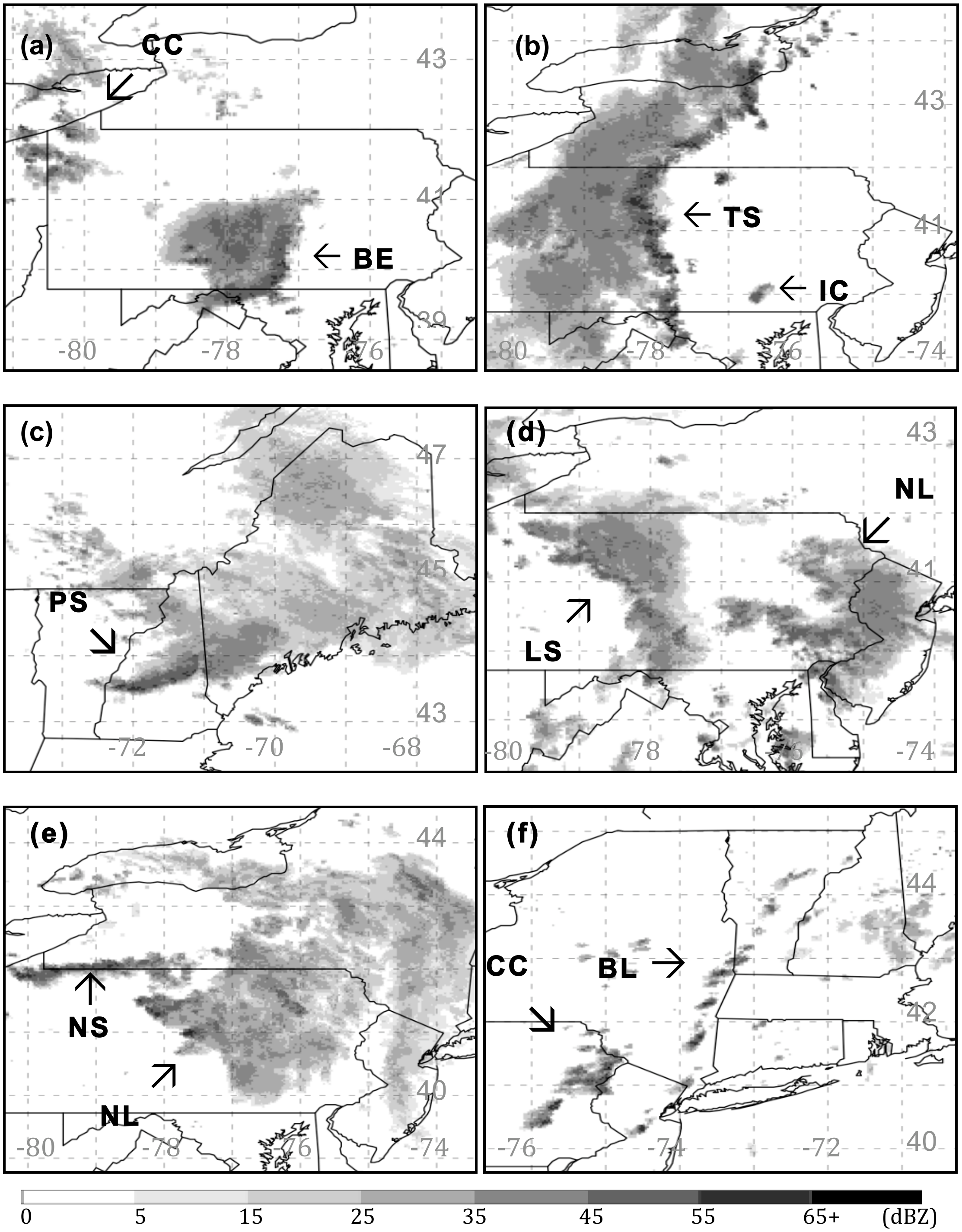

Figure 2.2 NOWrad radar reflectivity (shaded every 5 dBZ) at 2 km grid spacing showing (a) clusters of cells (CC) and bow echo (BE) at 1545 UTC 9 Aug 2007, (b) linear system with trailing stratiform precipitation (TS) and isolated cells (IC) at 2345 UTC 8 June 2007, (c) linear system with parallel stratiform precipitation (PS) 1815 UTC 9 July 2007, (d) linear system with leading stratiform precipitation (LS) and nonlinear (NL) system at 1230 UTC 12 July 2004, (e) linear system with no stratiform precipitation (NS) & nonlinear (NL) system at 0145 UTC 8 Aug 2007, (f) broken line (BL) and clusters of cells (CC) at 1715 UTC 12 June 2007.

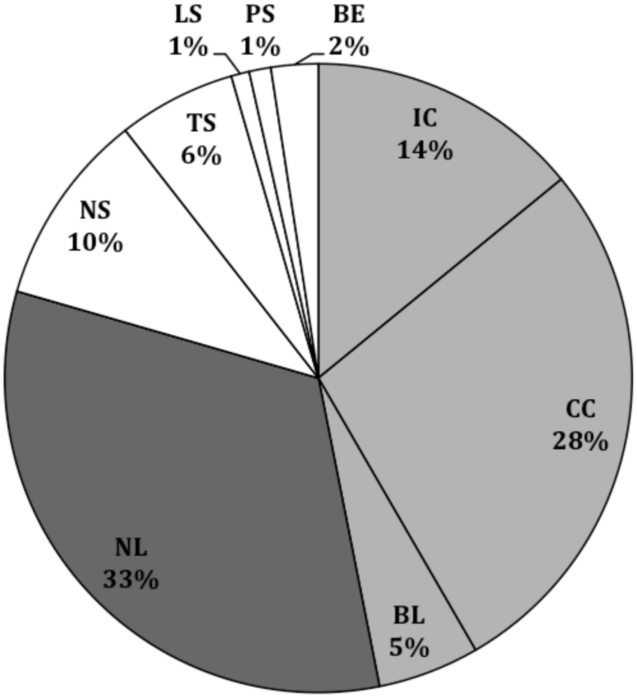

Figure 2.3 The percentage distribution of the convective structures over the northeast U.S. for the 2007 and aggregate 2002-2006 warm seasons (May-Aug). Cellular, nonlinear, and linear events are light shaded, dark shaded, and not shaded, respectively.

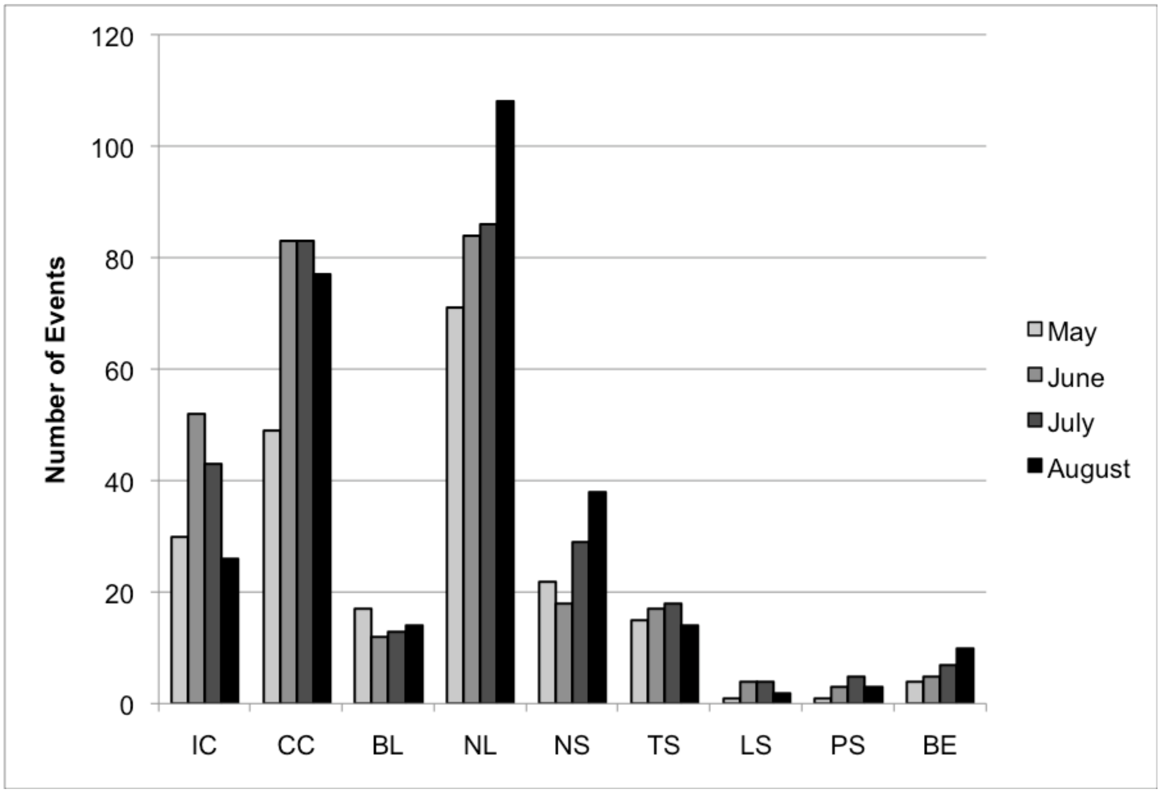

Figure 2.4 Monthly occurrence of northeast U.S. convective structures during the 2007 and aggregate 2002-2006 warm seasons.

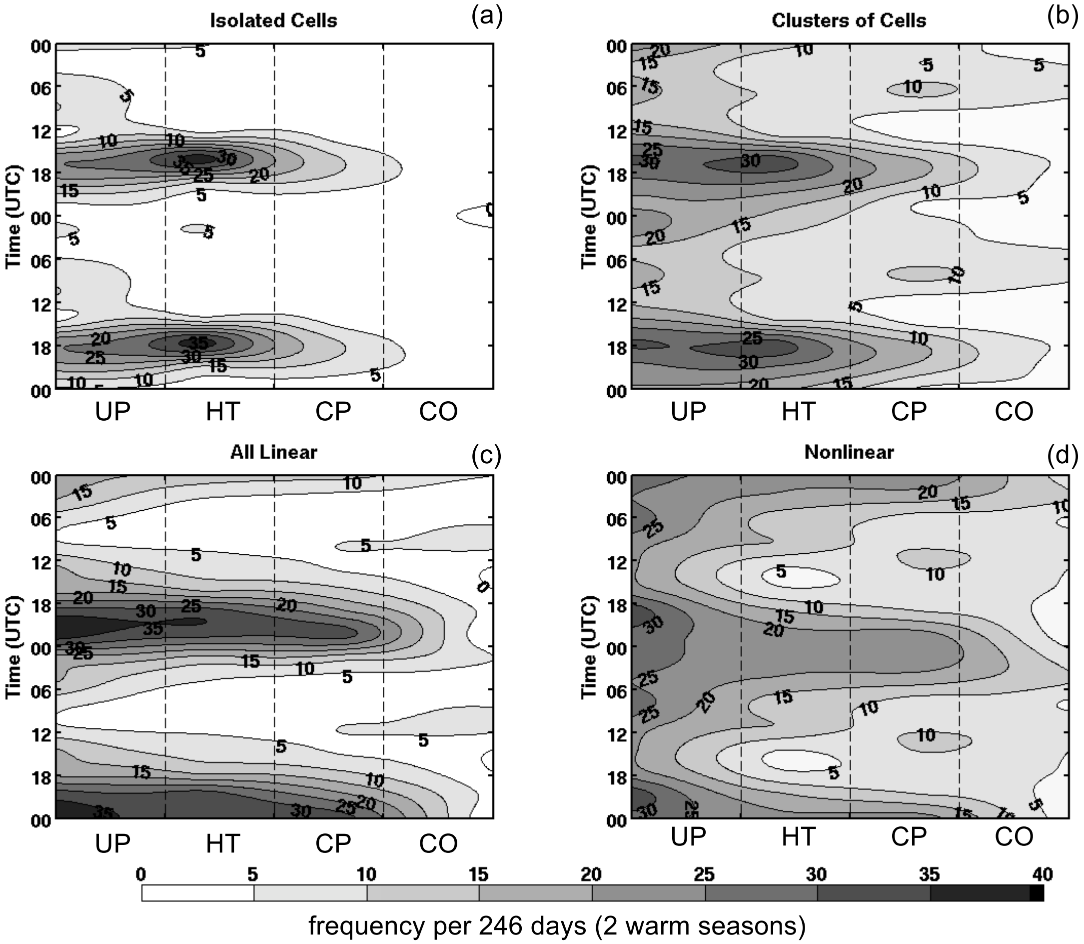

Figure 2.5 Hovmöller plot of the frequency of initiation as a function of time and region for (a) isolated cells, (b) clusters of cells, (c) all linear systems, and (d) nonlinear systems. Events are summed for both warm seasons (246 days) and normalized to account for variations in the region size.

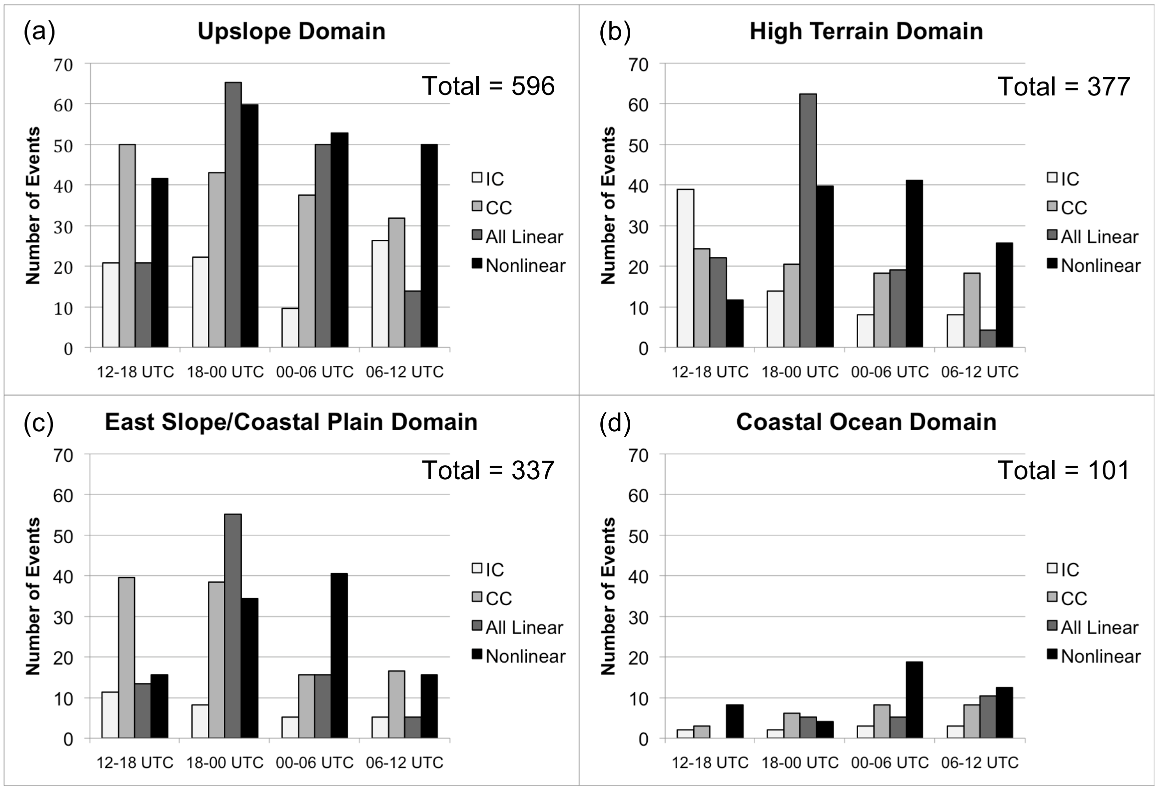

Figure 2.6 Number of events initiated for the IC, CC, all linear, and NL structures summed for each 6-h period during the day (in UTC) for the (a) upslope, (b) high terrain, (c) east slope/coastal plain, and (d) coastal ocean regions in Fig. 2.1. The number of events are summed for both warm seasons and normalized to account for variations in region size.

(a) T-24 MSLP, CAPE, 1000 θ_e & wnds (b) T-24 300 wnd, 500 hght, vor, wnd

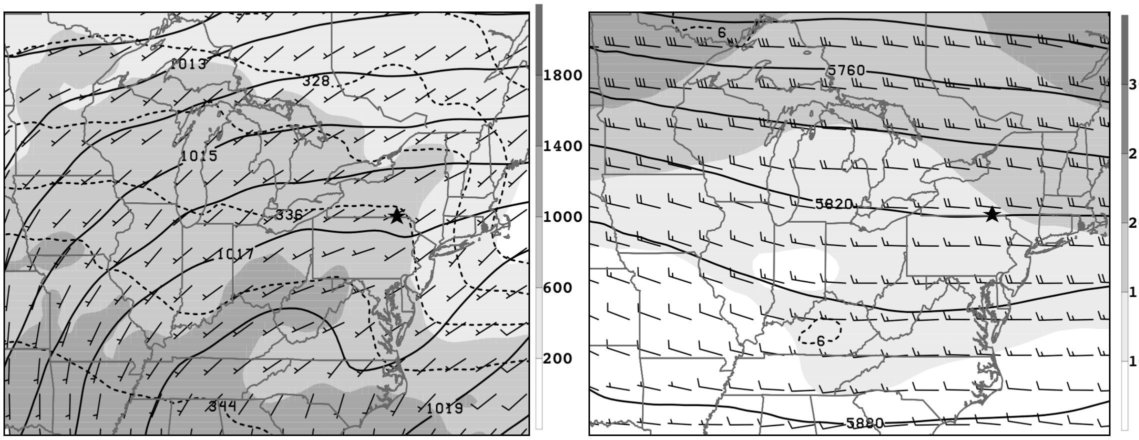

(c) T-12 MSLP, CAPE, 1000 θ_e & wnds (d) T-12 300 wnd, 500 hght, vor, wnd

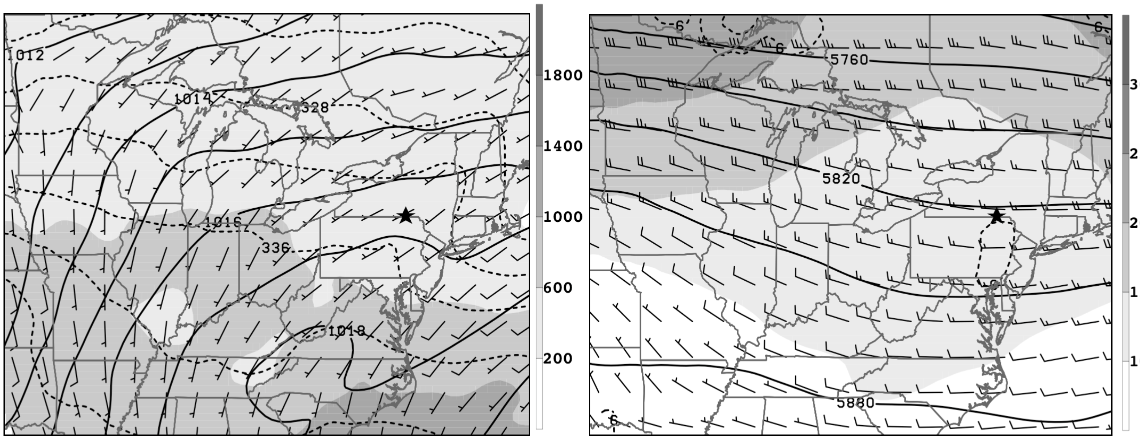

(e) T-0 MSLP, CAPE, 1000 θ_e & wnds (f) T-0 300 wnd, 500 hght, vor, wnd

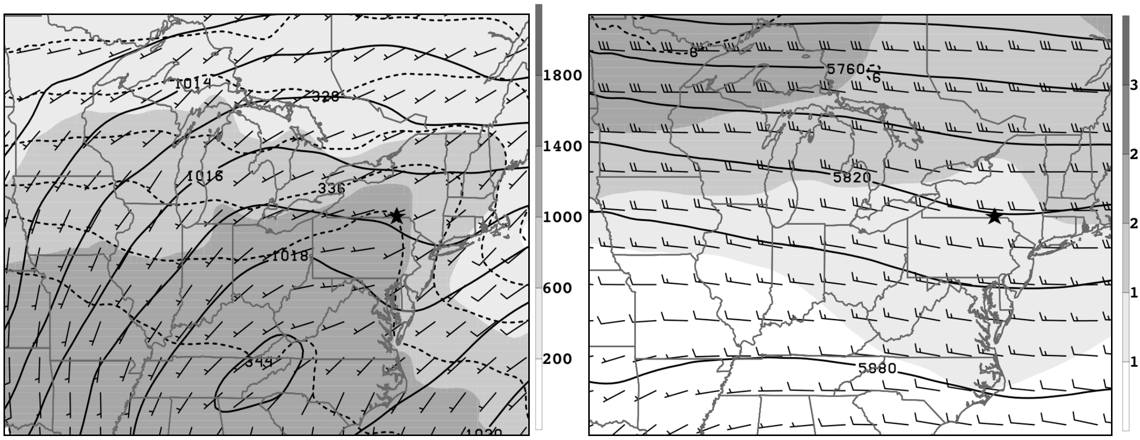

Figure 2.7 Feature-based NARR composites for cellular convective events in Table 2.1 showing (a) MSLP (solid every 1 hPa), 1000 hPa θ_e (dashed every 4 K), MUCAPE (shaded J kg^{-1}), and 1000 hPa wind (full barb = 5 m s^{-1}) at t-24h, (b) 500 hPa heights (solid every 30 dam), 500 hPa relative vorticity (dashed evry 6x10^{-5} s^{-1}), 300 hPa wind magnitude (shaded m s^{-1}), and 500 hPa wind (full barb = 5 m s^{-1}) for t-24h. (c) Same as in (a) but for t-12h, (d) as in (b) but for t-12h. (e) Same as in (a) but for t-0h. (f) Same as in (b) but for t-0h. A star indicates the compositing point. Geography is included only for scale reference.

(a) T-0 850 hght, wnd, tmpc, tmp adv (b) T-0 900 wnd, tmpc, frntgen

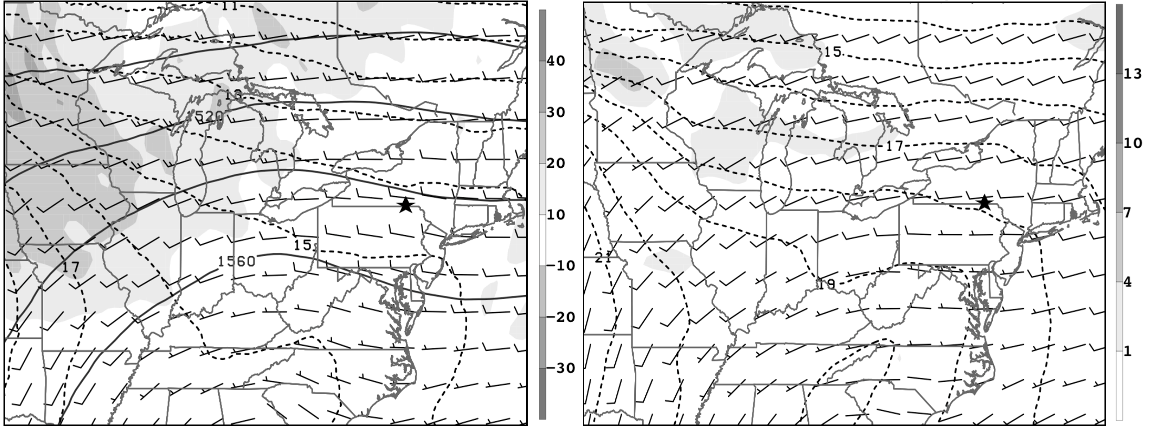

(c) T-0 850 hght, wnd, tmpc, tmp adv (d) T-0 900 wnd, tmpc, frntgen

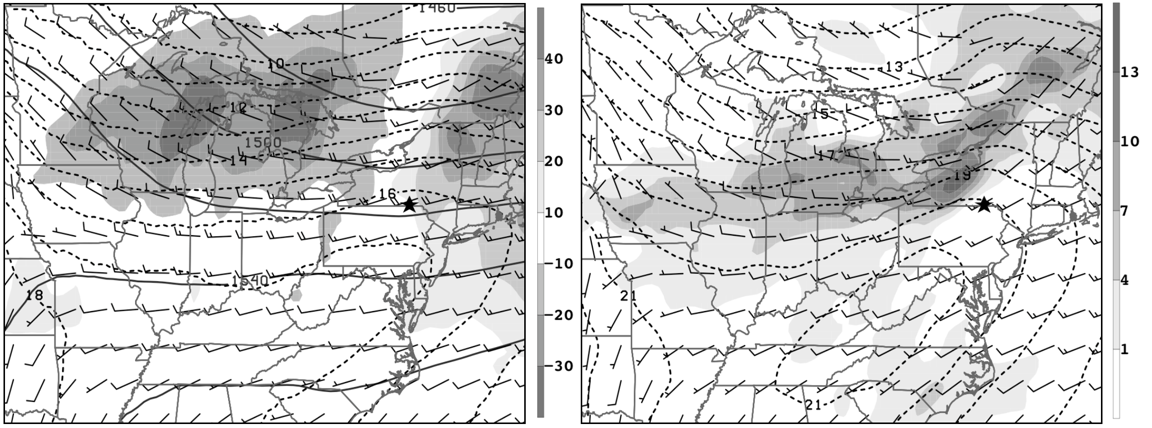

(e) T-0 850 hght, wnd, tmpc, tmp adv (f) T-0 900 wnd, tmpc, frntgen

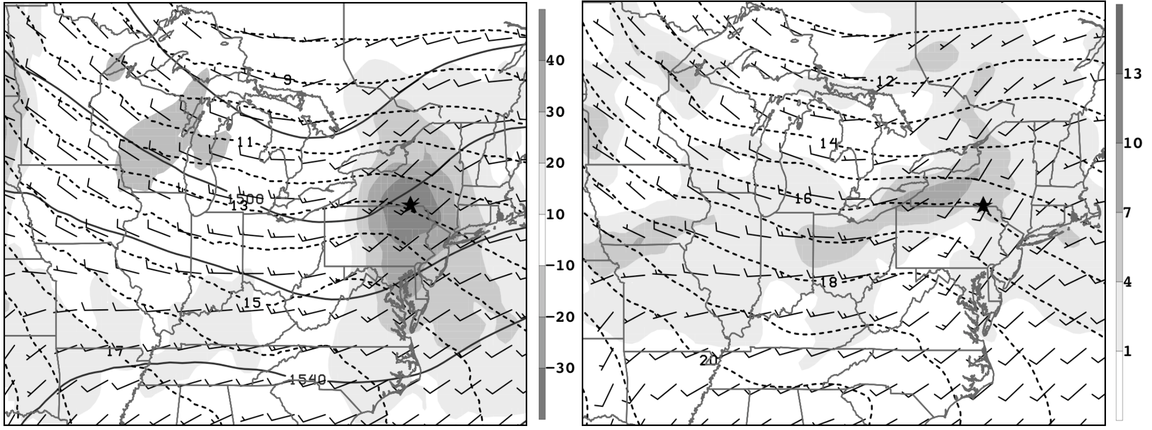

Figure 2.8 Feature-based NARR composite for cellular convection at t-0h showing (a) 850 hPa heights (solid every 20 dam), 850 hPa temperature (dashed every 1 ^{o}C), 850 hPa temperature advection (shaded every 10x10^{-6} ^{o}C s^{-1}), 850 hPa wind (full barb = 5 m s^{-1}), (b) 900 hPa temperature (dashed every 1 ^{o}C), 900 hPa frontogenesis (shaded every 3x10^{-2} K (100 km)$^{-1}$ (3 hr)$^{-1}$), 900 hPa wind (full barb = 5 m s^{-1}). (c) Same as (a) but for linear events. (d) Same as in (b) but for linear events. (e) Same as in (a) but for nonlinear events. (f) Same as in (b) but for nonlinear events. A star indicates the compositing point. Geography is included only for scale reference.

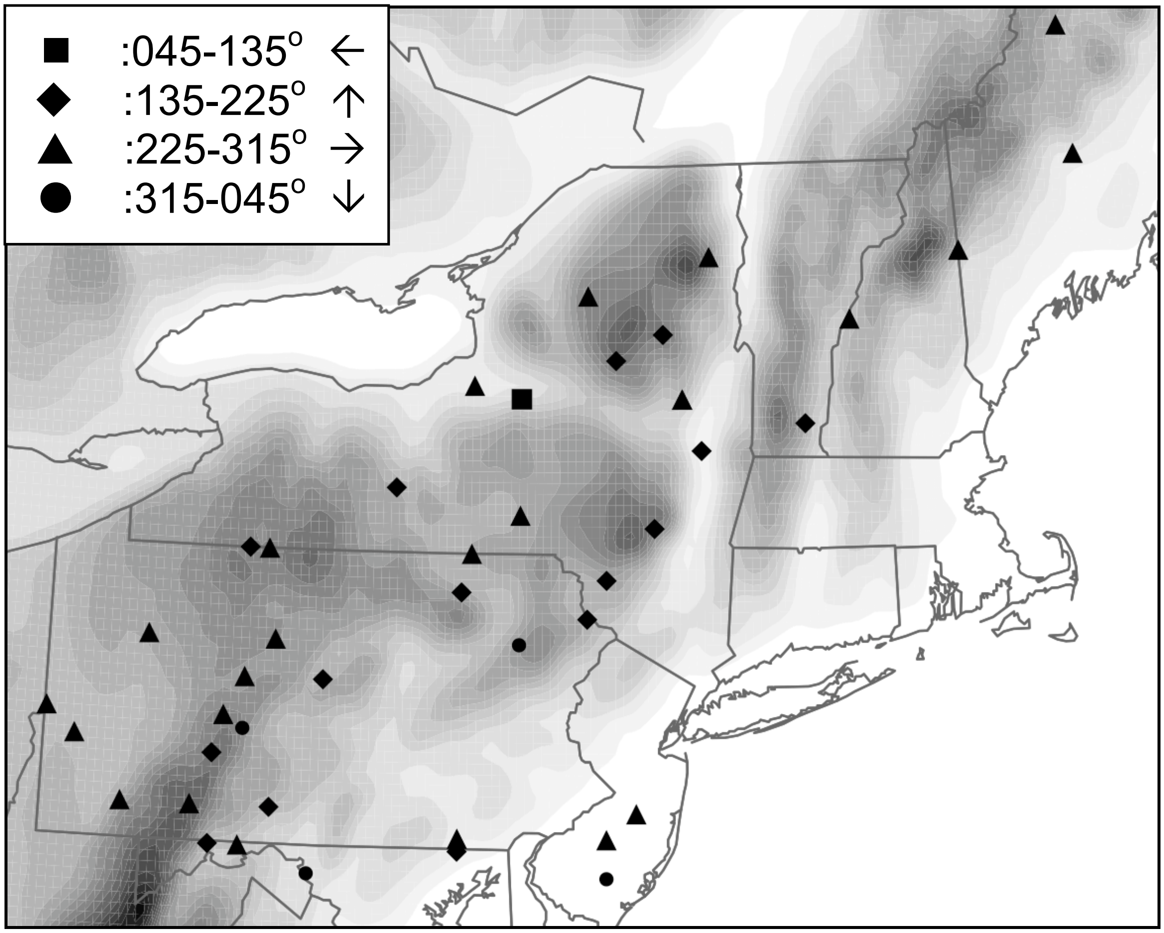

Figure 2.9 The initiation locations for 47 cellular events (Table 2.1) with respect to Northeast topography (shaded in m). The initiation is subdivided by 900 hPa flow regime (a) 045-135^o wind direction = square, (b) 135-225^o = diamond, (c) 225-315^o = triangle, and (d) 315-045^o = circle.

(a) T-24 MSLP, CAPE, 1000 θ_e & wnds (b) T-24 300 wnd, 500 hght, vor, wnd

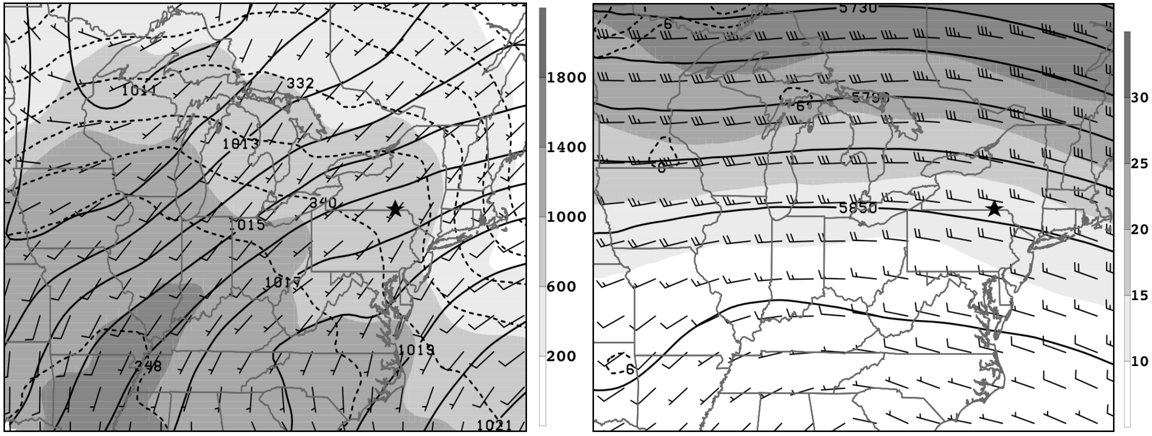

(c) T-12 MSLP, CAPE, 1000 θ_e & wnds (d) T-12 300 wnd, 500 hght, vor, wnd

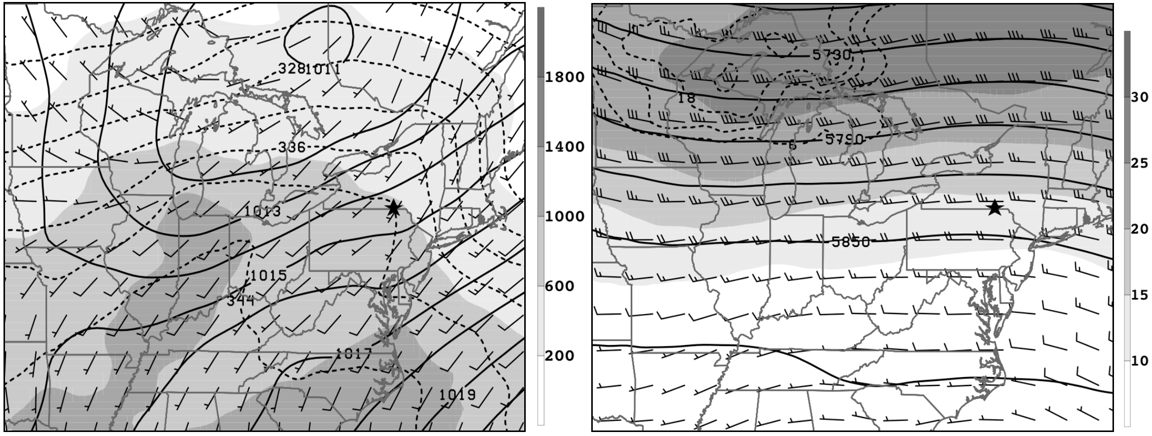

(e) T-0 MSLP, CAPE, 1000 θ_e & wnds (f) T-0 300 wnd, 500 hght, vor, wnd

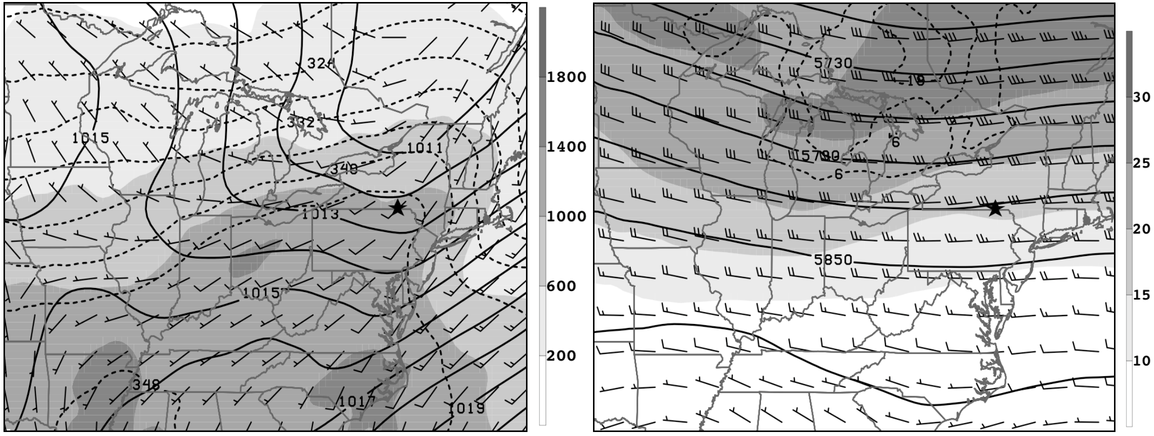

Figure 2.10 Feature-based NARR composites for linear convective events in Table 2.1 showing (a) MSLP (solid every 1 hPa), 1000 hPa θ_e (dashed every 4 K), MUCAPE (shaded J kg^{-1}), and 1000 hPa wind (full barb = 5 m s^{-1}) at t-24h, (b) 500 hPa heights (solid every 30 dam), 500 hPa relative vorticity (dashed every 6x10^{-5} s^{-1}), 300 hPa wind magnitude (shaded m s^{-1}), and 500 hPa wind (full barb = 5 m s^{-1}) for t-24h. (c) Same as in (a) but for t-12h, (d) as in (b) but for t-12h. (e) Same as in (a) but for t-0h. (f) Same as in (b) but for t-0h. A star indicates the compositing point. Geography is included only for scale reference.

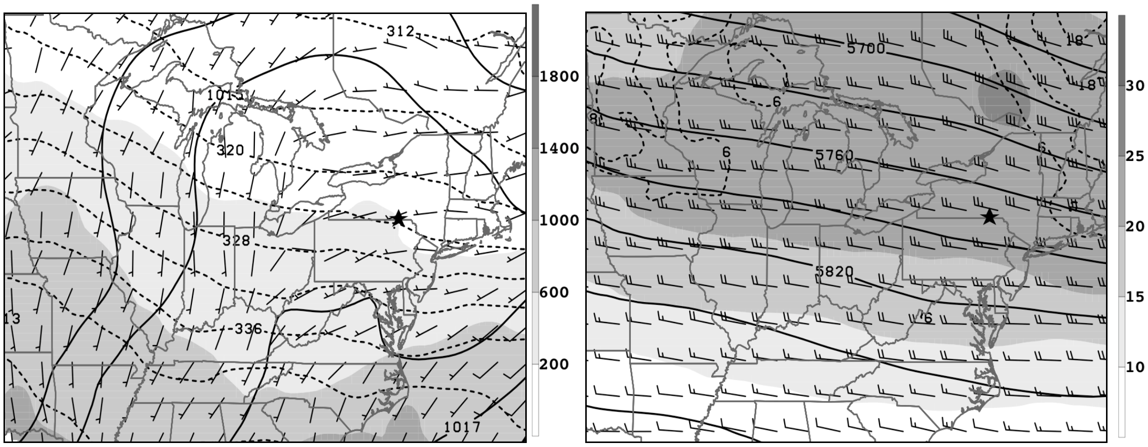
(a) T-24 MSLP, CAPE, 1000 θ_e & wnds

(b) T-24 300 wnd, 500 hght, vor, wnd

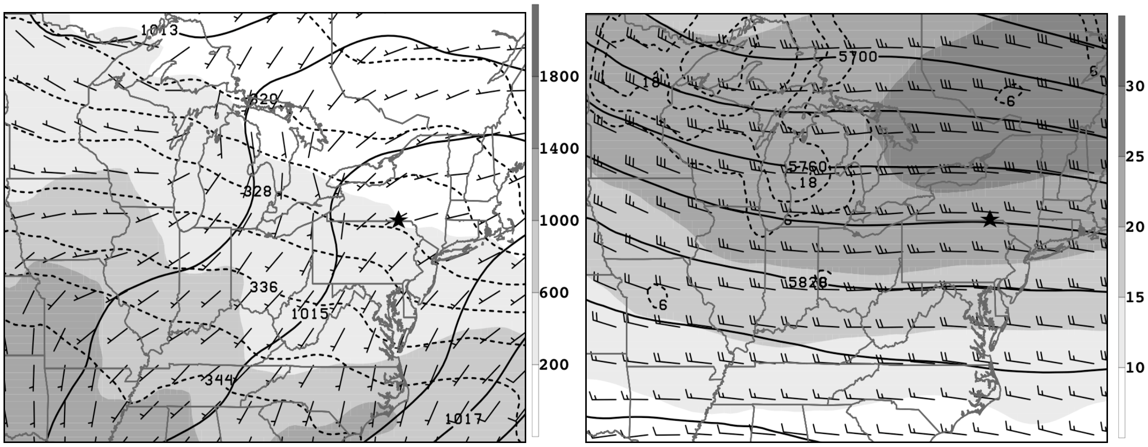
(c) T-12 MSLP, CAPE, 1000 θ_e & wnds

(d) T-12 300 wnd, 500 hght, vor, wnd

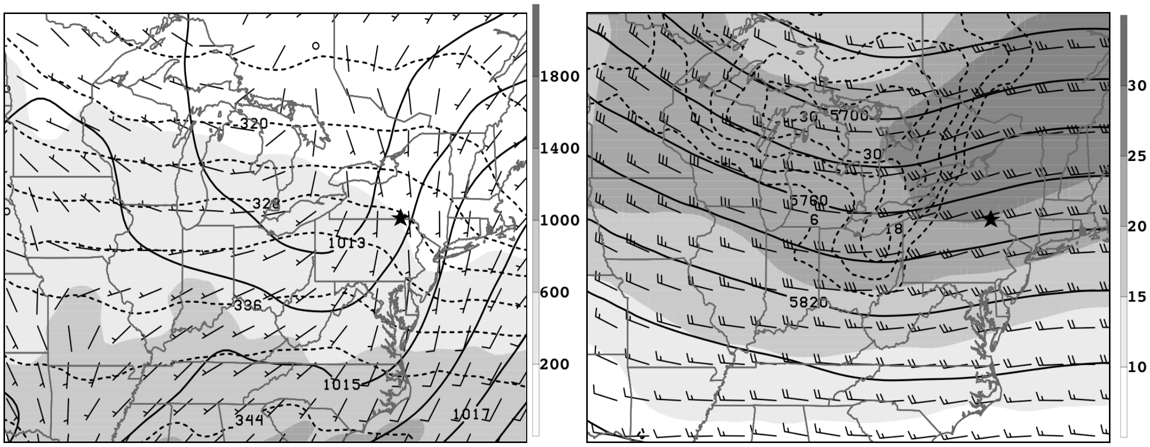
(e) T-0 MSLP, CAPE, 1000 θ_e & wnds

(f) T-0 300 wnd, 500 hght, vor, wnd

Figure 2.11 Same as Fig. 2.10 but for nonlinear events.

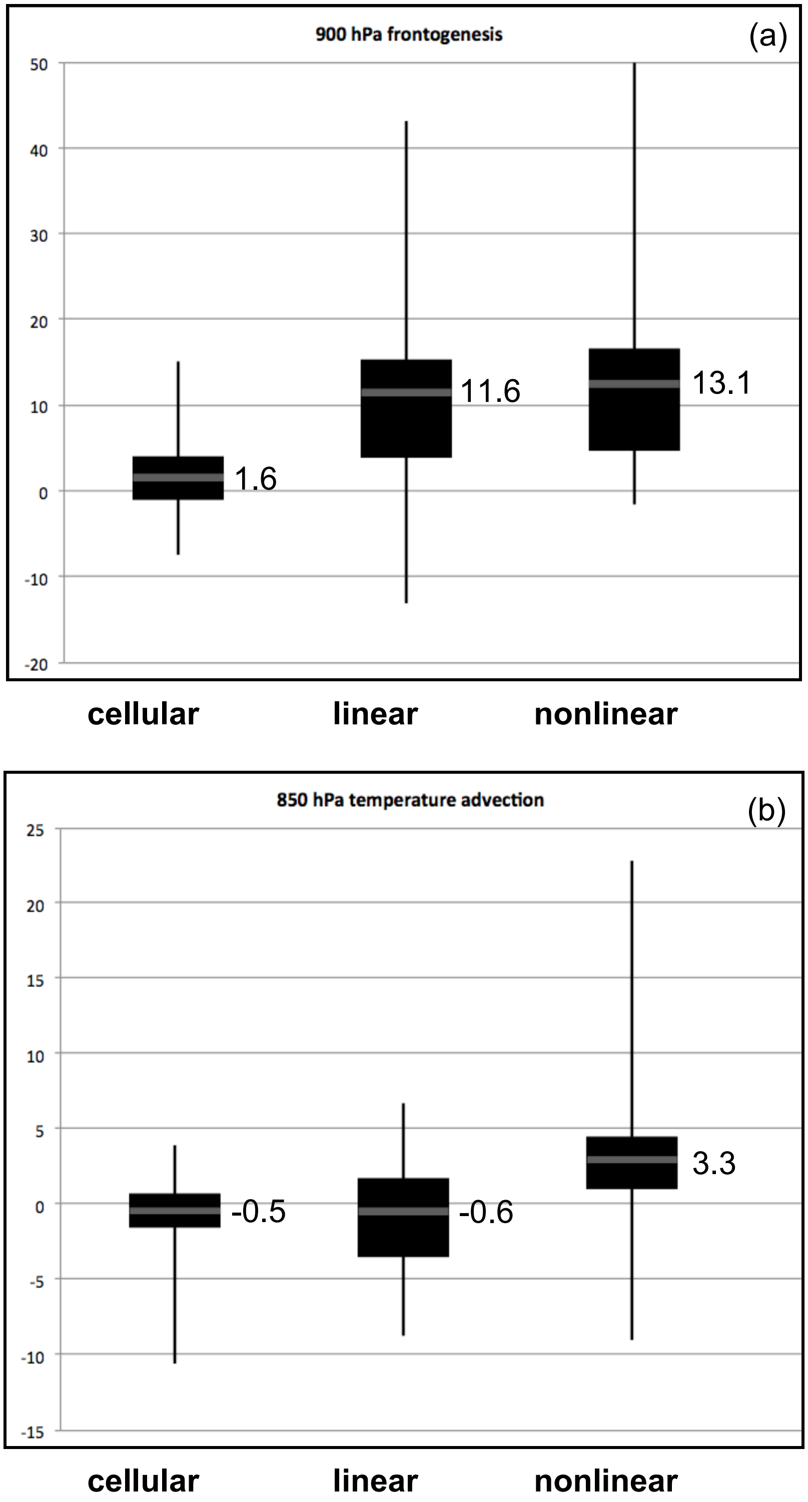

Figure 2.12 Box-and-whisker plots showing (a) 900 hPa frontogenesis (10^{-2} K 100 km^{-1} 3 hr^{-1}) and (b) 850-hPa temperature advection (10^{-5} ^{o}C s^{-1}) for the 47 cellular events, 38 linear, and 42 nonlinear events in Table 2.1. The bottom and top of the solid black box are the 25th and 75th quartile, respectively. The mean is denoted by a gray bar with its value also noted. The maximum and mimimum outliers are denoted by the vertical solid lines.

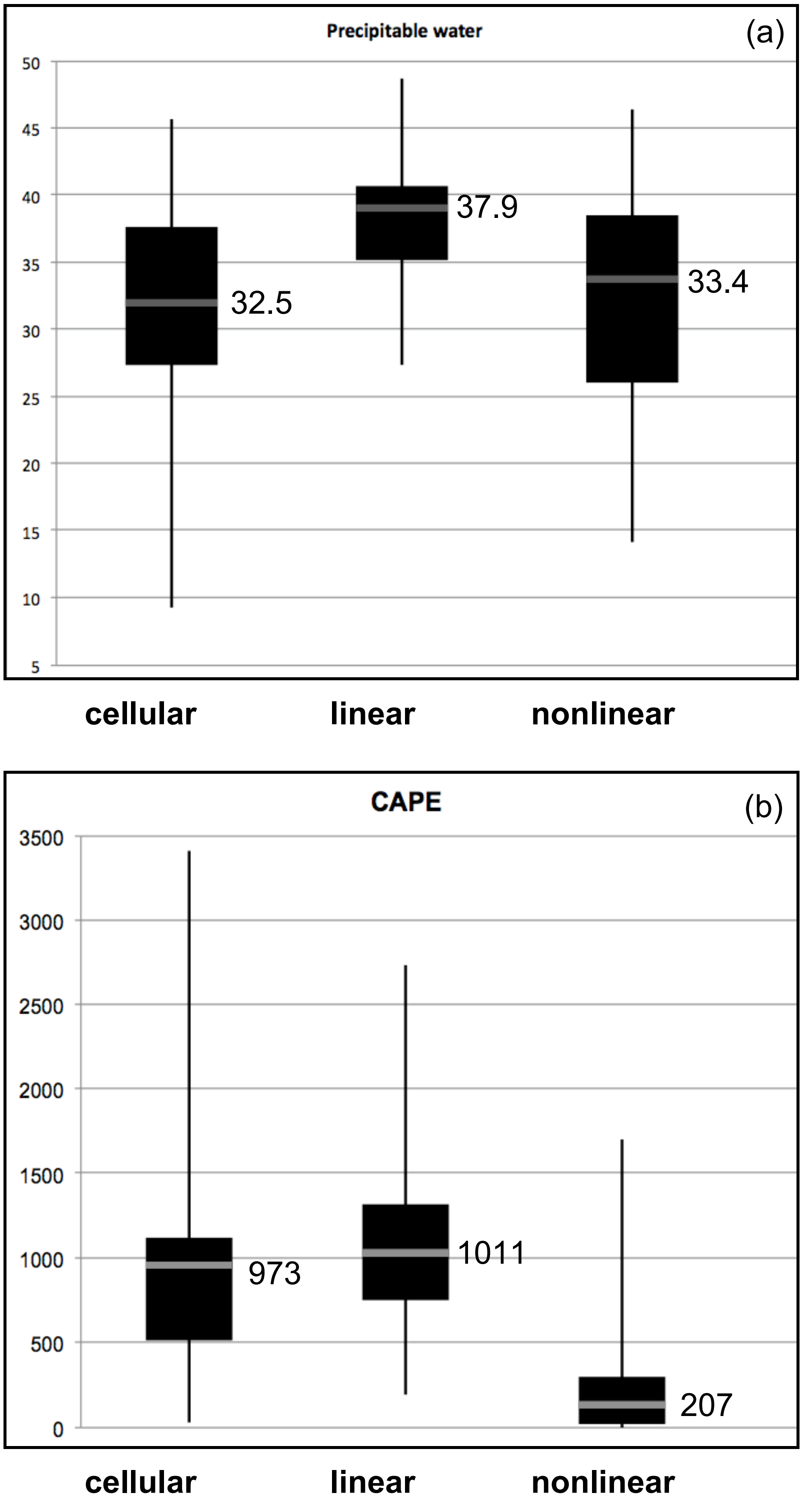

Figure 2.13 Same as Fig. 2.12 but for (a) precipitable water (mm), and (b) MUCAPE (J kg^{-1}).

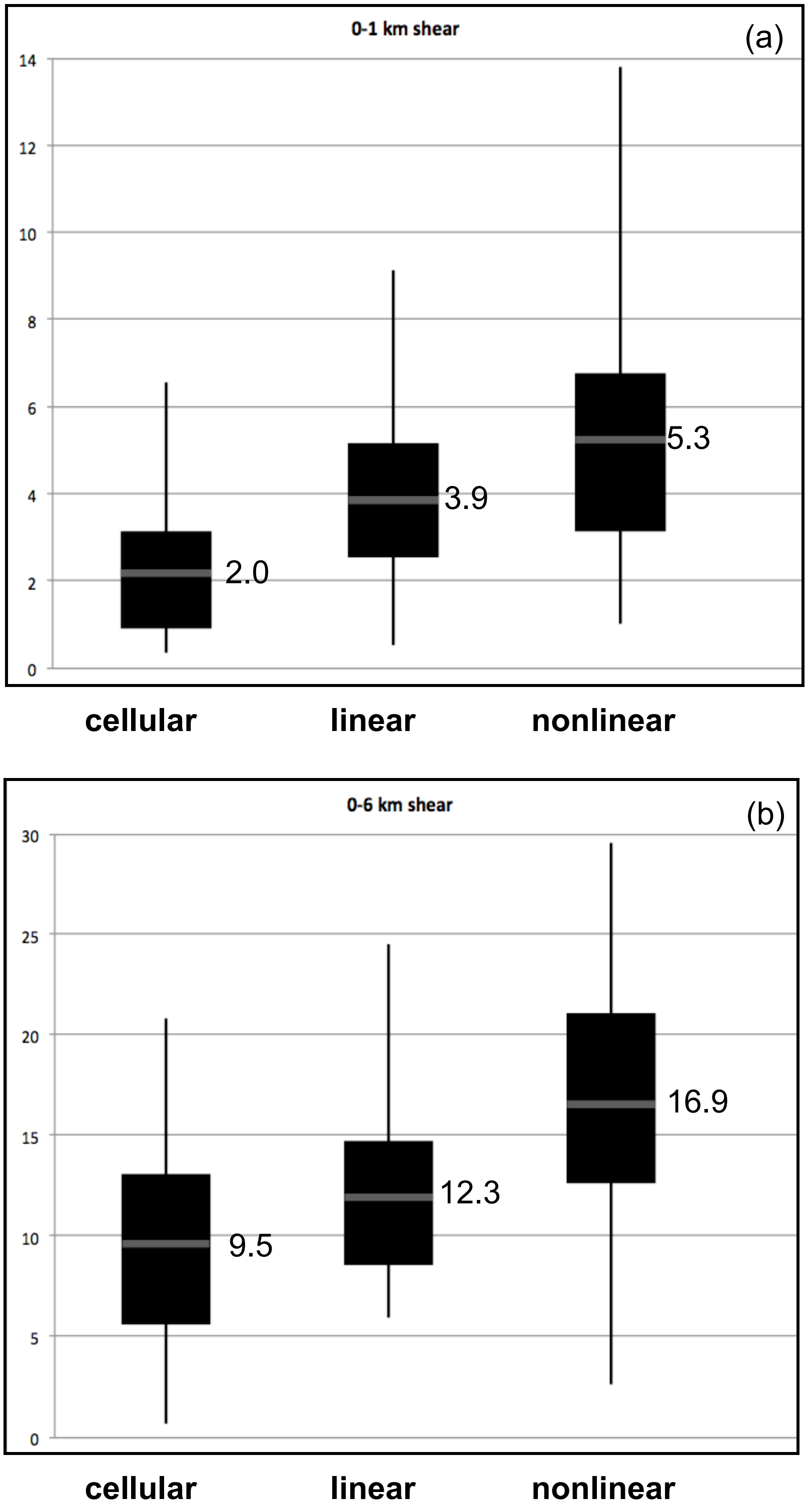

Figure 2.14 Same as Fig. 2.12 but for (a) 0-1 km shear (m s^{-1}) and (b) 0-6 km shear (m s^{-1}).

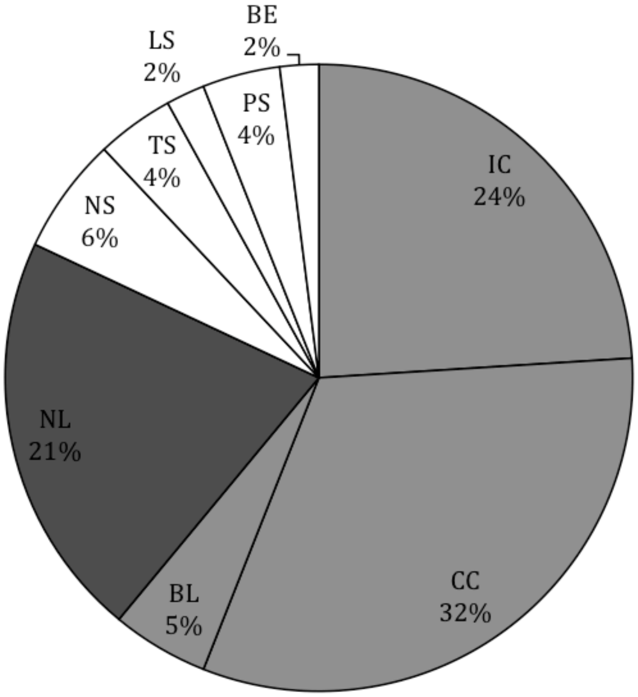

Figure 2.15 Structural distrubution of Midwest convective cases examined by Gallus et al. (2008) modified to account for the classification differences between this Northeast study and G08. See text for details.

Chapter 3:

Convective Storm Structures and Ambient Conditions Associated with Severe Weather over the Northeast U.S.

3.1 Introduction

Much of the previous literature on severe weather over the northeastern U.S. has focused on the large scale conditions associated with strong tornadoes and severe weather outbreaks (Johns 1984, Giordano and Fritsch 1991, Johns and Dorr 1996), while others have emphasized the role of terrain channeling in tornadogenesis over the Northeast (Riley and Bosart 1987, LaPenta et al. 2005, Bosart et al. 2006). There is still quite a bit we do not understand about the development of northeastern U.S. severe weather, especially concerning strong wind and hail events as well as non-outbreak conditions. From a predictability perspective, we currently do not know the most common type of severe weather associated with each organizational structure described in chapter 2. Also, the synoptic patterns, instability, and vertical shear associated with any severe weather event, not just outbreaks, are unknown. It is important to understand the conditions in which severe weather can develop over the region, as they may be more marginal than previously anticipated and compared to other regions of the country (i.e. central plains).

Section 3.2 describes the data and methods used in this chapter. Section 3.3 highlights the severe weather type associated with each convective organizational mode. Section 3.4 presents the synoptic and thermodynamic conditions associated with severe weather produced by each type of organized convection. Northeastern U.S. severe weather is compared to events over the central U.S. in section 3.5. The detailed synoptic and thermodynamic patterns associated with the severe convective types over the northeastern U.S. could not be compared to the central U.S, since Gallus et al. (2008) did not complete a synoptic breakdown associated with the various severe convective structures. Rather, we make several qualitative comparisons of various parameters between the Northeast and other studies investigating central Plains convection.

3.2 Data and Methods

a. Severe weather climatology

This paper classifies the organizational structures of convection over a domain covering the northeastern U.S. (Fig. 3.1) using the approach described in Lombardo and Colle (2010) and Gallus et al. (2008). For this chapter, the Northeast includes land areas only, excluding the Atlantic Ocean, since severe reports are typically only reported over land (Fig. 3.1). In Lombardo and Colle (2010), the convective structures over the northeastern U.S. were categorized through the manual examination of 2-km National Operational Weather Radar (NOWrad) reflectivity imagery every 15 minutes over two warm seasons (May-Aug), including 2007 and a second warm season of days randomly selected from 1 May – 31 August 2002-2006. The aggregate season was generated to compensate for the relatively large interannual storm frequency variability (Murray and Colle 2011). The dataset was used in this chapter, except that only those convective storms that produced severe weather were included in this climatology. Similar to

Lombardo and Colle (2010) and Gallus et al. (2008), the convective storms were categorized into three types of cellular convection (individual cells, clusters of cells, and broken lines), five types of quasi-linear systems (bow echoes, squall lines with trailing stratiform rain, lines with leading stratiform rain, lines with parallel stratiform rain, and lines with no stratiform rain), and nonlinear systems (cf. Fig. 2 in Lombardo and Colle 2010).

The severe weather days for the 2007 and aggregate warm seasons were identified utilizing both the Storm Prediction Center (SPC) and National Climatic Data Center (NCDC) storm reports archives. Over the Northeast, there were 310 severe weather events (2912 reports) over 118 days during the two warm seasons. A severe event is defined when a convective element produces at least one report of severe weather. Within one event, multiple reports may be recorded. Each storm report was manually matched to the convective structure that produced it. To increase the sample size of northeastern U.S. tornadoes, tornado reports were included for years when there is available NOWrad data (May-August 1996-2007), thus increasing the number of tornado reports from 56 (2002-2007) to 229 (1996-2007). Due to the differing record lengths between the tornado dataset (12 warm seasons) and the wind/hail dataset (2 warm seasons), it should be noted that a direct comparison could not be made between these datasets.

The convective classification was repeated for severe weather events over the Northeast southern coastal region, which includes New Jersey, Connecticut, Rhode Island, and several counties in southern New York (Fig. 3.1). For this coastal region, a similar identification and matching procedure was performed as described above for the Northeast; however, all 6 full warm seasons were used (May-August) from 2002-2007 in order to increase the sample size for the relatively small domain. In total, there are 256 severe events (1196 reports) over 166 days. For the coastal tornado events, an expanded dataset of tornado reports was generated from May-August of 1996-2007, which increased the number of the coastal tornadoes from 19 (2002-2007) to 41 (1996-2007). As with the Northeast data, the coastal tornado data and wind/hail data could not be directly compared with the coastal wind/hail results given the different set of years used.

Spatial composites of the ambient conditions were generated for the severe events over the coastal region. Since the impacts of the Northeast interior terrain on severe convection have been well documented (Wasula et al. 2002, LaPenta et al. 2005, Bosart et al. 2006), we focused our larger-scale composite near the less studied coastal region. To evaluate the synoptic and thermodynamic conditions that support severe weather over the coastal zone, spatial composites were constructed using the North American Regional Reanalysis (NARR) at 32-km grid spacing (Mesinger et al. 2006) for cellular (49 events), linear (45 events), and nonlinear (15 events) severe events from 2002-2007. For the composites, we used the closest 3-hr NARR time prior to the first severe weather report of a particular convective element. Since the coastal area of interest is relatively small, compositing with respect to geography preserves most of the flow structures associated with each event type while still relating the atmospheric features to various terrain and coastal features (i.e., Appalachian mountains, Atlantic coastal boundary). Variables such as 2D Miller (1948) frontogenesis and horizontal temperature advection are plotted at the levels in the lower troposphere at which the magnitudes are maximized.

Box-and-whisker plots were generated to illustrate the spread of the magnitude of particular atmospheric variables (e.g. most unstable CAPE, vertical shear) for each severe event type with the same convective structure. Rather than calculating area-averaged values over the full coastal domain (shaded area in Fig. 3.1) which would include some values over water interpolated to the coast areas given NARR's 32-km grid spacing, the atmospheric variables were taken from 4 representative points within the center of the coastal zone (Fig. 3.1), and those values were then averaged. These four points were moved to other inland locations within the coastal region, and the results did not change. Most unstable convective available potential energy (MUCAPE) is found by calculating CAPE using the equivalent potential temperature (θ_e) in each 30-hPa layer from 0 to 180 hPa above the surface and retaining the maximum CAPE value. Wind shear values are calculated using a vector difference between 2 layers (e.g. 0-1 km).

3.3 Northeast convective storm structures and severe weather

Figure 3.2 shows the percentage of severe events produced by each of the 9 convective organizational structures over the Northeast. While linear structures are the least common organization mode, comprising only a fifth of all convective modes (see Fig. 3 in Lombardo and Colle 2010), they are responsible for one third of all severe events (Fig. 3.2). Conversely, approximately half of all warm season convection organizes into cellular structures (Lombardo and Colle 2010), but they contribute to only ~39% of the severe events (Fig. 3.2). Nonlinear systems comprise about one third of all summertime convection as well as severe events.

Figure 3.3 illustrates the number of severe events, separated into severe wind, hail and tornado events, associated with each of the 9 organizational structures over the northeastern U.S. A bootstrap method (Zwiers 1990) was applied to the distribution of each type of severe event (wind, hail, tornado) to test for statistical significance between the 9 groups (e.g. clusters of cells, nonlinear). For each severe event type, a new distribution of convective structures of the same size was generated 1000 times by randomly selecting from the original sample. The 95% confidence intervals for each convective structure were determined by finding the 2.5th and 97.5th percentile of the sum of severe events (e.g. wind) produced by that particular convective type of the 1000 resamples. When comparing the results from the various severe weather types, if the 95% confidence intervals between the organizational structures do not overlap, the results are significantly different.

Severe (high) wind is the most common severe weather type over the Northeast (Fig. 3.3a) totaling 1969 wind reports, or 67.6% of the severe reports from the 2007 and aggregate warm seasons. The number of severe wind events for each of the 3 main convective types (cellular, linear, nonlinear) is comparable. However, differences arise when considering the contribution to severe wind events from each of the individual 9 sub-structures. For cellular structures, clusters of cells produce significantly (95% confidence) more severe wind events than isolated cells, while for linear convection, linear convection with no stratiform and trailing stratiform precipitation produce significantly more (95% confidence) severe wind events compared to the other linear types (leading stratiform, parallel stratiform and bow echoes). Nonlinear convection is associated with ~8 more severe wind events compared to cellular clusters, though this difference is not statistically significant.

Hail reports comprise approximately one third of all severe weather reports (927 reports) over the northeastern U.S. during the two warms seasons. Cellular convection is responsible for ~1.3 times as many hail events as both linear and nonlinear systems (85% significance level; not shown). Clusters of cells are the primary cellular structures responsible for the hail events, with nonlinear convection producing only slightly fewer (~4) events, although the difference is not statistically significant. Linear systems with trailing stratiform and no stratiform rain are the most common hail-producing linear structures.

For the expanded 1996-2007 year period with 229 tornadoes, Northeast cellular and linear convection produce approximately the same number of tornado events (~9 per year), which is significantly (95% confidence) more than produced by nonlinear systems (~2 per year; Fig. 3.3c). Considering the individual cellular structures, there is no statistical difference between the number of isolated cells and clusters of cells that produce tornado events. The same is true for the 5 types of linear structures.

To assess the risk of severe weather from each organizational structure, the number of severe reports per event (severe and non-severe) was calculated for each of the 9 convective types over the Northeast (Fig. 3.4). The number of reports depends not only on the severity of storm, but also on the storm areal coverage (e.g. trailing stratiform lines cover a greater area than isolated cells) and the storm duration. Of the 9 convective types (Fig. 3.4a), lines with trailing stratiform precipitation have the greatest frequency of severe wind (5.9 reports per event), followed by bow echoes (3.3 reports per event). Although convective lines are less common than cellular and nonlinear convection (Lombardo and Colle 2010), linear systems result in more severe wind reports per event at the 99% significance level (not shown). The other organizational structures only produce up to ~2 reports per event. However, for cellular convection, cellular clusters have 7 times the number of reports per event (2.1) compared to isolated cells (0.3). Therefore, not only are cellular clusters more common than isolated cells (Lombardo and Colle 2010), they are also more likely to produce more severe wind.

Cellular clusters produce the greatest number of hail reports per event (95% level with the exception of TS systems at 90%), with 1.6 reports per events which, compared to other cellular structures, is 1.5 times greater than for broken lines and 4 times larger than for isolated cells (Fig. 3.4b). For linear systems, the largest frequency of hail reports are from trailing stratiform lines, followed by lines with no stratiform, bow echoes, and line-parallel stratiform systems. No leading stratiform lines produced hail in our dataset. Nonlinear systems produce only 0.5 hail reports per event. Northeast tornado frequency is dominated by bow echoes (Fig. 3.4c). Cellular clusters, nonlinear systems, lines with trailing and no stratiform have similar frequencies, while the remaining convective structures produced no tornadoes in the period of study (Fig. 3.4c).

3.4 Coastal convective storm structures and severe weather

a. Distribution

The type of severe weather threat posed by organized convection over the Northeast coastal region (cf. Fig. 3.1) differs from the Northeast as a whole. Over the 2002-2006 warm seasons, there are 1196 coastal storm reports: 76.7% high wind, 21.7% hail, and 1.6% tornadoes. As compared to the fractional breakdown of severe weather types over the Northeast, the percentage of severe wind reports over the coastal area is 9.1% larger, the percentage of tornado reports near the coast doubles to 1.6%, and hail reports are ~10% less common over the coastal zone.

Coastal wind events are primarily caused by cells and lines (Fig. 3.5a), with only ~11% of severe wind events produced by nonlinear convection. Clusters of cells are statistically (95% confidence) the most common cellular structure associated with high wind events, while linear systems with trailing stratiform and no stratiform precipitation are the most common linear structures (95% confidence).

Cellular convection is associated with the largest number of coastal hail events at the 95% significance level, followed by linear convection, then finally nonlinear convection (Fig.

3.5b). While clusters of cells produce a larger number of hail events compared to isolated cells, this difference is not statistically significant. Linear structures with trailing stratiform and no stratiform precipitation are the most common linear structures associated with hail events at the 90% significant level (not shown).

Coastal tornado events are not produced by any one preferred convective organizational structure (Fig. 3.5c). One reason may be the limited sample size of events (41 tornadoes, 27 tornado events), but the results suggest that tornadoes over the Northeast coastal zone are equally likely to develop from cellular, linear and nonlinear structures.

b. Diurnal variations in coastal severe weather

The distribution of the 3 types of coastal severe weather reports is examined as a function of time of day (Fig. 3.6). Most (~75%) severe wind and hail reports occur from 1400 to 2000 EDT (1800-0000 UTC), with a tail in the distribution toward the late-evening hours of 2000-2300 EDT (0000-0300 UTC; Figs. 3.6a,b). The diurnal distribution for the tornado reports is less clear (Fig. 3.6c), though the 2100-0000 UTC maximum for all structures is statistically significant (95% level). While linear convection produces tornadoes almost exclusively from 1800-0000 UTC, cellular convection can become tornadic between 1500-0600 UTC, with a maximum from 2100-0000 UTC. Nonlinear systems produce tornadoes at any time of the day, with no clear temporal maximum.

c. Composites

1. Cellular storms

Certain organized convective structures are related to different severe weather types over the coastal zone. For example, hail is most often produced by cellular convection, while severe wind is primarily caused by cells and lines. Therefore, it would be useful to identify the environments that support severe weather associated with the 3 main organizational convective structures (cellular, linear, nonlinear). Figure 3.7 shows the NARR composite fields at the closest 3-hr time prior to the coastal cellular severe events. During these events (t-0h), there is a surface pressure trough in the lee of the Appalachians (Fig. 3.7a), which is a persistent feature during the past 24 h (not shown). A manual investigation of the individual events in the composite revealed that for ~38% of cellular severe events, this trough was not associated with a surface cold front, but rather a lee trough or some other type of inverted or mobile trough. Of the remaining events, 17% were associated with a surface cold front, 19% formed along the warm side of a stationary front, 11% along a warm front, 12% near a surface anticyclone, and 3% occurred after cold frontal passage (not shown).

At low-levels, the severe cellular storms are supported by moderate instability (mean MUCAPE > 1000 J kg^{-1}), with an axis of warm, moist air (1000-hPa θ_e ~340 K) extending over the coastal zone (Fig. 3.7a). Just above the surface, 950-hPa frontogenesis (>35×10^{-2} K 100 km^{-1} 3 hr^{-1}) is evident at the leading edge of a thermal ridge over northern New Jersey (Fig. 3.7b), with ageostrophic frontal circulations contributing to the ascent by causing in the lower-levels over NJ and southern NY (Fig. 3.7d), which helped initiate the convective storms (not shown). The magnitude of the composite 950 hPa frontogenesis for cellular events is relatively small in part from the composite smoothing, since there are a couple of events with frontogenesis values

$\geq 0.76 \times 10^{-2}$ K 100 km^{-1} 3 hr^{-1}. However, the 950 hPa frontogenesis located over northern NJ and southern NY does lead to a maximum in upward motion of -12×10^{-4} Pa s^{-1} at 950-900 hPa (not shown) near this same region, and contributes to the southern area of 800-400 hPa upward motion in Fig. 3.7d. For those cases in which the frontal forcing is too weak, convection can initiate from upslope flow along the windward terrain slopes over the northeastern U.S. (Lombardo and Colle 2010), as well as cold pool boundaries from other convection (Weckwerth and Wakimoto 1992).

Slightly east of the coastal frontogenesis maximum and centered over Long Island is a localized area of 900-hPa warm air advection ($>30\times10^{-6}$ °C s^{-1}; Fig. 3.7c). On average, this warming in the low-levels helped destabilize the column (not shown). The composite warm air advection is maximized at this level (not shown) and develops within 12 h leading up to the severe event, as 900-hPa winds rotate from westerly to southwesterly and the thermal gradient strengthens at this level.

At 300-hPa (Fig. 3.7d), the jet maximum (~20 m s^{-1}) is located ~1000 km poleward of the coastal region of interest, causing weak mid- and upper-level ascent due to ageostrophic jet circulations over northern NJ, northeastern PA, and eastern NY. Inspection of each cellular event reveals that ~25% develop in conjunction with a 500 hPa mid-level trough in close proximity. However, due to the wide variety of synoptic regimes that exist in the mid-levels during these severe coastal events, there is there is no mean trough in the composite field (Fig. 3.7d). Furthermore, there is Q-vector convergence over northern NJ, southern NY, and Long Island at 500 hPa (Fig. 3.7d) highlighting the quasi-geostrophic (Q-G) mid-level forcing for ascent during these events.

2. Linear systems

Twelve hours prior to a severe linear event (t-12h), there is a surface pressure trough in the lee of the southern and central Appalachians. A second trough, associated with a surface cold front, is ~450 km to the northwest over the lower Great Lakes, with the associated cold advection to the west of the trough (Figs. 3.8a,c). The individual events show that 73% of all linear events have a trough within the Appalachian lee with a frontal boundary to the west at t-12h, while only 36% of cellular events exhibit this synoptic pattern. An elongated area of 950-hPa frontogenesis ($>55\times10^{-2}$ K 100 km^{-1} 3 hr^{-1}) from northeastern Ohio into western New York (Fig. 3.8b) parallels the cold front, with weak warm air advection at 900 hPa (10×10^{-6} °C s^{-1}) over New Jersey, Long Island, and southern Connecticut.

By the time of the event (t–0h), the Appalachian lee trough amplifies in situ, while the surface cold front moves eastward toward the coast (Fig. 3.9a). The frontal position is less apparent in the composite than t-12h, since ~20% of the cold frontal boundaries merge with the pre-existing trough in the Appalachian less, while in a few other cases the front either stalled to the northwest or weakened. A majority (53%) of the severe linear events develop in association with the lee or prefrontal trough, while only 13% develop along the cold front that moves into the lee. The rest develop along a warm front (9%), stationary front (9%), or under a surface anticyclone (13%). Both the 950 hPa frontogenesis maximum (Fig. 3.9b) as well as the leading edge of 900-hPa cold air advection (Fig. 3.9c) are now located over the Appalachian terrain. The frontogenesis maximum over northern PA - southern NY state is greater in the linear composite than the cellular composite at the 80% level, indicating that it is a fairly distinguishing feature between the two convective types.

At t-0h, thermal ridge extends along the coastal plain from the southeastern U.S. to the Northeast, with average MUCAPE values exceeding 1000 J kg^{-1} over much of the coastal region and a 1000-hPa θ_e between 340 K and 344 K (Fig. 3.9a). A localized region of warm air advection (>70x10^{-6} ^{o}C s^{-1}; Fig. 3.9c) at 900 hPa is located to the east of a cold front along coastal southern New England, which helps destabilize the lower troposphere (not shown). A maximum in frontogenesis (>55x10^{-2} K 100 km^{-1} 3 hr^{-1}; Fig. 3.9b) develops over the coastal zone, with the associated ageostrophic circulations providing a mechanism for low-level ascent to support the severe weather (not shown). Approximately one quarter of the individual linear severe events have a larger frontogenesis values compared to the composite value, with the largest contribution to the vertical motion occurring in the lower levels. The magnitude of the temperature advection and frontogenesis averaged over the coastal domain for the composite linear event is not statistically different than the cellular composites.

Meanwhile, a broad 500 hPa mid-level trough moves eastward, with the associated downstream Q-vector convergence providing Q-G mid- and upper-level ascent over the coastal zone (Fig. 3.9d). Though the magnitude of the Q-vector convergence for linear events is 1.5 times larger compared to the cellular composite, this Q-vector convergence averaged over the coastal zone is not statistically different from the cellular composites (not shown). Over 80% of all severe linear events in this study develop under westerly to southerly 500-hPa flow, as compared to 60% for cellular events, yielding a more robust mid-level trough in the composite for linear events. However, only ~44% of the linear events are associated with a 500-hPa trough, while the other events either have a trough well to the north or west of the severe convection (~35%) or develop under an anticyclone or with no trough in close proximity (~20%). This large-scale variability during severe convective events is not uncommon. For example, Coniglio et al. (2004) found similar results for derechos that form the east of the Rockies, with the convection developing downstream of a 500 hPa trough (~40%), under a mid-level ridge (~20%), and under zonal mid-level flow (~12%).

At upper levels, linear severe convection develops near the right entrance region of a 300-hPa jet (>30 m s^{-1}), a favorable region for ascent as indicated by the upward vertical motion at mid to upper levels (Fig. 3.9d). Clark et al. (2009) showed that severe weather over the central Plains develops within the right entrance region of an upper level jet, especially severe wind, as well as along the jet axis in the exit region during hail and tornado events. They showed that there is a thermally direct circulation within the entrance region, with convergence in the lower-levels, divergence in the upper-levels, and deep ascent through the troposphere, consistent with the 4-quadrant jet model.

3. Nonlinear systems

At t-12h (Fig. 3.10), a surface trough resides in the Appalachian lee, with a weak north-south θ_e gradient across the Northeast at 1000 hPa (Fig. 3.10a). There is weak cold air advection over much of the Northeast, while weak warm air advection overlies Long Island and southeastern New Jersey, with the maximum located just east of the Maryland and Delaware coasts (Fig. 3.10b). Meanwhile, a 500 hPa trough is located over the Great Lakes (Fig. 3.10c), with Q-vector convergence downstream of the trough extending over the coastal zone, supplying a mechanism for Q-G ascent as revealed by the 800-400 hPa vertical motion (Fig. 3.10c). The core of a 300-hPa jet is located over the southeastern Great Lakes at this time (Fig. 3.10c).

By t-0h (Fig. 3.11), a mean surface low develops over Chesapeake Bay (Fig. 3.11a), with half of the composite members having a closed surface cyclone in the area. Only 20% of all severe cellular events and 11% of all severe linear events have a closed low in a similar region in the Appalachian lee. The Atlantic coastal plain environment remains weakly unstable compared to 12 h prior (Fig. 3.10a), with MUCAPE values approaching 600 J kg^{-1} and an average θ_e of ~332 K (Fig. 3.11a). An elongated area of enhanced 950-hPa frontogenesis (>15x10^{-2} K 100 km^{-1} 3 hr^{-1}) extends along the northern and northeastern edge of the surface cyclone from the Maryland-Pennsylvania border westward to southern New Jersey, as well as along a warm frontal boundary over Long Island (Fig. 3.11b), supporting convective development. Approximately 80% of the individual nonlinear severe events occur in association with stronger frontogenesis compared to the composite value. As the 900-hPa trough over the Atlantic coastal plain amplifies and the surface cyclone develops, warm air advection develops across New Jersey, Long Island, southern New York and western Connecticut (Figs. 3.10b, 3.11c). Maddox and Doswell (1982) highlighted the role of low-level warm air advection in initiating and organizing mesoscale convective complexes (MCCs).

At t-0h, the 500 hPa trough is located ~600 km to the west-northwest of the severe weather reports (Fig. 3.11d). Manual inspection revealed that 87% of the nonlinear severe events developed with southerly to westerly mid-level flow and ~80% were under the influence of a mid-level trough (not shown). At this time, there is 500 hPa Q-vector convergence over the coastal region, especially in northern New Jersey, eastern Connecticut and Rhode Island, providing mid- and upper-level Q-G ascent (Fig. 3.11d). The magnitude of Q-vector convergence over the coastal zone for nonlinear severe events is 2.5 times greater than during linear events and 4 times greater than during cellular events. These differences are significantly significant (95% level), indicating that mid-level forcing is an important ingredient during nonlinear severe events. In conjunction with the 950 hPa frontogenetical lift, localized 900 hPa temperature advection, and the mid-level Q-G ascent, severe nonlinear convection develops in the right entrance region of a 300 hPa jet (>25 m s^{-1}; Fig. 3.11d), which is within a region of ascent at mid-levels.

3.5 Discussion

a. Comparison of convective parameters between the central U.S. and Northeast

It is well known that both CAPE and vertical wind shear are important parameters in determining the strength and organization of convective storms (e.g. Weisman and Klemp 1982, Parker and Johnson 2000). However, several studies have highlighted the large variability in CAPE and wind shear values in which central U.S. severe storms can develop (Evans and Doswell 2001, Thompson et al. 2003, Cohen at al. 2007). Therefore, while the Northeast composites above (Figs. 3.7-3.11) provide a good depiction of the mean dynamic and thermodynamic conditions for the 3 types of convective structures, there is variance in the flow patterns and convective ingredients that are important, which have been noted by others (Evans and Doswell 2001, Thompson et al. 2003, Cohen at al. 2007). To highlight both the mean and the variability for each convective type near the coast, box-and-whisker plots are shown for MUCAPE and wind shear values averaged for 4 points over the coastal zone (see Fig. 3.1). Some of these results are compared with previous studies over the central U.S.

The mean MUCAPE values for both cellular and linear severe events near the coast are ~1200 J kg^{-1}, while for nonlinear events the mean is ~460 J kg^{-1} (Fig. 3.12a), and this difference in MUCAPE is statistically significant at the 95% level. Thompson et al. (2003) found that the mean mixed-layer CAPE (MLCAPE) for nontornadic supercells and nonsupercells were 1645 J kg^{-1} and 1280 J kg^{-1}, respectively. Thus, the mean MUCAPE for severe cells near the coast is similar to the average MLCAPE for central Plains nonsupercells. For Northeast severe linear events, the mean MUCAPE (1200 J kg ^{1}) is half as large as the mean CAPE observed during mature derecho producing MCSs over the central U.S. (2394 J kg^{-1}, Coniglio et al. 2004). MUCAPE values during coastal Northeast severe linear events (Fig, 3.12) are more consistent with MLCAPE seen during non-severe MCSs over the central Plains (Cohen et al. 2007). However, there is a large range in the MUCAPE values near the coast, with both the linear and nonlinear events occurring with instability as low as a few J kg^{-1}. On the other end of the spectrum, coastal Northeast cellular and linear events can develop in 3000 J kg^{-1} of MUCAPE, with nonlinear MUCAPE reaching over 2000 J kg^{-1} for some events.

The average 0-1 km shear during coastal Northeast severe cellular events near the coast is a modest ~2.6 m s^{-1} (Fig. 3.12b), a smaller mean value than for central U.S. nonsupercells (3.8 m s^{-1}; Thompson et al. 2003). The mean low-level shear during coastal Northeast severe linear events (4.5 m s^{-1}) is significant greater (95% level) than severe cellular events, although this mean shear value is smaller than during derecho producing MCSs in the central and eastern U.S. (10.6 m s^{-1}; Coniglio et al. 2004). Even during weakly forced (500 hPa Q-vector convergence) central U.S. derecho events, the mean 0-1 km shear is 1.5 times greater than the coastal Northeast severe linear convection (Coniglio et al. 2004).

An interesting difference between cellular and linear over the coastal Northeast is the spread of the middle 50% of events (Fig. 3.12b). The inter-quartile range (IQR) for all severe cellular events is relatively small, ranging from 1.4 to 2.6 m s^{-1}, while for severe linear events the values range from 2.0-7.7 m s^{-1}. Nonlinear severe events have a similar mean 0-1 km shear value (~4.4 m s^{-1}) as the linear events, although the top 50% of the nonlinear shear values are smaller compared to severe linear events. Overall, the spread of 0-1 km shear values for all severe nonlinear events is smaller than the cellular and linear severe events.

Mean deep layer shear (0-6 km) increases from cellular (~13.4 m s^{-1}), to linear (~14.9 m s^{-1}), to nonlinear (~18.8 m s^{-1}) severe Northeast coastal events (Fig. 3.12c). The mean deep layer shear value for nonlinear events is significantly larger than for linear events at the 80% level, and significantly larger than cellular events at the 95% level. Compared to the central U.S, the mean deep layer shear (0-6 km) for coastal Northeast cells is greater than nonsupercells over the central U.S. (8.4 m s^{-1}) noted in Thompson et al. (2003), but still less than the mean deep layer shear associated with central U.S. supercells (23 m s^{-1}). Deep layer (0-6 km) shear values for linear events found in our study are smaller than both severe and derecho producing central and eastern U.S. quasi-linear systems (Cohen et al. 2007). Cohen et al. (2007) showed that the IQR of 0-6 km shear for severe central U.S. lines is 14-21 m s^{-1}, and 17-26 m s^{-1} for derecho producing MCSs, which are more consistent with deep layer shear seen during severe coastal Northeast nonlinear events (Fig. 3.12c). The earlier study of Evans and Doswell (2001) found that the middle 50% of derechos that develop east of the Rockies form within 0-6 km shear values of 11.8-20.0 m s^{-1}, which is more consistent with values for severe Northeast coastal linear events.

It should be emphasized that both cellular and linear severe events occur under a wide range of deep layer shear values (3.6-41.1 m s^{-1}; Fig. 3.12c), while the spread of deep layer shear values during nonlinear severe events is smaller (10.2-31.6 m s^{-1}). This suggests that Northeast coastal severe weather can develop under relatively weak deep layer shear values, a result is similar to the central Plains study of Evans and Doswell (2001), who found that derechos can form in 0-6 km shears as low as 1 m s^{-1}. Typically, these events lack strong synoptic support (i.e. surface cold front, progressive mid-level trough) and they develop in more unstable conditions compared to those events with larger shear values (Evans and Doswell 2001). Approximately 33% of all coastal Northeast severe cellular events and 27% of linear events develop in <10 m s^{-1} of deep layer shear. Cellular events with weak (<10 m s^{-1}) deep layer shear are primarily severe wind events, while linear events with weak deep layer shear can be dominated by severe wind or produce a combination of severe wind and hail. Overall, the complexity of CAPE and shear values can create a potentially difficult forecast situation.

Given the above results, it is apparent that many severe events over the Northeast develop in environments with weaker CAPE and vertical wind shear than the central U.S. Forecasting severe weather over the coastal Northeast is a serious challenge given these more subtle conditions than the central U.S. However, the above composites do help provide some understanding of the basic flow patterns associated with the severe coastal Northeast convection, which can help alert forecasters during more marginal conditions. Furthermore, the role of synoptic scale lift is important in releasing the more moderate instability during Northeast severe events. Some of the key synoptic forcing mechanisms associated with the 3 main severe convective structures have been highlighted in the composites (Figs. 3.7-3.11), to draw the forecasters attention to the possibility of severe weather under these regimes.

b. Comparison of severe organizational structures over the central U.S. and Northeast

Gallus et al. (2008) identified the convective organizational structures responsible for various types of severe weather (wind, hail, tornadoes) over the central U.S. The following short discussion will compare the distribution of severe weather over the Northeast to the Gallus et al. (2008) study. Cellular convection over the central U.S. is responsible for 48% of all severe events, with 26% from isolated cells and 20% from clusters of cells (Gallus et al. Fig. 6). Over the northeastern U.S. (cf. Fig. 3.2), only 39% of all severe events are from cells, with the majority of severe weather developing from cellular clusters (25%) rather than isolated cells (9%). The fraction of severe events from linear structures is larger over the Northeast (32%) as compared to the central U.S. (23%). The greatest contribution to this difference is from linear systems with no stratiform precipitation, which are responsible for 13% of all severe events over the Northeast, but only 6% over the central U.S. Over both regions, nonlinear severe events produce 29% of all severe events.

The frequency of reports per event can also be qualitatively compared with the central U.S. Gallus et al. (2008) found that bow echoes have the largest number of severe wind reports per event over the central U.S, while over the Northeast the frequency of severe wind from bow echoes is smaller than for lines with trailing stratiform (Fig. 3.4). Over the central U.S, the highest frequency of small hail (less than 1-inch) is from bow echoes and broken lines, with broken lines producing the highest frequency of severe hail (1-2 inches). Over the Northeast, both clusters of cells and trailing stratiform lines have more hail reports per case than bow echoes. For tornado reports per event, broken lines and lines with parallel stratiform are most likely to cause tornadoes over the central U.S, while bow echoes have the greatest number of tornadoes per case over the Northeast.

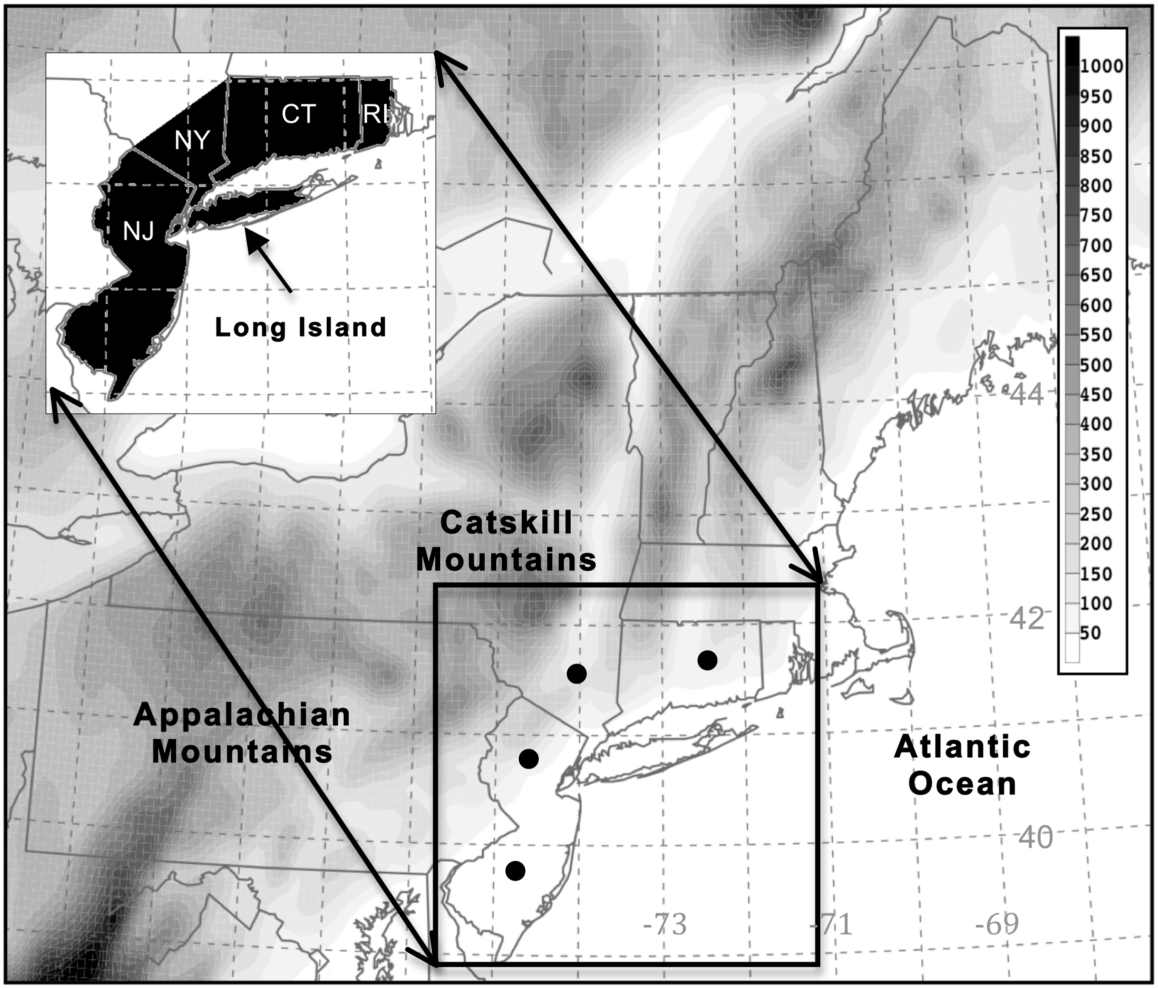

Figure 3.1 The northeastern U.S. and coastal domains (see black region in inset panel) used in this study. State abbreviations in the black box are NJ = New Jersey, NY= New York, CT = Connecticut, RI = Rhode Island. The four points used for average box-and-whisker plots (Fig. 12) are also shown. The latitude and longitude of these points are (39.8N, -74.7W) in southern NJ, (40.7N, -74.5W) in northern NJ, (41.5N, -74.0W) in NY, (41.7N, -72.6W) in CT. Terrain is gray shaded every 50 m.

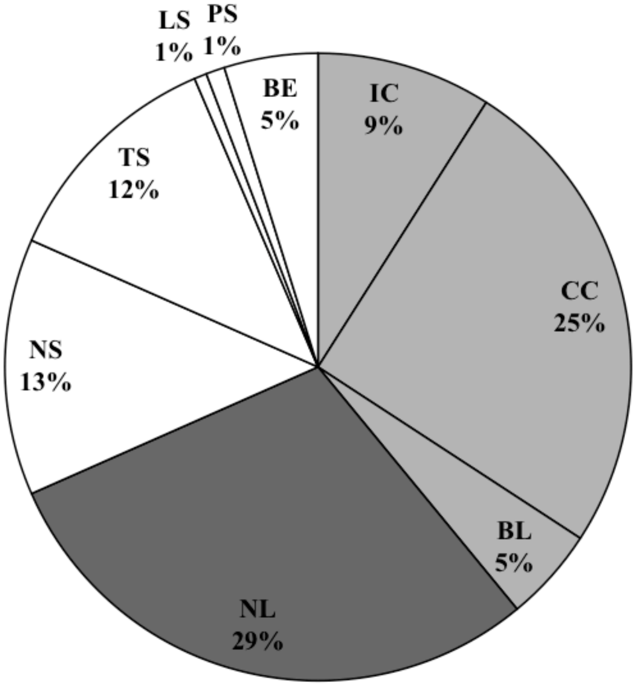

Figure 3.2 Percentage of severe events over the notheastern U.S. produced by each of the 9 convection structures, including isolated cells (IC), clusters of cells (CC), broken lines (BL), nonlinear (NL), no straiform linear (NS), trailing stratiform linear (TS), leading stratiform linear (LS), parallel stratiform linear (PS), and bow echoes (BE), examined during the 2007 and aggregate (2002-2006) warm seasons (May-Aug). Cellular events are lightly shaded, nonlinear events are darkly shaded, and linear events are not shaded.

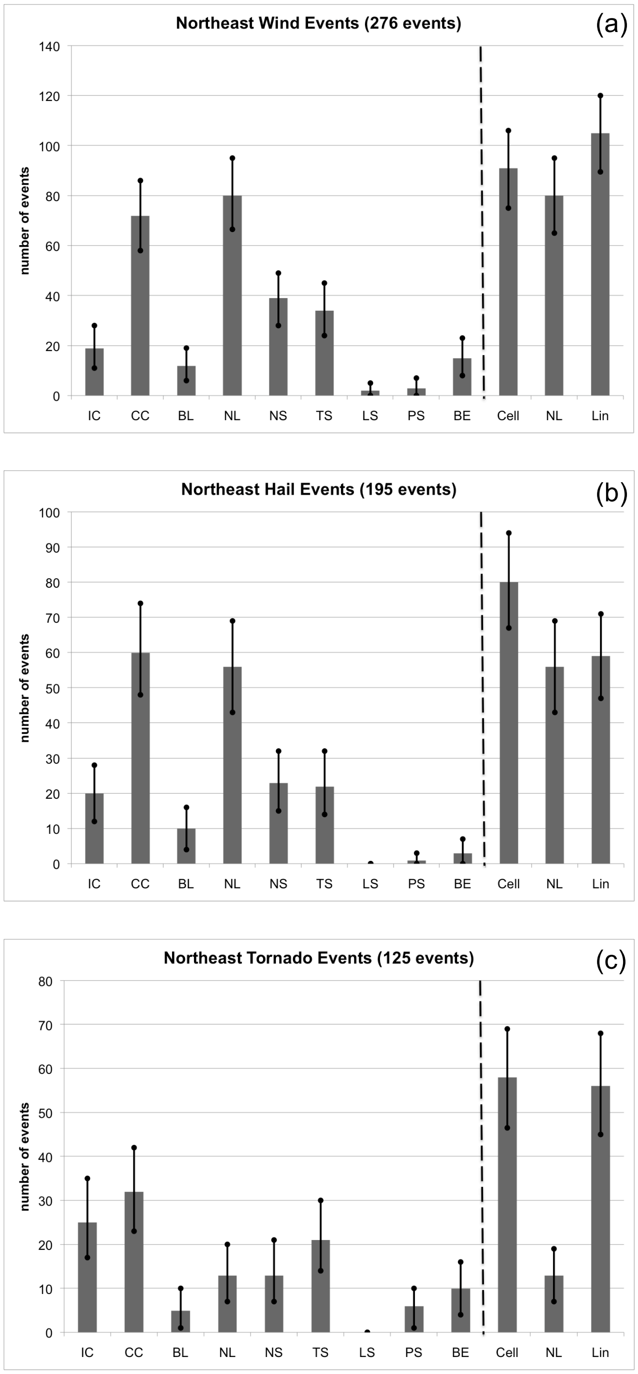

Figure 3.3 Number of northeastern U.S. severe (a) wind (b) hail events from the 2007 and aggregate (2002-2006) warm seasons (May-Aug), and (c) tornado events from the 1996-2007 warm seasons for each of the 9 convective types individually and grouped into the 3 main organizational types (cellular, nonlinear, linear). Error bars (solid black) mark the range of the 95% significance level.

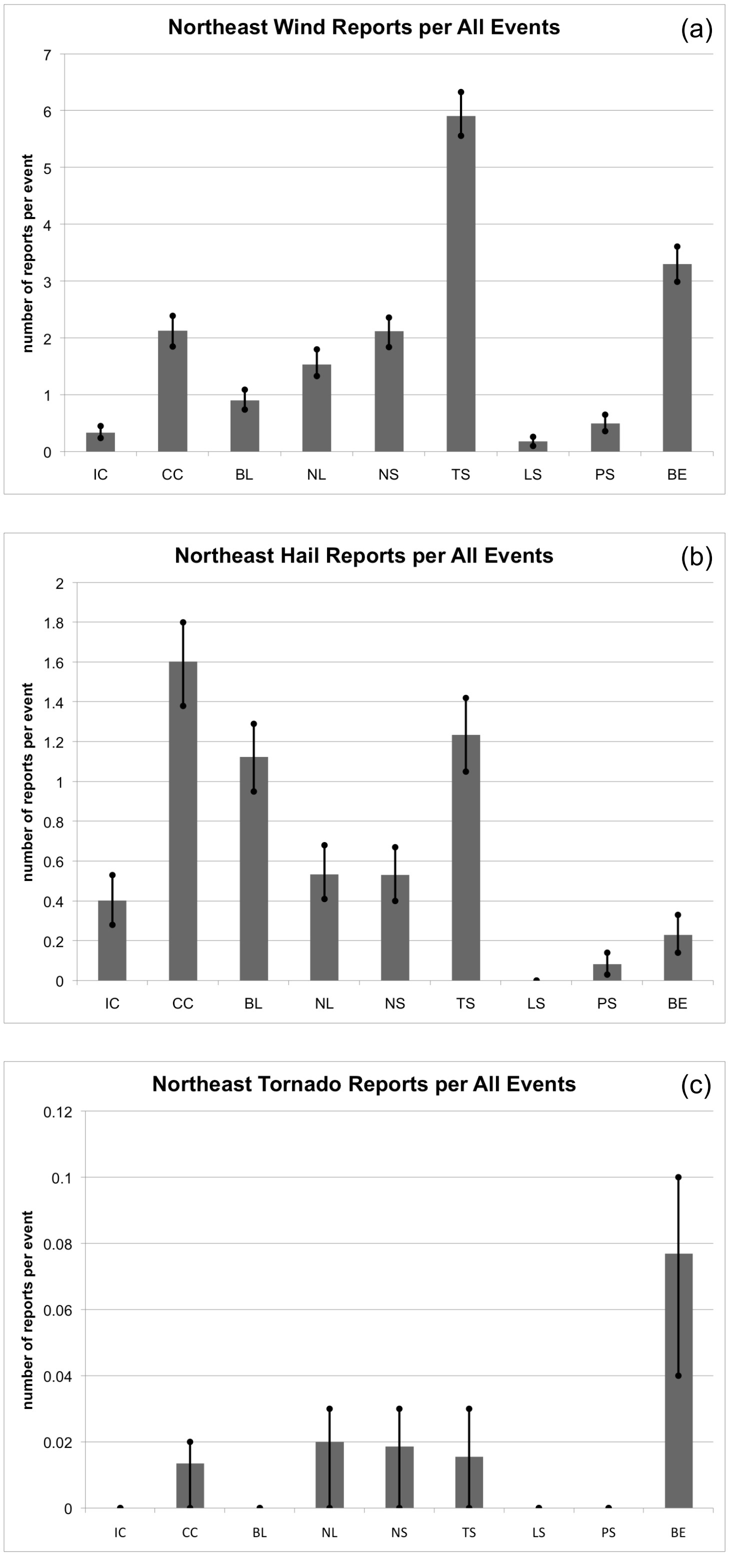

Figure 3.4 Number of severe reports per total number of events for each of the 9 organization structures over the Northeast using data from the 2007 & aggregate (2002-2006) warm seasons for (a) wind (b) hail (c) tornadoes.

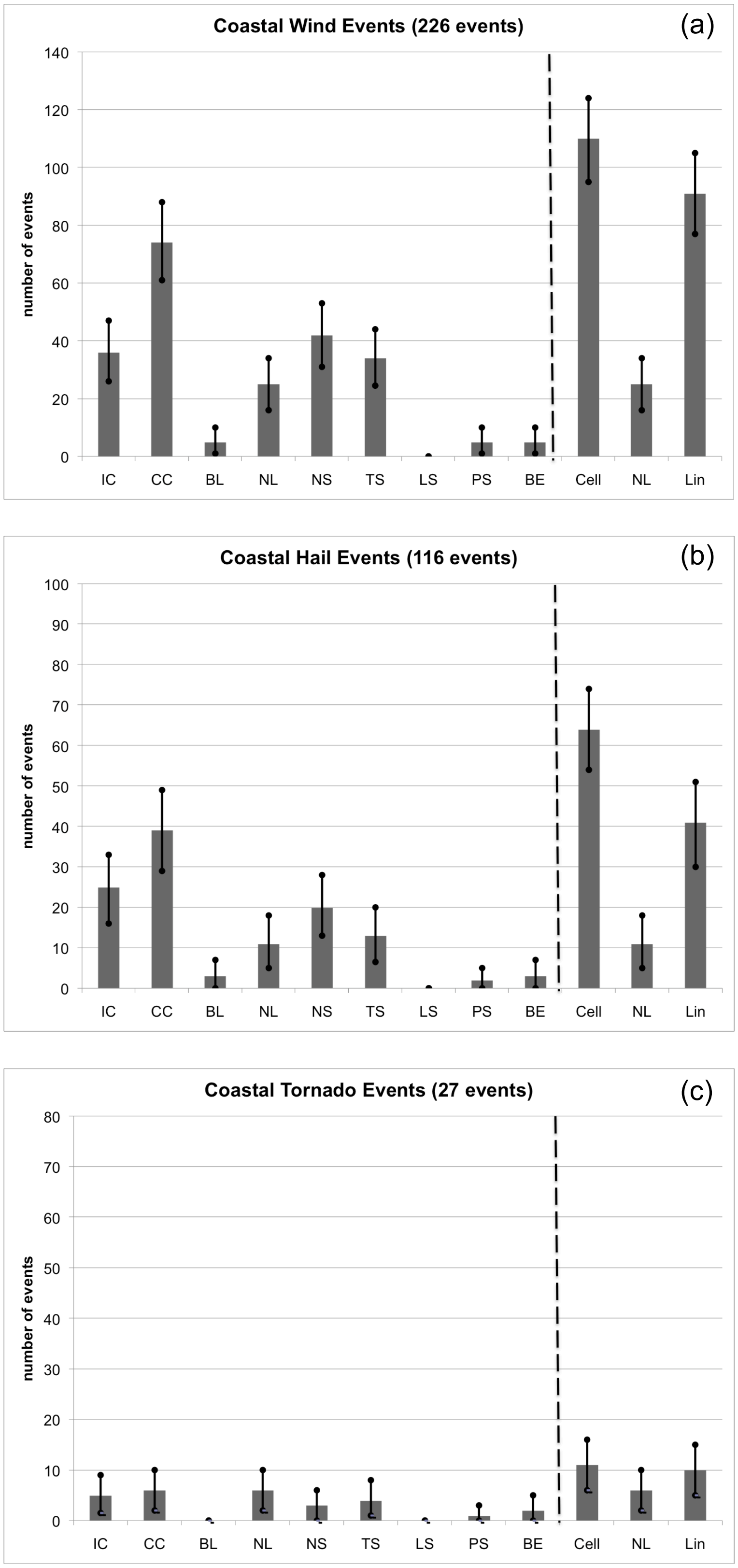

Figure 3.5 As in Fig. 2.3 except for the coastal severe (a) wind (b) hail events from the 2002-2007 warm seasons (May-Aug), and (c) tornado events from 1996-2007 warm seasons.

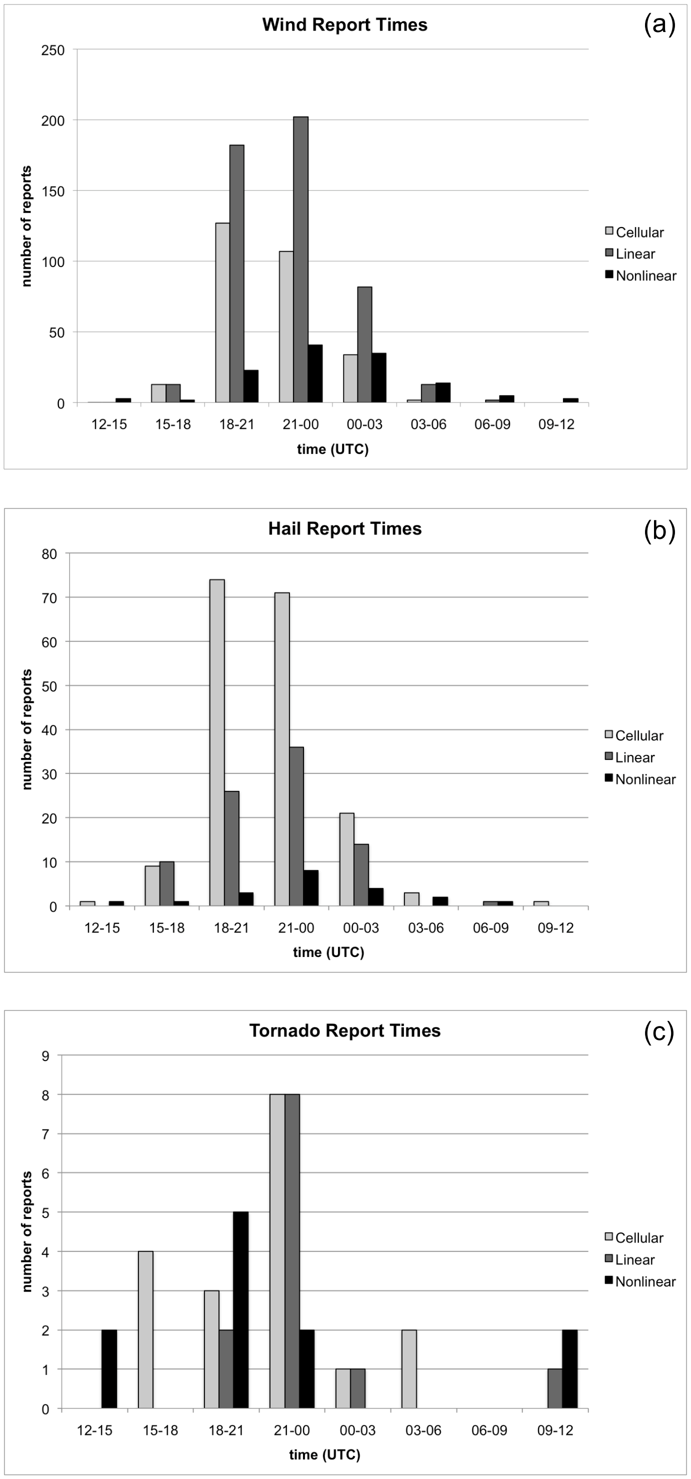

Figure 3.6 Number of severe weather reports over the coastal zone plotted as a function of time of day (3 hour bins) for cellular, linear, and nonlinear convective organizational structures from May-August 2002-2007 for (a) wind (b) hail, and from May-August 1996-2007 for (c) tornadoes.

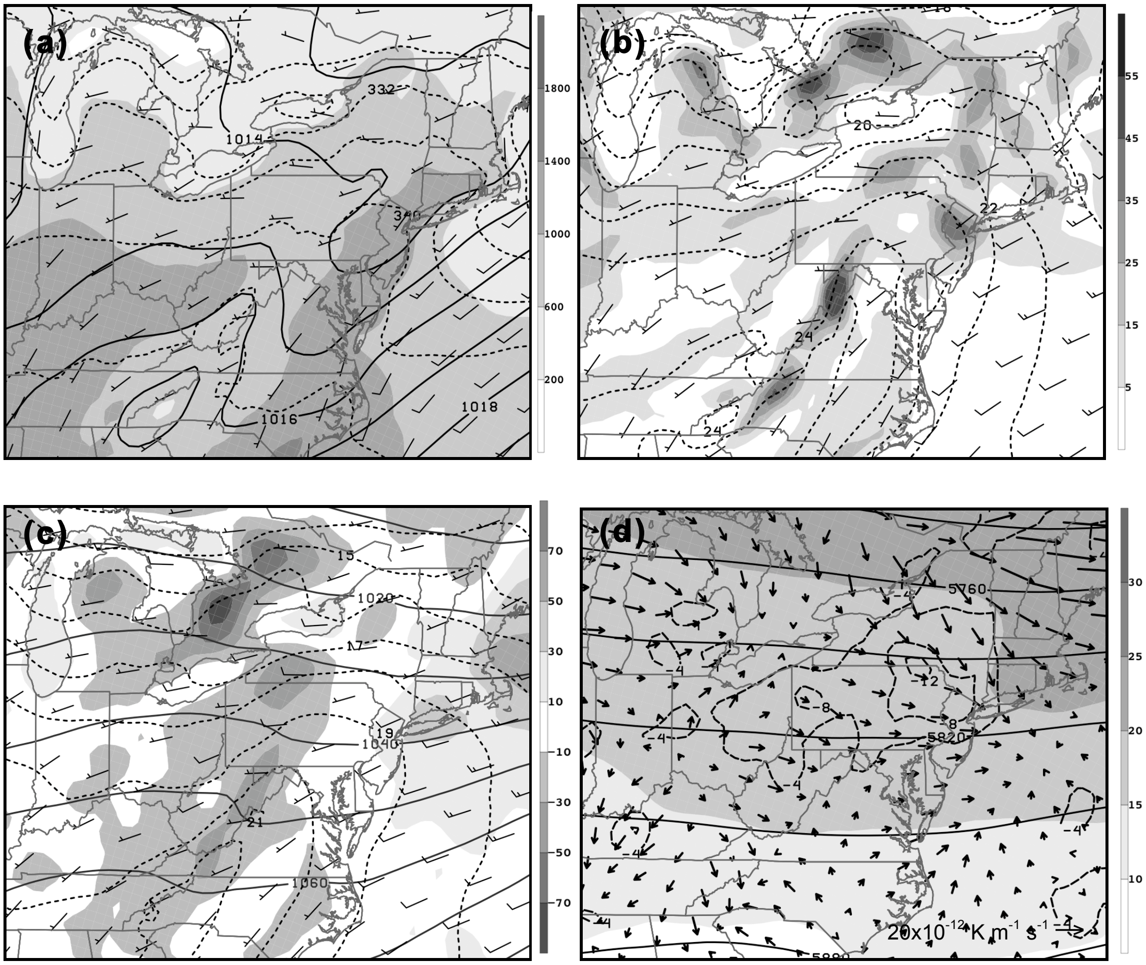

Figure 3.7 Spatial composites for the severe cellular events near the coast at t-0h of (a) sea level pressure (solid every 1 hPa), most unstable CAPE (shaded every 400 J kg^{-1}), equivalent potential temperature (dashed every 4 K), and 1000 hPa winds (full barb = 5 m s$^{-1)}$, (b) 950 hPa frontogenesis (calculated then composited; shaded every 1x10^{-2} K (100 km)$^{-1}$ (3 hr)$^{-1}$), 950 hPa temperature (dashed every 1 ^{o}C), and 950 hPa winds (full barb = 5 m s^{-1}), (c) 900 hPa temperature advection (calculated then composited; shaded every 1x10^{-6} ^{o}C s^{-1}), 900 hPa geopotential height (solid every 10 dam), and 900 hPa winds (full barb = 5 m s^{-1}), (d) 500 hPa geopotential height (solid every 20 dam), 500 hPa Q-vectors (10^{-12} K m^{-1} s^{-1}), and 300 hPa wind magnitude (shaded every 5 m s $^{-1}$), 800:400 hPa layer averaged omega (dashed, 10^{-4} Pa s^{-1}).

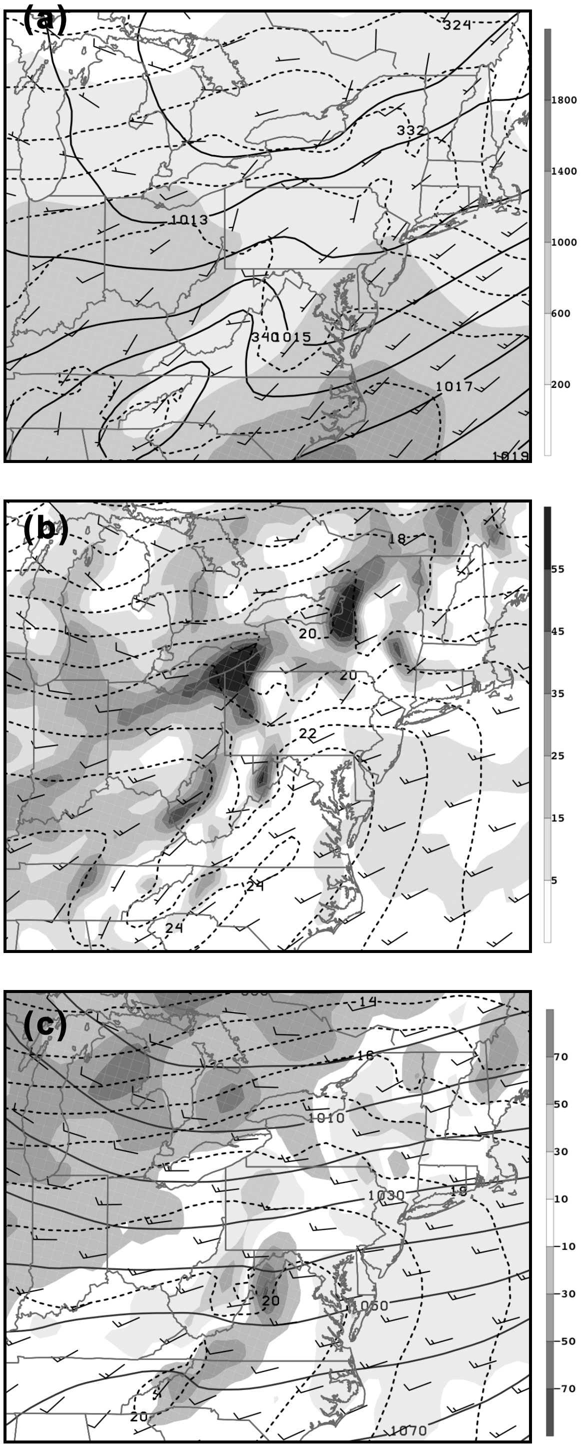

Figure 3.8 Same as in Figs. 3.7 (a)-(c) except for the severe linear events near the coast at t-12h.

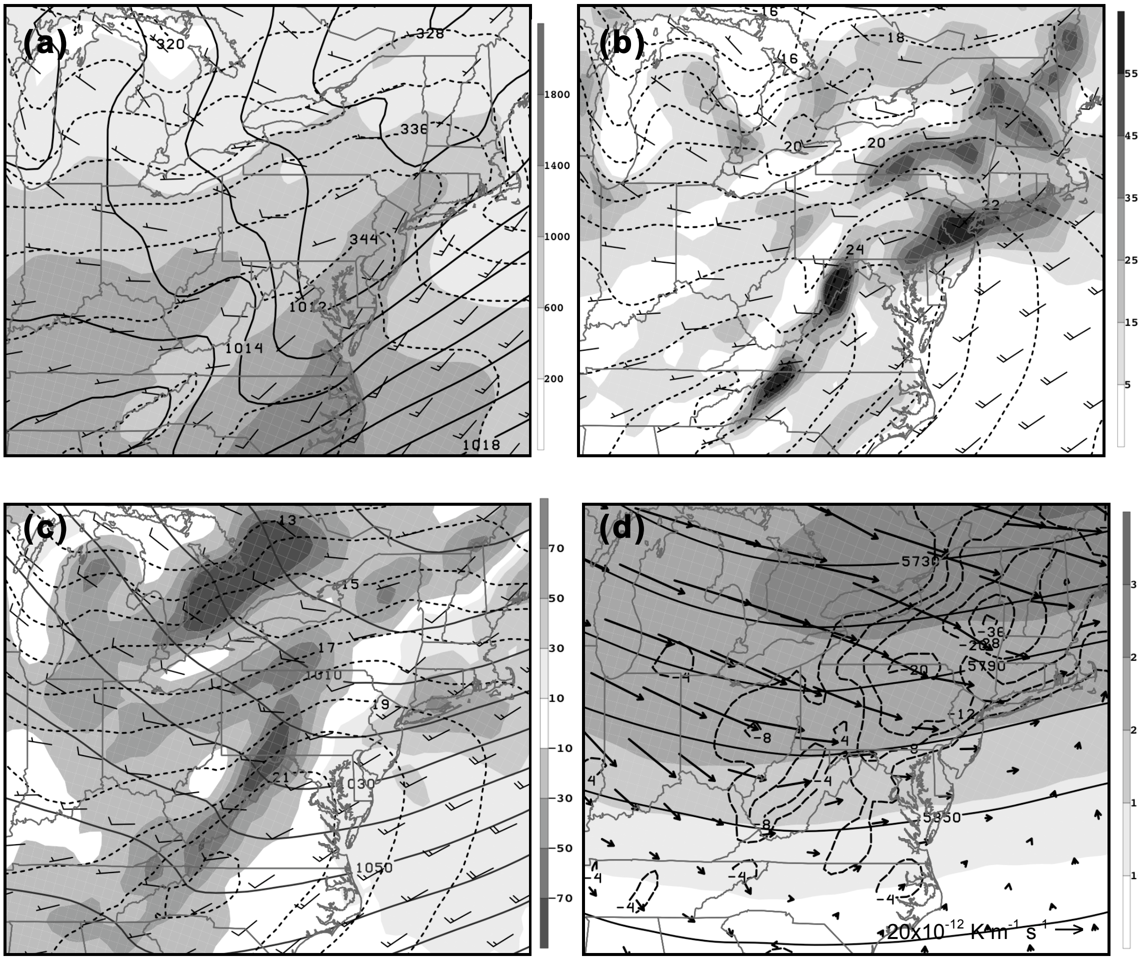

Figure 3.9 Same as in Fig. 3.7 except for the severe linear events at t -0h.

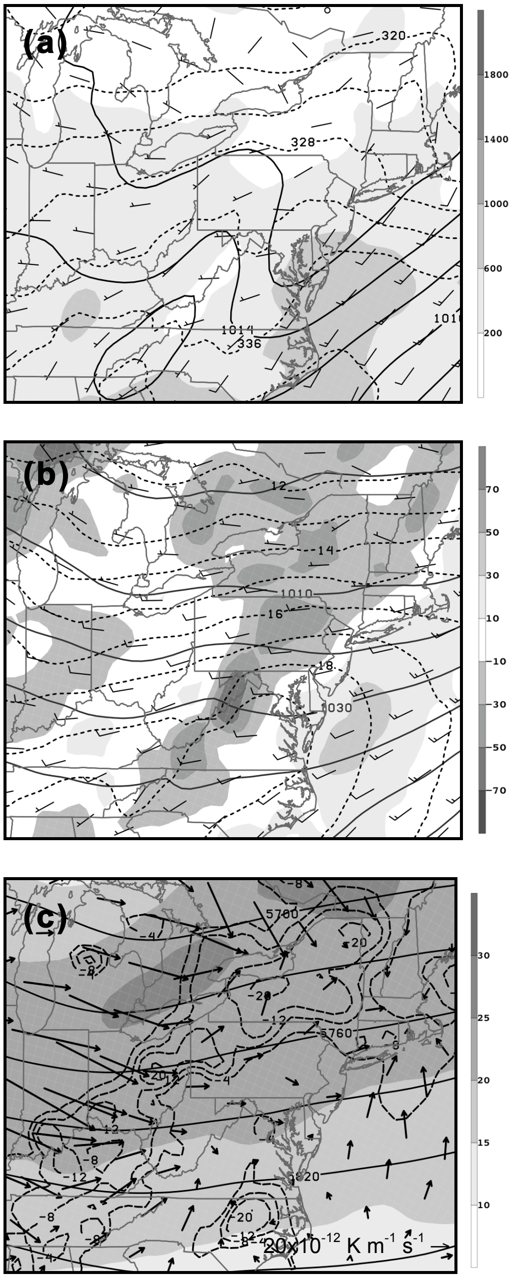

Figure 3.10 Spatial composites for the severe nonlinear events near the coast at t-12h showing (a) sea level pressure (solid every 1 hPa), most unstable CAPE (shaded every 400 J kg^{-1}), equivalent potential temperature (dashed every 4 K), and 1000 hPa winds (full barb = 5 m s^{-1}), (b) 900 hPa temperature advection (calculated then composited; shaded every 1x10^{-6} ^{o}C s^{-1}), 900 hPa geopotential height (solid every 10 dam), and 900 hPa winds (full barb = 5 m s^{-1}), (c) 500 hPa geopotential height (solid every 20 dam), 500 hPa Q-vectors (10^{-12} K m^{-1} s^{-1}), and 300 hPa wind magnitude (shaded every 5 m s $^{-1}$), 800:400 hPa layer averaged omega (dashed, 10^{-4} Pa s^{-1}).

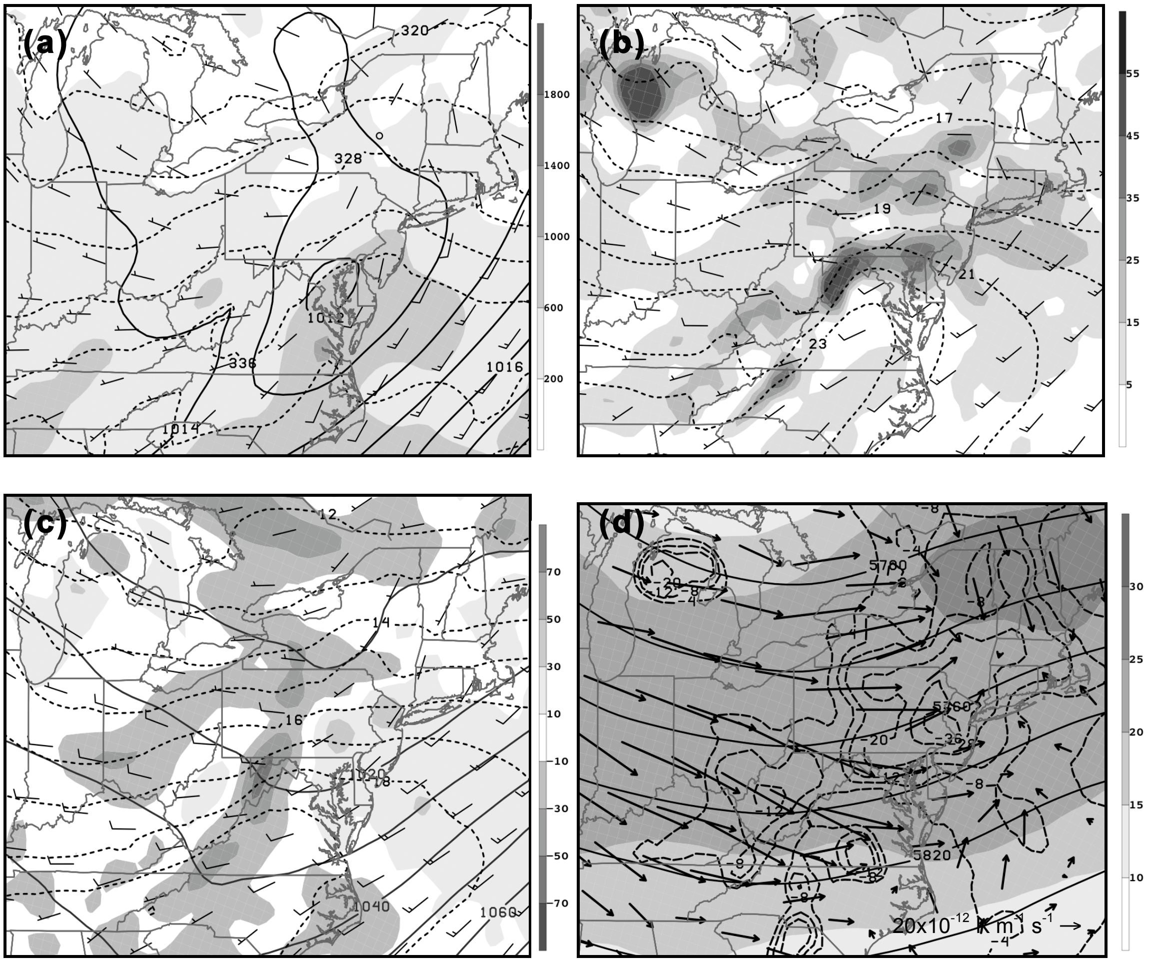

Figure 3.11 As in Fig. 3.7 except for the nonlinear severe events at t-0h.

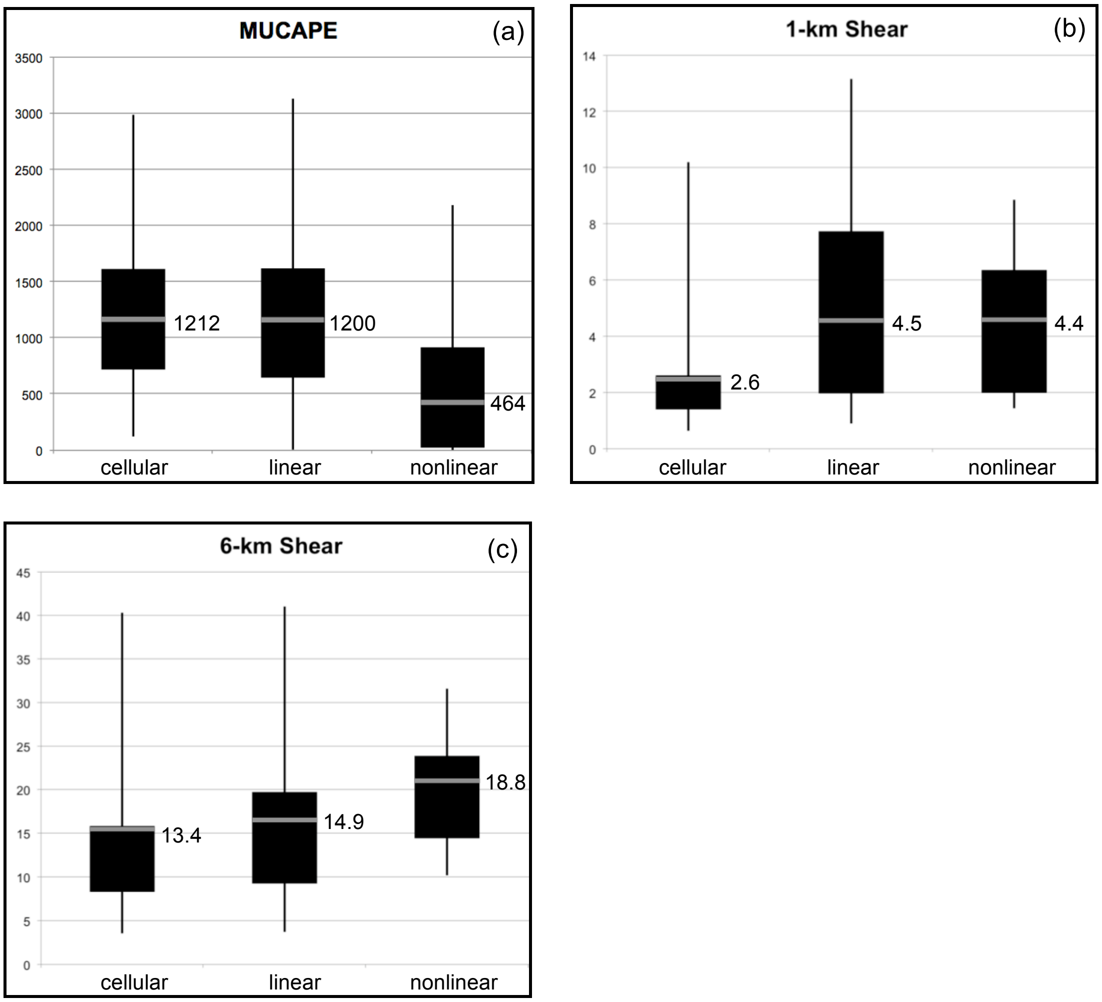

Figure 3.12 Box-and-whisker plots averaged over 4 points within the coastal region highlighted in Fig.1 showing (a) most unstable CAPE (J kg^{-1}), (b) 0-1 km shear (m s^{-1}), (c) 0-6 km shear (m s^{-1}) for the 49 cellular, 45 linear, and 15 nonlinear severe coastal events. The bottom and top of the solid black box mark the 25th and 75th quartiles, respectively. The gray bar denotes the mean and the value has been included. The maximum and minimum outliers are the top and bottom of the solid vertical black lines.

Chapter 4:

The interaction between quasi-linear convective structures and the Atlantic marine environment

4.1 Introduction

Observational evidence suggests that organized convection can be modified by water bodies such as lakes (i.e. Bosart and Sanders 1981; Bosart and Galarneau 2005, Workoff 2010), as well as the coastal ocean (Mapes et al. 2003; Lericos et al. 2007; Murray and Colle 2011). However, little is known about the interaction between convective storms and the coastal Northeast U.S. marine environment. Currently, we do not understand why some mesoscale convective systems decay upon reaching a coastal boundary, while others move over the relatively cool water uninfluenced for hours. Since linear convection is the most likely convective structure to produce severe weather over the region (Lombardo and Colle 2011; Chapter3), it is important we understand the processes that lead to the decay or maintenance of quasi-linear convective systems (QLCSs). Murray and Colle (2011) showed that southerly wind can reduce convection over much of southern New England, and showed that the more severe events along the coast occurred with more west-southwesterly low-level flow ahead of an approaching trough. However, this was just an average snapshot, so we do not know the detailed synoptic and thermodynamic conditions that favor a decaying QLCS over one that maintains its intensity over the Atlantic waters. Furthermore, we don't understand the impact of the varying land surface moving from inland areas to the open waters on the evolving convection. These variations include changes in surface friction which influences low level winds as well as temperature and moisture fluxes, changes in boundary layer moisture and temperature, and variations in instability. Some motivational questions include:

- What synoptic and thermodynamic environments favor the maintenance or decay of a QLCS at the coast?
- What are the storm structural differences between a maintaining QLCS and a decaying QLCS?
- Does air from within the marine layer become ingested into a QLCS as it moves over the ocean or are these systems fed by air above the marine inversion?
- What is the impact of the reduced instability and the decrease in surface friction over the water on a QLCS?

4.2 Composite Analysis

a. Marine properties

This chapter focuses on the interaction between quasi-linear convective systems and the Atlantic coastal marine environment over the northeastern U.S. (Fig. 4.1). By manually examining 2-km NOWrad radar reflectivity at 15-min temporal resolution over 6 warm seasons (May-August) from 2002-2007, 73 QLCSs were identified that encountered the Atlantic coastal boundary over the northeastern U.S. (Fig. 4.1). An initial hypothesis was that the decay location for a QLCS is a function of the sea surface temperature (SST), with linear systems that move over cooler waters having increased chance of decay due to a greater reduction in instability. With average sea surface temperatures increasing during the warm season from May (9-13 ^{o}C) through August (21-25 ^{o}C), QLCSs are expected to decay near the coast during the early part of the warm season when the SSTs are cooler, compared to later in the warm season.

Figure 4.1 illustrates the decay location of the 73 QLCSs identified in this study, plotted as a function of warm season (May-August) month. Decay is defined as when the radar reflectivity decreases below 50 dBZ with no reintensification along majority of line. For a uniformly decaying line, the whole line weakens below 50 dBZ and the center point of the line is defined as the decay location. More commonly, there is a non-uniformly decaying line, in which the coherent linear system breaks into individual cells. The intensity of the individual cells may still be 50 dBZ, though there is a decrease in intensity (dBZ) visible in every subsequent 15-minute reflectivity image. For non-uniformly decaying events, the first point the line weakens is used at the point of decay. As highlighted in figure 4.1, the decay locations for the QLCSs included in the dataset do not appear to be related to the warm season month, with just as many events decaying over the coastal ocean in May-June as July-August.

The individual QLCS events were then examined to determine how each linear system evolved upon encountering the Atlantic coastline. Sixty-five of the 73 events were classified into 4 different categories based on their evolution. The 8 events that were not categorized lacked gridded data for the analysis. Thirty-two events decayed at the coast (decay events; Fig. 4.2a-c). Eighteen events did not decay at the coast; rather they weakened over the ocean and within 100 km of the coast (slow decay events; not shown). Nine events maintained their intensity more than 100 km from the coastline (maintain events; Fig. 4.2d-f), and 6 events organized along the coastline (not shown). Those events that organized along the coast will not be addressed in this study.

The type of decay (decay, slow decay, maintain) was related to the strength of the marine layer over the Atlantic waters. As a proxy for marine layer strength, the depth of the marine layer inversion and the temperature change from the bottom to the top of the inversion was determined at the buoy 44025 location (40.25N; -73.17W; see 025 on Fig. 4.1). Hourly data at buoy 44025, as well as the Ambrose Light Tower discussed in section 4.3 (for location see Fig. 4.1), were obtained from the National Data Buoy Center. The vertical depth and temperature change of the marine layer were examined at buoy 44025 using the Rapid Update Cycle (RUC) data at 20-/40-km horizontal grid spacing (20-km grid spacing was only available after 2004) at the closest 3-h time prior to the QLCS crossing the Atlantic coastline. This location was selected so that the surface temperature of the model profile could be compared and adjusted to the observed temperature at a location over the Atlantic marine layer. The vertical temperature change within the marine layer is defined as the difference between the observed temperature at buoy 44025 and the RUC temperature at the top of the inversion. From the dataset, 5 decay events, 5 slow decay events, and 4 maintain events showed no inversion at the buoy 44025 location. For the remaining events, figure 4.3 illustrates the depth and temperature difference of the marine layer with respect to the type of decay. Given the scatter, it seems that the evolution of a QLCS is not strictly dependent on the strength of the marine layer.

b. Composites

Given the lack of a clear relationship between the decay location of a QLCS and SST, as well as the magnitude of the marine layer, we hypothesize that the evolution of a QLCS may be more dependent on the synoptic conditions and other thermodynamic constraints. To examine the synoptic and thermodynamic differences between each of the 3 decay types, feature-based composites were created using 32-km North American Regional Reanalysis (NARR) data centered on the point where the QLCS crossed the coastal boundary at the closest 3-hr NARR time prior to the crossing. While the vertical resolution for the RUC (37 levels) is higher compared to the NARR (29 levels), the NARR was used in place of the RUC gridded data in these analyses because the NARR contains a more complete dataset over the time period examined in this study. The point for the feature-based composite was chosen just ahead of the linear system (by ~0.75 degrees) to capture the ambient conditions encountered by the QLCS while preventing convective contamination. Using this center point, 1.5-degree latitude-longitude area averaged values for variables such as MUCAPE, CIN, frontogenesis, temperature advection, vertical wind shear, and Q-vector convergence were calculated and compared among the 3 groups. In the following set of figures (Fig 4.4, 4.6-7), the geography is there for reference only, since these are feature based-composites.

1. Decay events (32 events)

Figure 4.4 illustrates the feature-based composites associated with quasi-linear events that decay at the coast. At t-0 h, decay events are located near a surface pressure trough within a low-level thermal ridge (Fig. 4.4a). These events are supported by moderate instability (MUCAPE ~1250 J kg^{-1}) and weak convective inhibition (CIN ~ -15 J kg^{-1}; not shown), with 84% of these events crossing the coastal boundary during the warmest period of the day, between 1800-0300 UTC (Fig. 4.5). The steepest lapse rates during these events exist between 950-750 hPa and approach -7.5 C km^{-1} (not shown).

At 1000-hPa, mixing ratio values are ~15 g kg^{-1} (Fig. 4.4b) and the relative humidity (RH) at this level is ~68%. The RH values increase to 76% by 900 hPa in the mean (not shown), indicating that there is a potential for evaporative cooling at low levels. The 0-3 km vertical wind shear vector is from the west-northwest at 7.7 m s^{-1} (Fig. 4.4b).

At 1000 hPa, there is frontogenesis associated with the temperature gradient just east of the compositing point (Fig. 4.4a), with a value of 45x10^{-2} K 100 km^{-1} 3 hr^{-1} over the QLCS (not shown). A 900-800 hPa layer averaged frontogenesis of 15x10^{-2} K 100 km^{-1} 3 hr^{-1} is centered over the convective line, which is collocated with the surface pressure trough (Fig. 4.4a). The QLCS is located between a region of warm air advection to the east and cold air advection to the west, with limited temperature advection over the convective storms (Fig. 4.4c).

At mid-levels, there is a broad 500 hPa trough ~600 km to the west of the QLCS (Fig. 4.4d), with little Q-vector convergence near the convection, indicating minimal quasi-geostrophic forcing for ascent at mid-levels. The convection is located in the right entrance region of a 25 m s^{-1} 300 hPa jet (Fig. 4.4d), a favorable region for ascent due to ageostrophic jet circulations. Deep layer ascent (800-400 hPa omega ~ -2x10^{-3} Pa s^{-1}) is present over the QLCS, which is collocated with both the regions of frontogenetical forcing as well as the jet entrance region (Fig. 4.4d).

2. Slow decay events (18 events)

QLCSs that slowly decay upon reaching the coastline exhibit similar synoptic patterns as the decay events. They are located within the axis of a surface pressure trough, which is collocated with a thermal ridge (Fig. 4.6a). Similar to the decay events, about 72% of slow decay events cross the coastal boundary between 1800-0300 UTC (Fig. 4.5). The mean convective inhibition for slow decay events (CIN ~ -15 J kg^{-1}; not shown) is approximately the same as for decay events, however, the mean instability (MUCAPE) for the slow decay is slightly less, ~800 J kg^{-1} (Fig. 4.6a), with a 950-750 hPa lapse rate of -6.5 C km^{-1}. The 1000-hPa mixing ratio for the slow decay events is ~14.5 g kg^{-1}, with an RH of ~70% (Fig. 4.6b). The humidity slowly increases to 78% by 950 hPa and decreases down to 71% by 900 hPa (not shown). The 0-3 km vertical wind shear vector is 10.5-13 m s^{-1} from the west (Fig. 4.6b). There is a maximum in 1000 hPa frontogenesis (~65x10^{-2} K 100 km^{-1} 3 hr^{-1} of 1000 hPa) associated with the baroclinic zone ~200 km east of the compositing point (not shown). There is also a maximum in 900:800 hPa layer average frontogenesis (~26x10^{-2} K 100 km^{-1} 3 hr^{-1}) over the convection with weak warm air advection (2x10^{-2} C s^{-1}; Fig. 4.6c).

A 500-hPa trough axis is located ~400 km west of the QLCS, with 500 hPa Q-vector convergence over and to the east of the convection (Fig. 4.6d), indicating the presence of a Q-G forcing for ascent in the mid-levels. The 300-hPa jet core (25 m s^{-1}) is 600-800 km to the north of the organized convection, with the QLCS ~400 km to the southeast and near the entrance region of the weak jet (Fig. 4.6d). Deep ascent (800-400 hPa, -5x10^{-3} Pa s^{-1}) overlies the linear system, with the ascent collocated with both the 900:800 hPa frontogenesis maximum (Fig. 4.6c) as well as the 300 hPa jet entrance region (Fig. 6d).

Overall, slowly decaying QLCSs develop with stronger forcing for ascent, including greater low level frontogenesis as well as the presence of mid-level Q-G forcing mechanisms, both of which contribute to stronger vertical motion, compared to decaying events. Thermodynamically, the slowly decaying events form within less unstable yet more humid environments through the depth of the troposphere (not shown), compared to decaying events. Finally, the magnitude of the 0-3 km vertical wind shear vector over the coastal convection is ~3-5 m s^{-1} larger for slow decay events.

3. Maintain events (9 events)

The composite fields of QLCS events that maintain their intensity over the Atlantic marine environment highlights several synoptic-dynamic differences compared to the decay and slow decay events. The maintain events cross the Atlantic coastline with a surface pressure trough 250-300 km to the east of the convection and are located along a surface baroclinic zone (Fig. 4.7a), which is associated with 45x10^{-2} K 100 km^{-1} 3 hr^{-1} of 1000-hPa frontogenesis (not shown). Examination of the individual events reveals that 8 of the 9 events included in this composite develop east of a surface cold front, with the surface front ~200-1000 km to the west or northwest of the QLCS. The remaining event encountered the coast with a surface trough ~200 km to the west that was not associated with a cold front. No event organized along a cold front, though 3 events organized along or north of a surface warm front. A majority (67%) of these events reach the coast between 2100-0300 UTC (Fig. 4.5), with the mean MUCAPE approaching ~900 J kg^{-1} (Fig. 4.7a), and a 950-750 lapse rate of approximately -6.5 C km^{-1}. In the mean, the convective inhibition is about -40 J kg^{-1}, which is ~25 J kg^{-1} larger in magnitude compared to the decay and slow decay composites values. The 1000-hPa RH for the maintain events (~77%; Fig. 4.7) is 5-10% higher than the decay and slow decay events. The RH decreases slightly through the lowest 100 hPa, with RH values decreasing ~7% by 900 hPa (not shown). The 0-3 km northwesterly vertical wind shear vector over and ahead of the QLCS is 13-15.5 m s^{-1} (Fig. 4.7b), which is 6-7.5 m s^{-1} and ~2.5 m s^{-1} greater than the slow decay and decay events, respectively.

There is little to no frontogenetical forcing between 900-800 hPa in the mean (Fig. 4.7c), though the convection is collocated with a maximum of warm air advection, with $7x10^{-2}$ C s^{-1} of warming over the QLCS. It is worth emphasizing that all maintaining events occurred under warm air advection. This warm advection is not only a forcing term for ascent to help maintain the convection, but it also serves to help destabilize the layer just above the shallow marine layer.

During maintaining events, there is little mid- and upper-level support for ascent in the mean. The 300 hPa wind is uniform a 15 m s^{-1} over the QLCS, with broad westerly 500 hPa flow and minimal Q-vector convergence at that level (Fig. 4.7d). The main region of deep synoptic scale ascent is ~100 km west of the convection, and only $-2x10^{-3}$ Pa s^{-1} over the maintaining convective line (Fig. 4.7d).

b. Comparison between evolution types

There are several important differences between the 3 different QLCS evolutions (decay, slow decay, maintain) that are highlighted using box-and-whisker plots of 1.5 degree area averaged values calculated ahead of the linear convection for each individual event (Fig. 4.8). Approximately three-quarters of the slow decay events have greater 900-800 hPa frontogenesis values than the maintain events (Fig. 4.8a), although the differences between the decay events and the maintain events is small. Only 6% of slow decay events and 24% of all decay events occurred during 900-800 hPa frontolysis, while 43% of maintain events occurred under 900-800 hPa frontolysis. About 75% of all maintaining events are associated with temperature advection values larger than ~2.5x10-5 ^{o}C s^{-1}, while 75% of all decay and slow decay events have values less than ~2.5x10-5 ^{o}C s^{-1} (Fig. 4.8b). Though the sample size of the maintaining events is relatively small (9 events), the mean temperature advection value is greater than the mean for decaying events at the 95% significance level and at the 70% level for slow decay events (not shown).

Average vertical wind shear values have been calculated within the area immediately ahead of the moving QLCS and on the ocean side of the Atlantic coastal boundary. The 0-1 km mean vertical wind shear increases from decay events (4.6 m s^{-1}) to slow decay events (5.4 m s^{-1}) to maintaining events (7.1 m s^{-1}), with no maintaining event occurring with less than 5 m s^{-1} of 0-1 km shear (Fig. 4.8c). A similar trend exists for the 0-3 km mean shear, with values increasing from 7.7 m s^{-1} during decay events, 10.7 m s^{-1} during slow decay events, and 13.3 m s^{-1} during maintaining events. In the following section, the reasons why these differences (i.e. temperature advection, vertical wind shear magnitude) are important will be explored in more detail through observation analysis as well as numerical simulations of 2 representative case studies.

4.3 Case Studies

a. High resolution simulations

From the 73 QLCS in section 4.2, two events, the 31 May 2002 maintaining event and 23 July 2002 decaying event (Fig. 4.2), were selected and examined in further detail. Both events were simulated using the WRFV3.1.1 ARW (Advanced Research WRF) core at 2-km horizontal grid spacing, with a 500-m nest centered on NYC-Long Island region. The 32-km NARR was utilized for the initial atmospheric, SST, and soil conditions as well as the boundary conditions for both simulations. The maintaining event was simulated from 1200 UTC 31 May 2002 to 0600 UTC 1 June 2002, while the decaying event was simulated from 0600 UTC 23 July 2002 to 0300 UTC 24 July 2002.

Suites of experiments were performed to determine the appropriate microphysical parameterization, land surface model (LSM), and planetary boundary layer scheme for these 2 events. Numerous linear events were simulated using a variety of microphysical schemes including the WRF single moment 3-class microphysics (WSM3; Hong et al. 2004), WRF single moment 6-class microphysics (WSM6; Hong and Lim 2006), Thompson (Thompson et al. 2004, Thompson et al. 2008), Ferrier (Ferrier 1994), Lin (Lin et al. 1983, Rutledge and Hobbs 1984), and Morrison (Morrison et al. 2009). Morrison et al. (2009) showed through 2-D idealized simulations that the use of a double-moment microphysical parameterization, which predicts both mixing ratios and number concentrations of precipitation species, more accurately produces widespread trailing stratiform precipitation in convective linear systems compared to single-moment schemes. Primarily, the reduced evaporation rates in the trailing stratiform region of the linear systems in the 2-moment scheme leads to greater mixing ratios and thus rainfall within the stratiform region (Morrison et al. 2009). Within the set of northeastern U.S. convection simulations performed in the current work that tested a variety of microphysical parameterization schemes, the Morrison scheme most accurately captured the organization structure of convection, especially for systems with stratiform precipitation. Therefore, convective lines for both case studies in this work were explicitly generated using Morrison microphysics scheme (Morrison et al. 2009). For the model and observed radar comparisons, total precipitation mixing ratio is used rather than simulated radar reflectivity, since a conversion from mixing ratio to dBZ did not exist for the Morrison scheme, and any attempt to do this would introduce large uncertainties.

Numerous planetary boundary layer (PBL) schemes including Yonsei University (YSU; Hong et al. 2006), Mellor-Yamada Janjic (MYJ; Janjic 1990), Mellor-Yamada Nakanishi and Niino Level 2.5 (MYNN2.5; Nakanishi 2001, Nakanishi and Niino 2004), Mellor-Yamada Nakanishi and Niino Level 3 (MYNN3; Nakanishi and Niino 2006), Bougeault and Lacarrere (BouLac; Bougeault and Lacarrere 1989), ACM2 (Pleim 2007a,b) in conjunction with the Pleim-Xiu LSM (Pleim and Xiu 2003, Pleim 2006) were utilized. With the exception of the ACM2 PBL scheme, the various PBL schemes were tested in conjunction with the thermal diffusion land surface model (LSM) as well as the community Noah LSM (Chen et al. 1996, Koren et al. 1999, Betts et al. 1997, Ek et al. 2003). Those simulations that produced little or unrealistic convection for at least one of the 2 case studies were rejected, which included the BouLac, the ACM2, and the MYNN3. For those that reproduced the evolving convective structures most accurately (MYJ, MYNN2.5, YSU) compared to the observed convection, a detailed analysis was performed comparing the surface fields, boundary layer structure, as well at the large-scale synoptic fields produced by the model to the observations. The simulations that best reproduced the convective evolution, the synoptic patterns, the mesoscale structures, as well as the boundary layer profile for the case studies were selected.

For the 2 case studies examined in this research, the Mellor-Yamada Nakanishi and Niino Level 2.5 (MYNN2.5) planetary boundary layer (PBL) scheme (Nakanishi 2001, Nakanishi and Niino 2004) was used as well as the thermal diffusion land surface model (LSM). In both the 31

May and the 23 July 2002 control simulations, the thermal diffusion LSM predicted more accurate 10 m winds and showed a weaker 2 m temperature warm bias compared to the community Noah LSM (Chen et al. 1996, Koren et al. 1999, Betts et al. 1997, Ek et al. 2003). All PBL schemes produced some errors when compared with the observations. Overall, for the 31 May 2002 event, the Mellor-Yamada Janjic (MYJ; Janjic 1990) PBL scheme was too cool (1-4 ^{o}C) while the winds in the Yonsei University (YSU; Hong et al. 2006) PBL scheme were too weak (~2.5 m s^{-1}; ~5 kts), which could impact both surface fluxes as well as shear profiles. For the 23 July 2002 event, the YSU boundary layer was too dry causing an unreal reduction in instability, with both the MYJ and the MYNN2.5 performing better. For consistency, the same PBL scheme, LSM scheme, and microphysical scheme was selected for both case studies and therefore the parameterizations that performed the best considering both cases were selected. Sensitivity tests were performed to evaluate the impact of the marine environment on the evolving convective structures during these 2 events.

Figure 4.9 illustrates the location of each convective line from initiation location through decay. Once the system begins to decay, its location is no longer marked on the map. The 31 May 2002 event initially develops as a few convective cells over western NY-PA and organizes into a line by ~1900 UTC (Fig. 4.9). The line moves southeastward and decays offshore ~200 km south the southern Long Island coast at 0445 UTC 01 June 2002. In contrast, the 23 July 2002 quasi-linear convective system moves into the Northeast domain from the west as weak stratiform line (not shown), and develops a leading convective edge at 1600 UTC over eastern NY (Fig. 4.9). The convective system moves southeastward and decays along the Atlantic coastal boundary from NJ northeastward to CT by ~2200 UTC 23 July 2002. The following sections will examine each event in detail.

b. 31 May 2002 event

1. Synoptic and mesoscale evolution

At 1200 UTC 31 May 2002, approximately 12 hours before the QLCS encounters the Atlantic coastline, the 500-hPa trough axis is located over the eastern Great Lakes, with the 60-75 m s^{-1} 300 hPa jet extending southeastward into the base of the upper level trough (Fig. 4.10a). By 2100 UTC 31 May 2002, the 500 hPa trough axis is located over eastern NY (Fig. 4.10b), consistent with the composite mean (Fig. 4.6d). Areas of 500 hPa Q-vector convergence are over PA ($6x10^{-15}$ K m^{-2} s^{-1}) as well as western New England ($4x10^{-15}$ K m^{-2} s^{-1}) indicating that quasi-geostrophic forcing for ascent is present over the Northeast (Fig. 4.10b), which is not represented in the composite mean (Fig. 4.6d). The magnitude of the 300 hPa jet has increased to ~30 m s^{-1} by this time, with the coastal zone located in the jet exit region (Fig. 4.10b).

At the surface, a low pressure system is centered over James Bay in Canada, ~800 km north of Toronto, with a trailing cold front extending southwestward through Lake Huron towards Iowa at 1200 UTC (Fig. 4.10c). By 2100 UTC 31 May, the surface low and the associated cold front move eastward, with the front extending southwestward through NY and PA (Fig. 4.10d). Initially, the convective line organizes along this surface boundary by 1900 UTC (not shown), but moves ~100-150 km ahead of the feature around this time (Figs. 4.2d; 4.10d).

Figure 4.11 provides a closer look at the surface features at 2100 UTC 31 May, highlighting the presence of two surface troughs over the Northeast in the 2-km WRF domain, one over western NY associated with the cold front and a second ~100 km to the east (Fig. 4.11a) collocated with the convective line (not shown). The convective line located ahead of the cold front is consistent with the composite analysis above (Fig. 4.7a). The surface trough to the east of the cold front is a prefrontal trough that developed at 0300 UTC 31 May 2002, weakened at 1200 UTC and redeveloped by 1500 UTC (not shown). Both the surface trough associated with the cold front and the prefrontal trough are in the manual analysis, though the lack of surface observations to the north makes it difficult to identify the northern extent of the structures (Fig. 4.11b). A thermal ridge is located in the Appalachian lee, with temperatures as high as 30 ^{o}C in the simulation (Fig. 4.11a), approximately 1 ^{o}C cooler than the surface observations (Fig. 4.11b). Given this thermal ridge and the cooler sea surface temperatures to the east, a strong surface baroclinic zone is located along the Atlantic coastline (Figs. 4.11a,b). The simulation reproduces the coastal baroclinic zone well, with the model temperature and dew point at the buoy 44025 location (see Fig. 4.1 for location) matching the observations at this time (not shown). At the Ambrose Light Tower (ALSN6) location (see Fig. 4.1 for location), the 30 m model temperature is ~0.5 ^{o}C cooler than the observations at this time (~1.5 ^{o}C cooler at 18 UTC), and the winds were within 1.5 m s^{-1} (not shown). Relatively moist air with high dew points between 17-18 ^{o}C is extends northward from NJ, Long Island, and into CT/MA (Fig. 4.11a). The dew points in the WRF are ~1 ^{o}C too low in areas such as western CT (Fig. 4.11b).

Low-level warm air advection is important to the development of instability over the coastal zone, especially from northern NJ, northward over Long Island, into MA. At 1500 UTC in the 2-km WRF, which is ~9 hours prior to the line encountering the coastline, MUCAPE values in the Appalachian lee are between 1600-2000 J kg^{-1}, although over Long Island and CT they decrease from 800 J kg^{-1} to 0 J kg^{-1} from west to east (Fig. 4.12a). The 925 hPa temperature at JFK (see Fig. 4.9 for location) is 18 ^{o}C at this time (Fig. 4.13a). There is warm air advection over the coastal zone at 950 hPa seen in both the horizontal wind field (Fig. 4.12a) as well as the veering profile of wind in the JFK sounding (Fig. 4.13a). By 2100 UTC, the 925 hPa temperature at JFK has increased to 24 ^{o}C (Fig. 4.13b), which helped extend the area of maximum MUCAPE eastward towards the coast, with MUCAPE values over Long Island and CT increasing to 400-1600 J kg^{-1} (Fig 4.12b). At this time, there is continued warm air advection over the region (Figs. 4.12b, 4.13b), such that by 0000 UTC 1 June, the warmest temperatures in the vertical are at 925 hPa in the simulated OKX (see Fig. 4.9 for location) sounding over eastern Long Island (Fig. 4.13c). The WRF (Fig. 4.13c) is too cool by 2-3 ^{o}C compared to the OKX sounding profile at 0000 UTC (Fig. 4.13d), especially within the boundary layer.

A similar evolution of the instability can be seen in the NARR analyses, though the MUCAPE maximum is located ~150 km to the southwest of the maximum seen in the model at 1500 UTC (Fig. 4.12c), and the magnitude of the NARR MUCAPE is larger compared to the simulation (2000-2400 J kg^{-1}). By 2100 UTC, the magnitude of the NARR instability is similar to that seen in the simulation over Long Island and CT, though the maximum over southern NJ remains ~400 J kg^{-1} higher (Fig. 4.12d).

2. Radar and QLCS evolution

Figure 4.14 illustrates the radar reflectivity evolution of the QLCS as it encounters the Atlantic coastal zone using the WSR-88D radar at OKX and NOWrad composite data as well as the 2-km WRF simulation. At 2258 UTC 31 May, the QLCS is ~75 km north-northwest of the Atlantic coastline. At this time, the QLCS is ~150-200 km to the east of the surface cold front

(Fig. 4.11a) and within a region of instability as well as warm air advection (Fig 4.12b), which is consistent with the composites (Figs. 4.7a,c). By 0043 UTC, the linear system reaches the coastline, remaining a coherent system (Fig. 4.14b), and by 0200 UTC it moves south of Long Island over the Atlantic coastal waters (Fig. 4.14c).

The 2km (Fig. 4.14d-f) and 500 m (not shown)[1] WRF realistically simulates the structure of the linear convection (linear system with no trailing stratiform precipitation) as well as the orientation of the line, though the simulated QLCS is less robust compared to the observations. This is partially because the simulated MUCAPE was less than observed (Fig. 4.12). The 2-km linear system in WRF is ~90 minutes faster than the observed linear system, with the simulated convective line located ~75 km north-northwest from the coast at 2130 UTC (Fig. 4.14d). By 2230 UTC, the simulated QLCS is located over Long Island Sound, though there is a weakness in the convective line from NYC eastward to central Long Island (Fig. 4.14e). The simulated line moves southeastward and is located south of Long Island over the Atlantic waters at 0145 UTC 1 June 2002 (Fig. 4.14f).

Although the model showed some deficiencies in developing the QLCS, it was able to reproduce important characteristics in the vertical. The cross section location for each time was selected within close proximity to the OKX radar to obtain an accurate intensity of the QLCS. Care was taken to be sure the cross section was parallel to the radar beam to obtain an accurate radial velocity structure along the section. At 2258 UTC behind the main convective core within the trailing stratiform precipitation, a 20-25 m s^{-1} rear inflow jet (RIJ) is observed between 950-750 hPa (Figs. 4.15a,b). This elevated feature continues to exist as the linear system encounters Long Island Sound, while the convective core tilts rearward with height at 0043 UTC 31 May 2002 (Figs. 4.15c,d). Due to missing archived Level 2 data beyond 0100 UTC 1 June 2002, no cross sections could be taken while the QLCS was over the Atlantic waters.

The 2 km WRF output realistically simulates the magnitude and intensity of the RIJ. At 2130 UTC (Fig. 4.16a), the maximum of a ~20 m s^{-1} RIJ is located between 900-800 hPa, behind the main convective core within the stratiform precipitation region, as the convective core tilts rearward with height. One hour later as the QLCS is over Long Island Sound, the simulated convective line loses its rearward tilt becoming more upright with no trailing stratiform precipitation, and the presence of the classic RIJ is less distinct (Fig. 4.16b). There is an enhancement in the winds between 900-800 hPa (Fig. 4.16b), similar to the observations (Fig. 4.15d). However, given that the model does not develop the stratiform precipitation region at this time (Fig. 4.16b), unlike the observations (Fig. 4.15d), the simulated RIJ weakens. It should be noted that numerous cross sections of varying orientations and locations throughout the lifecycle of the QLCS were taken to determine whether the model accurately reproduced the elevated RIJ (not shown).

By 2345 UTC 31 May, the simulated QLCS is within the 500 m model domain allowing for a comparison with the output from the 2 km domain (Figs. 4.16b,c). As observed, there is still a well defined leading convective line; however, the 500-m grid spacing has multiple precipitation cores at the leading edge given the greater spatial resolution. The 500-m also has a weakening of the RIJ at the leading edge of the system similar to the 2-km output. Both

---

[1] The 2 km output is shown in place of the 500 m at this point of the analysis since the 500 m domain does not cover the full evolution of the QLCS shown in Figure 4.14.

resolutions under-predict the spatial extent of the stratiform precipitation region to the west of the leading convective line.

The 500 m domain is used for the remainder of the analysis given its greater spatial resolution. While over the coastal Atlantic waters, the most robust section of the QLCS is along the western portion of the line due east of NJ (Fig. 4.14f). This may be due to the interaction of the QLCS with the climatological shallow (< 500 m) wind maximum referred to at the New York Bight jet (Colle and Novak 2010). This feature develops off the coastal waters of NJ during the spring and summer months, due to a combination of an enhanced thermal gradient along the coast in conjunction with the north-south orientation of the coastline (Colle and Novak 2010). Furthermore, this western segment of the line experiences the simplest interaction with the Atlantic coastline. The segments of the convective line to the east (over CT) first encounters Long Island Sound, then Long Island, and then the Atlantic waters, while the segment of the convective line to the west simply encounters the Atlantic waters. The following analysis will be performed on the more robust section of the line with the simplest interaction with the marine environment.

At 2300 UTC 31 May, the QLCS is located along and on the inland side of the Atlantic coastal boundary (Fig. 4.17a). At this time there is enhanced 100 m south-southwesterly flow over the coastal waters, which creates localized regions on convergence along the southern shores of Long Island and CT (Fig. 4.17a). By 0030 UTC 1 June, the QLCS begins to move eastward away from the inland areas including Long Island toward the Atlantic coastal waters (Fig. 4.17b). The QLCS encounters the New York Bight jet, which creates enhanced convergence (not shown) along the leading edge of the QLCS and thus stronger ascent along the convective line (Fig. 4.17b). At this time, the system has an upright convective core with gust front lifting by the cold pool at the leading edge (Fig. 4.18a). The diabatically rain cooled air generated by the convection is behind the main convective core (Fig. 4.18b). The QLCS system is moving into a region of both potential and conditional instability, given the θ_e decrease with height from the surface up to ~600 hPa (Fig. 4.18b) and a decrease in the saturated equivalent potential temperature (θ_{es}) with height, respectively (not shown). The marine layer over the ocean is associated with a layer of potential stability, with θ_e increasing from ~330 to 338 K between the surface and ~925 hPa (Fig. 4.18b), with a maximum dry Brunt Vaisala frequency of 0.04 s^{-1} (not shown). A ~30 m s^{-1} core of an elevated winds is located between 800-650 hPa at this time (not shown). However, at this time, there is little acceleration of winds behind the system visible in the storm relative circulation vector (i.e. weak RIJ), which is consistent with the minimal stratiform precipitation behind the convective line (Fig. 4.18b).

At 0015 UTC (Fig. 4.18b), there is a storm relative component in the lowest 150-200 hPa is moving toward the QLCS that ascends at the leading edge at ~1 hPa s^{-1} (~10 m s^{-1}; Fig. 4.18b). A closer look reveals that air in the lowest ~25 hPa moves through the leading edge of the gust front rather than being forced up into the updraft (Fig. 4.18c) given the marine layer stability. Air parcels lifted from the surface are stable, but those lifted from ~975 hPa (~350 m) can reach their LFC (~825 hPa) through gust front lifting and accelerate upwards.

By 0100 UTC 1 June as the QLCS moves over the Atlantic, a segment of the line bows eastward and is located ~100 km west of the eastern NJ shoreline (Fig. 4.17c). Vertical motion along the convective line continues to be strong as the QLCS traverses the NY Bight jet (Fig. 4.17c). At this time the linear system is over the deeper marine layer as depicted in the thermodynamics fields (Figs. 4.18d,e), with the potential temperature surfaces associated with the cold pool merging with the potential temperature surfaces associated with the marine layer

(Fig. 4.18d). Air parcels continue to ascend at ~10 m s^{-1} due to lifting along the leading edge of the gust front, while the convective core remains upright (Fig. 4.18d). The core of the ~30 m s^{-1} winds remains between 800-600 hPa, (not shown), and the development of a ~20 m s^{-1} RIJ is visible in the storm circulation vectors (located at the 90 km location in the horizontal) within this vertical level (Fig. 4.18e). Atkins and Cunningham (2006) showed through idealized numerical simulations that a low-level stable layer could prevent a RIJ associated with a bow echo from descending to the surface.

The diabatically rain cooled air associated with the cold pool remains behind the leading edge of the system while the line is encountering the potentially stable layer associated with the marine inversion (Fig. 4.18e). Air within the bottom of this stable marine layer continues to move from front to back near the surface, while air at the top of the stable layer is ingested into the updraft (Fig. 4.18f). It should be noted that numerous cross section orientations and at different times in the lifecycle of the QLCS reveal similar circulation patterns (not shown).

Forward and backward 1 minute trajectories (interpolated from 15 minute 500-m WRF output) were launched along the QLCS to better understand the source of the air ingested into the system along the entire bowing segment. While hundreds of trajectories were launched, only a representative few are shown to help simplify the interpretation (Fig 4.19). In figure 4.19, the location of the air parcel along each trajectory that corresponds to the precipitation mixing ratio time is marked with a blue diamond. However, this was not done for parcels located at the beginning or the ending of the trajectory path to prevent masking the height scale depicted by the trajectory width.

Figures 4.19a,b illustrate 1 minute backward trajectories launched at 0130 UTC 1 June from 7 km. Many levels surrounding this height were tested as well, ranging from 4-10 km, and the results were similar (not shown). There are 3 main source regions of the mid-level air within the QLCS. Air at the back edge of the stratiform precipitation region originates from west of the QLCS at mid-levels between 6.5-7.5 km (trajectory 1,2; Figs. 4.19a,b) following the mid-level westerly flow (Fig. 4.10b). The parcels ending within the convective line (trajectories 3,4; Fig. 4.19a) as well as within the heavy precipitation behind the line (Fig. 4.19b) originates from the southwest between 300-500 m. The parcels move northeastward with the low level ambient flow (Fig. 4.12b) until they interact with the QLCS convective updrafts, which cause them to rise rapidly to 5 km and turn easterly following the ambient mid-level flow. The air out ahead of the QLCS as well as along the leading convective edge (trajectory 5) also originates in the mid-levels (~5.2 km) ahead of the QLCS (Figs. 4.19a,b), moves east-northeasterly, and is eventually overtaken by the faster moving QLCS (Fig. 4.19b).

Forward trajectories with a 1 minute temporal resolution were launched within the lowest several km to explore whether parcels in the lowest several 100 m of the boundary layer are ingested upwards into the QLCS. Trajectories 7 and 8 launched from 300 m as well as 6, 9, and 10 launched from 10 m only ascend to 500 m in the vertical (Figs. 4.19c,d), Most parcels below 200 m move northeasterly following the low-level flow and those above move more westerly (Fig. 4.12b). These low-level parcels are overcome by the QLCS within 15 minutes of release, rising very little due to the enhanced stability of the marine layer (Fig. 4.19d) This result was also found for trajectories further east of the linear system as well (not shown). Although this is the most common outcome for parcels between 10-300 m, it is possible for a trajectory to ascend to a higher altitude (~3-4 km; not shown).

Trajectories released at ~500 m ASL are more likely to ascend to 4.5-9 km within the QLCS (trajectories 12 and 13; Fig. 4.19e,f). However, trajectories originating at 500 m ASL can remain at low levels, such as trajectories 11 and 14, which only rise to 1.5 and 0.8 km respectively. Those that are ingested into the convective system at 500 m rise rapidly (trajectories 12, 13; Fig. 4.19f), while those that remain in the lowest 500 m are overtaken by the QLCS (trajectories 11,14; Fig. 4.19f).

c. 23 July 2002 event

1. Synoptic and mesoscale evolution

Approximately 12 hours prior to the QLCS reaching the Atlantic coastline (23 July 2002), a 500-hPa trough axis is located over eastern Great Lakes, with Q-vector convergence situated ~500 km to the north of the northeastern U.S. (Fig. 4.20a). The 300 hPa jet core (~60 m s^{-1}) is over Quebec, while a secondary jet maximum is located over the northern tier of the U.S. By 2100 UTC 23 July, the mid-level trough moves eastward over the Northeast U.S and there is little Q-vector convergence over the Northeast (Fig. 4.20b). The lack of mid-level forcing is consistent with the composite results (Fig. 4.4d). The 300 hPa jet remains along the New England-Canadian border (Fig. 4.20b), also as in the composite in Fig. 4.4d.

At 1200 UTC 23 July, a surface low-pressure system associated with the mid-level trough is over Quebec, with a trailing cold front extending southwestward through western NY and northern IN (Fig. 4.20c). Within the next 4 hours, the convective line develops along this baroclinic zone (Fig. 4.9). The convective storms remain collocated with the cold front and are located along the Atlantic coastal boundary by 2100 UTC 23 July (Fig. 4.20d). This collocation is consistent with the composite structure for decay (Fig. 4.4a) and slow decay events (Fig. 4.6a).

Figures 4.21 and 4.22 highlight the 2-km WRF and the observed evolution of the surface features as the cold front and the associated QLCS approaches the Atlantic coastal boundary. At 1800 UTC (Figs. 4.21a, 4.22a), the surface trough and the associated baroclinic zone are located 100-150 km to the northwest of the Atlantic coastline. The magnitude of the frontal baroclinic zone is slightly weaker in the simulation, with 1-2 ^{o}C cooler temperatures to the east of the baroclinic zone and 1-2 ^{o}C warmer temperatures to the west of the baroclinic zone (Fig. 4.21a). The placement of the surface trough and the associated baroclinic zone in the simulation are accurate. The 2-km WRF predicts the correct 30 m temperature and wind compared to data from the Ambrose Light Tower (not shown). The more southerly wind at Ambrose and along the NJ coast in the model is associated with the NY Bight jet. Dew point temperatures to the north of the front are well represented in the model, while they are 1-2^{o}C too cool in the warm sector over the ocean (Figs. 4.21a, 4.22a).

By 2100 UTC 23 July, as the cold front approaches the coastline, there is a weak mesohigh over the southeastern NY (Fig. 4.12b) as a result of the diabatic cooling within the trailing stratiform precipitation region of the QLCS (Fig. 4.2b), The 2-km WRF struggles to capture the mesoscale details of this pressure feature (Fig. 4.22b). Temperatures to the west of the cold front are ~2 ^{o}C too warm in the WRF, while the temperatures in the narrow warm sector are ~2 ^{o}C too cool, especially over southern NJ (Fig. 4.22b). At buoy 44025, the temperature and dew points remain ~1 ^{o}C too cool compared to the observations (Figs. 4.21a, 4.22b), Meanwhile, the simulated temperature at the Ambrose Light Tower location is accurate and the simulated winds at 30-m (not shown) are ~2.5 m s^{-1} too weak compared with the observations (Fig. 4.22b).

The QLCS moves into an unstable environment approaching the coast. At 1800 UTC 23 July, there is 1600-2000 J kg^{-1} of both simulated and NARR MUCAPE along the coastal domain extending eastward over Long Island (Figs. 4.23a,c), with most of this instability based at the surface rather than elevated (not shown). At this time, there is little warm air advection over the coast ahead of the surface cold front (Fig 4.23a), which is consistent with the composite temperature advection fields for decay (Fig. 4.4c) and slow decay events (Fig. 4.6c). By 2100 UTC 23 July, the instability remains over the coastal region and Long Island, with the simulated and NARR MUCAPE values ranging 1200-1600 J kg^{-1} (Figs. 4.23b,d). Temperature advection is near neutral along the coast, with cold air advection associated with the surface cold front over northwestern NJ, southern NY, and western CT.

The observed and simulated soundings are compared at 0000 UTC and 1200 UTC at OKX (Fig. 4.24a,b). At 1200 UTC, the 500 m WRF reproduces the magnitude of the low level inversion below 900 hPa, though the top of the simulated inversion is ~25-50 hPa too high in the vertical and the temperatures are ~1^{o}C too cool through the profile (Figs. 4.24a,b). Above the top of the inversion, lapse rates are close to dry adiabatic in both the WRF and the observations, with surface based values of CAPE of ~800 J kg^{-1} in the WRF and ~930 J kg^{-1} in the observations (not shown). At this time there is little veering of the winds above the frictional boundary layer, thus little temperature advection.

By 1800 UTC, the simulated marine inversion at JFK (see Fig 4.9 for JFK location) is relatively weak (isothermal below 950 hPa), with weak veering winds from the surface to 700 hPa (Fig. 4.24c). At LGA to the north (see Fig. 4.9 for location), comparisons were also made between the Aircraft Communications Addressing and Reporting System (ACARS) profile data at LGA at 1656 UTC and the WRF profile at the same location at 1700 UTC (not shown). Both indicate a dry adiabatic layer from the surface to 900 hPa, with temperatures decreasing from 32 ^{o}C at the surface to 21 ^{o}C at 900 hPa (not shown). By 2100 UTC, surface temperatures decrease 1-2 ^{o}C helping to reestablish the low level inversion, although both elevated instability (Fig. 4.23b) and surface base instability remains (not shown). Overall, an absence of instability does not appear to be the reason the QLCS decayed upon encountering the coastline.

2. Radar and QLCS evolution

Figure 4.25 illustrates the radar reflectivity evolution of the 23 July decaying event as it approaches the Atlantic coastal boundary. At 2016 UTC, the convective system is located 50-100 km to the northwest of the coastline. The gust front, as indicated by the thin blue line over southern CT, is 5-10 km to the south of the convective line (Fig. 4.25a). Within one hour, the QLCS becomes less uniform as it reaches the coast (Fig. 4.25b). By 2115 UTC, the leading convective line weakens and becomes more cellular (Fig. 4.25c). The line continues to decay as it progresses southeastward (Figs. 4.25b,c).

At 2015 UTC, the leading edge of the 2-km simulated convection is located 50-100 km to the northwest of the Atlantic coast (Fig. 4.25d), similar to the observations (Fig. 4.25a), though the convective line is not as uniform as the observations. By 2115 UTC, the QLCS approaches the coastline (Fig. 4.25e), organizing into a more coherent convective line compared to one hour earlier (Fig. 4.25d). This may be a reflection of model spin up as well as the fact that the maximum simulated MUCAPE is near the coast (Fig. 4.23b). At this time, the stratiform region is less organized (Fig. 4.25e) compared to the observations (Fig. 4.25b). As the simulated QLCS crosses the coastline, the leading edge weakens becoming more cellular in nature (not shown) as in the observed evolution (Fig. 4.25c). By 2300 UTC, the simulated QLCS is clearly decaying

(Fig. 4.25f), though the model was slightly slower to weaken the QLCS compared to the observations.

Figures 4.26 and 4.27 illustrate the observed and simulated vertical structure of the QLCS as it moves southward towards the coast. The simulation at both 2 km and 500 m is able to accurately reproduce the evolution of the RIJ as the QLCS approaches the coast. Given that the analysis of this evolution falls entirely within the 500 m domain, it will be used in place of the 2 km model output. About 50-100 km north of the CT coastline at 2016 UTC, the QLCS in the observed OKX radar and 2-km WRF exhibits an upright convective core (Figs. 4.26a, 4.27a), with a 15-20 m s^{-1} RIJ extending vertically from the surface to ~900-850 hPa (Figs. 4.27a, 4.26b). As the QLCS encounters the coast about one hour later, the intensity of the convection decreases (Figs. 4.26c, 4.27b) while the RIJ weakens slightly (Figs. 4.26d, 4.27b). As the QLCS crosses the coastal boundary at 2215 UTC, the intensity (dBZ) of the line further diminishes with the convective core approximately half the height in the vertical as the previous hour (Figs. 4.26e, 4.27c) as the magnitude of the RIJ continues to weaken (Fig. 4.26f, 4.27c).

Figure 4.28 highlights the evolution of the QLCS in the 500 m WRF domain. At 2130 UTC, the linear system is located along the Atlantic coastline (Fig. 4.28a), with enhanced ascent along the southern shore of Long Island due to convergence associated with the NY Bight jet. At this time, there is lifting at the leading edge of the cold pool of the QLCS (Fig. 4.29a), which is ~6 km to the east of the marine layer, as depicted by the cooler potential temperatures to the southeast. There are two regions of ascent, one at low levels at the leading edge of the cold pool (6 m s^{-1}) and another in the mid- and upper-levels (8 m s^{-1}) ~8 km behind the area of low-level ascent, indicating the presence of a tilted updraft with height. This is visible in the storm relative circulation vectors as well, with upright ascent arrows in the lower levels that tilt upwind with height (Fig. 4.29b). The circulation vectors also highlight the RIJ (~20 m s^{-1}) located from the surface up through ~900 hPa. There is diabatically rain cooled air below this level comprising the cold pool (Fig. 4.29a). The QLCS is within a potentially (and conditionally; not shown) unstable environment with θ_e (θ_{es}) values decreasing from the surface to ~550 hPa (Fig. 4.29b). As in the 31 May 2002 event, there is a layer of potential stability below 950 hPa associated with the marine layer to the east (Fig. 4.29b). This marine layer has a maximum Brunt Vaisala frequency of 0.036 s^{-1}, which is slightly less stable compared to the 31 May 2002 event (Figs. 4.18b,e). The weaker marine layer is reflective of the warmer SSTs in mid July than in late May. Unlike the 31 May 2002 event, there is upward motion, though weak, from the surface into the leading edge of the convection (Fig. 4.29c), which is consistent with the presence of ~500 J kg^{-1} of ambient surface based CAPE (not shown). Ahead of the QLCS, the LFC of the ambient environment is between ~880-830 hPa (not shown). While most of the ascent appears to be ahead or above the cold pool within the ambient environment, there is a region of ascent that originates within the cold pool itself at this time, within an area of storm relative converging circulation vectors (Fig. 4.29c).

By 2200 UTC 23 July, the QLCS moves closer to the Atlantic waters as well as the enhanced low-level winds offshore (Fig. 4.28b). As the cold pool encounters the cooler, more stable marine environment, the leading edge of the cold pool is located ~5 km ahead of the main convective core and the region of ascent (4 m s^{-1}) has shifted to within the cold pool (Fig. 4.29d). The deep tropospheric ascent continues to tilt back towards the stratiform region of the QLCS as seen in the circulation vectors. This ascending motion produces clouds, but it struggles to generate precipitation (Fig. 4.29e). Weisman (1992) illustrated that a tilted updraft causes a parcel ascending within that updraft to mix more with the ambient air, altering the thermodynamic properties (i.e. decreasing the θ_e) of a parcel lifted from the lower atmosphere, and potentially decreasing the buoyancy and moisture of the parcel. This may also allow for greater entrainment of drier air into the parcel as it ascends (Weisman 1992), especially during a slower ascent, making it more difficult to generate precipitation. The relative humidity (RH) values in the lowest 50-100 hPa ahead of the QLCS within the marine layer are only between 50-70%, and the RH values above 600 hPa are less than 50% (not shown). This is unlike the 31 May event where the low level RH values are between 60-80%, and 50-90% above 600 hPa (not shown). The smaller low-level relative humidity during the 23 July 2002 event is consistent with the composites (Figs. 4.4b, 4.6b), and it allows for a greater chance of evaporative cooling. The role of low- and mid- level dry air favoring enhanced diabatic cooling and the development of a stronger cold pool has been documented in the literature (Gilmore and Wicker 1998, James et al. 2006). Through idealized simulations of quasi-linear convective systems, James et al. (2006) showed that relatively dry air at low- and mid-levels favors the development of a stronger cold pool, compared to more moist environments, causing the linear convective line to tilt upshear.

Closer examination of the ascending air relative to the cold pool reveals that the main region of surface based ascent originates within the cold pool at 2200 UTC (Fig. 4.29f). Those parcels within the cold pool have relatively weak MUCAPE (~500 J kg^{-1}) and a LFC near ~725 hPa (not shown). Therefore, any parcels ingested into the QLCS from the cold pool itself are less buoyant compared to the surrounding environment and will require lifting to a greater altitude to release the instability.

By 2230 UTC, there is noticeable weakening of the convective line as it continues to move southeastward over the Atlantic waters (Fig. 4.28c). The leading edge of the cold pool is no longer aligned with the main convective core and it is located 10-15 km ahead of the QLCS (Fig. 4.29g). There is continued weak lifting (2 m s^{-1}) along the gust front creating only clouds (Fig. 4.29h). The diabatically rain cooled air associated with the cold pool has surged ahead of the convective core (Fig. 4.29h). The circulation vectors depict a more front to rear flow rather than ascending motion (Fig. 4.29h), with mid- and upper level ascent of 2-4 m s^{-1} within the leading convective core (Fig. 4.29g). Air parcels from the cold pool continue to ascend into the QLCS, with MUCAPE values of 250 J kg^{-1} and an LFC of ~775 hPa. The cold pool continues to move away from the convective line and the system dissipates (not shown).

Forward and backward trajectories highlight the source regions of air ingested into the QLCS as it progresses out over the Atlantic waters (Fig. 4.30). Figures 4.30a,b illustrate 1 minute backwards trajectories (interpolated from 15 minute 500-m WRF output) launched from 5 and 6 km at 2300 UTC, though parcels release from other levels in the mid- and upper levels have similar trajectories (not shown). Trajectories ending within the mid-levels of the QLCS (Fig. 4.30b) travel from southwest to northeast following the predominant tropospheric flow (Figs. 4.20b, 4.23b), Trajectories such as 1 and 2 originate within the low levels between 0.6-0.8 km and ascend rapidly once they interact with the convective updrafts (Fig. 4.30a). Parcels along trajectories such as 3, 5, 7, and 8 originate between 4-5 km ASL with little ascent along their paths (Fig. 4.30a).

As suggested by Figs. 4.29c,f,i, the air near the surface may be ingested into QLCS. Most forward trajectories originating ahead of the QLCS launched at 10 m and 100 m move southeasterly parallel to the motion of the cold pool and terminate near the leading edge of the decaying convective line (Figs. 4.30c,d). Trajectories originating near 10 m (11, 12, 13) only ascend to between 0.3-0.4 km, while trajectories launched from 100 m (9-10 and 14-17) ascend much higher (Fig. 4.30c,d). Trajectories 10, 14, and 15 rise slowly ahead of the system and reach

0.4-0.7 km while traveling along a southeasterly path parallel to the RIJ (Fig. 4.30c,d). Trajectories 9, 16, and 17 ascend more quickly to 1.2-2.4 km as they interact with the convective updraft. At these higher altitudes, they turn northeasterly following the ambient tropospheric flow (Figs. 4.20b, 4.23b). Care was taken to launch trajectories from within the leading edge of the cold pool ahead of the precipitation. Many of those trajectories travel into the convective updraft as well, indicating that more stable air with a higher LFC compared to the surrounding environment is being ingested into the convective updraft (not shown). Overall, there is more near-surface based ascent in this July event than the above May 2002 event. The ascending motion of parcels originating at both 10 m as well as 100 m is consistent with the presence of relatively weak marine layer (Fig. 4.29) and surface based instability (200-500 J kg^{-1}; not shown) during this July event.

For the forward trajectories launched from 500 m (Figs. 4.30e,f), trajectories 18 and 23 only rise to 1-1.4 km ASL and are under the influence of the surface based RIJ (Fig. 4.30e). These are the only trajectories that end at the leading edge of the decaying convection, while all other trajectories end further behind the line (Fig. 4.30f). Trajectories 19-22 and 24 move along a southeasterly path until they interact with the convective updraft during which they ascend more quickly. As they ascend, they turn northeasterly following the environmental flow rising to 2.1-4.3 km (Figs. 4.20b, 4.23b).

4.4 Discussion

a. Comparison between the 31 May and 23 July 2002 event

Rotunno et al. (1988) proposed a theory ('RKW' theory) for long-lived squall lines supported by gust front lifting. They showed that deeper lifting at the leading edge of the cold pool is favored through a balance of the horizontal vorticity generated by change in buoyancy perpendicular to the line induced by the convectively generated cold pool and the environmental wind shear perpendicular to the line over some depth in the lower troposphere described by

$$\rho_o \frac{d}{dt}\frac{\eta}{\rho_o} = -\frac{\partial B}{\partial x}. \tag{4.1}$$

In Eqn. (4.1), ρo(z) is the base state density, B is the total buoyancy, u is the velocity perpendicular to the convective line, w is the vertical velocity, x is the cross line distance, and η is the along line vorticity (in the y-direction) defined by

$$\eta \equiv \frac{\partial u}{\partial z} - \frac{\partial w}{\partial x}. \tag{4.2}$$

Rotunno et al. (1988) describe the existence of an optimal state, during which the convective updraft will realize the full CAPE without interference by the cold pool or the ambient shear. By performing a control volume analysis on Eqn. 4.1 around the cold pool and assuming (1) $\eta \cong \partial u/\partial z$, (2) the reference frame is fixed with the moving edge of the cold pool, (3) steady state balance, (4) the buoyancy of the air approaching the cold pool is negligible, (5) the air within the cold pool is stagnant relative to the edge of the cold pool, and first assuming a case with no shear, yields

$$u^2_{L,d} = 2\int_0^H (-B_L)\,dz, \tag{4.3}$$

where u^2 is the speed of the horizontal wind at the top of the left edge of the control volume. If it is assumed that the temperature of the cold pool is constant,

$$B_L = g\frac{\Delta\theta}{\theta_o} \equiv g', \tag{4.4}$$

where $\Delta\theta$ is the potential temperature perturbation of the cold pool and θ_o is the ambient potential temperature. Eqns. (4.3) and (4.4) reduce to

$$u^2{}_{L,d} = 2g'H \equiv c^2 \tag{4.5}$$

where u is essentially the speed of the control volume, i.e. the speed of the cold pool defined as c. Now considering a case with shear and assuming that the low-level flow exits as a vertically oriented flow through turning by the cold pool (i.e. u at the top of the control volume = 0 and the change in vertical motion across this volume = 0),

$$\Delta u = u_{R,d} - u_{R,0} = -u_{R,0} = \sqrt{2g'H} \tag{4.6}$$

This last assumption describes the optimal balance where the evacuation of mass is perpendicular to and through the top of the volume, rather than traveling along a more sloped trajectory. Considering Eqn. (4.6) in terms of the control volume (see Rotunno et al. 1988 Eqn. 5), the RHS of Eqn. (4.6) is interpreted as the flux of positive vorticity associated with the low-level shear imported into the control volume and the LHS is the buoyant generation of negative vorticity by the cold pool within the control volume. Following Eqn. (4.5), the LHS of Eqn. (4.6) is related to the speed of the cold pool. For a more complete derivation and explanation of assumptions, see Rotunno et al. 1988.

Weisman and Rotunno (2004) clarified these ideas through the derivation of unitless ratio C/ΔU, suggesting that the optimal state for deep gust from lifting occurs when C/ΔU ≈ 1, creating an upright updraft. If C > ΔU, the circulation associated with the cold pool, as well as the speed, overwhelms the circulation associated with the low-level ambient shear, causing the flux of mass along the leading edge of the cold pool is tilted back towards the cold pool. Therefore, the updraft tilts upshear. For C < ΔU, the opposite occurs with the updraft tilting downshear. The latter 2 scenarios are unfavorable for the maintenance of a cold-pool driven QLCS. These ideas have been tested through numerical experiments using a variety of numerical models (Bryan et al. 2006) and the basic theory is still able to predict squall line structure.

Several studies have illustrated the importance of tropospheric deep shear for the organization and maintenance of mesoscale convective systems (e.g. Coniglio and Stensrud 2001, Coniglio et al. 2004, Parker and Johnson 2004a,b). Through observational analyses, Stensrud et al. (2005) highlighted that most long lived squall lines form in environments with shear over deeper layers than the 2.5-5 km suggested by ‘RKW’ theory, suggesting that the C/ΔU relationship will not accurately predict squall line structure. However, Bryan et al. (2006) pointed out that the applicability of ‘RKW’ theory has not been tested for a broad range of environments. This is an opportunity to apply the basic principles of ‘RKW’ theory over the northeastern U.S. environment. Furthermore, though ‘RKW’ theory alone does not completely describe the large-scale structure and the evolution of a squall line, it is an important piece of the story. This is especially true when introducing variations within the lower troposphere, such as changes in surface properties as well as the boundary layer, since ‘RKW’ theory is sensitive to balances within the lower troposphere.

Equation (4.3) is utilized to calculate the balance between the speed of the cold pool generated by the convective line and the environmental shear from the surface to 2.5 km following Weisman and Rotunno (2004). For the purpose of this study, the simplified calculation of buoyancy shown in Eqn. (4.4) described in Rotunno et al (1998) is applied, rather than the full equation including the effects of rain loading as described in Weisman and Rotunno (2004). To justify the exclusion of the rain loading in the calculation, buoyancy was estimated including the effects of mixing ratio on the calculation at a couple times yielding a difference of only ~1-2 m s^{-1}.

For this analysis, the cold pool is defined as the region in which the potential temperature values are less than the ambient surface potential temperature. For the 31 May 2002 event, it is defined as the 300 K surface and for the 23 July 2002 event it is the 304 K surface, with the values remaining consistent through the lifetime of the convection, even as it interacts with the marine layer. The potential temperature of the cold pool (θ_{cp}) is calculated as the average potential temperature from the surface to the top of the cold pool defined above, while ambient potential temperature (θ_o) is calculated as the average potential temperature in the environment immediately ahead of the cold pool from the surface to the depth of the cold pool. The potential temperature perturbation of the cold pool (θ') is the difference between the cold pool average θ and the average ambient θ.

Table 4.1 summarizes the values used to perform the calculation as well as the final results. All values have been calculated using 15-minute intervals to capture the changing structure of the cold pool (magnitude and depth) as well as the variations within the environment, including changes in the vertical wind shear as well as the inclusion of the cooler potential temperature values associated with the marine layer within the calculation of θ_o. These values have been calculated over a variety of line perpendicular cross sections for both the 31 May and the 23 July 2002 events over the full lifecycle of the systems (not shown). For brevity, only the values that correspond to the times in figure 4.18 for the 31 May event and figure 4.29 for the 23 July event are shown (Table 4.1).

Recall that as the 31 May 2002 maintaining QLCS moved over the Atlantic, it maintained its upright convective core (Fig. 4.18). The theoretical cold pool speed is estimated between 15.3-19.3 m s^{-1}, while the ambient 0-2.5 km vertical wind shear is ~15 m s^{-1}, which gives a $C/\Delta U$ ranging between 1-1.2. These calculations were performed along a cross section perpendicular to the eastward motion of the convective line. Calculations were performed over several other cross section orientations, more perpendicular to the orientation of the leading edge of the convective line rather than the motion, yielding a range of shear values between 14.5-18 m s^{-1}, with a range of $C/\Delta U$ values between 0.74-0.97. Given these range of values, 'RKW' theory predicts an upright convective structure which matches the observations. For the 23 July 2002 decaying QLCS, figure 4.29a shows that the leading edge of the cold pool is already located ahead of the main convective line as the storm crosses the coastal boundary (Fig. 4.28a). By the next hour (2230 UTC), the magnitude of θ' associated with the cold pool increases from 4 to 5.5 K, while the ambient 0-2.5 km vertical wind shear eventually decreases to 5 m s^{-1} by the end of the period (Table 4.1). The $C/\Delta U$ during this evolution ranges between 1.6-2.6, suggesting an upshear tilted updraft, which matches the evolution of the QLCS (Fig. 4.28b,c).

b. Sensitivity Tests

The application of the basic principles behind 'RKW' theory to the 2 events examined in this study suggest that the properties of the cold pool as well as the strength of the ambient vertical wind shear appear important to the evolution of the 2 events. In the following section, the physical processes responsible for the maintenance of the 31 May 2002 event and the decay of the 23 July 2002 event are explored through the application of a series of WRF sensitivity experiments at 2 km grid spacing.

The cold pool of a QLCS is generated through diabatic cooling processes, primarily the evaporation of precipitation within the storm. During the 23 July 2002 event, the diabatically generated cold pool moves ahead of the convective line causing the QLCS to tilt upshear (Fig. 4.29). The role of the evaporative cooling is tested by reducing the cooling to 15% of the control simulation beginning at 13 h (1900 UTC 23 July 2002) into the simulation (Table 4.2). Turning off evaporative cooling completely was attempted, but this led to unrealistic meso-circulations in the WRF (not shown). At 2200 UTC, the CTRL QLCS is located along the Atlantic coastline (Fig. 4.31a) and within the hour it decays (Fig. 4.31b). By 0000 UTC, only the stratiform rain shield remains along the coast (Fig. 4.31c) and by 0300 UTC there is no almost no precipitation (Fig. 4.31d). For the simulation with reduced evaporative cooling (15%EVAP), 3 hours after decreasing the evaporative cooling, the QLCS is noticeably more organized and robust (Fig. 4.31e) compared to the CTRL QLCS at the same time (Fig. 4.31a). By 1700 UTC, the 15%EVAP QLCS is located along the Atlantic coast increasing while in intensity (Fig. 4.31f), though it is moving more slowly to the southeast compared to the CTRL run which is decaying at this time (Fig. 4.31b). Three hours later, the 15%EVAP convection is crossing over the Atlantic coastal boundary, remaining a coherent linear system (Fig. 4.31g), while the CTRL convective line has decayed 2 hours prior to this time (Fig. 4.31c). By 0600 UTC, a bowing segment develops within the 15%EVAP simulation just south of Long Island (Fig. 4.31h).

A cross section comparison between the CTRL and the 15%EVAP linear systems at 1700 UTC highlight the main structural differences. At this time, the cold pool in the CTRL simulation is ~20 km ahead of the leading convective line (Fig. 4.32a), while it is collocated with the main convective core for the 15%EVAP line (Fig. 4.32b). However, the calculation of the C/ΔU relationship results in a value of ~2 for both events (Table 4.1). Firstly, the environmental shear is approximately the same during both simulations. Secondly, the θ' of cold pool is slightly stronger for the 15%EVAP run while the depth of the cold pool is shallower, which have opposing influences when calculating the speed of the cold pool (Eqn. 4.3, 4.4). While it seems counterintuitive that the cold pool during the 15%EVAP simulation is stronger, it is because the ambient θ is warmer during the 15%EVAP simulation compared to the CTRL (Table 4.1). At the time the calculation was performed (2300 UTC), the 15%EVAP QLCS is just on the ocean side of the coastline while the CTRL QLCS is further southeast over the Atlantic waters under a greater influence of the marine layer. At an earlier time in the CTRL simulation (2100 UTC) when the CTRL QLCS is at a similar location as the 15%EVAP QLCS seen in Fig. 4.31f, the potential temperature perturbation of the cold pool is 1 K colder and the cold pool is 600 m deeper compared to the 15%EVAP cold pool (Table. 4.1). With a stronger cold pool and the influence of a weaker vertical wind shear, this yields a much larger C/ΔU of 3.5 (Table 4.1) for the 2 km CTRL QLCS compared to the 15%EVAP QLCS when they are at similar locations spatially.

There is still some development of meso-circulations along the convective line during the 15%EVAP simulation, causing it to loose the structural properties of a QLCS. Cross sections through the 15%EVAP convection as it traverses the Alantic waters (0200-0600 UTC) reveals that the system has a warm core structure, with no obvious cold pool (not shown). Since 'RKW' theory predicts the structural differences of cold pool driven systems (Rotunno et al. 1998, Weisman and Rotunno 2004), it may not be applicable to the convective system by this time

(0600 UTC). Other thresholds were tested (i.e. 22%EVAP, 30%EVAP) in an attempt to remove the development of the unrealistic circulations (not shown), The further reduction in evaporative cooling caused the QLCS to evolve in a similar manner to the 15%EVAP simulation (22%EVAP) or to decay similar to the CTRL (30%EVAP).

A similar sensitivity test was applied to the 31 May 2002 event, though the evaporative cooling was increased by a factor of 10 (Table 4.2) in an attempt increase the magnitude of the cold pool and cause the system to decay. Within an hour of increasing the evaporative cooling, the system was decaying south of Long Island over the Atlantic waters (Fig 4.33a). Given the enhanced evaporative cooling, the magnitude of the potential temperature perturbation associated with the cold pool was ~10 K with a depth of ~1750 m (Fig. 4.33b), causing the intensity of the convection to increase rapidly and subsequently decay rapidly (Fig. 4.33c). In this scenario, the C/ΔU of ~2 correctly predicts the decay of the QLCS due to an enhancement of the cold pool through diabatic processes (Table 4.1).

While it is clear that diabatic processes are important to the evolution of both the 23 July and 31 May QLCSs, the role of the ambient vertical wind shear perpendicular to the convective line was also explored. For the 31 May maintaining event, the ambient vertical wind shear was modified in an attempt to force the QLCS out of balance following the basic ideas of 'RKW' theory. To alter the wind shear, the roughness length over the Atlantic Ocean was increased from 0.0001 m to 0.5 m, a value representative of the forested areas of the northeastern U.S. This resulted in a decrease of winds within the lowest 300 m.

Initially, the hourly evolution of the 31 May event at 2 km resolution is presented. At 0000 UTC in the CTRL run, the convective line crosses the Atlantic coast, though much of the line is still located over land (e.g. NJ, Long Island; Fig. 4.34a). By 0100 UTC, it is south of Long Island over the Atlantic waters as a segment of the convective line begins to bow out (Fig. 4.34b). The bowing segment continues eastward and begins to weaken over the Atlantic waters by 0200 UTC, while the western section of the QLCS becomes more organized off the coast of NJ (Fig. 4.34c). By 0300 UTC, the eastern portion of the convective line has dissipated while the western segment continues to move east-southeastward (Fig. 4.34d).

In the 0.5ZNT simulation at 0000 UTC, the convective line looks similar to the CTRL run, though the 10 m wind values are 2.5-7.5 m s^{-1} weaker over the Atlantic waters compared to the control simulation (Fig. 4.34e). By 0100 UTC, a segment of the convective line bows out as in the CTRL simulation, though the intensity of the bow is weaker (1-2 g kg^{-1} smaller precipitation mixing ratio) during the 0.5ZNT simulation (Fig. 4.34f). The bowing segment in the 0.5ZNT experiment continues to dissipate over the Atlantic waters, more rapidly compared to the CTRL simulation (Fig. 4.34g). However, by 0300 UTC, the western portion of the line in the 0.5ZNT simulation appears more coherent compared to the CTRL (Fig. 4.34h)

It was originally anticipated that the weaker QLCS over the ocean water during the 0.5ZNT simulation was due to the change in vertical wind shear, but further examination reveals that the line perpendicular vertical wind shear has changed little compared to the CTRL simulation (Fig. 4.34a,b). The 0-2.5 km line perpendicular wind shear is 22.5 m s^{-1} for the CTRL simulation (Fig. 4.34a) and 22 m s^{-1} for the 0.5ZNT (Fig. 4.34b). This calculation was performed on cross sections taken perpendicular to the movement of the QLCS as shown in Figs. 4.34a,e. To test the sensitivity of this calculation to the orientation of the cross section, the 0-2.5 km line perpendicular wind shear was calculated along an orientation more perpendicular to the leading edge of the line, rather than the motion of the line, as shown in figure 4.34b. The line perpendicular vertical wind shear was still only ~0.5 m s^{-1} greater in the CTRL compared to the

0.5ZNT simulation (not shown). The difference in line perpendicular wind shear between the CTRL and the 0.5ZNT simulation was calculated for the western part of the convective line over the coastal NJ waters at 0200 UTC as well (Figs. 4.34c,g). The orientation of the cross section used in this calculation is shown in Fig. 4.34c, and again the CTRL has a ~0.5 m s^{-1} larger shear value (not shown).

Though there was little change in the vertical wind shear, the magnitude of the marine layer as represented by the vertical gradient in potential temperature within the boundary layer is weaker in the CTRL (Fig. 4.35c) compared to the 0.5ZNT run (Fig. 4.35d), with the potential temperature above the surface ~4 K cooler in the 0.5ZNT simulation. The increase in the strength of the marine inversion is consistent with decreased mixing within the boundary layer due to a reduction of the winds in the lowest 300 m. The ambient RH within the boundary layer is greater in the 0.5ZNT experiment, consistent with reduced mixing as well as the stronger marine inversion (Figs. 4.35c,d). The enhanced marine inversion reduces the MUCAPE as much as 500 J kg^{-1} (not shown). Regardless of this decrease in MUCAPE, the western portion of the QLCS in the 0.5ZNT simulation was slightly stronger due to enhanced convergence in the lowest 100 hPa leading to greater vertical motions compared to the CTRL simulation (not shown).

For the 23 July 2002 event, it was hypothesized that the relatively cool ocean helped to weaken the system. To test this, the surface properties and temperature of the Atlantic Ocean were changed to that of a forested area of the northeastern U.S. To accomplish this, several surface properties were modified such as (1) the LANDMASK value was changed from ocean to land, (2) the land use index (LU_INDEX) was changed from ocean to deciduous broadleaf forest which is the vegetation type over a majority of the Northeast, (3) any surface and 2 m temperatures colder than 293 K were increased to the 293 K threshold which allowed for temperatures over the removed ocean to resemble temperatures along the coastal zone at t=0h. The results of this sensitivity experiment are summarized in figure 4.36. At 1600 UTC, the QLCS approaches the location of the old Atlantic coastal boundary (Fig. 4.36a), with several stronger convective cores compared to the CTRL run (Fig. 4.31a). By 1700 UTC, the QLCS decays (Fig. 4.36b) regardless of the removal of the ocean, at a similar location spatially to the CTRL (Fig. 4.31b). Cross sections illustrate that the leading edge of the cold pool during the LAND simulation is ~12 km ahead of the convective line (Fig. 4.36c), while for the CRTL simulation it is ~22 km (Fig. 4.32a), suggesting that the QLCS is decaying more slowly during the LAND run.

When converting the ocean to a land surface, several factors that impact the evolving convection are altered simultaneously, including an increase in friction which translates to a reduction in the low-level winds and the conversion to a drier, warmer boundary layer compared to the marine layer which impacts the ambient instability. Difference plots between the CTRL simulations and the LAND run highlight some of these variations. During the CTRL run, the line-perpendicular winds in the lowest 50 hPa are 1-3 m s^{-1} greater moving towards the QLCS between 950-800 hPa, and the winds are 1-3 m s^{-1} greater moving away from the QLCS (Fig. 4.26a). This indicates that there is greater vertical wind shear in the lower troposphere in the CTRL run than the LAND run. The decreased vertical wind shear in the LAND simulation favors the decay of the linear system.

Differences in the relative humidity highlight the decreased boundary layer moisture in the LAND simulation, though there is an increase in relative humidity values between 950-800 hPa (Fig. 4.37b), coincident with the top of the boundary layer in the LAND run. For the LAND simulation, the deeper, mixed out boundary layer and the removal of the marine layer translates greater surface based CAPE values ranging from 100-1800 J kg^{-1} over the location of the former Atlantic Ocean (Fig. 4.37c), which would enhance the likelihood of a long lived convective system, consistent with the evolution in figure 4.36. A difference plot of CTRL-LAND surface based CAPE taken one hour before the QLCS encounters the coast (15 h) to prevent convective contamination illustrates that the higher values of instability (100-300 J kg^{-1}) extend over the coastal plain, supporting the development of a few stronger convective cores in the LAND experiment (Fig.4.36a) compared to the CTRL (Fig. 4.36b).

While several parameters are altered simultaneously in the LAND experiment, a sensitivity test was performed to isolate the role of the increase in friction by the introduction of a land surface and consequently the impacts on the vertical wind profile. Similar to the 31 May 2002 sensitivity test, the roughness length for the 23 July 2002 event over the Atlantic Ocean was increased from 0.0001 m to 0.5 m, a value representative of the northern U.S. land surface, in order to isolate the frictional effects on the vertical wind shear. In the sensitivity run, the line perpendicular wind near the surface decreased only ~1 m s^{-1}, causing the vertical wind shear to remain approximately the same as the CTRL run (not shown). As anticipated, both the structural evolution as well as the speed of the decay of the 0.5ZNT QLCS simulation is the same as the CTRL run (not shown).

As seen in figure 4.23, the magnitude of the MUCAPE along the coast and over the coastal waters the during the 23 July decaying event decreased slightly as the QLCS moved toward the coastline between 1800 and 2100 UTC. This decrease in instability may be due to the reduction in solar heating due to the increasing the solar zenith angle. Perhaps if the QLCS encountered the coastline earlier in the day at a time when the instability was greater, the lifetime of the convection could have been extended. To explore the role of the reduction of ambient instability, the solar heating was modified during the 23 July control simulation, allowing for more solar heating and ultimately an increase in MUCAPE. The simulation was run with the same specifications as the CTRL until 3 PM local time (13 h, 2000 UTC 23 July 2002) at which the solar heating was fixed for the duration of the simulation (Table 4.2). At 2100 UTC, one hour after fixing the solar heating to a constant value, both the leading convective edge of the QLCS and the trailing stratiform region of the convection in the 3PM_SOLAR run (Fig. 4.38a) is stronger and more coherent compared to the CTRL run (Fig. 4.38b). This is due to the increased elevated instability, as much as 2000 J kg^{-1} greater compared to the CTRL, ahead of the linear convection, including over the Atlantic waters (Fig. 4.39). By 2200 UTC, the 3PM_SOLAR convection is already decaying over the Atlantic waters (Fig. 4.38c), moving more rapidly southeastward compared to the CTRL run (Fig. 4.38d). This decay occurs regardless of the enhanced instability ahead of the system at this time over the marine environment (Fig. 4.39b). A similar increase was seen in surface based CAPE values as well (not shown). The largest contribution to the larger instability values was the increased moisture in the lower levels leading to a decrease in the height of the LFC.

For the 23 July 2002 event, the QLCS decayed in all sensitivity tests that modified a contributing influence of the marine layer (i.e. shear, instability), yet it maintained its intensity through a reduction in diabatic cooling. This suggests that the role of the marine layer may be secondary to the diabatic processes internal to the convective system during this event. An increase in diabatic cooling during the 31 May event resulted in a more rapid decay of the QLCS, indicating that diabatic processes within the cold pool are important during this event as well. However, the intensity and longevity of the 31 May QLCS does appear to be sensitive to the environment over the marine waters. A reduction in winds within the lowest 300 m, which in turn resulted in a stronger marine inversion, led to a weaker QLCS over the Atlantic waters. The weaker QLCS was likely the result of an increased marine inversion and thus a decrease in MUCAPE, rather than a change in the line perpendicular vertical wind shear. As shown above, the NY Bight may lead to some local enhancements of the line as it encounters the coast, but these appear to be short-lived.

Overall, the impact of the marine layer was not the primarily factor governing the evolution of these cases. Another clue that this is the case is that the evolution of the convection over the adjacent land over NJ follows the same evolution as over the ocean (Fig. 4.36). Other events may have more of a marine impact, which will require future investigation.

Table 4.1 Values used in the calculation of equation (4), where θ_o is the base state potential temperature (K), θ' is the potential temperature perturbation associated with the convectively generate cold pool (K), h_c is the height of the cold pool, C is the theoretical speed of the cold pool (m s^{-1}), and ΔU is the line perpendicualr wind shear (m s^{-1}) from 0-2.5 km.

Time	θ_o (K)	θ' (K)	h_c	C (m s^{-1})	2.5 km ΔU (m s^{-1})	C/ΔU
0030 UTC 1 June 2002 12.5 h 500m CTRL	300.25	3.75	880 hPa 1200 m	19.3	15.0	1.3
0100 1 June 2002 13 h 500 m CTRL	298.25	2.75	870 hPa 1300 m	15.3	15.0	1
2130 UTC 23 July 2002 15.5 h 500 m CTRL	304.5	4	870 hPa 1300 m	18.3	7.5	2.5
2200 UTC 23 July 2002 16 h 500 m CTRL	302	5	850 hPa 1500 m	14.0	9.0	1.6
2230 UTC 23 July 2002 16.5 h 500 m CTRL	301.5	5.5	870 hPa 1300 m	13.0	5.0	2.6
2300 UTC 23 July 2002 17 h 2 km CTRL	301.75	2.25	880 hPa 1200 m	13.2	7.0	1.9
2300 UTC 23 July 2002 17 h 2 km 15%EVAP	304	3	910 hPa 900 m	13.2	6.0	2.2
2100 UTC 23 July 2002 15 h 2 km CTRL	305.5	4	860 hPa 1500 m	13.9	4.0	3.5
2245 UTC 1 May 2002 10.75 h 2 km 10EVAP	301	10	825 hPa 1750 m	33.8	16.0	2.1

Table 4.2 Matrix of sensitivity tests performed.

Event	Sensitivity	Start Time	Description
020723	15%EVAP	13 h	Multiplied the temperature tendency equation involving the evaporation of rain, melting of snow and graupel by 15%
020531	10EVAP	10.5 h	Multiplied the temperature tendency equation involving the evaporation of rain, melting of snow and graupel by 10
020531	0.5ZNT	0 h	Increased the roughness length over water from 0.0001 m to 0.5 m
020723	LAND	0 h	Changed the Atlantic Ocean surface properties and temperature to that of the adjacent forested area of the Northeast
020723	0.5ZNT	0 h	Increased the roughness length over water from 0.0001 m to 0.5 m
020723	3PM_SOLAR	13 h	Fixed the solar heating at 3 PM local time

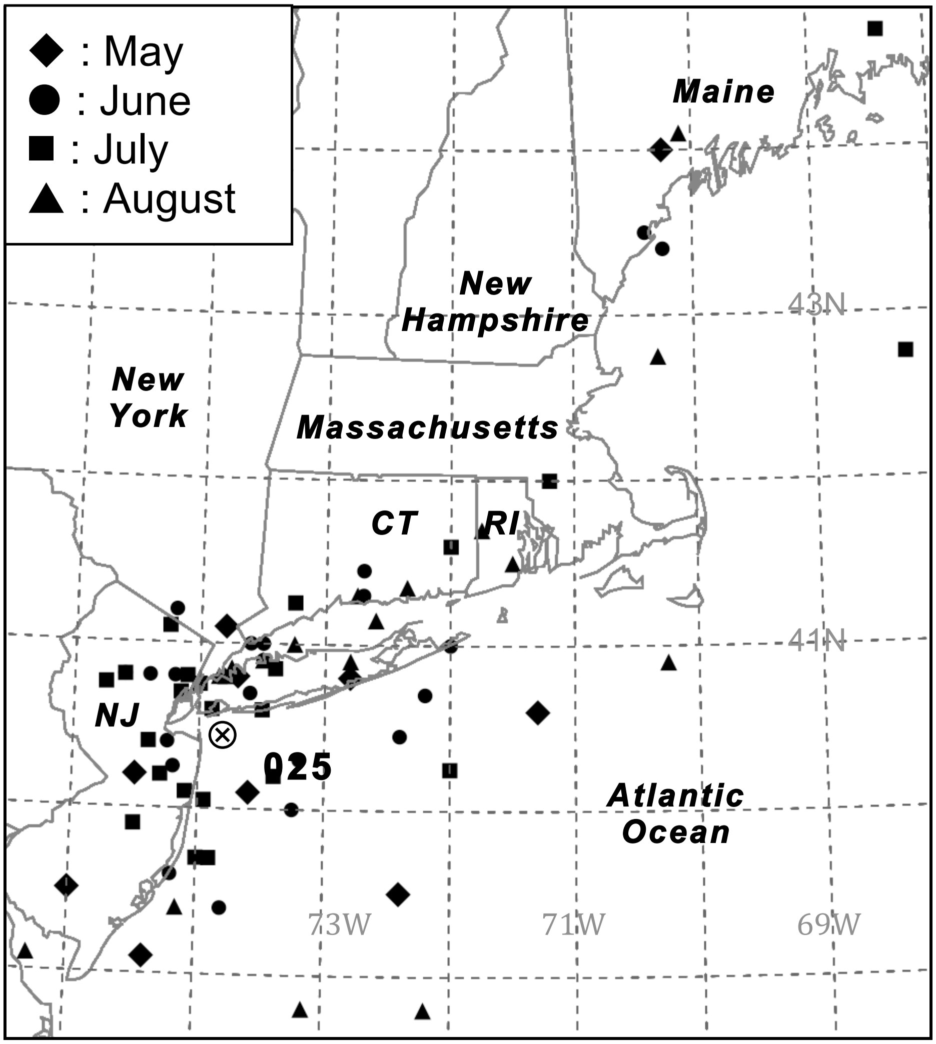

Figure 4.1 Decay locations for 73 quasi-linear convective systems over the northeastern U.S. from May-August 2002-2007 categorized by month with 10 May events, 21 June events, 23 July events, and 19 August events. The approximate location of buoy 44025 is indicated by the 025, while the location of the Ambrose Light Tower (ALSN6) is denoted by ⊗.

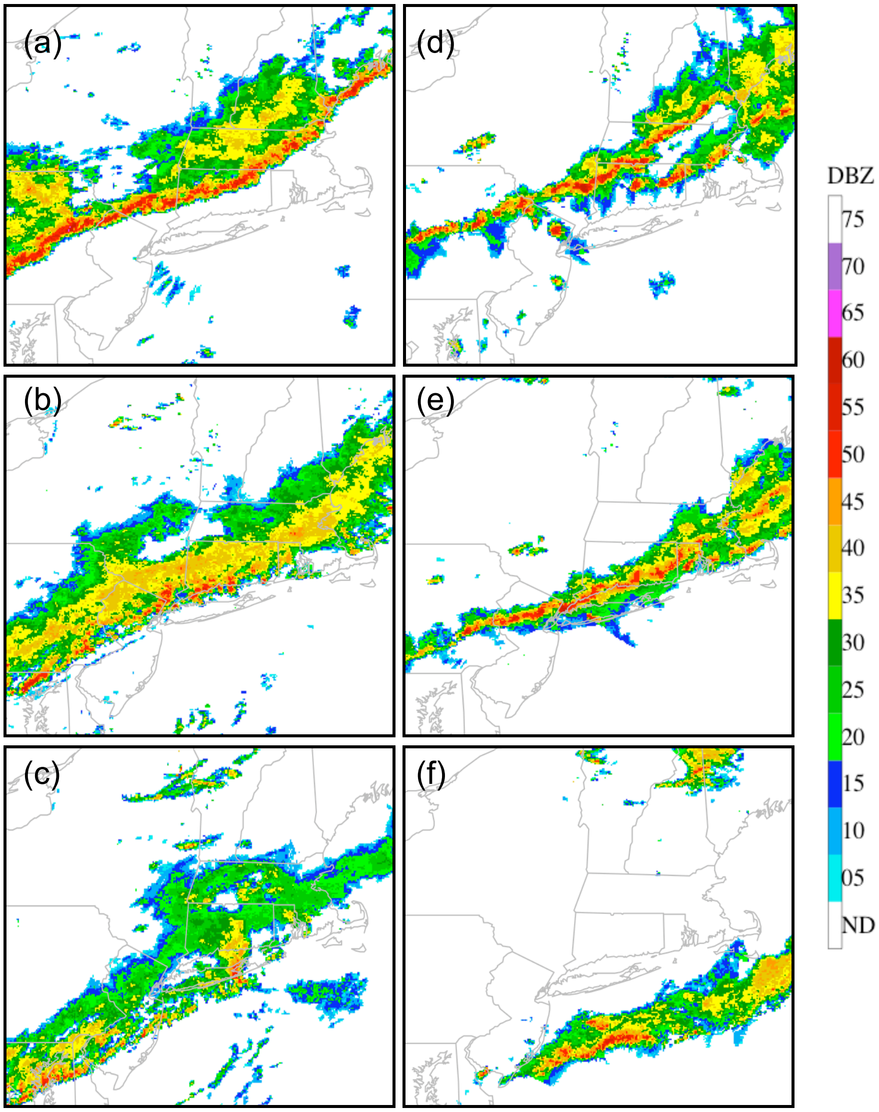

Figure 4.2 2-km NOWrad radar reflectivity at (a) 2000 UTC 23 July 2002, (b) 2200 UTC 23 2002 July, (c) 0000 UTC 24 July 2002, (d) 2300 UTC 31 May 2002 event, (e) 0030 UTC 01 June 2002, (f) 0430 UTC June 2002.

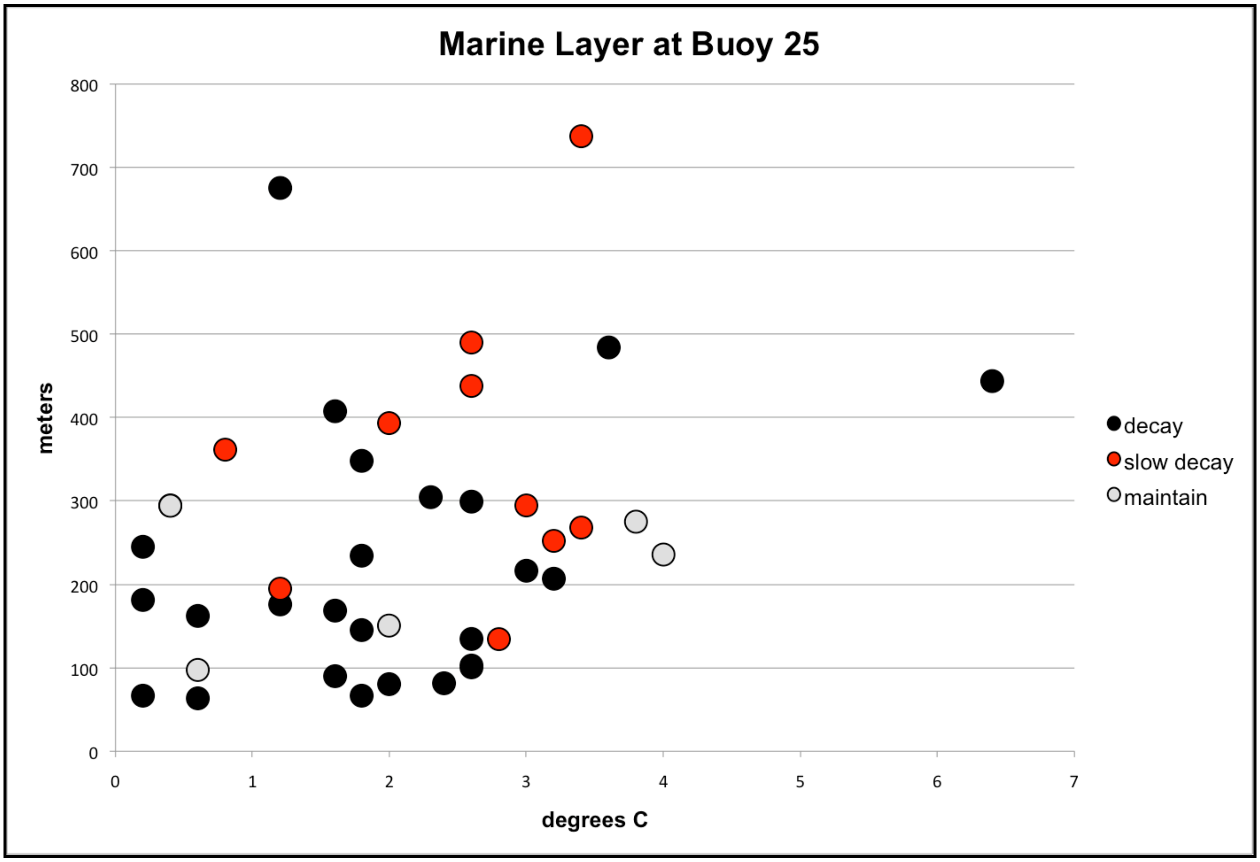

Figure 4.3 Marine layer depth verses temperature difference bewteen the top and bottom of the marine layer calculated at the Buoy 25 location (40.25N,-73.166W).

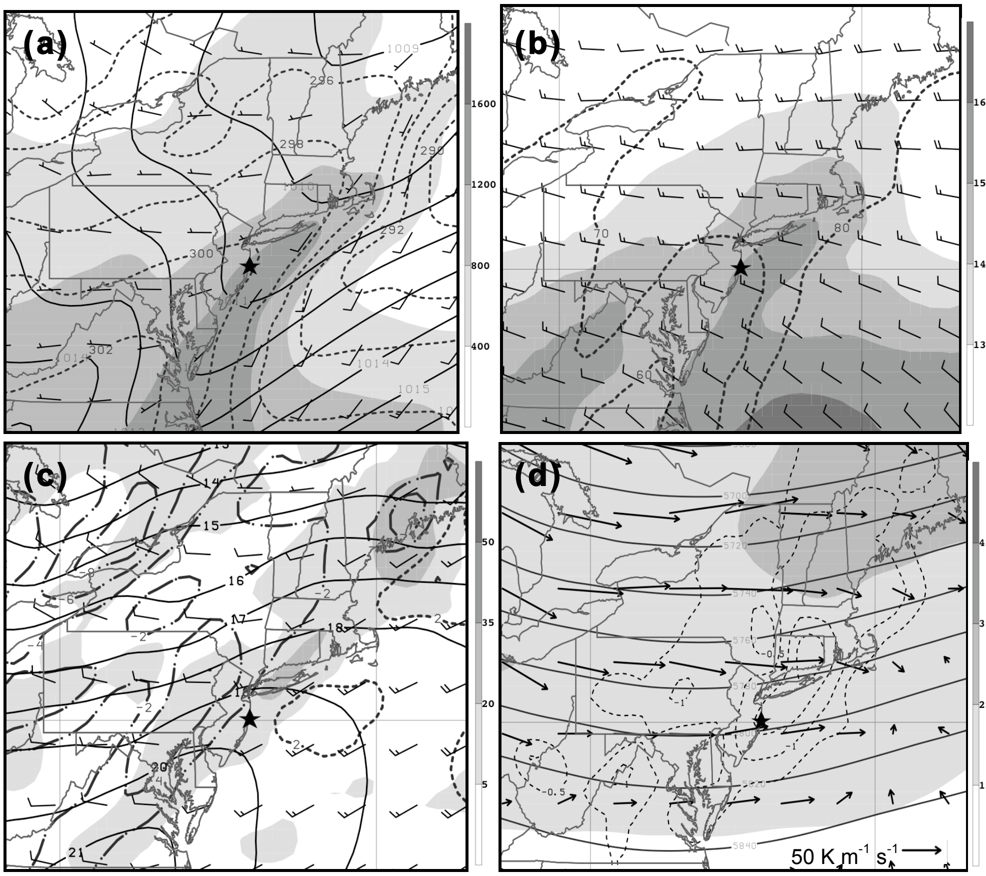

Figure 4.4 Feature-based NARR composites for the decay events showing (a) MSLP (solid every 1 hPa), 10 m θ (dashed every 2 K), MUCAPE (shaded J kg -1), 10 m winds (full barb = 5 m s^{-1}), (b) 1000 hPa mixing ratio g kg^{-1} (shaded every 1 g kg^{-1} beginning at 13 g kg^{-1}), 1000 hPa relative humidity (dashed every 10%), 0-3 km vertical wind shear vector (full barb = 5 m s^{-1}), (c) 900:800 frontogenesis (shaded every 15x10^{-2} K (100 km)$^{-1}$ (3 hr)$^{-1}$, beginning at 5x10^{-2} K (100 km)$^{-1}$ (3 hr)$^{-1}$), 900 hPa temperature advection (positive temperature advection dashed and negative temperature advection dash-dot every 2x10^{-5} ^{o}C s^{-1}), 900 hPa temperature (solid every 1 ^{o}C), 900 hPa winds (full barb = 5 m s^{-1}), (d) 300 hPa wind magnitude (shaded every 10 m s^{-1}), 500 hPa geopotential heights (solid every 20 dam), 800:400 layer-averaged omega (dashed every 1x10^{-3} Pa s^{-1}), 500 hPa Q-vectors (10^{-12} K m^{-1} s^{-1}). A star indicates the compositing point. Geography is included only for scale reference.

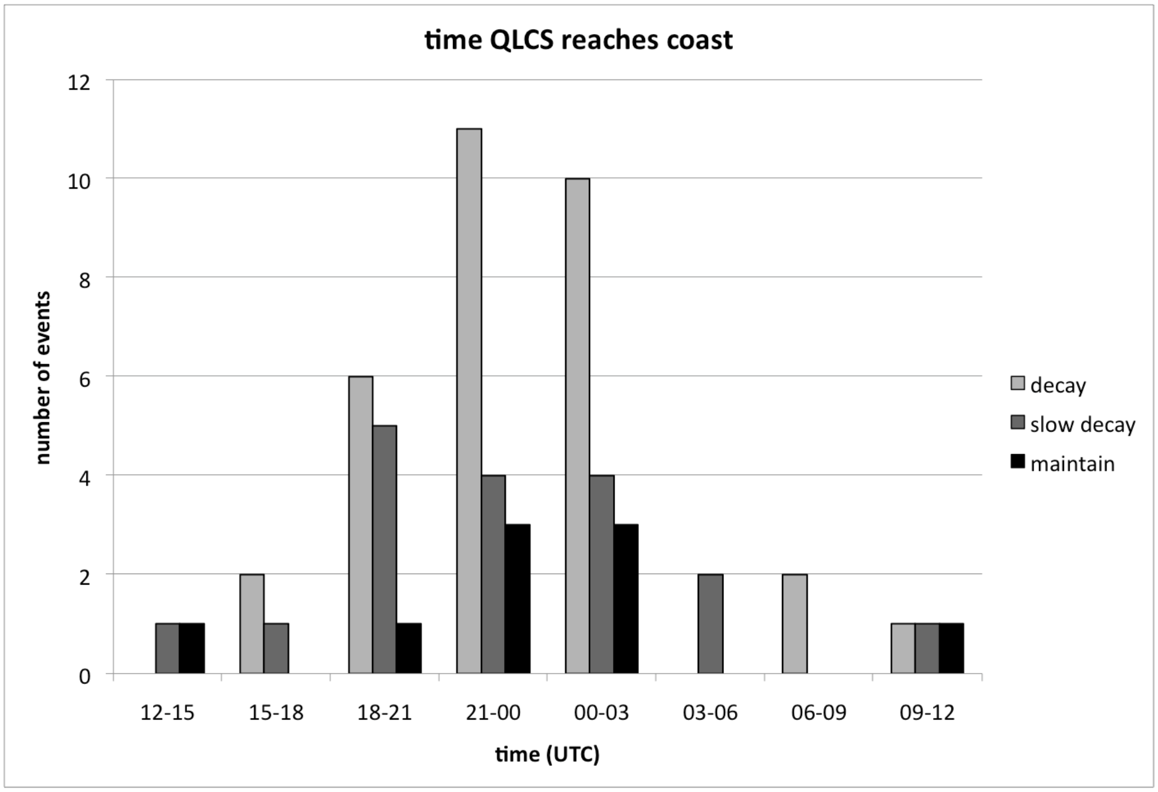

Figure 4.5 Number of quasi-linear convective systems that encounter the northeastern U.S. coastline in this study plotted as a function of time of day (3 hour bins) for decay, slow decay, and maintain events.

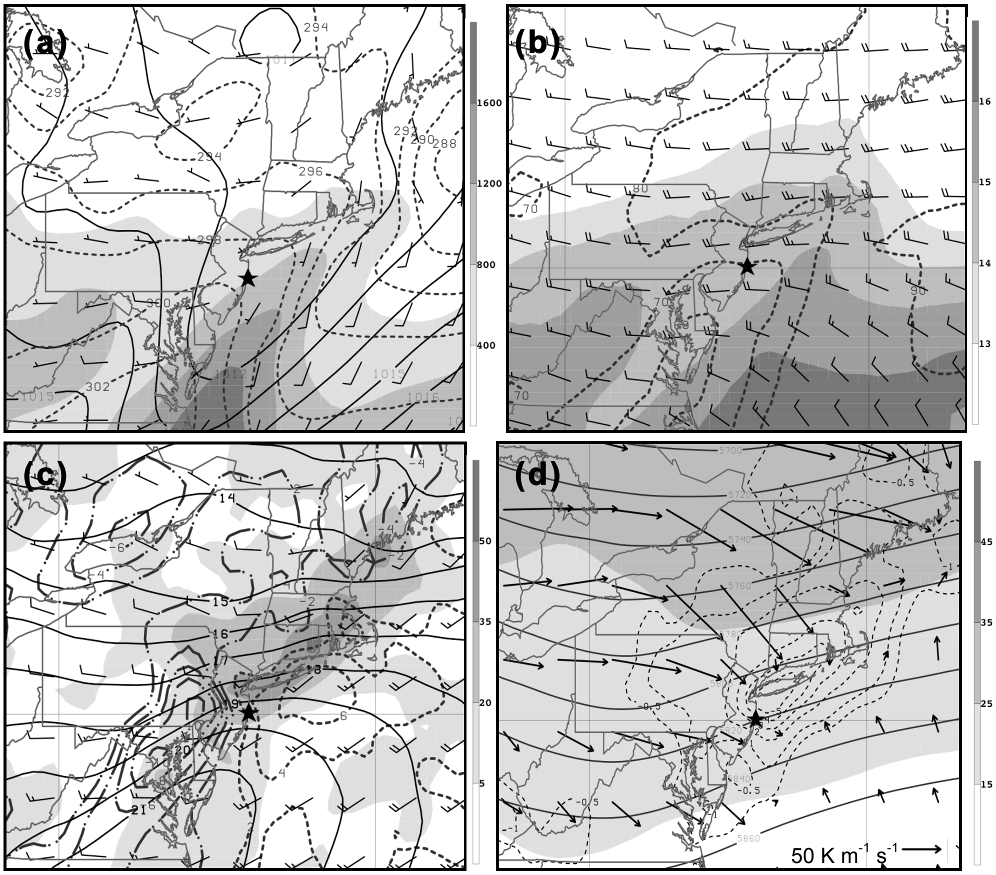

Figure 4.6 Feature-based NARR composites for the slow decay events showing (a) MSLP (solid every 1 hPa), 10 m θ (dashed every 2 K), MUCAPE (shaded J kg -1), 10 m winds (full barb = 5 m s^{-1}), (b) 1000 hPa mixing ratio g kg^{-1} (shaded every 1 g kg^{-1} beginning at 13 g kg^{-1}), 1000 hPa relative humidity (dashed every 10%), 0-3 km vertical wind shear vector (full barb = 5 m s^{-1}), (c) 900:800 frontogenesis (shaded every $15x10^{-2}$ K $(100 km)^{-1}$ $(3 hr)^{-1}$, beginning at $5x10^{-2}$ K $(100 km)^{-1}$ $(3 hr)^{-1}$), 900 hPa temperature advection (positive temperature advection dashed and negative temperature advection dash-dot every $2x10^{-5}$ ^{o}C s^{-1}), 900 hPa temperature (solid every 1 ^{o}C), 900 hPa winds (full barb = 5 m s^{-1}), (d) 300 hPa wind magnitude (shaded every 10 m s^{-1}), 500 hPa geopotential heights (solid every 20 dam), 800:400 layer-averaged omega (dashed every $1x10^{-3}$ Pa s^{-1}), 500 hPa Q-vectors (10^{-12} K m^{-1} s^{-1}). A star indicates the compositing point. Geography is included only for scale reference.

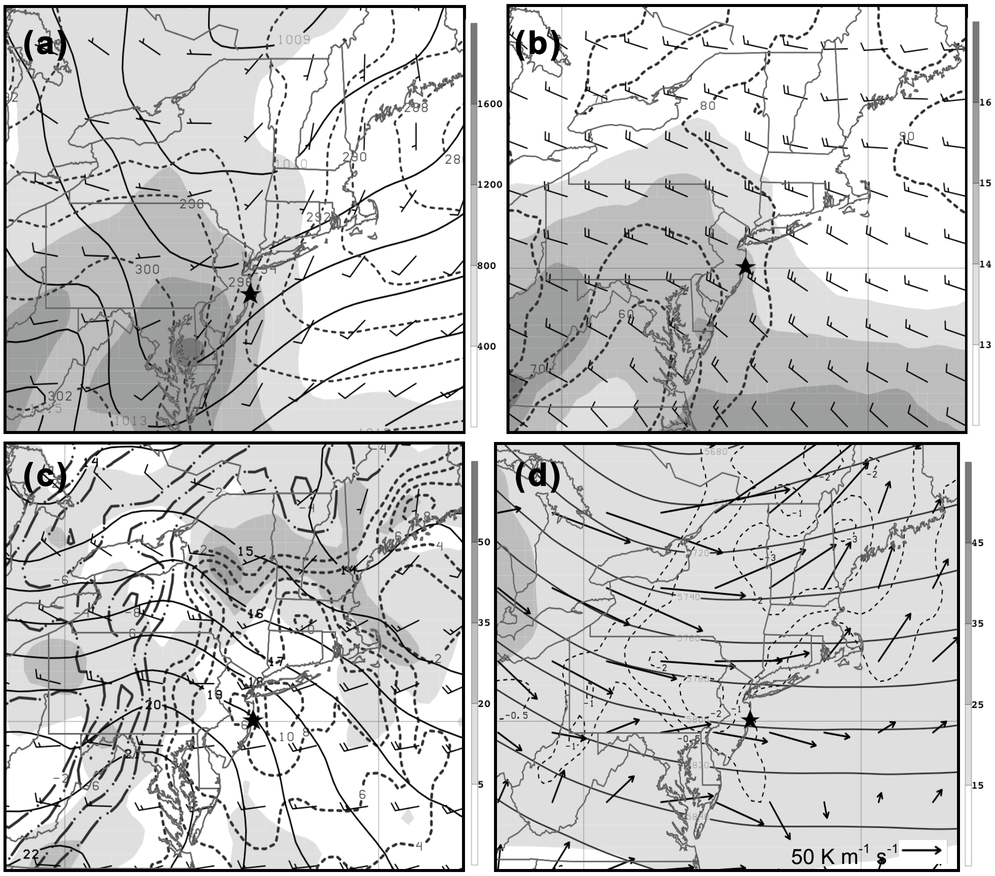

Figure 4.7 Same as in Fig. 4.6 except for the maintaining events.

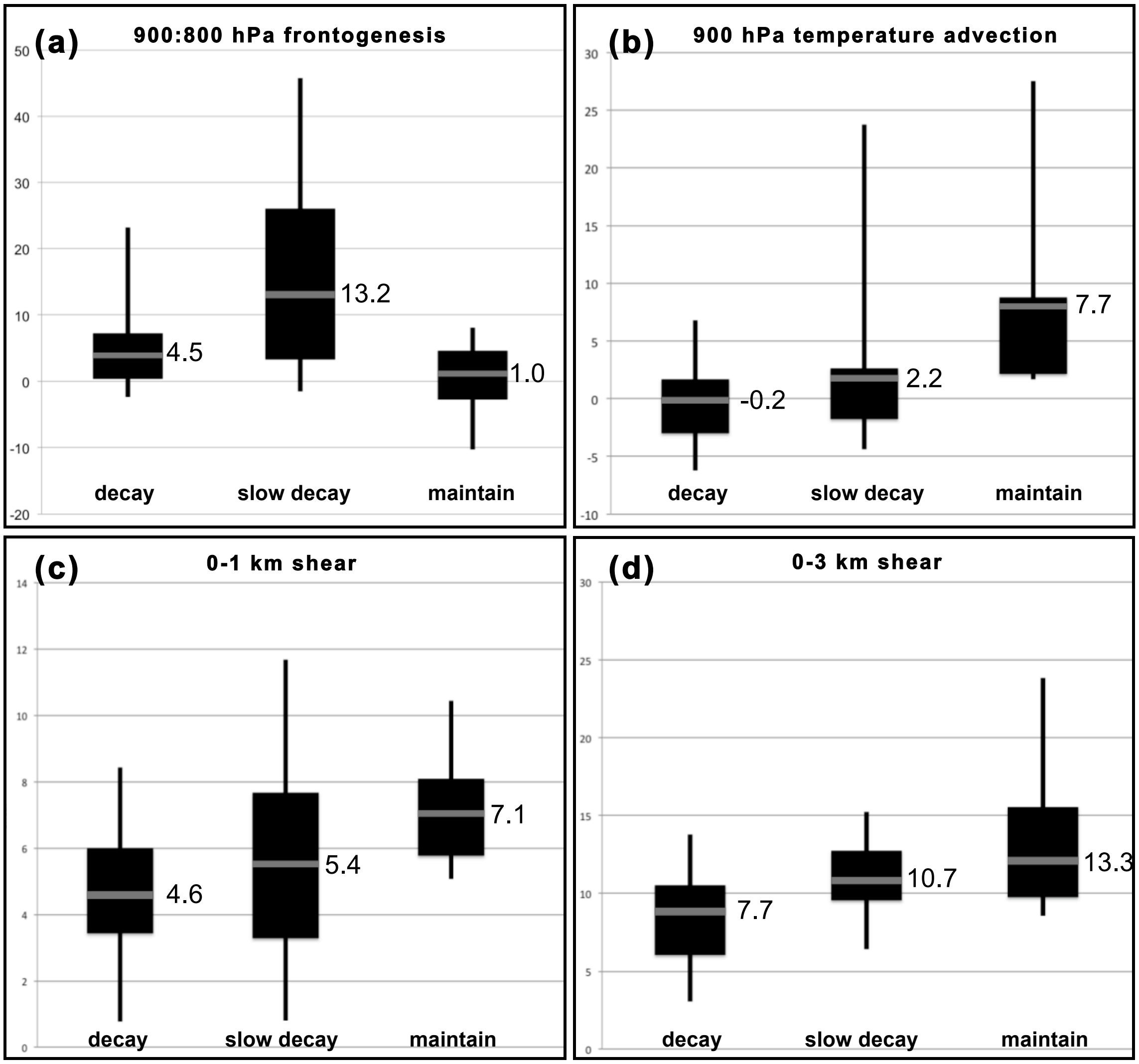

Figure 4.8 Box-and-whisker plots showing 1.5-degree latitude-longitude area averaged values of (a) 900:800 hPa layer averaged frontogenesis (10^{-2} K (100 km^{-1}) (3 hr^{-1})), (b) 900 hPa temperature advection (10^{-5} ^{o}C s^{-1}), (c) 0-1 km vertical wind shear (m s^{-1}), (d) 0-6 km veritical wind shear (m s^{-1}) for the 32 slow decay events, 18 decay events, and 9 maintain events. The bottom and top of the solid black box are the 25th and 75th quartile, respectively. The mean is denoted by a gray bar with its value also noted. The maximum and mimimum outliers are denoted by the vertical solid lines.

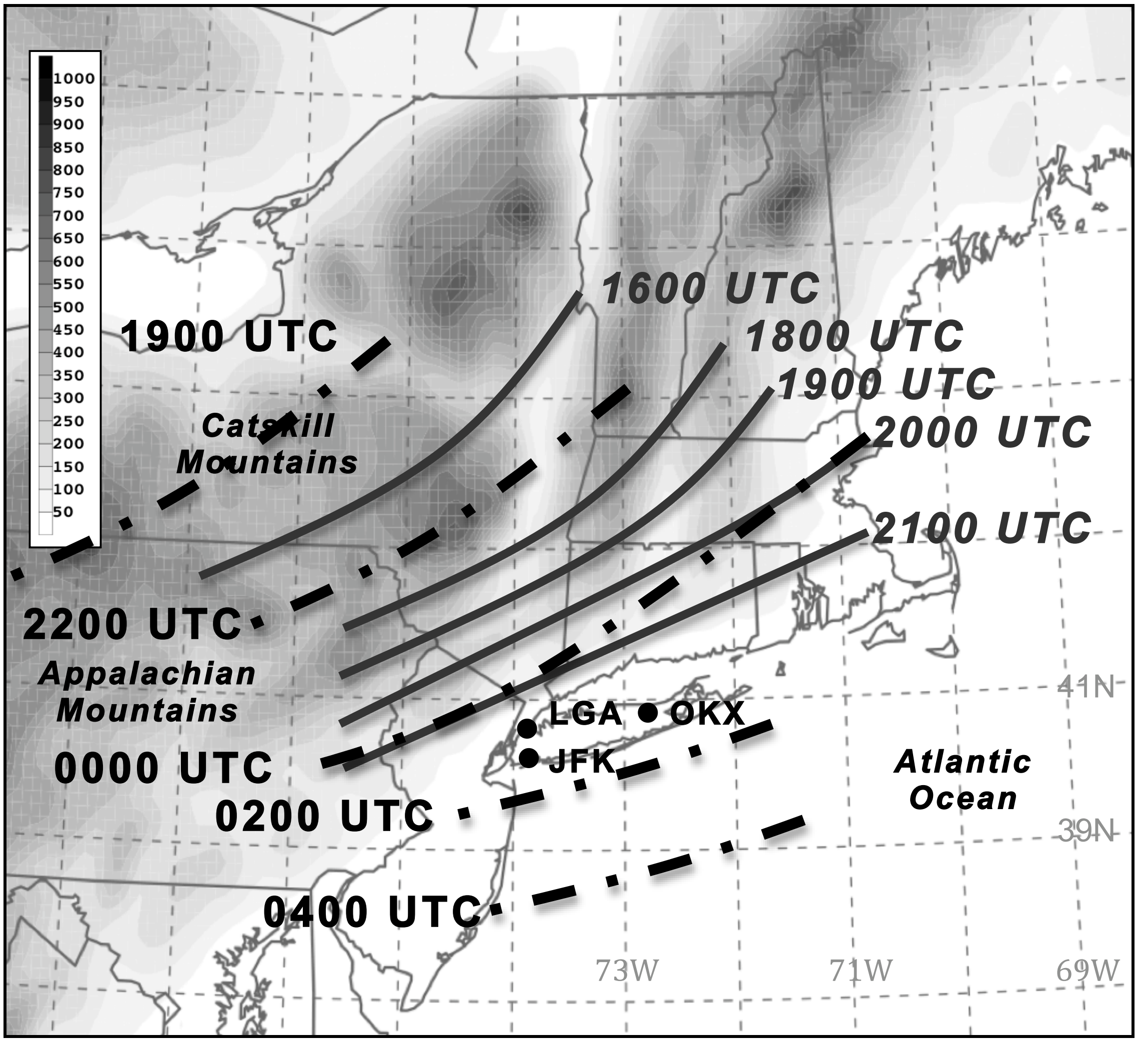

Figure 4.9 The location of the 31 May 2002 event and 23 July 2002 event from origin to decay. The 31 May 2002 maintain event locations are marked with black dash-dot line beginning at 1900 UTC and the 23 July 2002 decay event is locations are marked with gray solid line beginning at 1600 UTC. After each respective origin time (1900 UTC for 31 May 2002 event, 1600 UTC 23 July 2002), each line indicates the location of coherent quasi-linear convective system before decay (as defined in the text). Once decay occurs, no line is drawn.

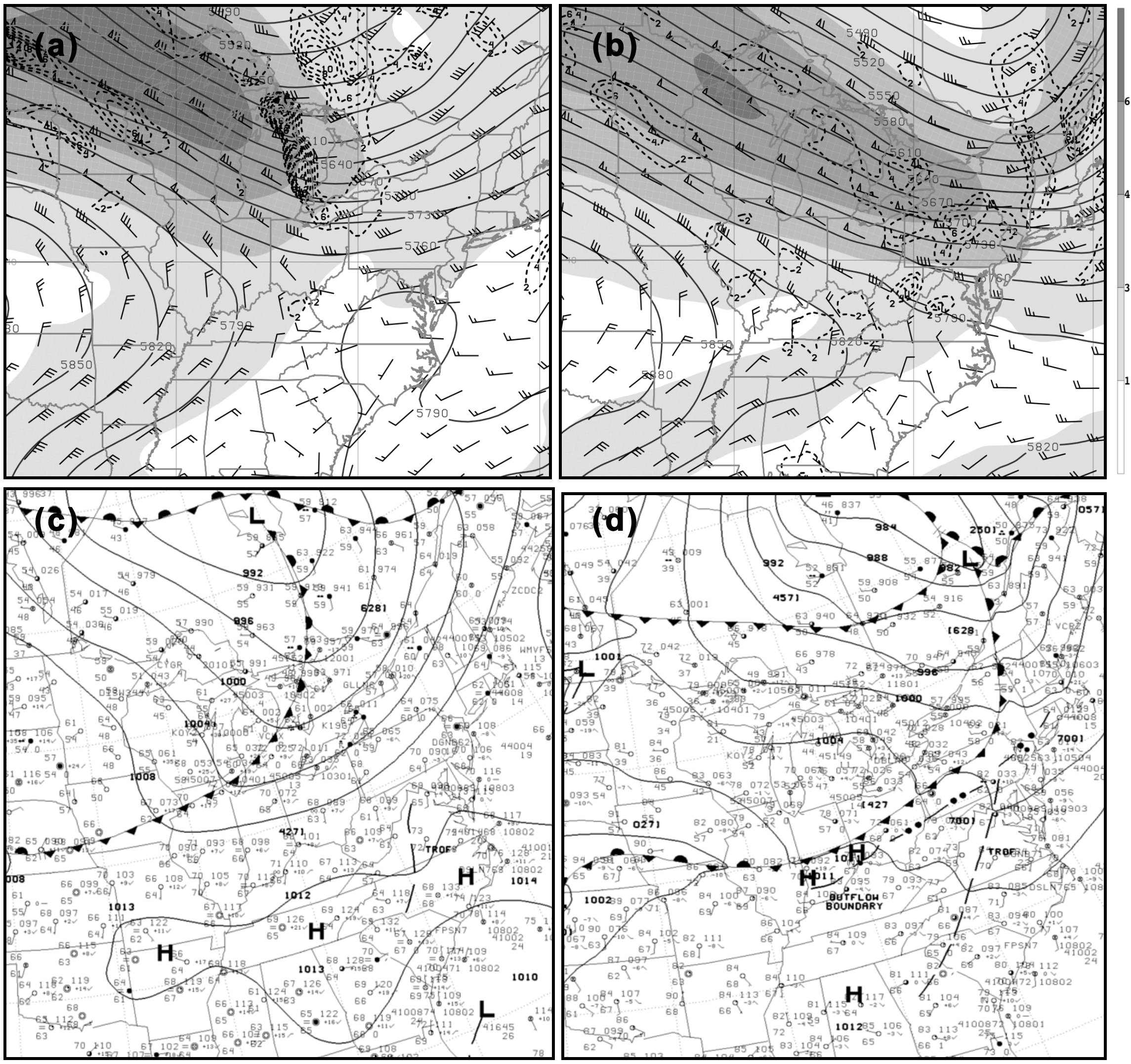

Figure 4.10 300 hPa wind magnitude (shaded every 15 m s^{-1}), 500 hPa geopotential heights (solid every 30 dam), 500 hPa Q-vector convergence (dashed every 2x10^{-15} K m^{-2} s^{-1}), 500 hPa winds (full barb = 5 m s^{-1}) at (a) 1200 UTC 31 May 2002, (b) 2100 UTC 31 May 2002; surface analysis at (c) 1200 UTC 31 May 2002, (d) 2100 UTC 31 May 2002.

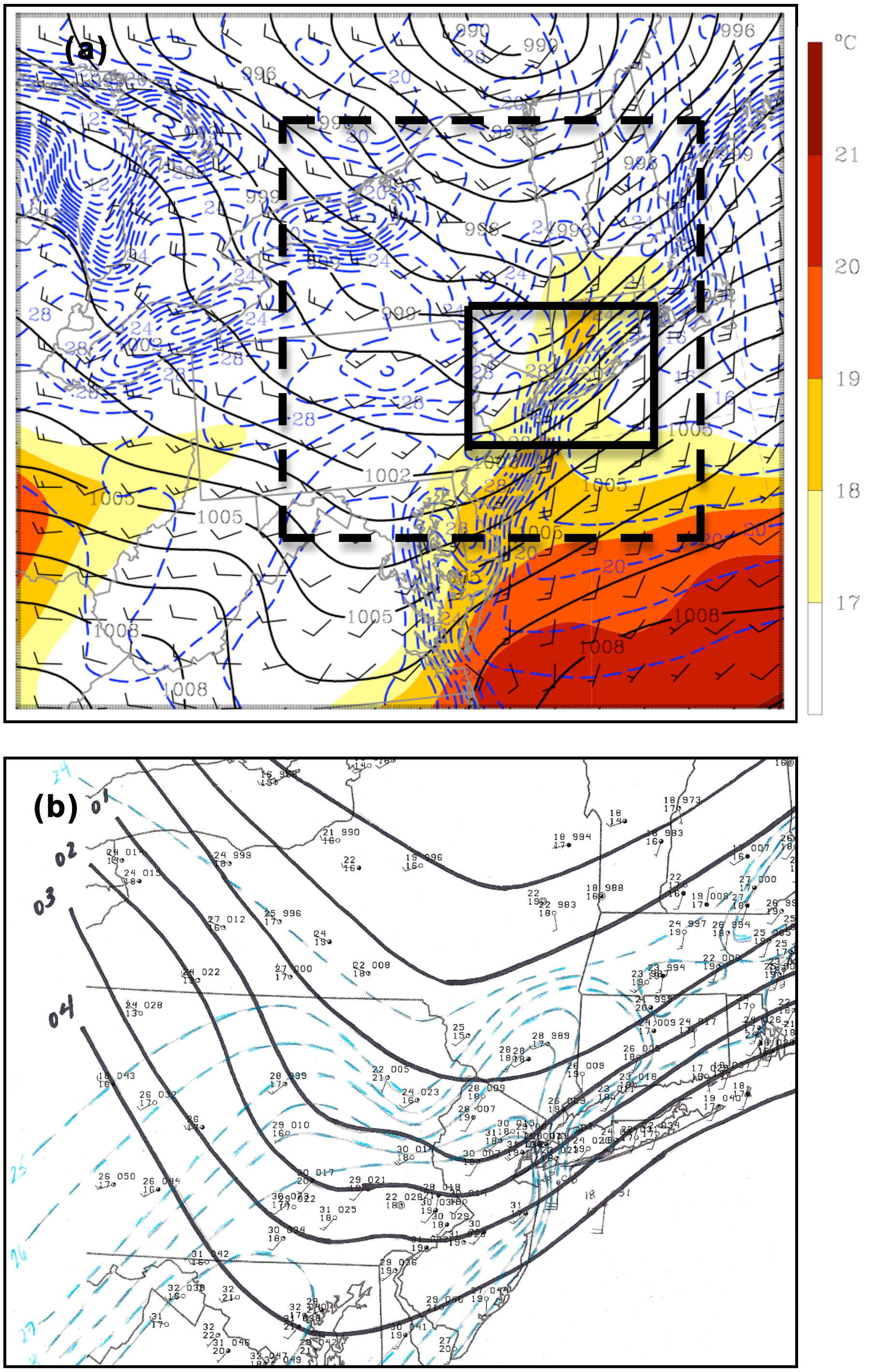

Figure 4.11 (a) 2 km full WRF domain with 500 m nested domain (black box) showing MSLP (solid every 1 hPa), 2 m temperature (dashed blue every 1^{o}C), 2 m dew point (shaded every 1^{o}C beginning at 18^{o}C), 10 m winds (full barb = 5 m s^{-1}) at 2100 UTC 31 May 2002, (b) 2100 UTC 31 May 2002 hand surface analysis including temperature (^{o}C), dew point (^{o}C), and winds (kts). The dashed box in (a) marks the outline of the hand analysis shown in (b).

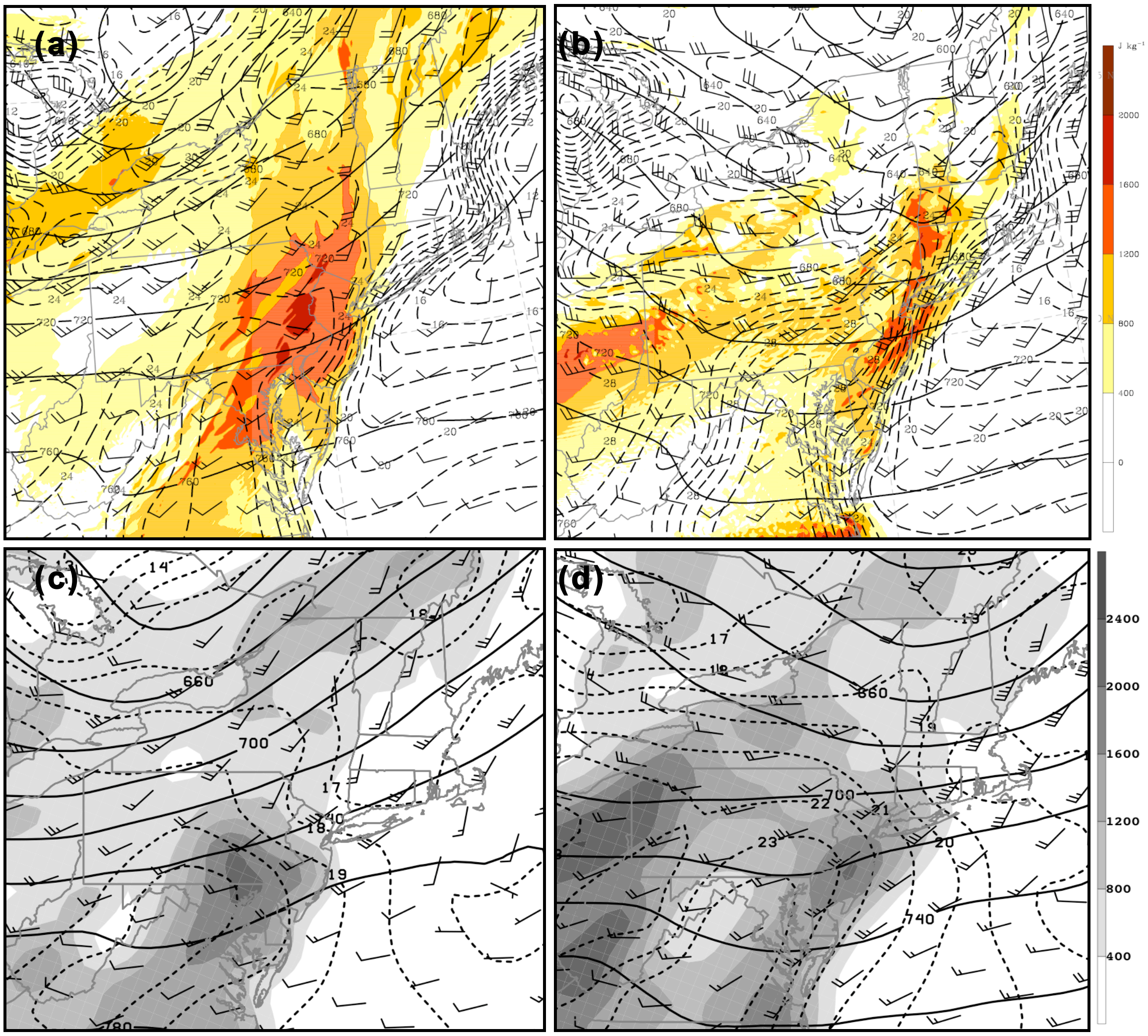

Figure 4.12 2 km WRF MUCAPE (shaded every 400 J kg^{-1}), 925 hPa geopotential heights (solid every 20 dam), 925 hPa temperature (dashed every 1 ^{o}C), 925 hPa winds (full barb = 5 m s^{-1}) (a) 1500 UTC 31 May 2002 (b) 2100 UTC 31 May 2002; NARR MUCAPE (shaded every 400 J kg^{-1}), 925 hPa geopotential heights (solid every 20 dam), 925 hPa temperature (dashed every 1 ^{o}C), 925 hPa winds (full barb = 5 m s^{-1}) at (c) 1500 UTC 31 May 2002, (d) 2100 UTC 31 May 2002.

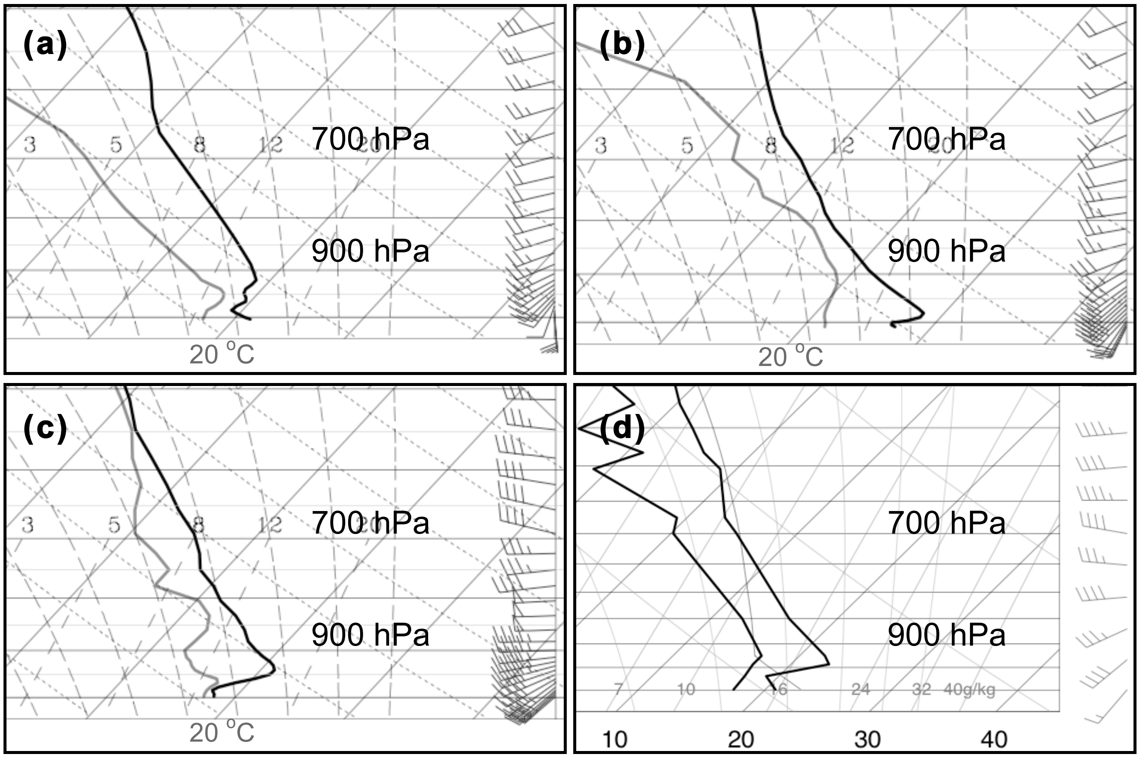

Figure 4.13 (a) 1500 UTC 31 May 2002 500 m WRF sounding at JFK location (b) 1800 UTC 31 May 2002 500 m WRF sounding at JFK location (c) 0000 UTC 1 June 2002 500 m WRF sounding at OKX location (d) 0000 UTC 1 June 2002 sounding from OKX.

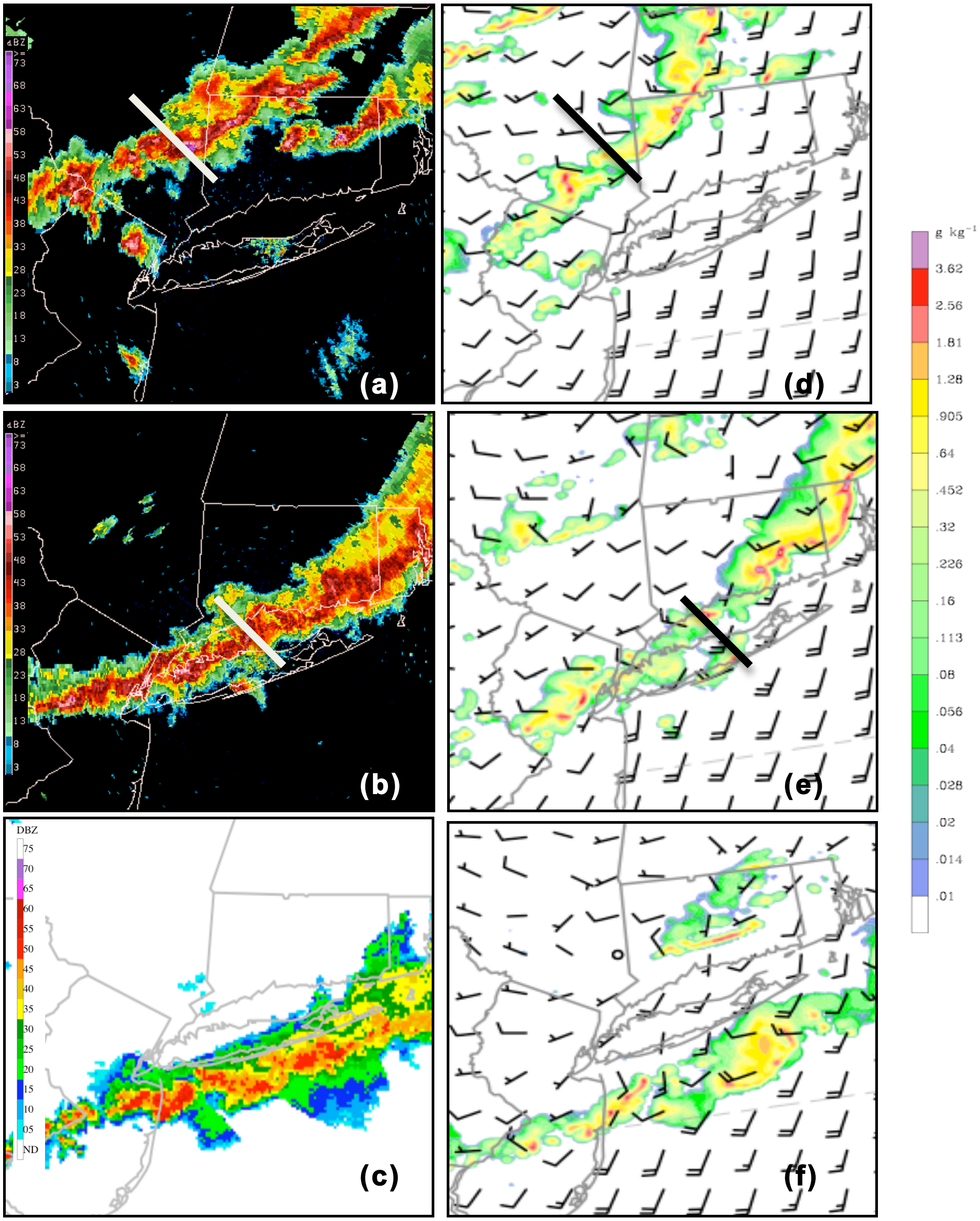

Figure 4.14 (a) Level II radar reflectivity at 2258 UTC 31 May 2002 (b) Level II radar reflectivity at 0043 UTC 1 June 2002 (c) NOWrad radar reflectivity at 0200 UTC 1 June 2002; 2 km WRF precipitation mixing ratio (shaded, g kg^{-1}) and 10 m winds (full barb = 5 m s^{-1}) at (d) 2215 UTC 31 May 2002 (10.25 h), (e) 2345 UTC 1 June 2002 (11.75 h), (f) 0145 UTC 1 June 2002 (13.75 h). The NOWrad radar reflectivity was used in place of the Level 2 radar reflectivity due to the lack of Level 2 data after 0100 UTC on 1 June 2002.

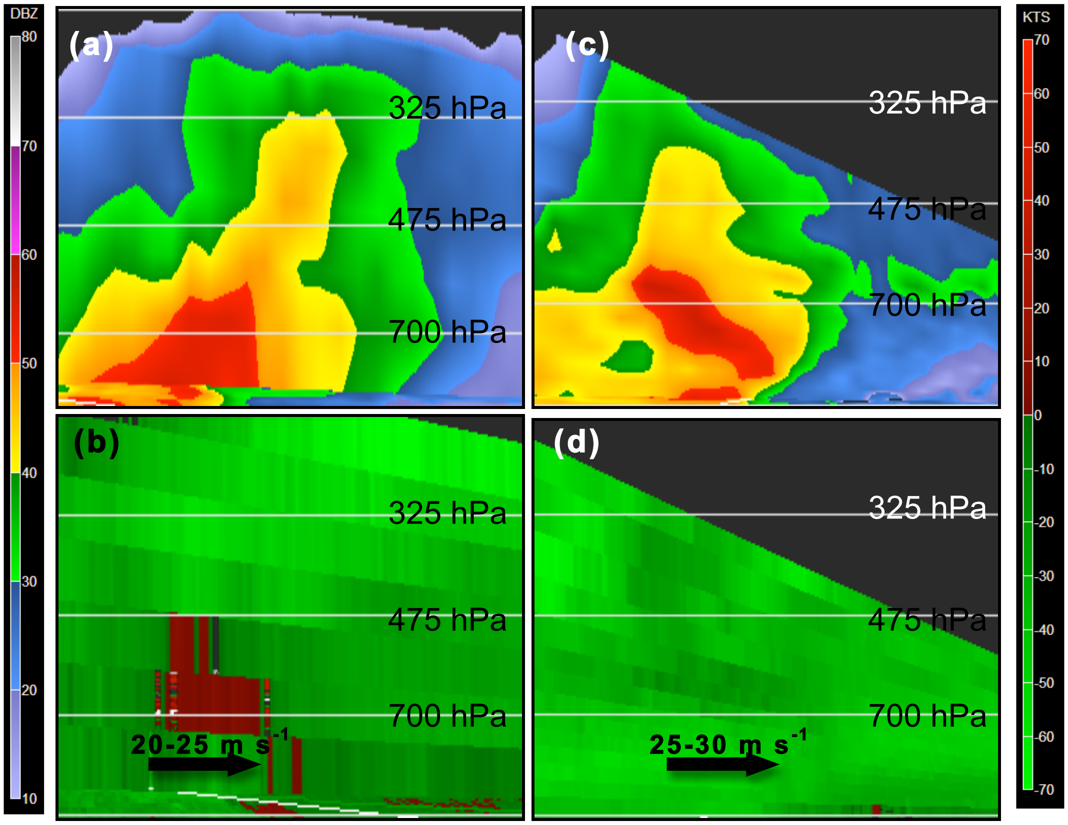

Figure 4.15 2258 UTC 31 May 2002 (a) Level II radar reflectivity (dBZ), (b) Level II radar velocity (kts), (c) same as (a) but for 0043 UTC 1 June 2002, (d) same as (b) but for 0043 UTC 1 June 2002. The cross section location for (a) & (b) is marked with a white line in figure 4.14a. The cross section location for (c) & (d) is marked with a white line in figure 4.14b.

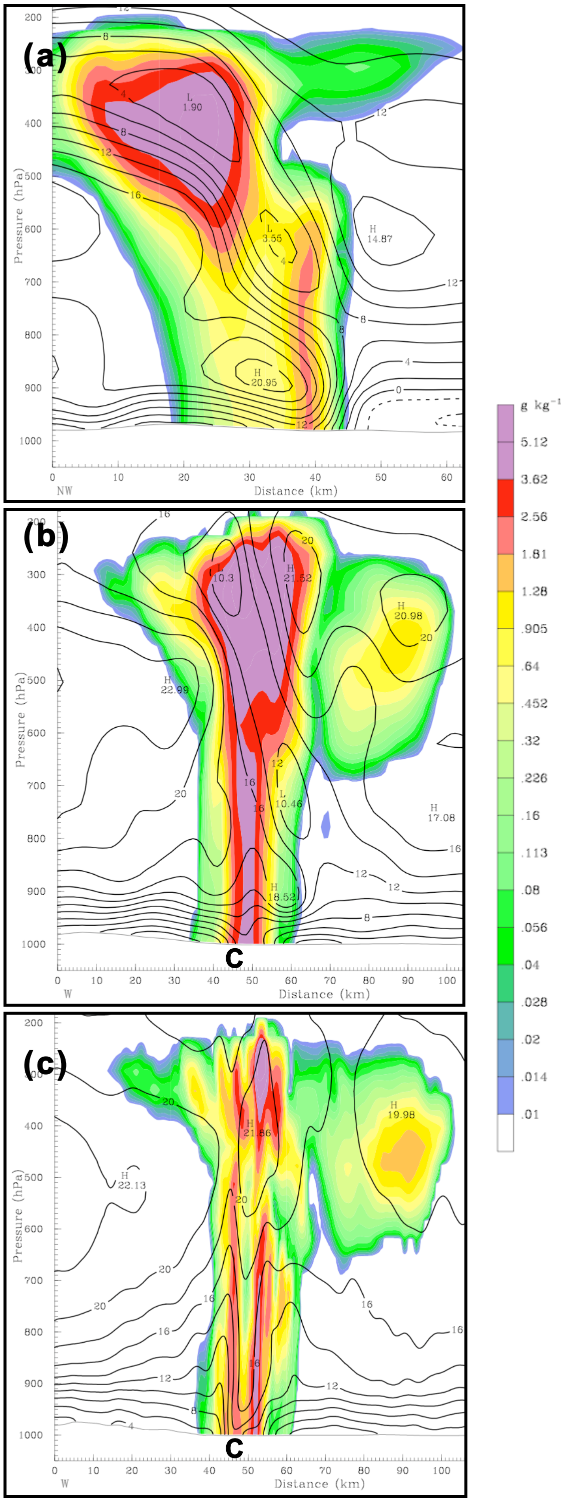

Figure 4.16 2 km WRF precipitation mixing ratio (shaded, g kg^{-1}) and horizontal wind speed magnitude (black every 1 m s^{-1}) in the plane of the cross section at (a) (10.25 h) 2215 UTC 31 May 2002 (b) (11.75 h) 2345 UTC 21 May 2002 (c) same as (b) but for the 500 m domain. The cross section location for (a) is marked with a white line in figure 4.14d. The cross section location for (b) & (c) is marked with a white line in figure 4.14e. The location of the coastline is marked with a **C**.

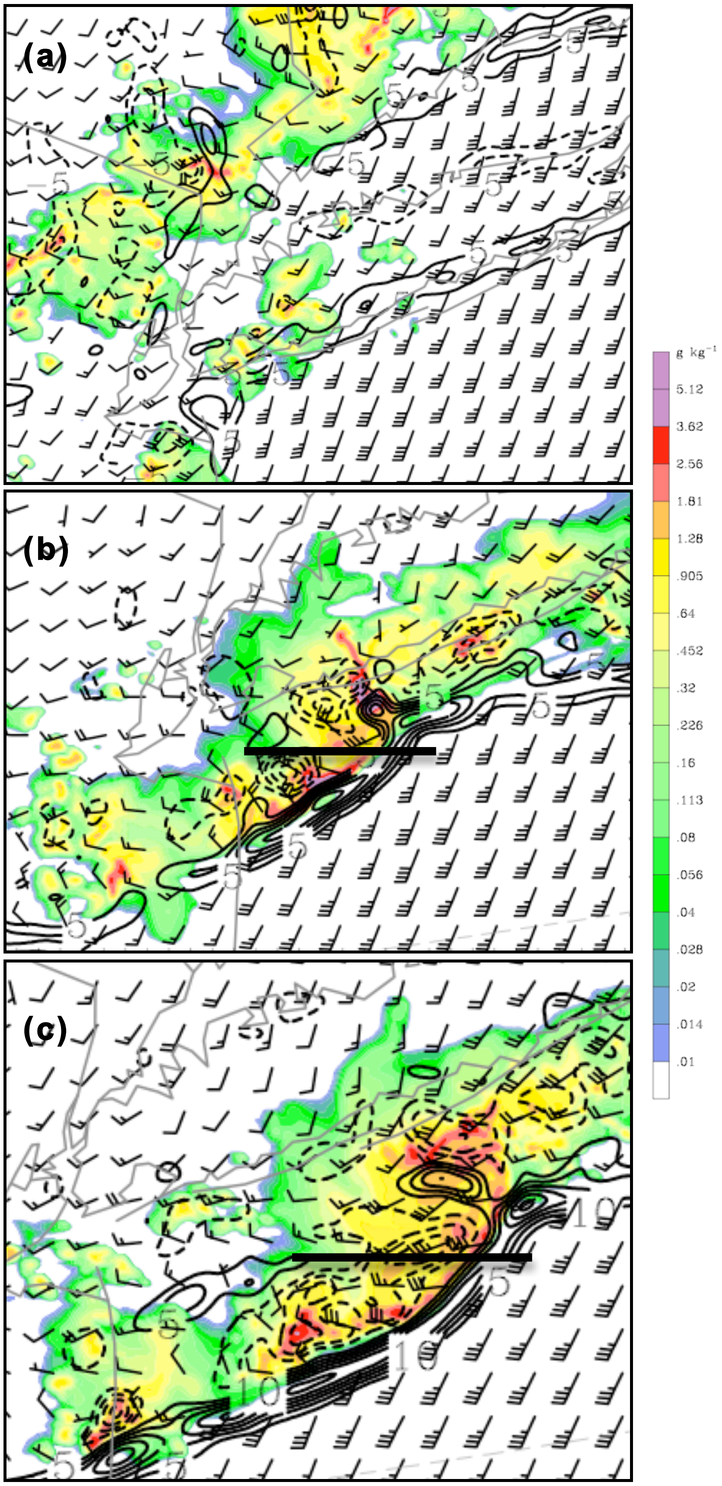

Figure 4.17 500 m WRF precipitation mixing ratio (shaded, g kg^{-1}), 100 m vertical motion (every 5 x10^{-2} m s^{-1}), and 100 m winds (full barb = 5 m s^{-1}) at (a) (11h) 2300 UTC 31 May 2002, (b) (12.5h) 0030 UTC 1 June 2002, (c) (13h) 0100 UTC 1 June 2002.

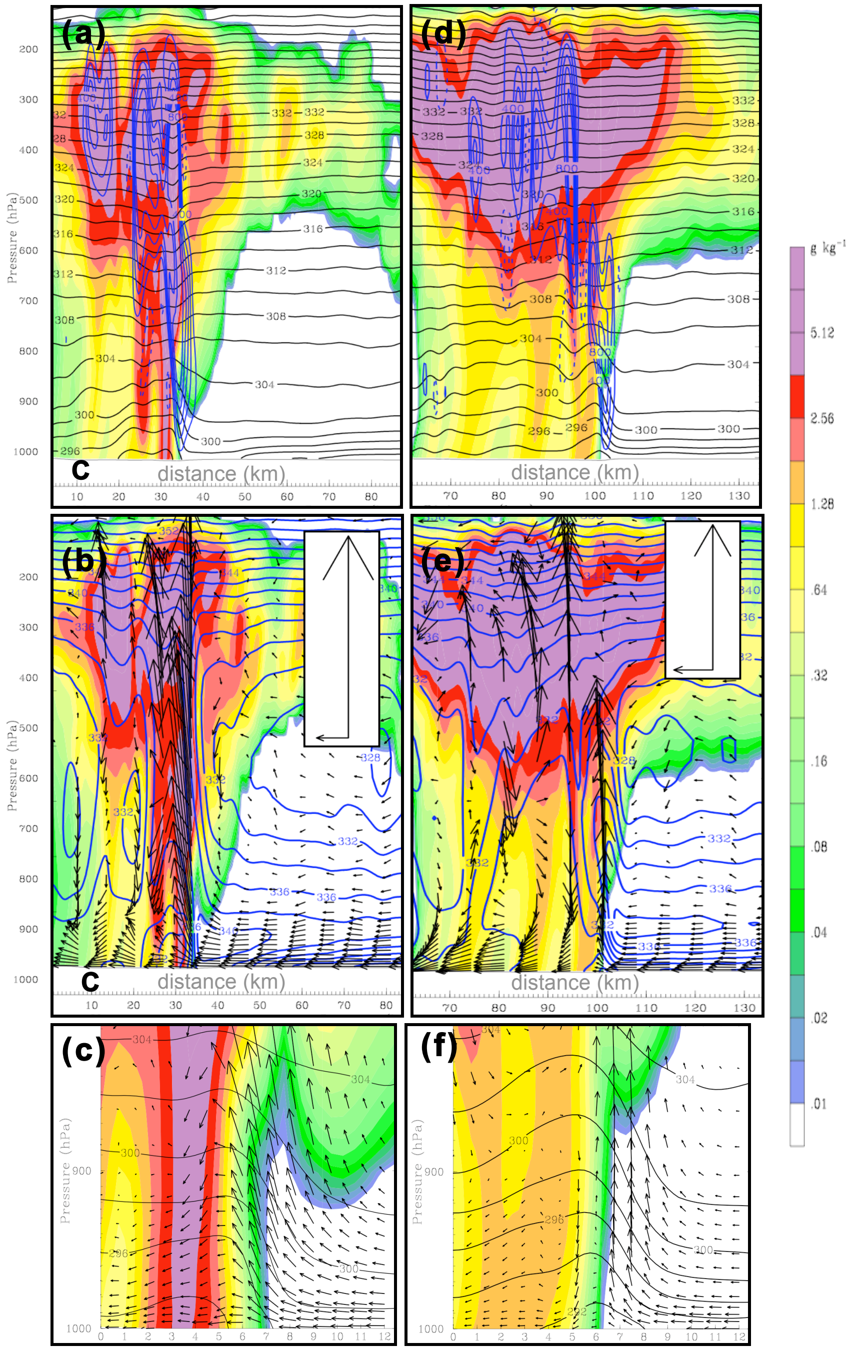

Figure 4.18 500 m WRF cross sections at 0030 UTC 1 June 2002 (12.5h) of (a) precipitation mixing ratio (shaded, g kg^{-1}), θ (black every 2 K), vertical motion (blue every 2x10^{-2} m s^{-1}, ascent in the solid lines and descent in the dashed lines), (b) precipitation mixing ratio (shaded, g kg^{-1}), θ_e (blue every 2 K), storm relative circulation vectors, (c) precipitation mixing ratio (shaded, g kg^{-1}), θ (black every 2 K), storm relative circulation vectors, (d) same as (a) but for 0100 UTC (13h), (e) same as (b) but for 0100 UTC (13h), (f) same as (c) but for 0100 UTC (13h). For (b), the maximum horizontal vector is 29.9 m s^{-1} and the maximum vertical vector is 127.1 Pa s^{-1}. For (e), the maximum horizontal vector is 28.1 m s^{-1} and the maximum vertical vector is 91.8 Pa s^{-1}. The cross section location for (a)-(c) and (d)-(f) is marked with a black line in figure 4.17b and 4.17c, respectively. The location of the coastline is marked with a **C**.

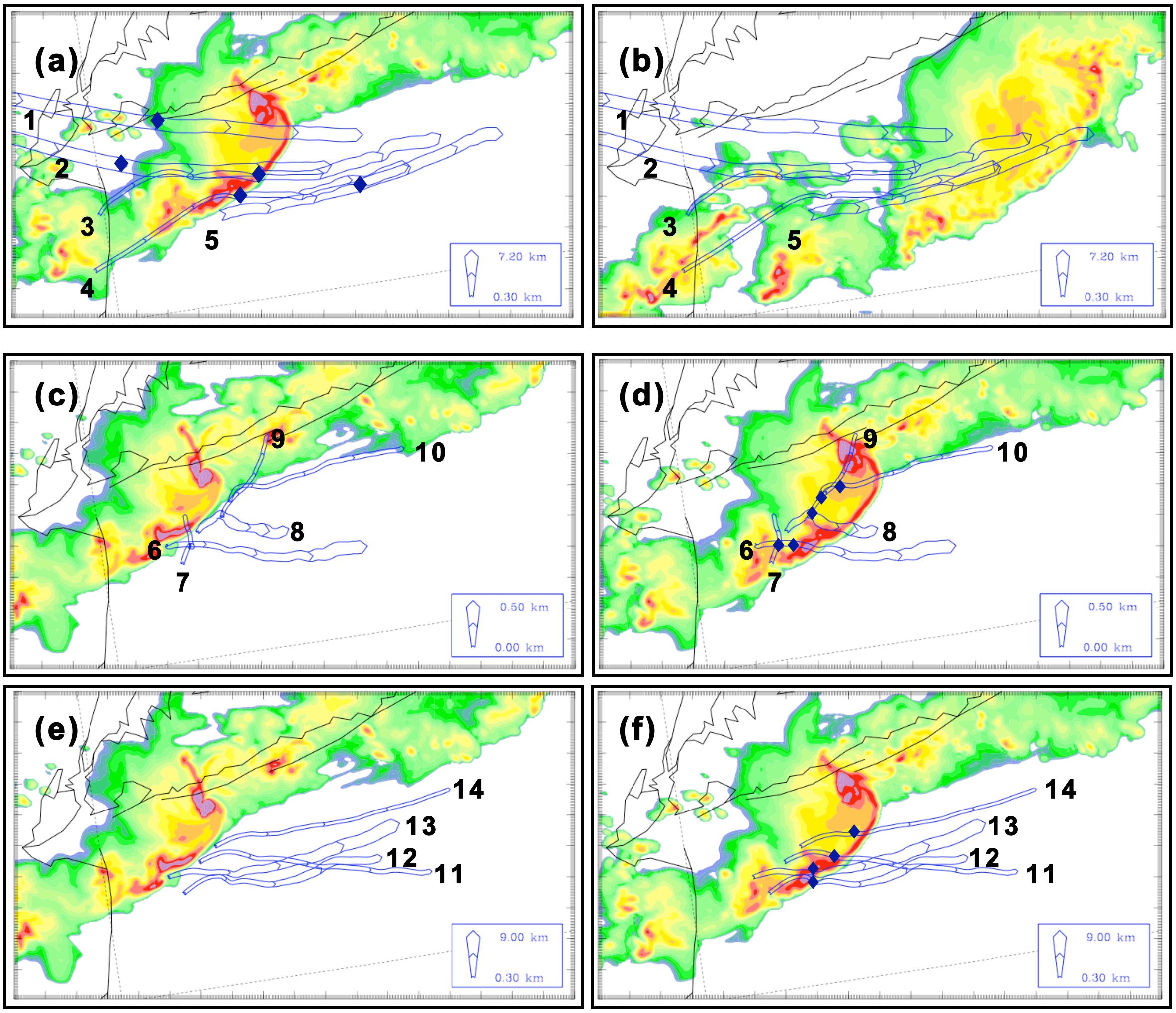

Figure 4.19 500 m resolution backward 1 minute trajectories beginning at 7 km launched at 13.5 h (0130 UTC 1 June 2002) and precipitation mixing ratio (g kg^{-1}) at (a) 12.75 h (0045 UTC 1 June 2002) (b) 13.50 h (0130 UTC 1 June 2002), forward 1 minute trajectories starting at 10 m and 300 m launched at 12.5 h (0030 UTC 1 June 2002) and precipitation mixing ratio (g kg^{-1}) at (c) 12.5 h (0030 UTC 1 June 2002) (d) 12.75 h (0045 UTC 1 June 2002), forward 1 minute trajectories starting at 500 m launched at 12.5 h (0030 UTC 1 June 2002) and precipitation mixing ratio (g kg^{-1}) at (e) 12.5 h (0030 UTC 1 June 2002) (f) 12.75 h (0045 UTC 1 June 2002). For all trajectories, each blue line marks a 15 minute increment.

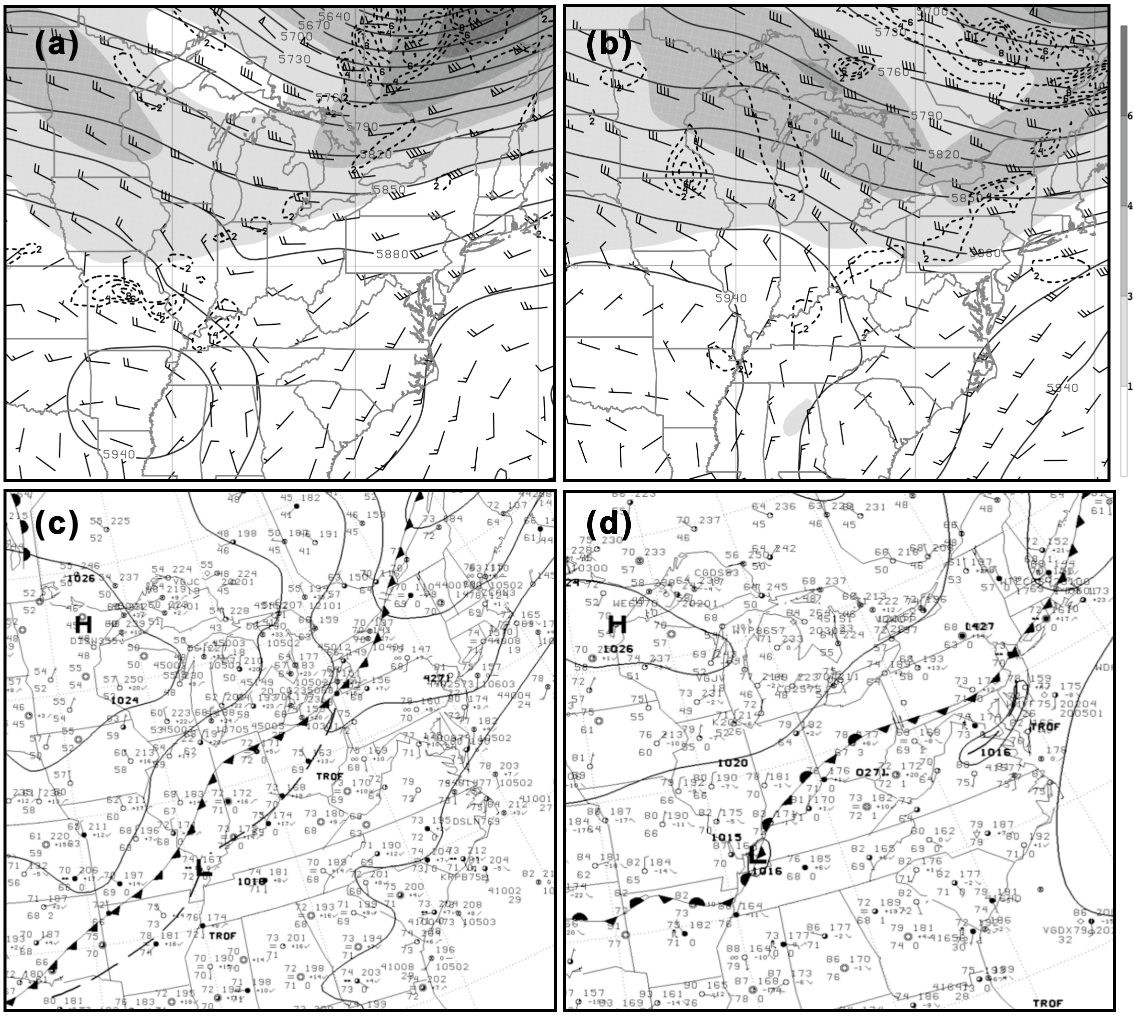

Figure 4.20 300 hPa wind magnitude (shaded every 15 m s^{-1}), 500 hPa geopotential heights (solid every 30 dam), 500 hPa Q-vector convergence (dashed every 2x10^{-15} K m^{-2} s^{-1}), 500 hPa winds (full barb = 5 m s^{-1}) at (a) 1200 UTC 23 July 2002, (b) 2100 UTC 23 July 2002; surface analysis at (c) 1200 UTC 23 July 2002, (d) 2100 UTC 23 July 2002.

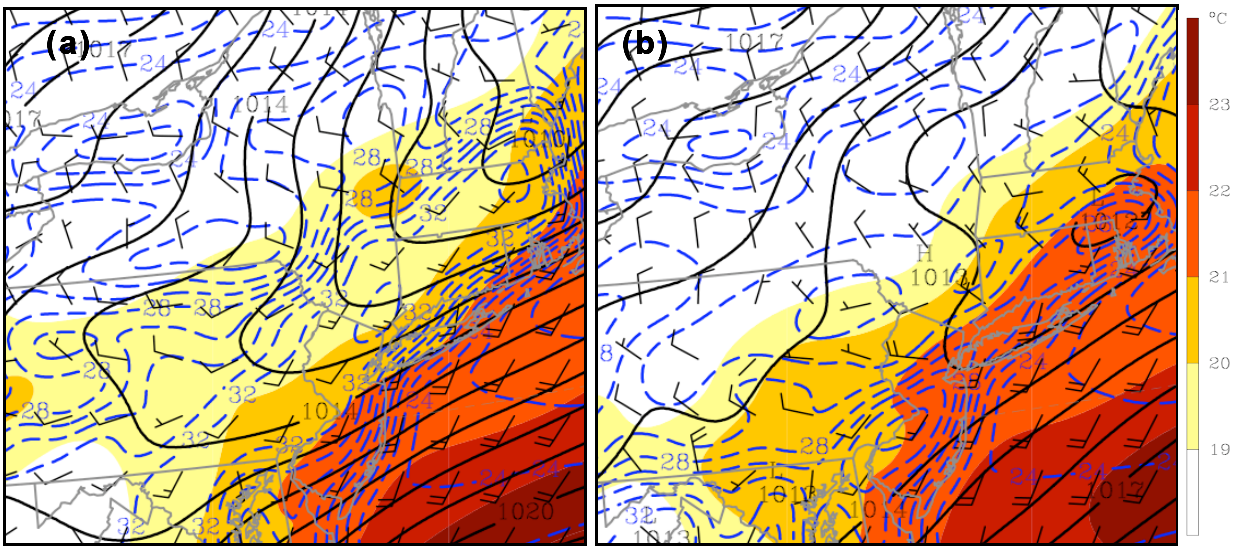

Figure 4.21 2 km WRF showing MSLP (solid every 1 hPa), 2 m temperature (dashed blue every 1^{o}C), 2 m dew point (shaded every 1^{o}C beginning at 18^{o}C), 10 m winds (full barb = 5 m s^{-1}) for 23 July 2002 at (a) 1800 UTC (b) 2100 UTC.

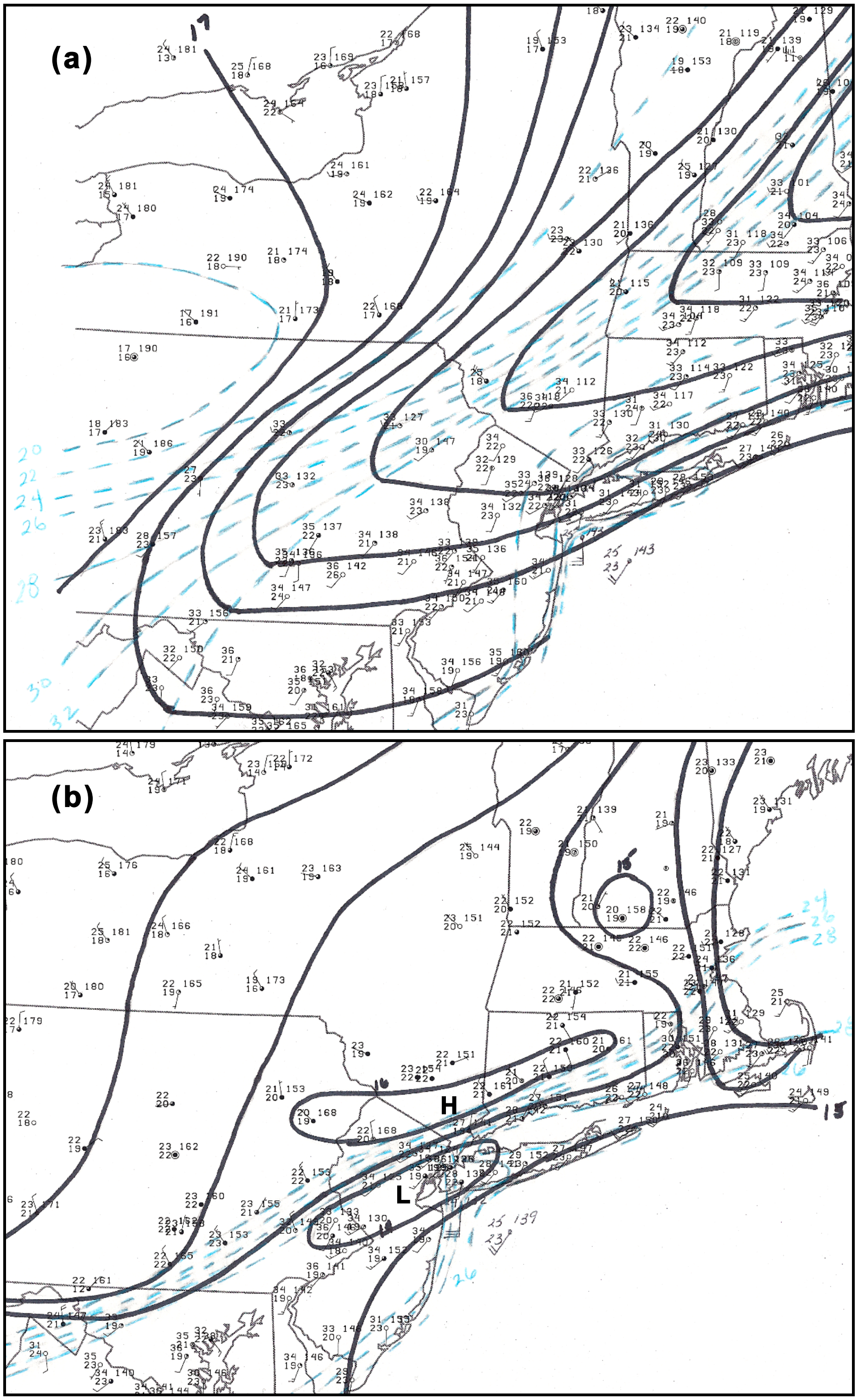

Figure 4.22 31 May 2002 hand surface analysis including temperature (°C), dew point (°C), and winds (kts) at (a) 1800 UTC (b) 2100 UTC.

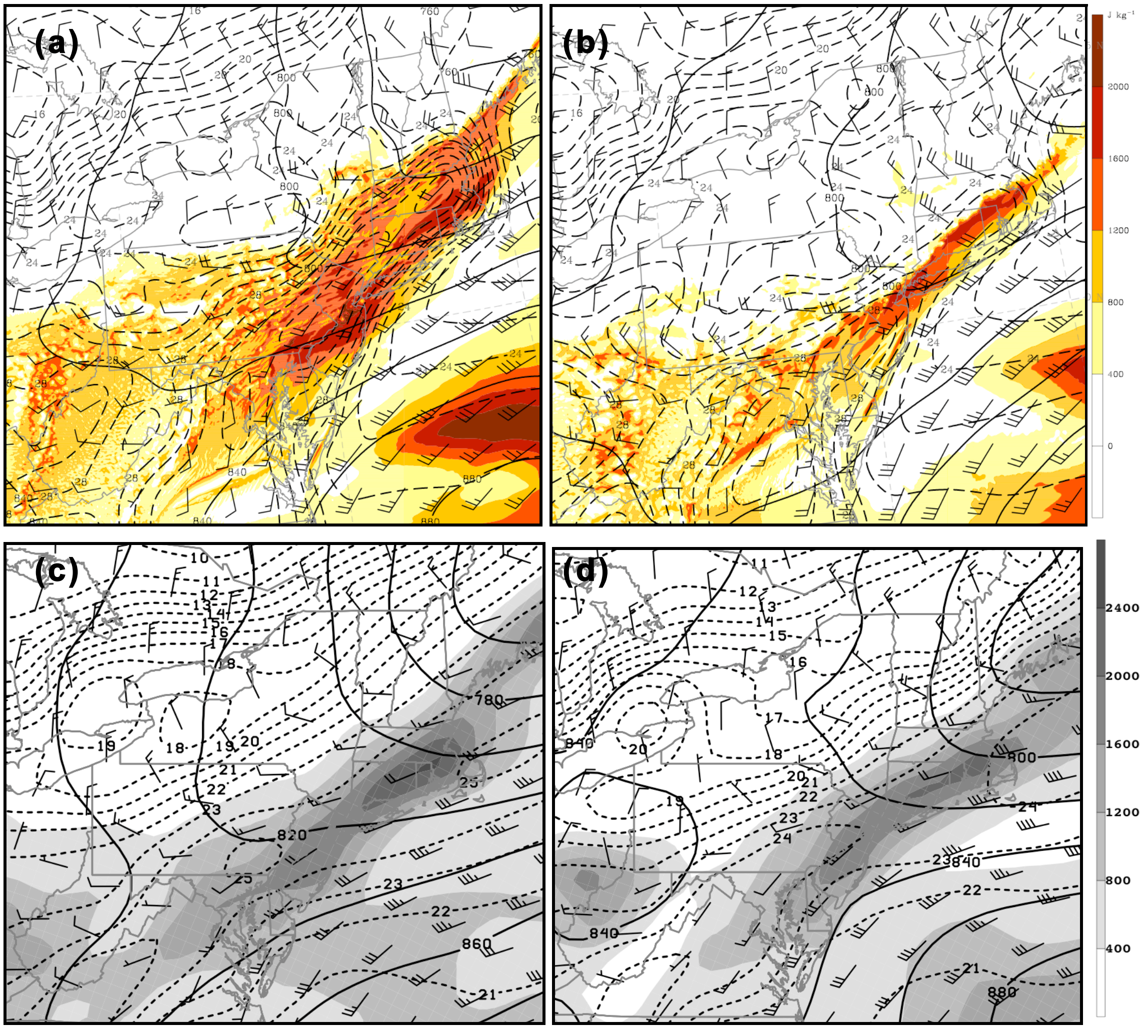

Figure 4.23 2 km WRF MUCAPE (shaded every 400 J kg^{-1}), 925 hPa geopotential heights (solid every 20 dam), 925 hPa temperature (dashed every 1 ^{o}C), 925 hPa winds (full barb = 5 m s^{-1}) at (a) 1800 UTC 23 July 2002 (b) 2100 UTC 23 July 2002; NARR MUCAPE (shaded every 400 J kg^{-1}), 925 hPa geopotential heights (solid every 20 dam), 925 hPa temperature (dashed every 1 ^{o}C), 925 hPa winds (full barb = 5 m s^{-1}) at (c) 1800 UTC 23 July 2002, (d) 2100 UTC 23 July 2002.

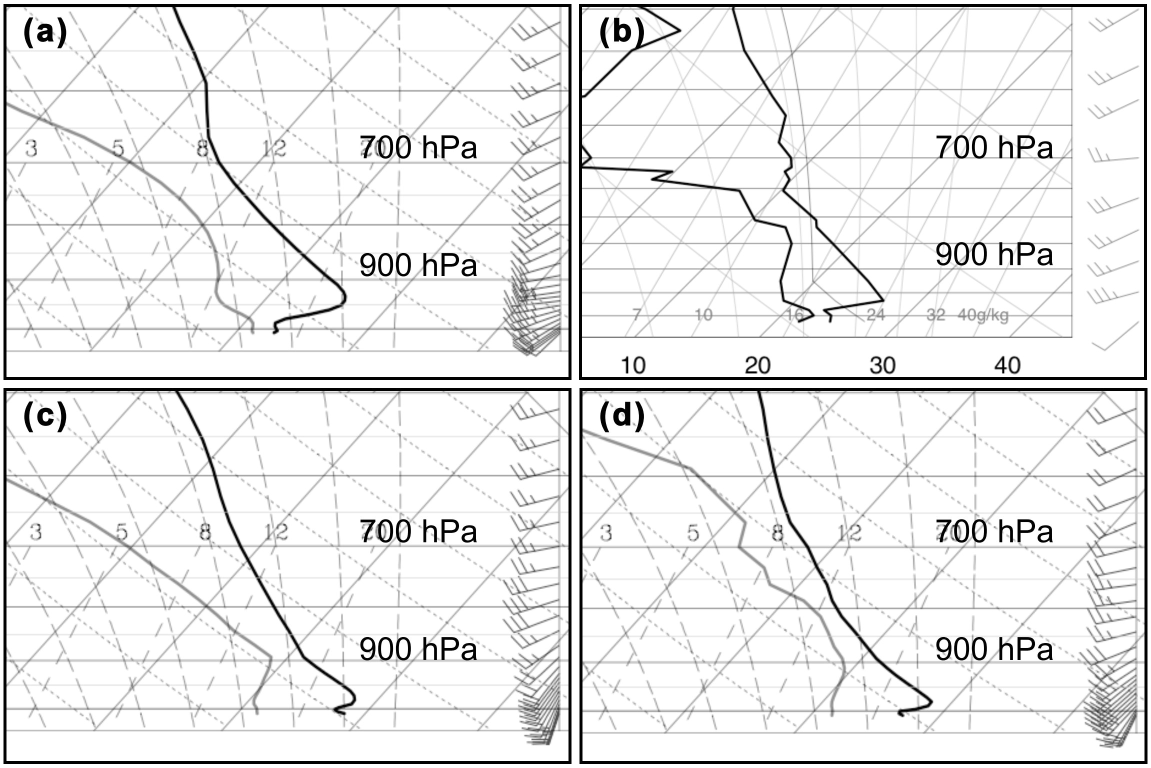

Figure 4.24 (a) 1200 UTC 23 July 2002 500 m WRF sounding at OKX location (b) 1200 UTC 23 July 2002 sounding from OKX (c) 1800 UTC 23 July 2002 500 m WRF sounding at JFK location (d) 2100 UTC 23 July 2002 500 m WRF sounding at JFK location.

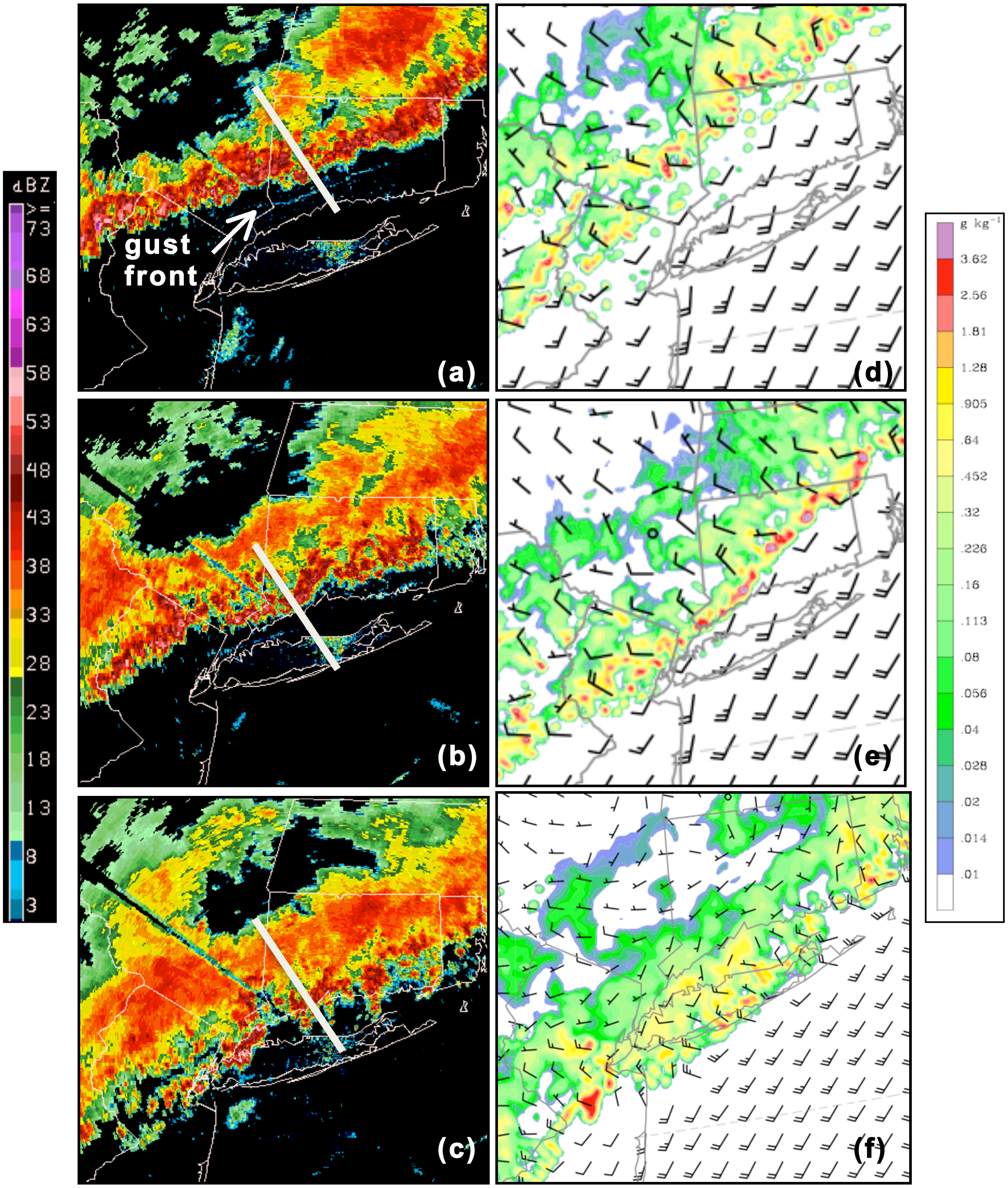

Figure 4.25 Level II radar reflectivity at for 23 July 2002 at (a) 2016 UTC, (b) 2115 UTC, (c) 2215 UTC, 2 km WRF precipitation mixing ratio (g kg^{-1}) and 10 m winds (full barb = 5 m s^{-1}) for 23 July 2002 at (d) 2015 UTC (14.25 h), (e) 2115 UTC (15.25 h), (f) 2300 UTC (17 h).

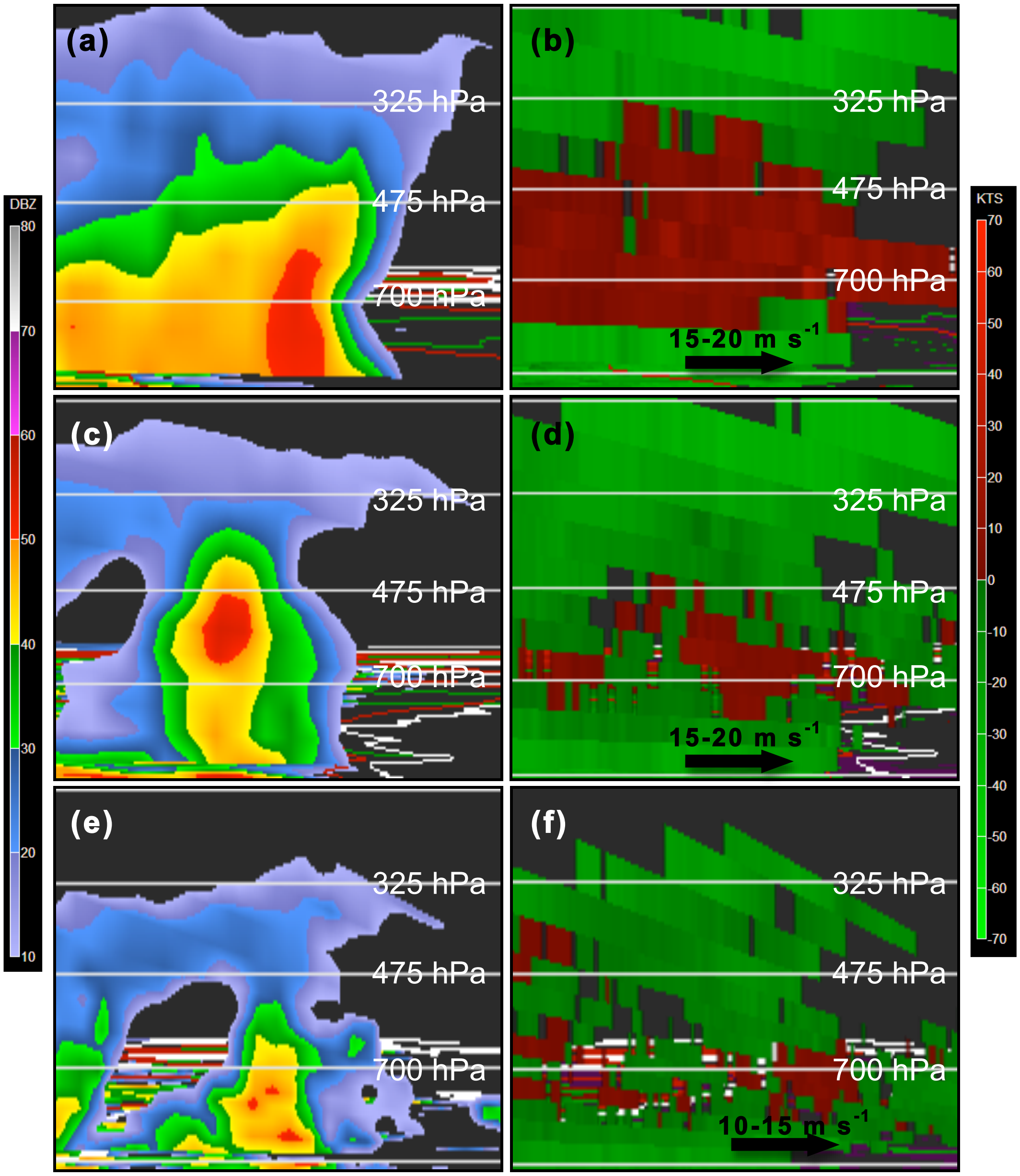

Figure 4.26 2016 UTC 23 July 2002 (a) Level II radar reflectivity (dBZ), (b) Level II radar velocity (kts), (c) same as (a) but for 2115 UTC, (d) same as (b) but for 2115, (e) same as (a) but for 2215 UTC, (f) same as (b) but for 2215 UTC. The cross section location for (a) & (b) is marked with a white line in figure 25a. The cross section location for (c) & (d) is marked with a white line in figure 4.25b. The cross section location for (e) & (f) is marked with a white line in figure 4.25c.

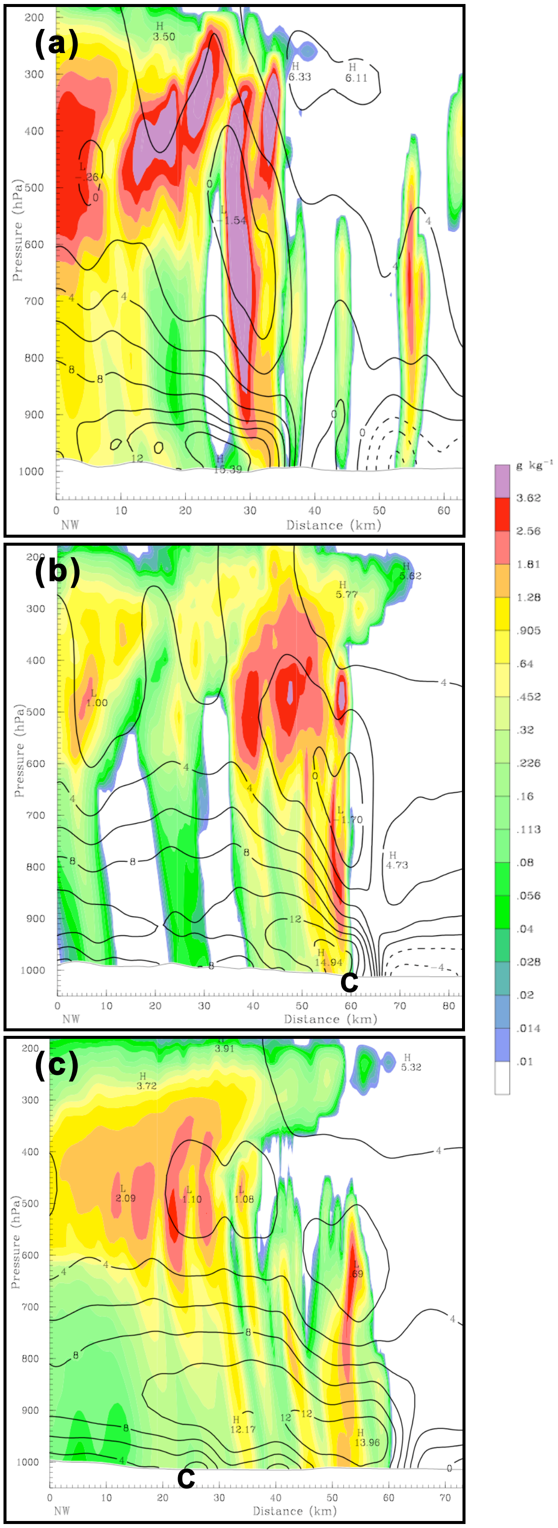

Figure 4.27 500 m WRF cross sections of precipitation mixing ratio (shaded, g kg^{-1}) and horizontal wind speed magnitude (black every 1 m s^{-1}) in the plane of the cross section for 23 July 2002 at (a) 2015 UTC (14.25 h), (b) 2115 UTC (15.25 h), (c) 2215 UTC (16.25 h). The cross section location for (a) is marked with a white line in figure 25a, for (b) in figure 4.26b, for (c) figure 4.25c. The location of the coastline is marked with a **C**.

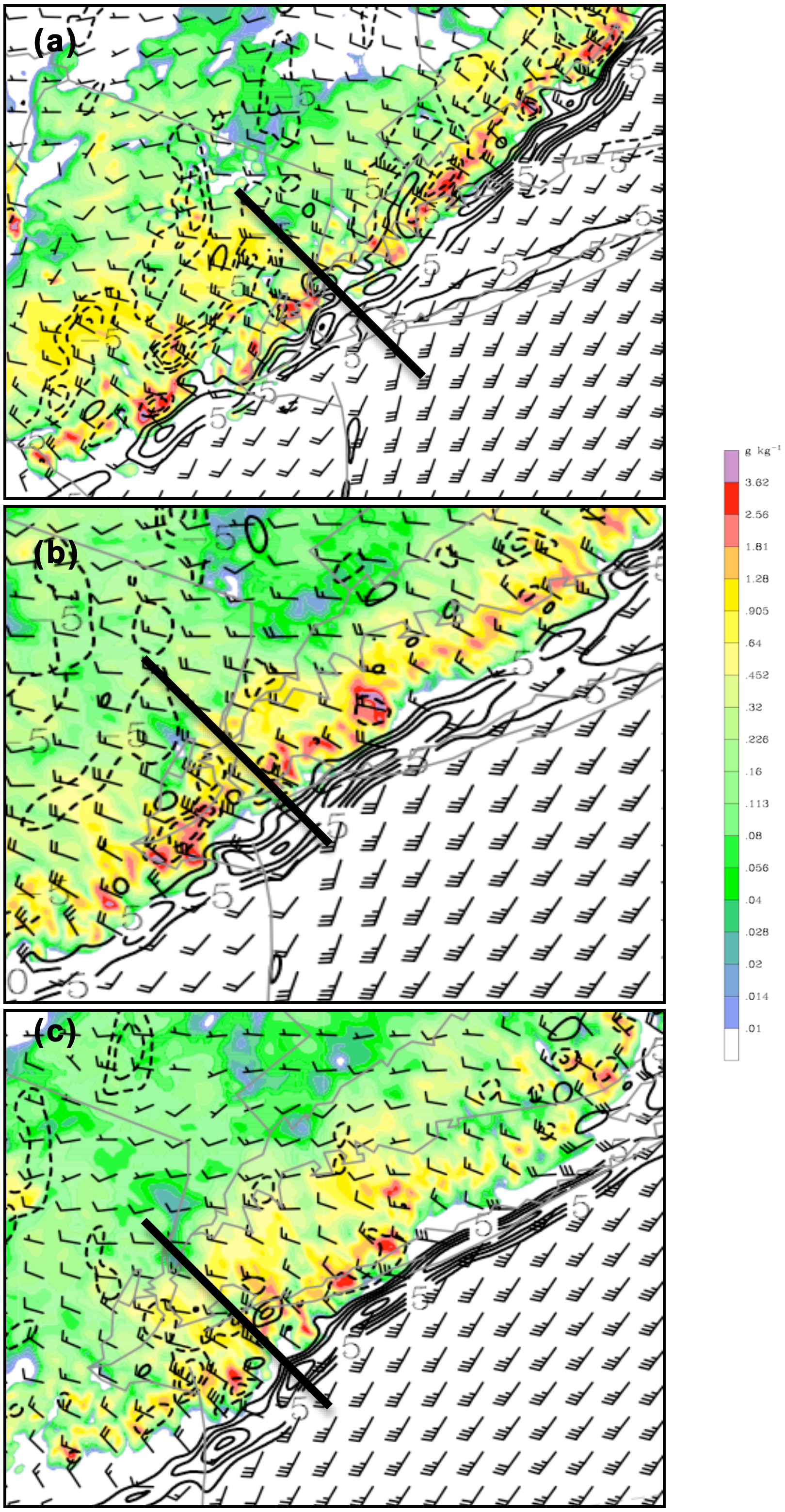

Figure 4.28 500 m WRF precipitation mixing ratio (shaded, g kg^{-1}), 100 m vertical motion (every 5 x10^{-2} m s^{-1}), and 100 m winds (full barb = 5 m s^{-1}) for 23 July 2002 at (a) (15.5 h) 2130 UTC (b) (16 h) 2200 UTC (c) (16.5 h) 2230 UTC.

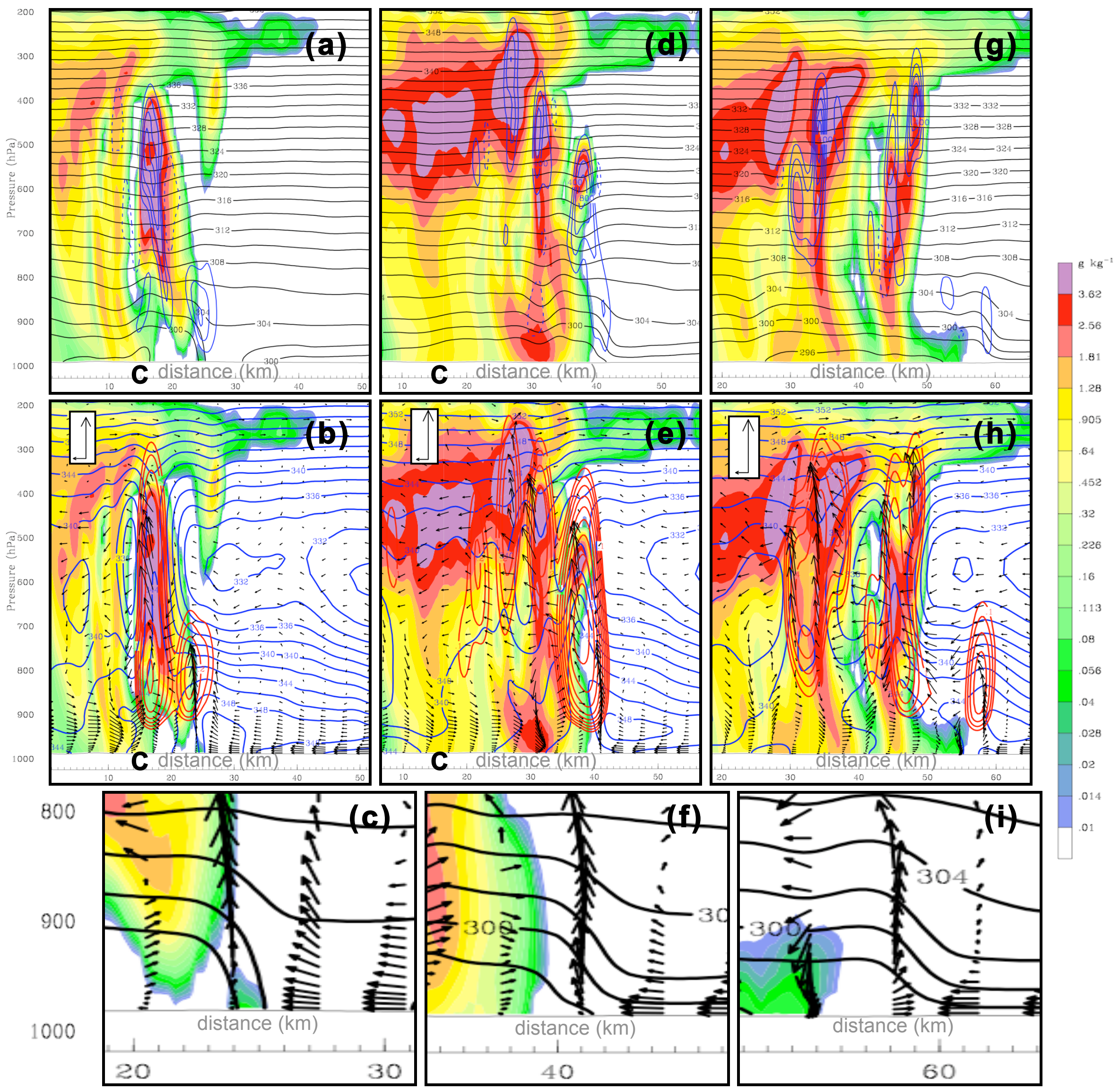

Figure 4.29 500 m WRF cross section at 2130 UTC 23 July 2002 (15.5 h) of (a) precipitation mixing ratio (shaded, g kg^{-1}), θ (black every 2 K), vertical motion (blue every 2x10^{-2} m s^{-1}, ascent in the solid lines and descent in the dashed lines), (b) precipitation mixing ratio (shaded, g kg^{-1}), cloud water mixing ratio (red, g kg^{-1}), θ_e (blue every 2 K), storm relative circulation vectors, (c) precipitation mixing ratio (shaded, g kg^{-1}), θ (black every 2 K), storm relative circulation vectors, (d) same as (a) but for 2200 UTC (16 h), (e) same as (b) but for 2200 UTC (16 h), (f) same as (c) but for 2200 UTC (16 h), (g) same as (a) but for 2230 UTC (16.5 h), (h) same as (b) but for 2230 UTC (16.5 h), (i) same as (c) but for 2230 UTC (16 .5 h). For (b), the maximum horizontal vector is 13.4 m s^{-1} & the maximum vertical vector is 71.2 Pa s^{-1}. For (e), the maximum horizontal vector is 12.3 m s^{-1} & the maximum vertical vector is 76.1 Pa s^{-1}. For (h), the maximum horizontal vector is 13.2 m s^{-1} & the maximum vertical vector is 81.7 Pa s^{-1}. The cross section location for (a)-(c), (d)-(f), (g)-(i) is marked with a black line in figure 4.28a, 4.28b, 4.28c, respectively. The location of the coastline is marked with a **C**.

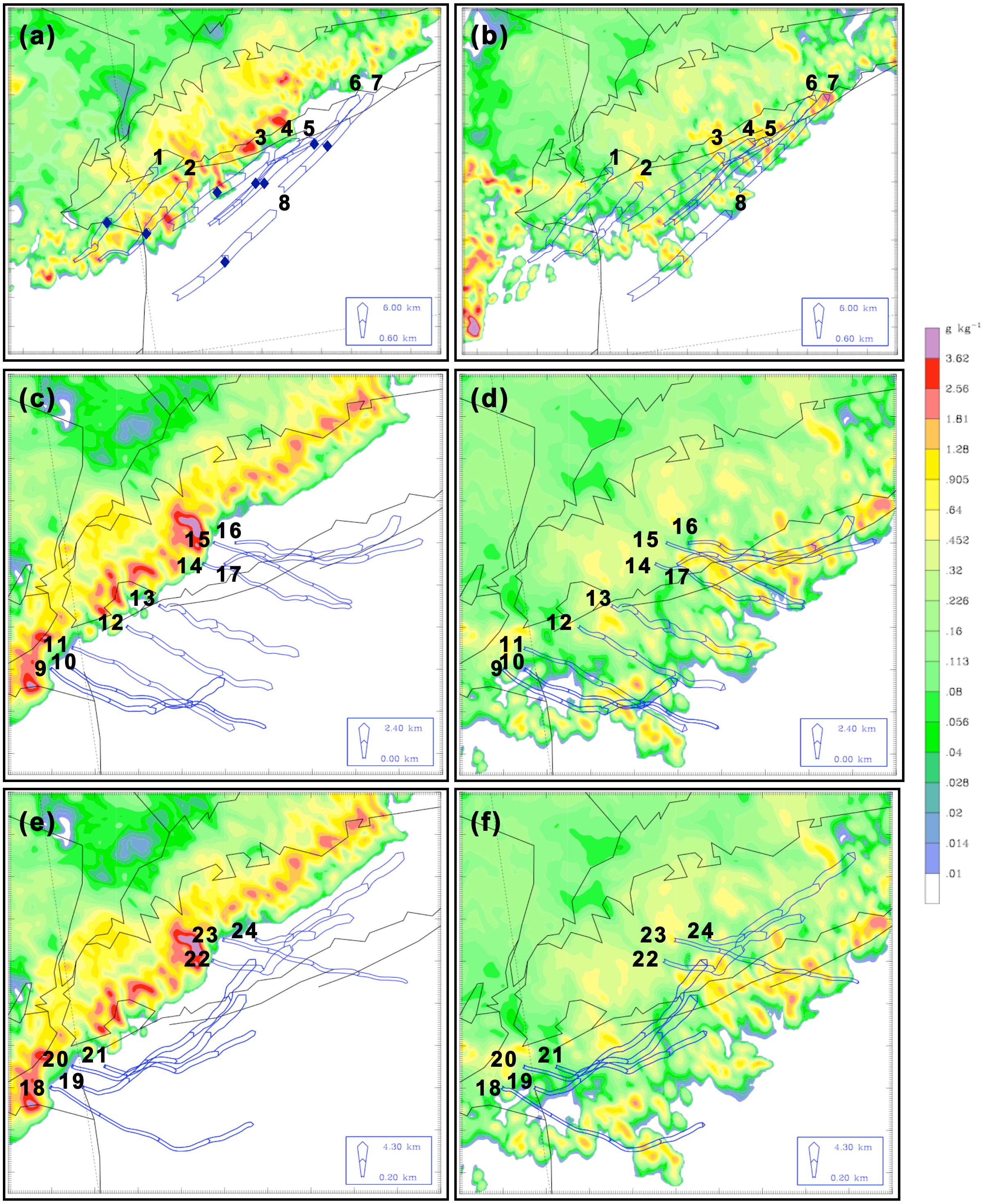

Figure 4.30 500 m resolution backward 1 minute trajectories beginning at 5 km and 6 km launched at 17 h (2300 UTC 23 July 2002) and precipitation mixing ratio (g kg^{-1}) at (a) 16.5 h (2230 UTC 23 July 2002) (b) 17 h (2300 UTC 23 July 2002), forward 1 minute trajectories starting at 10 m and 100 m launched at 16 h (2200 UTC 23 July 2002) and precipitation mixing ratio (g kg^{-1}) at (c) 16 h (2200 UTC 23 July 2002) (d) 17 h (2300 UTC 23 July 2002), forward 1 minute trajectories starting at 500 m launched at 16 h (2200 UTC 23 July 2002) and precipitation mixing ratio (g kg^{-1}) at (e) 16 h (2200 UTC 23 July 2002) (f) 17 h (2300 UTC 23 July 2002).

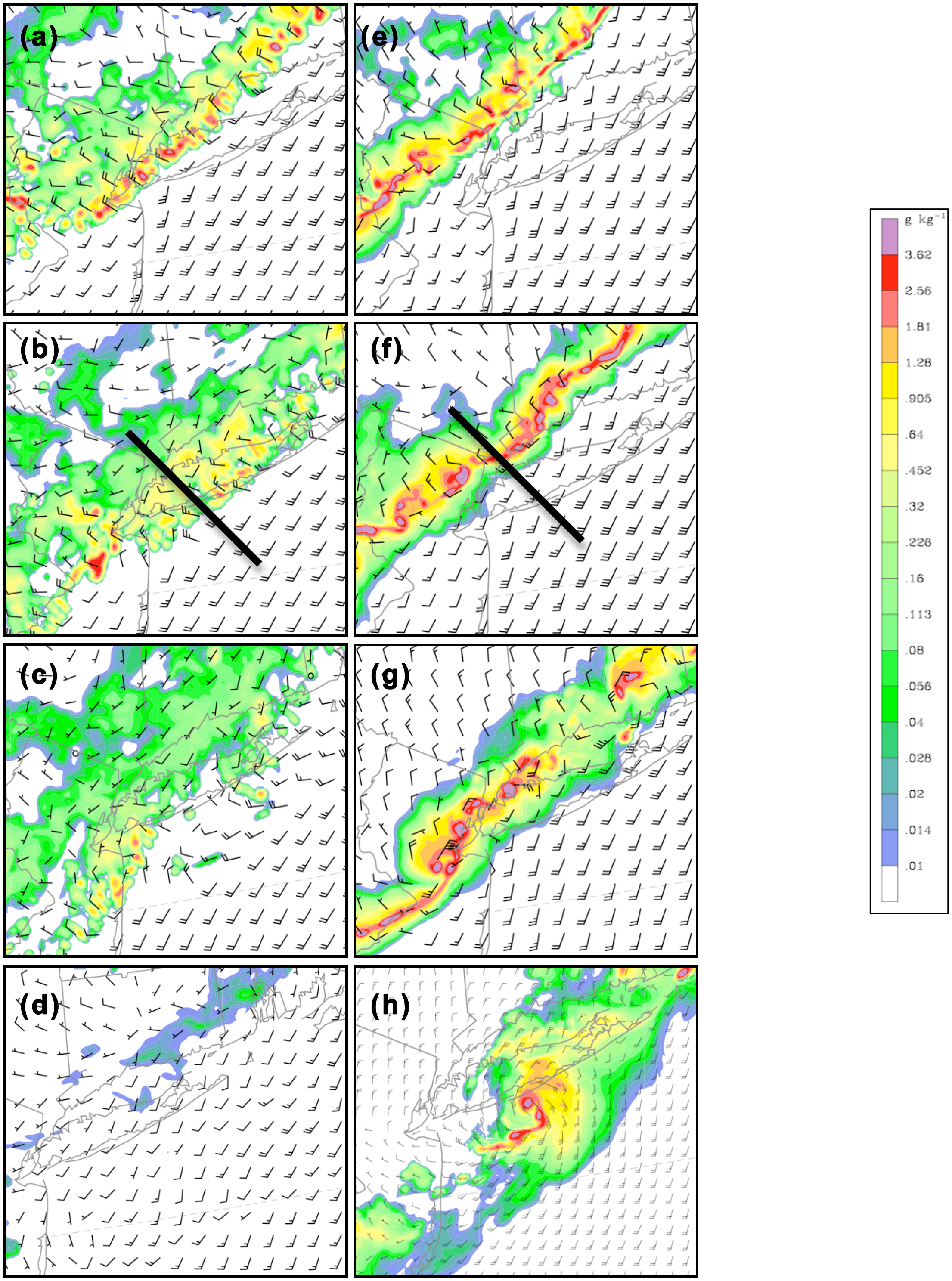

Figure 4.31 2 km WRF precipitation mixing ratio (shaded, g kg^{-1}) and 10 m winds (full barb = 5 m s^{-1}) for the 23 July 2002 control simulation at (a) (16 h) 2200 UTC, (b) (17 h) 2300 UTC, (c) (18 h) 0000 UTC 24 July 2002, (d) (21h) 0300 UTC 24 July 2002, and for the 15%EVAP simulation at (e) (16 h) 2200 UTC, (f) (17 h) 2300 UTC, (g) (20 h) 0200 UTC 24 July 2002, (h) (24h) 0600 UTC July 2002.

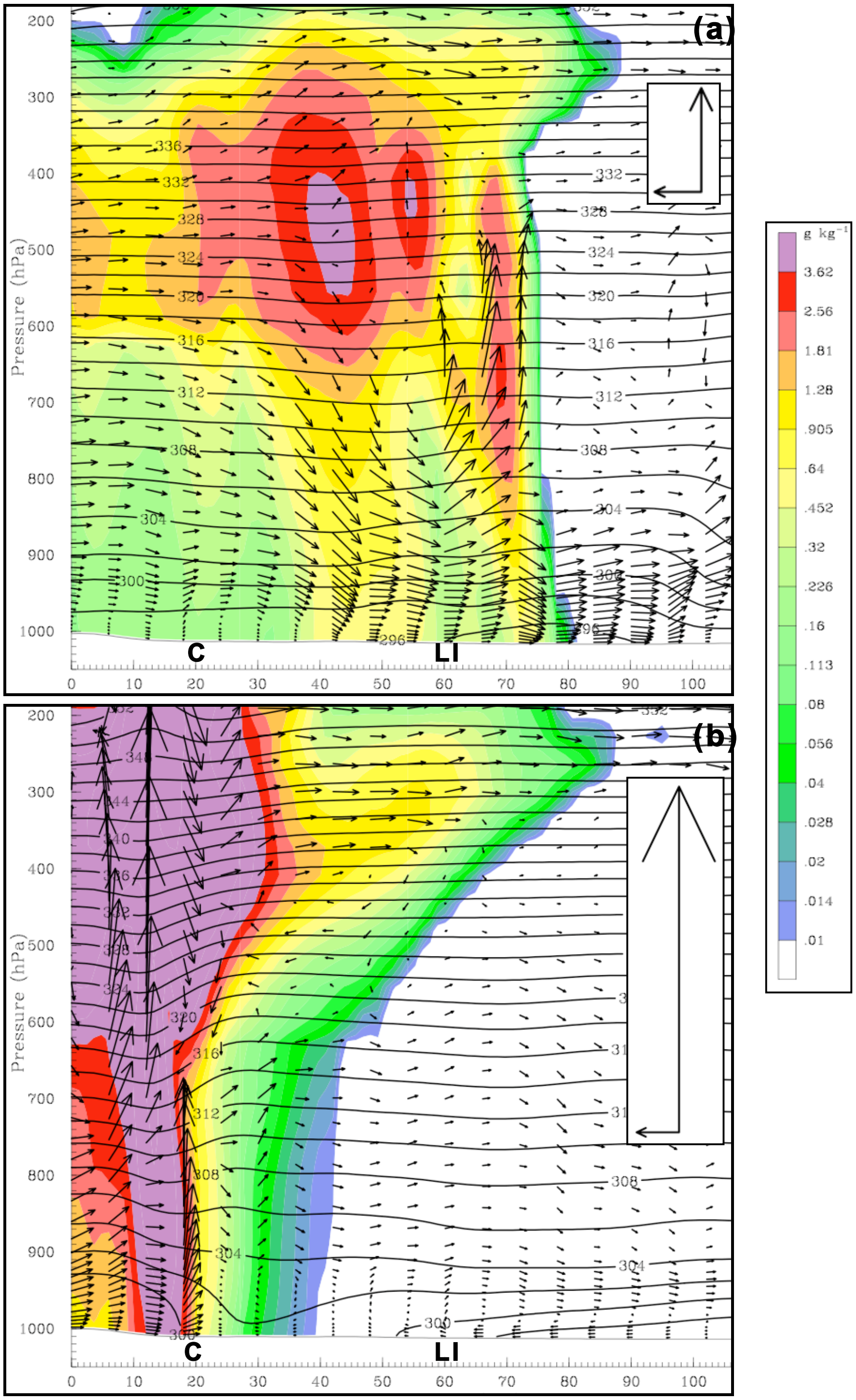

Figure 4.32 Cross section of 2 km WRF precipitation mixing ratio (shaded, g kg^{-1}), potential temperature (black every 2 K), and circulation vectors at (17 h) 2300 UTC 23 July 2002 for the (a) CTRL simulation and (b) 15%EVAP simulation. For (a), the maximum horizontal vector is 17.7 m s^{-1} and the maximum vertical vector is 36.5 Pa s^{-1}. For (b), the maximum horizontal vector is 19.2 m s^{-1} and the maximum vertical vector is 145.0 Pa s^{-1}. The cross section location for (a) is shown in figure 4.31b, and for (b) in figure 4.31f. The location of the coastline is marked with a **C** and Long Island with an **LI**.

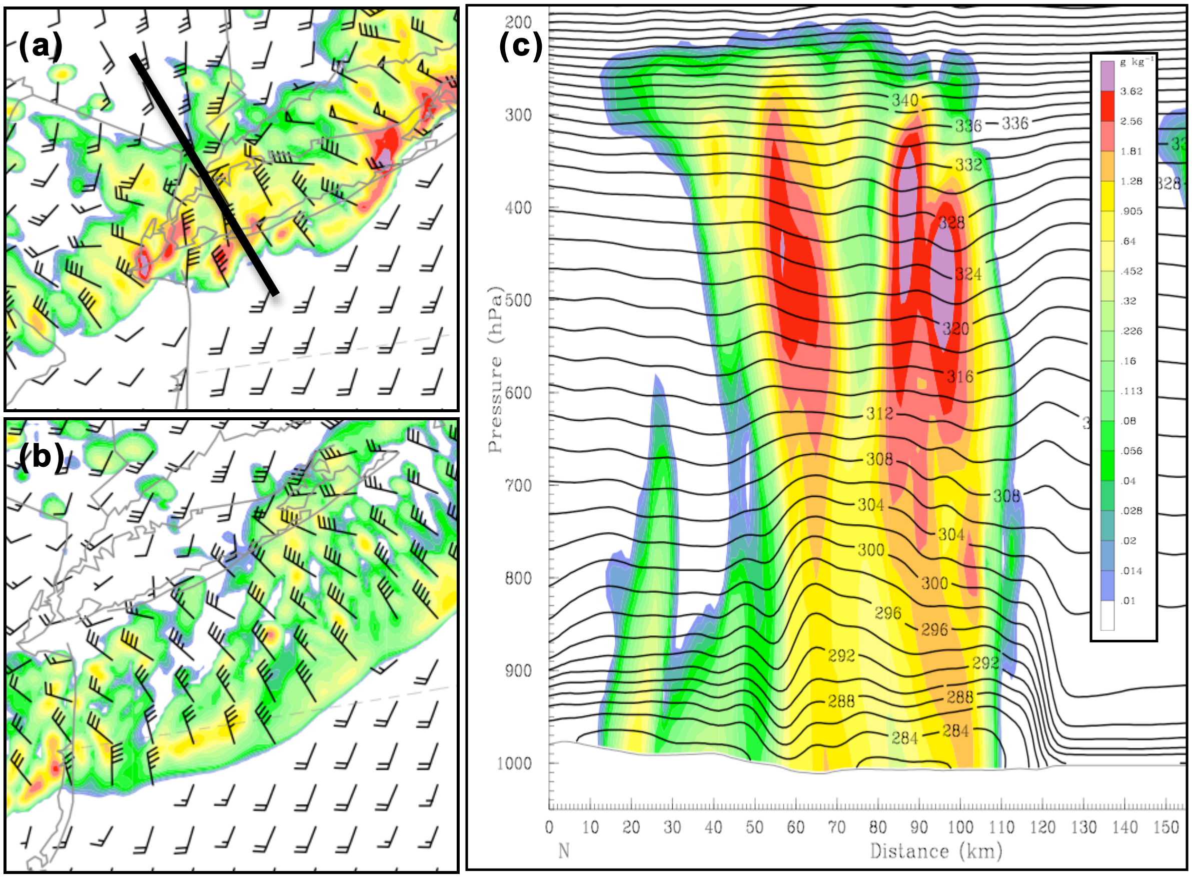

Figure 4.33 2 km WRF for the 10EVAP simulation at (11.5 h) 2330 UTC 31 May 2002 of (a) precipitation mixing ratio (shaded, g kg^{-1}) and 10 m winds (full barb = 5 m s^{-1}), (b) cross section of precipitation mixing ratio (shaded, g kg^{-1}) and potential temperature (black every 2 K), (c) (12.5 h) 0030 UTC 1 June 2002 precipitation mixing ratio (shaded, g kg^{-1}) and 10 m winds (full barb = 5 m s^{-1}). The cross section location for (b) is shown in (a).

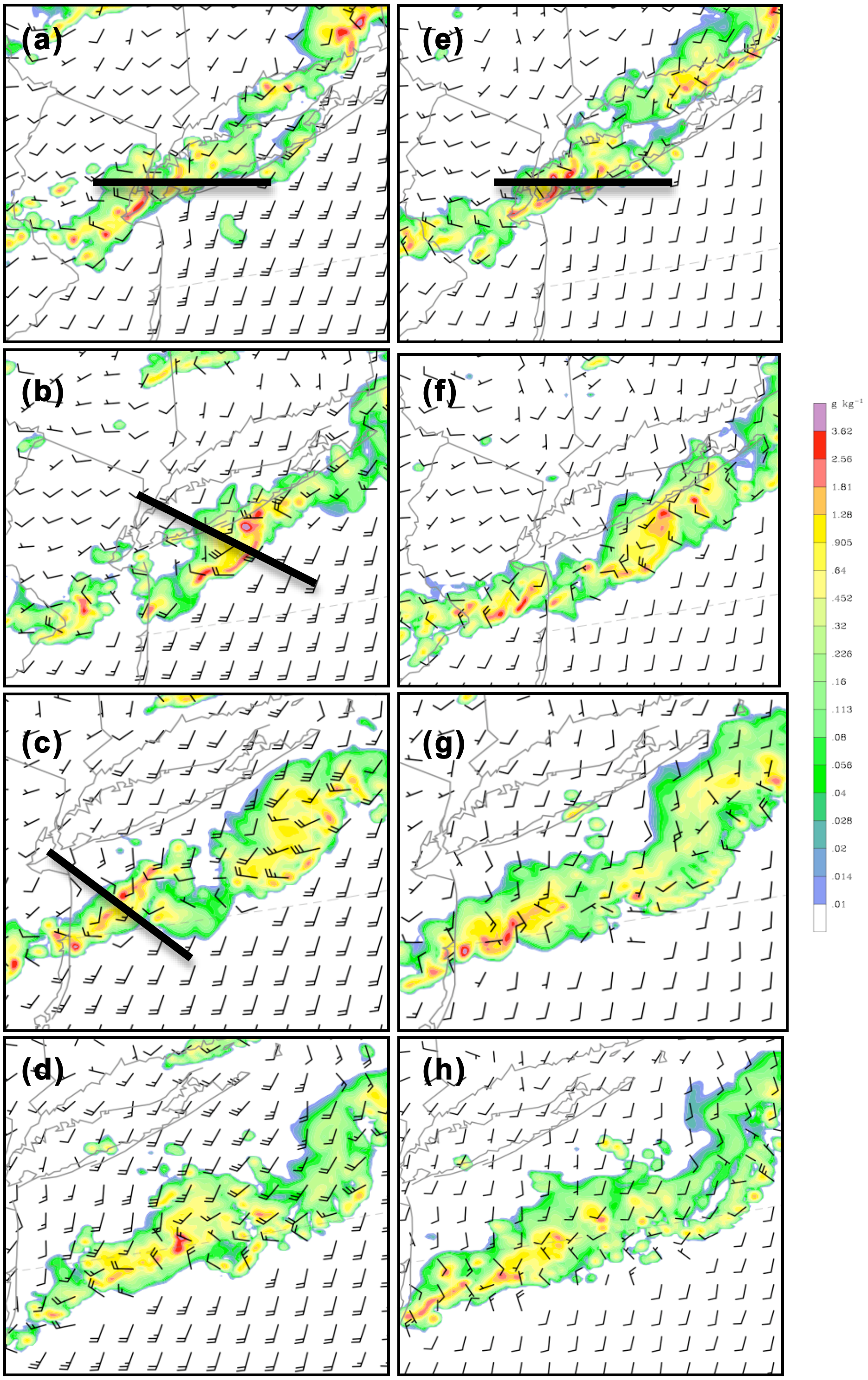

Figure 4.34 2 km WRF precipitation mixing ratio (shaded, g kg^{-1}) and 10 m winds (full barb = 5 m s^{-1}) for the control simulation for 1 June 2002 at (a) (12 h) 0000 UTC, (b) (13 h) 0100 UTC, (c) (14 h) 0200 UTC, (d) (15 h) 0300 UTC, and for the 0.5ZNT simulation for 1 June 2002 at (e) (12h) 0000 UTC, (f) (13 h) 0100 UTC, (g) (14 h) 0200 UTC, (h) (15 h) 0300 UTC.

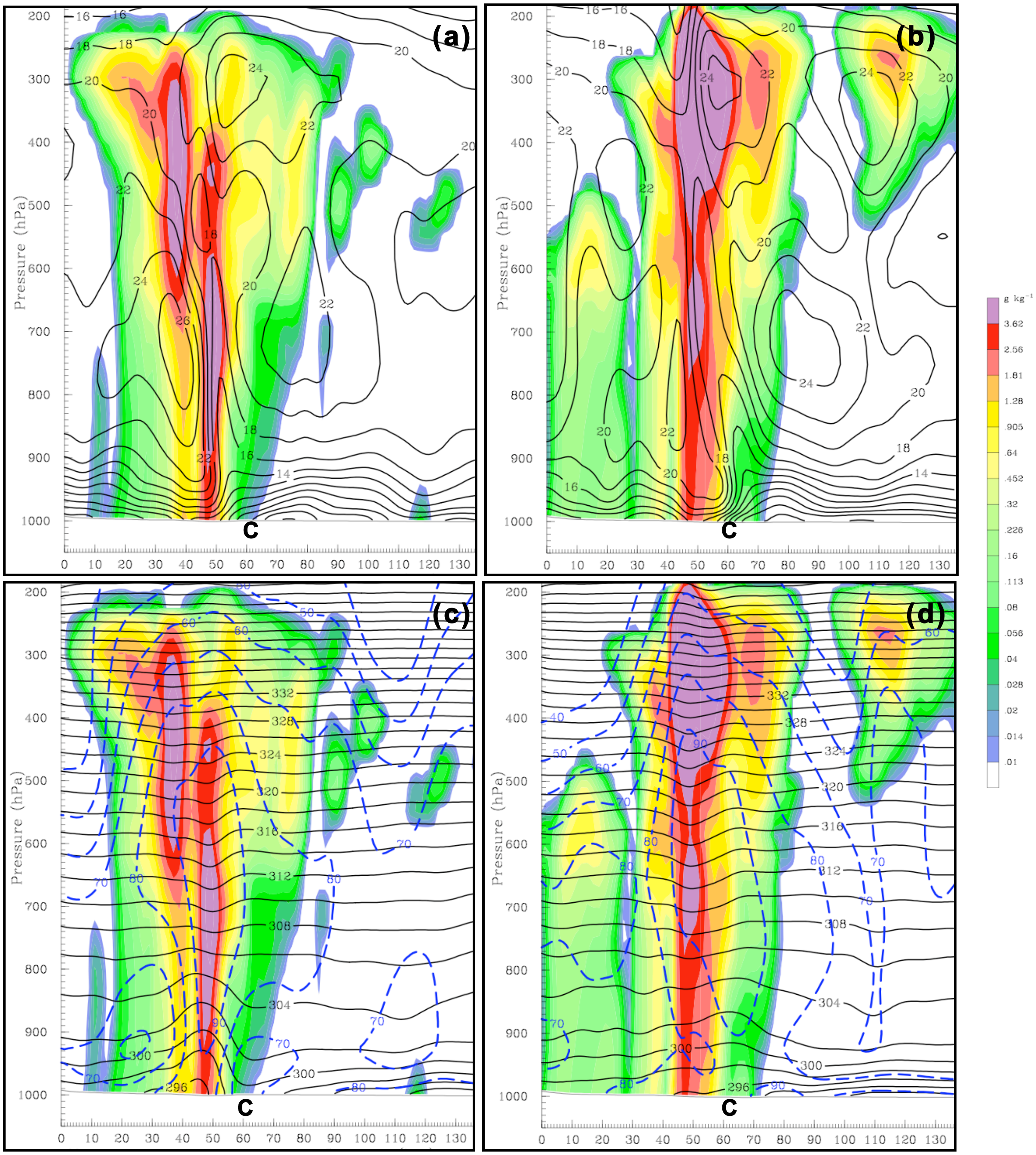

Figure 4.35 Cross section of 2 km WRF at (12 h) 0000 UTC 1 June 2002 of precipitation mixing ratio (shaded, g kg^{-1}) and line perpendicular wind speed (black every 2 m s^{-1}) for the (a) control simulation, (b) 0.5ZNT simulation, (c) same as (a) but of precipitation mixing ratio (shaded, g kg^{-1}), potential temperature (black every 2 K), relative humidity (blue dashed every 10%), (d) same as (b) but of precipitation mixing ratio (shaded, g kg^{-1}), potential temperature (black every 2 K), relative humidity (blue dashed every 10%). The cross section location for (a) & (c) is shown in figure 4.33a, and for (b) & (d) in figure 4.33e. The location of the coastline is marked with a **C**.

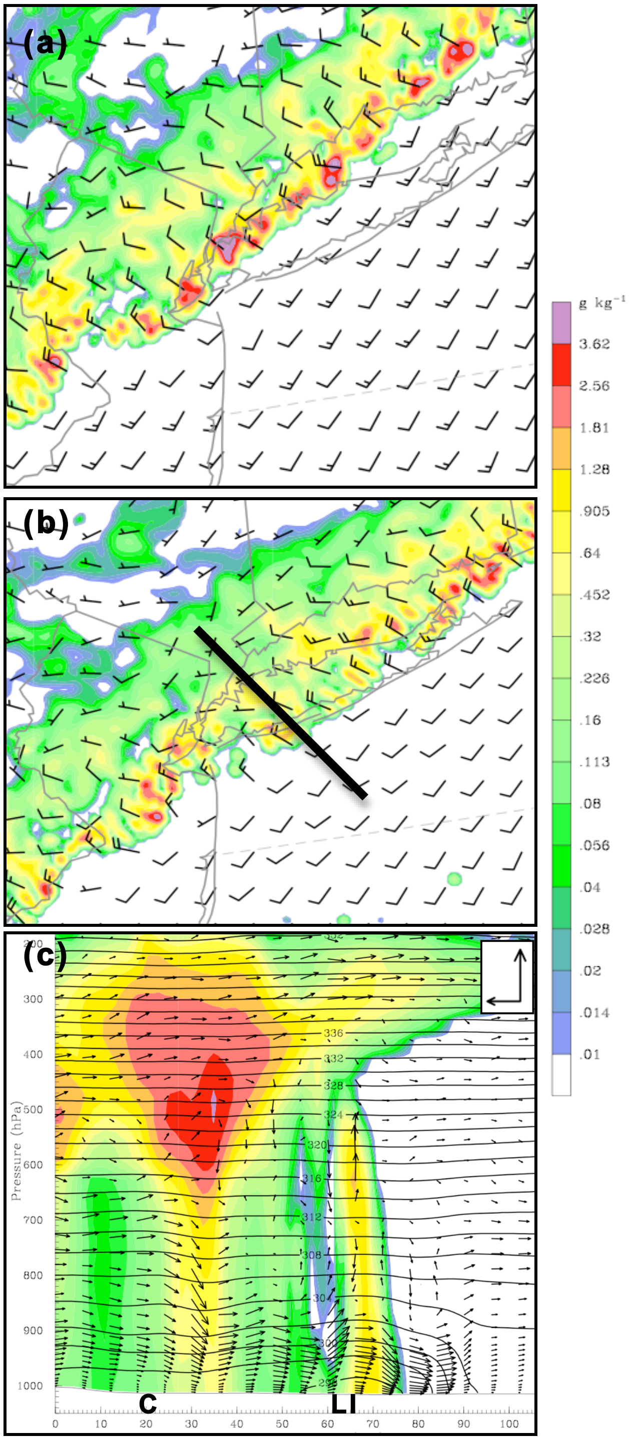

Figure 4.36 2 km WRF precipitation mixing ratio (shaded, g kg^{-1}) and 10 m winds (full barb = 5 m s^{-1}) for the LAND simulation for 23 July 2002 at (a) (16 h) 2200 UTC, (b) (17 h) 2300 UTC, (c) cross section of precipitation mixing ratio (shaded, g kg^{-1}), potential temperature (black every 2 K), and circulation vectors at (17 h) 2300 UTC. The maximum horizontal vector is 16.7 m s^{-1} and the maximum vertical vector is 21.1 Pa s^{-1}. The location of the coastline in (c) is marked with a **C** and Long Island with an **LI**.

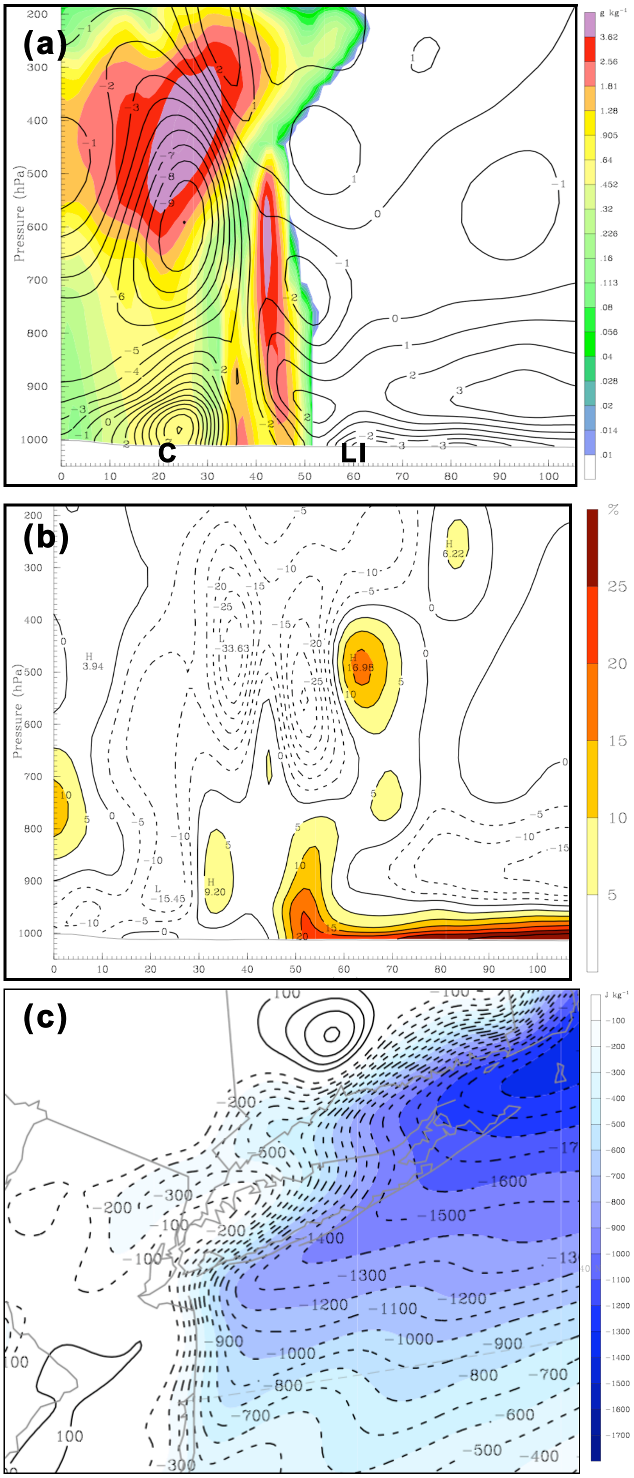

Figure 4.37 2200 UTC 23 July 2002 (16h) of (a) 2 km WRF LAND precipitation mixing ratio (shaded, g kg^{-1}) and CTRL-LAND difference plot of line perpendicular wind speed (black every 1 m s^{-1}), (b) CTRL-LAND difference plot of relative humidity (black every 5%, values >5% are shaded), (c) 2100 UTC 23 July 2002 (15h) CTRL-LAND difference plot of surface based CAPE (black every 100 J kg^{-1}, values less than 100 J kg^{-1} are shaded). The location of the coastline in (a) is marked with a **C** and Long Island with an **LI**.

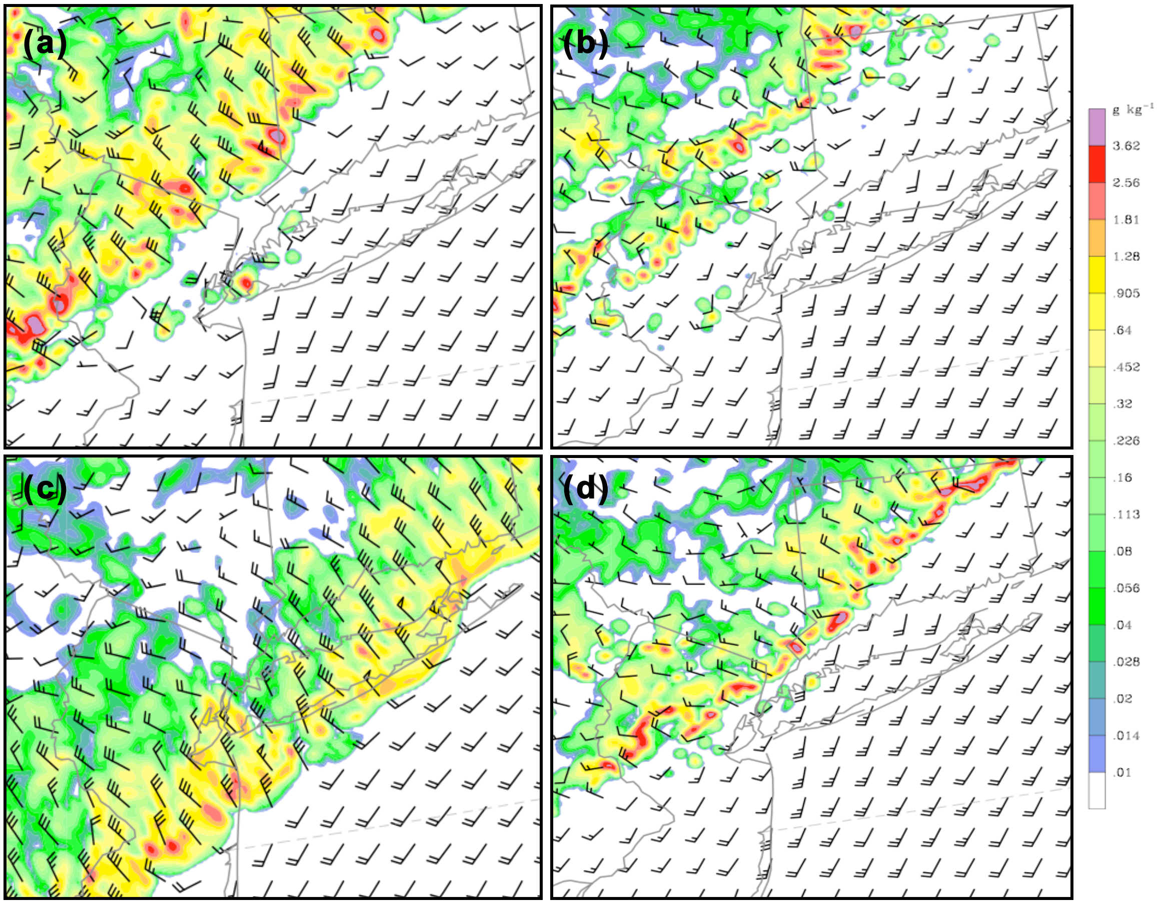

Figure 4.38 2 km WRF precipitation mixing ratio (shaded, g kg^{-1}) and 10 m winds (full barb = 5 m s^{-1}) on 23 July 2002 at (a) (14 h) 2100 UTC for the 3PM_SOLAR run, (b) same as (a) but for the CTRL run, (c) (15 h) 2200 UTC for the 3PM_SOLAR run, (d) same as (c) but for the CTRL run.

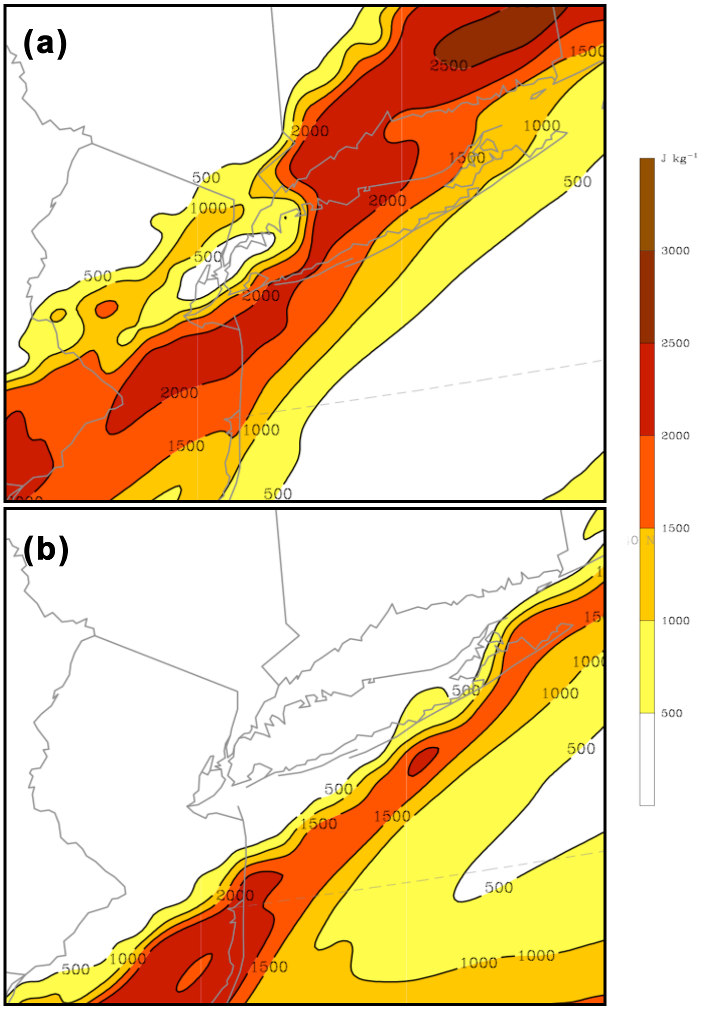

Figure 4.39 2 km WRF 3PM_SOLAR-CTRL difference plot of MUCAPE (shaded >500 J kg^{-1} every 500 J kg^{-1}) for 23 July 2002 at (a) (14 h) 2100 UTC, (b) (15 h) 2200 UTC.

Chapter 5:

Conclusions and Future Work

5.1 Summary

This study has investigated the dynamic and thermodynamic conditions associated with evolving warm season convective organizational structures over the northeastern U.S, exploring the processes governing the organization of these structures as well as their interaction with the Atlantic marine environment. The climatology, environmental conditions, and dynamical evolution of different convective structures are explored using composite analyses of convective events over multiple warm seasons, analyses of observational and gridded data, in depth analyses of individual case studies, and high-resolution numerical simulations and sensitivity experiments. These methods provided insight into the atmospheric flow regimes and the physical mechanisms associated with the organization of different convective structures over the northeastern U.S, as well as the processes that dominate the evolution organized convective structures over the coastal marine environment.

5.2 Conclusions

(a) Northeastern U.S. convective research

Northeastern U.S. warm season convection has been less studied than the convective systems over the central U.S. Chapter 2 addresses this issue by being the first study to systematically identify the various types of convective organizational structures, such as cells, quasi-linear, and nonlinear convection, over the northeastern U.S, exploring their favored development locations and initiation/organization mechanisms with respect to the complex topography across the region.

The development of the various convective structures is dependent on the ambient synoptic conditions, underlying terrain, and diurnal heating cycle. Cellular convection is the dominant convective mode between 1200-1800 UTC. Cellular convection develops within ~1000 J kg^{-1} of instability on average, and ~2 m s^{-1} (9.5 m s^{-1}) of 0-1 km (0-6 km) shear. Topography may be helping to trigger many of these storms, since they develop primarily over the high terrain as well as the upslope areas of the Appalachian terrain. These cells can also develop along mesoscale boundaries such as sea breeze convergence zones within the Atlantic coastal plain.

From the mid-afternoon into the early evening (1800-0000 UTC), the most common convection mode transitions from cells to quasi-linear convective systems (QLCS). QLCSs organize along surface troughs, supported by ageostrophic circulations with low-level frontogenesis, and have an average ambient instability similar to cellular convective events. The average vertical wind shear during linear events is significantly (95% level) higher compared to cellular events, with 3.9 m s^{-1} of 0-1 km shear and 12.3 m s^{-1} of 0-6 km shear. There is limited organization of linear convection over the coastal Atlantic Ocean.

By the early evening into the overnight (0000-0600 UTC), nonlinear convection is the most common developing structure over the northeastern U.S, which is consistent with the fact that these systems are less reliant on instability (MUCAPE ~200 J kg^{-1}), and are supported by relatively deep dynamical forcing. In the mean, nonlinear systems organize along warm fronts associated with larger-scale baroclinic systems, collocated with low-level warm air advection as well as ascent regions of upper-level jet circulations. Ambient vertical wind shear values are the highest during nonlinear events, with 5.3 m s^{-1} of 0-1 km shear and 16.9 m s^{-1} of 0-6 km shear, with both values statistically greater (90-95%) compared to linear and cellular events.

Another unique aspect of this work is the comparison of environments that support northeastern U.S. convection described above with the central U.S. Mean CAPE values during Northeast linear convective events are similar to linear events over the central Plains. Within the mean, there is a large spread in CAPE for individual northeastern U.S. linear events, indicating that Northeast linear convection can develop in environments typically not anticipated to support convection, though this can be the case for central U.S. storms as well (e.g. Evans and Doswell 2001). Furthermore, in the mean, linear events over the Northeast develop with approximately half the ambient 0-6 km vertical wind shear than convective lines over the central states. Meanwhile, the deep layer shear values for northeastern U.S. nonlinear systems more closely resembles shear values that support central Plains quasi-linear convection. It is important to recognize that the environmental conditions that support various convective structures over the Northeast are not always the same as those that support convection in other parts of the country.

(b) Convective research within the coastal region

From the first part of this work (chapter 2), it was shown that the development of convection over the northeastern U.S. decreases moving eastward from the Appalachian upslope region towards the Atlantic waters, with only 7% of all Northeast convection examined in this study organizing over the marine environment. Given that (severe) convection can occur over the coastal zone (e.g. 8 Aug 2007 NYC tornadoes), the question becomes 'What dynamic and thermodynamic conditions favor severe weather over the northeastern U.S. coastal region?'. With this important forecast question as motivation, chapter 3 categorized the convective structures that are most commonly associated with 3 main types of severe weather (wind, hail, tornadoes) over the northeastern U.S. coastal region (NJ, southern NY, CT, and RI), as well as the evolution of the dynamic and thermodynamic processes leading to environments favorable for these severe organizational structures.

Classification of severe weather type related to each convective organizational structure showed that severe wind is primarily produced from cells and lines over the Northeast coastal region. These cells near the coast are responsible for ~1.5 times as many hail events as lines and almost 6 times as many compared to nonlinear convection. No one convective structure is favored to produce tornadoes. While this may be due to the small sample size of coastal tornadoes, further analysis is required to fully understand the relationship between convective structure and tornadogenesis over the coastal zone. While 75% of all severe wind and hail events occur during the warmest part of the day (1800-0000 UTC), the development of coastal tornadoes is more evenly distributed throughout the day, though 44% are reported between 2100-0000 UTC.

Composite analyses highlighted the thermodynamic conditions associated with each severe convective organizational structure over the coastal region. During severe cellular coastal events, ageostrophic circulations associated with weak frontogenesis provide a lifting mechanism to support the development of severe cells, while low-level temperature advection helps to destabilize the environment (average MUCAPE ~1200 J kg^{-1}). This is different than all cellular events (severe and non-severe) over the Northeast, which are typically driven by upslope flows with weaker dynamical support. In the mean, there is little mid-level Q-G forcing for ascent during severe coastal cellular events. On average, severe cellular events form in 2.6 m s^{-1} of 0-1 km shear, with a deep layer (0-6 km) shear value of 13.4 m s^{-1}.

For severe convective lines, a majority of these phenomena organize within a prefrontal trough located within the Appalachian lee, ~600 km to the east of a surface cold front, though the ageostrophic circulations associated with the upstream cold front are important during these events as well. Almost half of the linear events develop in association with a progressive 500-hPa trough moving towards the coastal zone, with an ambient instability similar to severe cellular events. The mean 0-1 km shear during severe coastal linear events is 4.5 m s^{-1}, a significantly (95%) larger value compared to cellular events, with a mean deep layer shear value of 14.9 m s^{-1}.

During severe nonlinear events, both ageostrophic circulations associated with low-level baroclinic zones as well as mid-level Q-G forcing are important. While these events are associated with tropospheric deep forcing, the mean environmental instability is about one-third compared to severe cellular and linear events. While nonlinear events have a similar mean 0-1 km shear value (~4.4 m s^{-1}) as the linear events, the average deep layer shear value (18.8 m s^{-1}) is significantly greater than during linear (80%) and cellular (95%) events.

Comparing severe events over the coastal region to all convective storm events over the Northeast, on average there is ~175-250 J kg^{-1} more elevated instability associated with the severe events for all convective types, 0.5-1 m s^{-1} greater 0-1 km vertical wind shear and 2-4 m s^{-1} 0-6 km wind shear, as well as more dynamical support overall. While these trends in values are expected, it is interesting to note that the mean values for variables considered important to the organization of convection, such as CAPE and shear, are not noticeably larger compared to all convective storms over the Northeast. Therefore, it seems that CAPE and shear may not always be the most obvious delimiter between severe and non-severe storms over the Northeast, rather those with more forcing for ascent have a higher likelihood of becoming severe.

Linear convection is associated with more severe weather events compared to cellular and nonlinear structures over the Northeast coastal zone (chapter 3). These destructive convective phenomena are examined in more detail in chapter 4, through the investigation of the evolution of quasi-linear convective systems in a coastal environment. Quasi-linear convective events encountering the Atlantic coastline were categorized based on their evolution upon encountering the marine environment, organizing the events into those that decay at the coast, events that slowly decay over the Atlantic waters after crossing the coastal boundary, and those that maintain their intensity greater than 100 km from the coast.

Feature-based composites indicate that decaying and slowly decaying QLCSs are located within a surface pressure trough collocated with a maximum of low-level frontogenesis, which is associated with a developing low-level baroclinic zone between a region of warm air advection to the east and cold air advection to the west. These features were seen in the composites of coastal severe linear events as well from chapter 3. Relative humidity values within the lowest 100 hPa during decay and slow decay events are ~68% and ~70%, respectively, indicating that there is a potential for low-level evaporative cooling which may act to enhance the generation of the cold pool. Some of the main differences between the composite decay and slow decay events include weaker instability, the presence of mid-level Q-G forcing for ascent, and a stronger low-level frontogenesis maximum during the slow decay events. This indicates that slow decay events are less dependent on instability and are associated with more robust dynamical forcing.

The dynamic and thermodynamic environments associated with maintaining linear systems are noticeably different than decaying and slowly decaying events. Maintaining linear events over the coastal waters are located ~250-300 km downstream of a surface pressure trough, within a region of low-level warm air advection and little frontogenesis between 900-800 hPa. The warm air advection helps destabilize the environment ahead of the QLCS. These events also have 10% greater low-level RH values than both types of decay events, implying a decreased potential for evaporative cooling in the lowest 100 hPa.

Differences in instability do not seem to be an intuitive delimiter determining the type of QLCS evolution, with decay events having the greatest instability ahead of the QLCS (1200-1600 J kg^{-1})_compared to slow decay (800-1200 J kg^{-1}) and maintaining events (400-800 J kg^{-1}). More importantly are differences in 0-3 km vertical wind shear, which is important to the organization of convective lines. The 0-3 km shear vector associated with decaying QLCS events is 7.7 m s^{-1} from the west-northwest, 10.5-13.5 m s^{-1} from the west for slow decay events, and 13-15.5 m s^{-1} from the northwest for maintaining events.

The differences between the decay and maintain events are further explored for two case studies, the 31 May 2002 (maintain event) and 23 July 2002 (decay event). These two events are examined in detail using a combination of observations, including the NARR, surface observations, sounding profiles as well as ACARS profiles, in conjunction with numerical simulations. All simulations are conducted using the WRF ARW core at 2 km resolution with a 500 m nest centered over the coastal NYC area, with the Morrison microphysical scheme, the thermal diffusion LSM, and the MYNN2.5 PBL scheme.

Synoptically, the 23 July 2002 decaying QLCS organizes along a developing baroclinic zone (i.e. cold front), with little low-level temperature advection over the QLCS. Conversely, the 31 May event is ~200 km downstream of the surface front, within a region of warm air advection that helps to destabilize the environment ahead of the QLCS. The dynamic and thermodynamic conditions during both the 23 June decay and the 31 May maintain events are consistent with the respective composite analyses. The differences in shear and CAPE in the composite are also consistent with the case studies. The 23 June decaying QLCS experiences a line-perpendicular wind shear of ~4-9 m s^{-1}, which is smaller compared to the 15-18 m s^{-1} shear during the 31 May maintaining event. Meanwhile, the instability along the coast during the 23 July event ranges from 1600-2000 J kg^{-1}, which is ~400 J kg^{-1} greater than for the 31 May event.

Trajectory analyses highlight the source region of air ingested into the QLCSs for each case study as they cross the Atlantic coastline and move over the coastal waters. As the 31 May maintaining linear system traverses the ocean, the air within the lowest 300 hPa travels underneath the convective line without being consumed by the updraft due to the stable marine layer and a lack of surface based CAPE. Meanwhile, the air slightly above that layer (above ~500 m) is ingested into the convective updraft. Since there is an absence of ambient surface-based CAPE though elevated instability along the gust front from ~975 hPa (~350 m), the QLCS can persist with this flow partitioning at low levels. In contrast, during the 23 July decaying event, there is both surface based (200-500 J kg^{-1}) and elevated instability (1200-1600 J kg^{-1}), with parcels as low as 100 m ahead of the QLCS ascending into the updraft, and those as low as 10 m ascending ~0.5 km as well. Regardless of the presence of surface based CAPE, the 23 July event weakens at the coastline, suggesting that other physical processes are causing the QLCS to decay.

The evolution of the developing cold pool in conjunction the varying ambient vertical wind shear perpendicular to the squall line are important in determining the evolution of the two QLCSs examined in this study. The cold pool is located behind the main convective core for the 31 May event, while it is located slightly ahead of the convective updraft for the 23 July event. The ambient low-level shear downstream of maintaining linear events, seen in both the composite and 31 May case study, is greater compared to the shear for the decaying event, in a composite sense as well as the individual 23 July event. These observations may be related to the low-level balance theory describing the evolution of squall lines proposed by Rotunno et al (1988). 'RKW' theory states the balance between the horizontal vorticity associated with the baroclinicity across the leading edge of the diabatically generated cold pool and the horizontal vorticity produced by the lower-tropospheric line-perpendicular winds shear helps to maintain a linear convective system. For the 23 July event, as the QLCS moves over the Atlantic waters, the cold pool overwhelms the ambient vertical wind shear as predicted by this theory. The cold pool moves faster than the convective line and the updraft tilts upshear, leading to the decay of the system. For the 31 May event, the cold pool and the ambient shear are in balance, thus leading to an upright convective core and a more extended lifetime for the system. The potential temperature perturbation for the cold pool is ~1-2 K weaker for the 31 May event than 23 July event. The development of a stronger potential temperature perturbation during the 23 July event is associated with the less humid environment described above. The relative humidity values in the lowest 25-50 hPa during the 31 May event were 50-60%, while they were only 40-50% during the 23 July event. Above 600 hPa, the RH values were less than 50% during the 23 July event though they were between 50-90% during the 31 May event. Additionally, the line-perpendicular vertical wind shear is approximately twice as strong during the 31 May event as in the 23 July event.

Sensitivity experiments were performed to test the role of diabatic cooling, and in turn the influence of a variation in cold pool strength, during each event. By decreasing the diabatic cooling from precipitation during the 23 July event by 85%, the updraft associated with the convective line remained upright and the lifetime of the QLCS was extended at least 8 hrs. During this experiment, the potential temperature associated with the cold pool was ~1 K warmer and the depth was ~600 m shallower compared to the control QLCS, indicating that diabatic processes are important to the evolution of the 23 July squall line. However, during the sensitivity experiment, the QLCS evolved from a system driven by cold pool dynamics to a warm core convective system where cold pool dynamics are no longer dominant. For the 31 May event, by increasing the diabatic cooling, the QLCS generated a colder and deeper cold pool resulting in an upshear tilted system that rapidly decayed, which is consistent with the basic principles of squall line theory. In both events, diabatic processes are important to the evolution of the QLCSs.

Since the evolutions of linear systems are sensitive to the ambient shear, variations in boundary layer winds due to frictional variations moving from the inland areas to the marine environment may influence the evolution of a linear system. To test this, the roughness length over the coastal waters was increased from the ocean value to a value equivalent to the northeastern U.S. land during the 31 May event. This caused the wind within the lowest 300 m to decrease as much as 8 m s^{-1}, though the line perpendicular shear was only reduced by 0.5 m s^{-1}. Therefore, while the intensity of the leading convective line was reduced, the cause was likely not the change in vertical wind shear. The decrease in winds in the lowest 25-50 hPa lead to reduced mixing within the boundary layer. This resulted in a stronger marine inversion, depicted by a cooler boundary layer, as much as 4 K, as well as a more humid environment with an ~10% increase in RH in the lowest couple kilometers. This in turn likely helped to weaken the convection for this experiment.

To more directly test the role of the marine layer during the 23 July decay event, a sensitivity test was performed in which the Atlantic Ocean was essentially replaced by a land area, equivalent to the forested areas of the Northeast. While the initial hypothesis proposed that the removal of the ocean would result in an extended lifetime of the linear system, the convective line experienced the same decay process as the control run, both spatially and temporally. Closer examination of the impacts of the removal of the ocean revealed that there was an increase in instability, but the boundary layer over the removed ocean was deeper, warmer, and drier, with a reduction in line-perpendicular vertical wind shear. The warmer boundary layer lead to a larger potential temperature perturbation associated with the cold pool, though the magnitude of the cold pool itself was approximately the same. The reduced wind shear could not balance the horizontal vorticity with the relative enhancement of the cold pool.

As the 23 July event approached the Atlantic coastline, the instability along the coastal zone began to weaken and this decrease in instability may have contributed to the decay of the QLCS. To increase the ambient instability, the solar heating was fixed at a constant value beginning 13 hrs into the simulation, or 3 PM local time. Even with an increase in surface based instability of 100-300 J kg^{-1}, the experiment yielded a decaying linear system over the Atlantic coastal waters.

For both the 31 May and the 23 July event, the diabatic processes within the cold pool were more influential on the evolution of the QLCS than the marine environment. However, there are likely decay cases in which there is a more straightforward weakening as a result of the decrease in CAPE due to the cooler coastal waters. Evidence of this was seen in the 0.5ZNT 31 May sensitivity experiment, in which the magnitude of the marine inversion increased leading to a reduction in MUCAPE and a weaker QLCS.

(c) Practical guidance for forecasters

As indicated through this work, forecasting warm season convection over the northeastern U.S. is complicated by numerous topographical variations, including mountain ranges as well as the Atlantic coastal boundary. The more marginal dynamic and thermodynamic conditions that support convection, especially severe convection, over the Northeast compared to the central U.S. can further complicate these forecasts. Several key findings from this study may prove useful to forecasters when faced with such challenging forecasts.

This work highlighted the mean dynamic and thermodynamics conditions that support various types of convective organizational structures, both severe and non-severe. While understanding these favored conditions is important, one should appreciate the range of variability within the mean, especially for severe convective events. It is worth emphasizing that coastal severe weather can develop in environments with low MUCAPE, as well as small values of shallow and deep layer vertical wind shear. Even though the instability and shear values on a particular day may fall short of the expected values for severe weather, values typically determined through studies of central U.S. convection, severe weather may still be possible given the presence of dynamical support.

The unique conditions associated with the development of tornadoes across the region make forecasting coastal tornadoes particularly challenging and worth revisiting. While coastal tornadoes typically form during the late afternoon hours, there is a secondary maximum in tornado development during the early morning hours. Furthermore, no one convective organizational structure favors the development of coastal tornadoes, making them equally likely from all types of severe convection.

For QLCS encountering the Atlantic marine environment, these systems may not undergo the expected or anticipated evolution given the ambient dynamic and thermodynamic conditions. In the mean, both decaying and slowly decaying QLCS are associated with developing baroclinic zones (i.e. fronts). The 23 July 2002 decaying QLCS was also associated with a surface cold front as to moved offshore over the Atlantic waters. Therefore, even those QLCSs supported by a developing lower-troposheric baroclinic zone can undergo decay over the Atlantic waters.

The magnitude of the marine layer as the associated offshore instability may not always have the strongest influence on the evolution of the QLCS. Other physical processes may have a stronger influence the evolution of a QLCS as seen for the 23 July event, during which enhanced diabatic cooling caused the linear system to decay. Furthermore, the presence of offshore instability (CAPE/MUCAPE) does not imply that a convective system will maintain its intensity over the coastal waters. For the 23 July 2002 event, the linear system decayed in spite of the instability offshore. Similarly, the composite analysis indicated that there was little difference between the mean downstream MUCAPE for decay, slow decay, and maintain events. Rather than instability, offshore vertical wind shear may be a better delimiter between these 3 types of evolutions, with decay events having the smallest 0-3 km shear values and maintain events having the largest.

Considering numerical guidance of these warm season convective linear systems, numerical models are more likely to accurately capture QLCS events that are more strongly synoptically forced compared to those with little dynamical support. Also, these simulated systems tend to be weaker than the observed convective lines.

5.3 Future Work

The last section of this research (chapter 4) sought to uncover the role of the marine layer on the evolution of QLCSs moving eastward over the northeastern U.S. Atlantic coastal boundary and out over the Atlantic coastal waters. The exploration of 2 case studies revealed that the marine layer is not always the most influential factor, and other processes internal to the QLCS may be more dominant. For the 23 July 2002 decaying event, the evolution of the QLCS was primarily controlled by the diabatic cooling processes within the system. The relatively strong diabatic cooling led to the development of a cold pool that overwhelmed the system and moved ahead of the main convective line leading to decay. Sensitivity tests showed that this evolution would have occurred regardless of the presence of the marine layer.

While the marine layer had little influence on the decay of the 23 July 2002 event, this may not be the case for other QLCS that decay upon encountering the marine layer. There may be other events that decay due to the reduced instability offshore over the marine waters. The influence of a reduction in stability was illustrated in a sensitivity experiment of the 31 May 2002 maintaining event. A reduction of the low level winds over the marine waters led to an increase in the magnitude of the marine inversion and thus a decrease in MUCAPE offshore. The weaker offshore instability led to a weaker QLCS compared to the control simulation, though the system still maintained itself over the coastal waters.

Given these findings, this research has opened up several areas for possible future work, especially concerning the interaction of quasi-linear convective systems with the marine boundary layer. Some topics of interest include:

(a) Physical mechanisms associated with evolving QLCSs in a marine environment

Given the complexity of this problem, a combination of several approaches should be applied to better understand the physical mechanisms controlling the evolution of a QLCS encountering a marine environment including:

(a.1) Further classification of decay events with respect to different physical mechanisms

It is likely a subset of events which decay upon encountering the Atlantic marine layer may be primarily influenced by the relatively cooler marine waters while others are controlled by other physical processes inherent to the QLCS. To better understand the difference between these types of decaying events, it is necessary to filter those QLCS events that are mainly modified by the coastal waters from those events during which the role of the marine layer is secondary. Since the role of dry air can be important as shown by the analysis of the 23 July 2002 decaying QLCS event, one can categorize events with respect to the amount of dry air aloft (relative humidity) according to a determined threshold value to potentially identify those events during which diabatic processes are more important. With these new subsets of events, the offshore CAPE, MUCAPE, CIN, and MUCIN can be calculated to assess the stability of each of these events. For those events during which diabatic processes may play a more dominant role compared to the marine layer, the evolution of the QLCS may be less sensitive to the amount of CAPE over the coastal waters. In other words, these types of decay events may occur even with instability offshore, as seen for the 23 July 2002 event in this current study. For those events that are more strongly influenced by the marine layer, there is likely little to no offshore instability.

(a.2) Additional case studies

This work provides a detailed examination of two quasi-linear convective systems that encounter the Atlantic marine environment. While these events are representative cases as suggested by the composite analyses, it would be useful to repeat this analyses for a few other events. The 23 July decaying event is more sensitive to variations in diabatic processes than the marine environment, but this may not be the case for other decaying quasi-linear convective systems. Also during the 23 July event, the less humid low- and mid-level environment may have played a role in enhancing the diabatic cooling and generating a stronger, faster moving density current than would otherwise have developed in a more humid environment. However, in a composite sense, mid-level (600-500 hPa) relative humidity values during decaying and maintaining events are similar, with slow decay events having ~15% larger relative humidity values. This suggests that diabatic processes may not be the full story. A simple reduction in instability over the relatively cool marine waters may cause a QLCS to decay, even in environments with more favorable mid-level moisture.

Trajectory analyses need to be repeated for other maintaining events to see if the source region of air parcels traveling into the convective updraft is elevated, as seen for the 31 May event. A similar analysis should be performed for several other decaying events to see if surface based parcels as well as parcels originating from within the convectively generated cold pool travel into the system. Perhaps this is a common mechanism further promoting the decay of linear events that are already beginning to tilt upshear with diabatically cool air pushing ahead of the convective line.

(a.3) Other sensitivity experiments

While this study performed a series of sensitivity experiments in an attempt to understand the role of the marine layer as well as the internal processes of the evolving convection, a variety of other sensitivity experiments could be performed to understand the response of convective systems to other environmental variations not explored in this work. For example, the sea surface temperature may be raised or lowered representative of a different month or season, to evaluate the evolution of a particular QLCS event if it were to occur during a different time of the year. This type of sensitivity experiment may be designed for a climate change scenario as well, by increasing the surface temperature over the water and the land, in addition to the atmospheric condition, to understand the response of a coastal QLCS in a warming climate.

(a.4) Idealized simulations

While the analyses of individual case studies are important, their complexity makes it difficult to examine individual components of the problem in isolation. Simulating the interaction of quasi-linear convective systems and a marine environment in an idealized framework could provide a means to understanding the impact of one particular environmental variable (e.g. strength of the marine layer) on the evolving convection, while holding all other variables relatively constant (e.g. CAPE). For example, the response of a QLCS to a varying magnitude as well as a varying depth of the marine layer may be tested. The magnitude of the marine layer will have an impact on the offshore instability, so the response of an evolving QLCS to the variations in this instability may be evaluated as well. From here, one can see if this response is sensitive to the overall ambient instability (CAPE). Perhaps a more robust QLCS that develops within a higher CAPE environment may be less sensitive to the marine environment and the associated decrease in instability, compared to a weaker QLCS in a lower overall CAPE environment

The influence of presence of dry air at various levels, including the lowest 100-200 hPa as well as the mid-levels (700-500 hPa), on the evolution of QLCSs may be tested as well. From the 23 July 2002 event, the dry air seemed to increase the evaporative cooling of precipitation leading to the generation of a strong cold pool and thus the decay of the QLCS regardless of the presence of offshore instability. The role of dry air at various levels in the troposphere on the evolution of a QLCS can be evaluated in environments with varying instability, including those with both high and low values of offshore instability. For all of these experiments described above, tracers could be launched to examine the source region of the air ingested into the QLCS and comparisons could be made to the observational analyses. It may be hypothesized a subset of events that survive over the marine environment may be elevated while a subset of those that decay may be surface based. However, the combination the environmental instability variations across the domain, the structure of the marine layer, and the tropospheric moisture profile that supports either elevated or surface based systems needs to be identified.

The role of the vertical wind shear can be addresses more directly as well. For the 23 July case study, one could hypothesize that the QLCS could have maintained its intensity over the Atlantic waters if the magnitude of the vertical wind shear were equivalent to that in the 31 May case. In an idealized framework, one can systematically alter the magnitude of the shear, the directional component to the shear, as well as the vertical depth of the shear to test this idea.

(b) Addressing weaknesses in numerical simulations for Northeast convective events

One common issue throughout this work was the difficulty in obtaining a mesoscale simulation of a northeastern U.S. convective event that was consistent with observations. Many different convective events were simulated applying a variety of domain sizes and resolutions, a suite of different parameterizations (e.g. LSM, PBL, microphysics), as well as a variety of data for the initial and boundary conditions, including those with hydrometeor data. Most simulations produced convection that was weaker than the observations or it lacked convection completely. Even for the two control simulations in this study, the convective systems still exhibited weaknesses that were not observed in reality. A very worthwhile research endeavor would be to explore the reasons behind the consistently underrepresented Northeast convection in the models. One consistent thread is that the models have a better chance of more accurately simulating convection during the events with stronger synoptic forcing, compared to those with weak forcing. If the sources of the biases can be identified, the mesoscale models may potentially be improved upon, allowing for more accurate convective simulations and ultimately convective forecasts in the future.

References

Ahijevych, D. A., C. A. Davis, R. E. Carbone, and J. D. Tuttle, 2004: Initiation of precipitation episodes relative to elevated terrain. *J. Atmos. Sci.*, **61**, 2763–2769.

Atkins, N. T., and J. J. Cunningham, 2006. The influence of low-level stable layers on damaging surface winds within bow echoes. Preprints, *23rd Conf. on Severe Local Storms*, St. Louis, MO, Amer. Meteor. Soc.

Banacos, P. C., and M. L. Ekster, 2010: The association of the elevated mixed layer with significant severe weather events in the northeastern United States. *Wea. Forecasting*, **25**, 1082–1102.

Betts, A., F. Chen, K. Mitchell, and Z. Janjic, 1997: Assessment of the land surface and boundary layer models in two operational versions of the NCEP Eta model using FIFE data. *Mon.Wea. Rev.*, **125,** 2896-2916.

Bluestein, H.B., and M.H. Jain, 1985: Formation of mesoscale lines of precipitation: Severe squall lines in Oklahoma during the spring. *J. Atmos. Sci.*, **42**, 1711–1732.

Blanchard, D.O., 1990: Mesoscale Convective patterns of the southern High Plains. *Bull. Amer. Meteor. Soc.*, **71**, 994–1005.

Bosart, L. F., and T. J. Galarneau Jr, 2005. The influence of the Great Lakes on warm season weather systems during BAMEX. *Preprints 6th Coastal Meteorology Conference, 10-13 Jan 2005,* American Meteorological Society.

Bosart, L. F., and F. Sanders, 1981: The Johnstown flood of July 1977: A long-lived convective system. *J. Atmos. Sci.*, **38**, 1616–1642.

Bosart, L. F., A Seimon, K. D. LaPenta, and M. J. Dickinson, 2006: Supercell tornadogenesis over complex terrain: The Great Barrington, Massachusetts tornado on 29 May 1995. *Wea. Forecasting*, **21**, 897–922.

Bougeault, P. and P. Lacarrère, 1989 : Parameterization of orography-induced turbulence in a meso-beta scale model, *Mon. Wea. Rev.,*117,1870-1888.

Brooks, H. E., C. A. Doswell, and M.P. Kay, 2003: Climatological estimates of local daily tornado probability for the United States. *Wea. Forecasting*, **18**, 626–640.

Bryan, G. H., J. C. Knievel, M. D. Parker, 2006: A multimodel assessment of RKW theory's relevance to squall-line characteristics. *Mon. Wea. Rev.*, **134**, 2772–2792.

Carbone, R. E., J. D. Tuttle, D. A. Ahijevych, and S. B. Trier, 1992: Inferences of predictability associated with warm season precipitation episodes. *J. Atmos. Sci.*, **59**, 2033–2056.

Carlson, T. N., and F. H. Ludlam, 1968: Conditions for the occurrence of severe local storms. *Tellus*, **20**, 203-226.

Changnon, S. A., 1980: Evidence of urban and lake influences on precipitation in the Chicago area. *J. Appl. Meteor.*, **19**, 1137–1159.

Chen, F., K. Mitchell, J. Schaake, Y. Xue, H. Pan, V. Koren, Y. Duan, M. Ek, and A. Betts, 1996: Modeling of land-surface evaporation by four schemes and comparison with FIFE observations. *J. Geophys. Res.,* **101**, 7251-7268.

Clark, A. J., C. J. Schaffer, W. A. Gallus, Jr., and K. Johnson-O'Mara, 2009: Climatology of storm reports relative to upper-level jet streaks. *Wea. Forecasting*, **24**, 1032-1051.

Cohen, A. E., M. C. Coniglio, S. F. Corfidi, and S. J. Corfidi, 2007: Discrimination of mesoscale convective system environments using sounding observations. *Wea. Forecasting*, **22**, 1045-1062.

Colle, B. A., and D. R. Novak, 2010: The New York Bight jet: Climatology and dynamical evolution. *Mon. Wea. Rev.*, **138**, 2385-2404.

Coniglio, M. C., and D. J. Stensrud, 2001: Simulation of a progressive derecho using composite initial conditions. *Mon. Wea. Rev.*, **129**, 1593–1616.

Coniglio, M. C., D. J. Stensrud, and M. B. Richman, 2004: An observational study of derecho-producing convective systems. *Wea. Forecasting*, **19**, 320–337.

Coniglio, M. C, H. E. Brooks, S. J. Weiss, and S. F. Corfidi, 2007: Forecasting the maintenance of quasi-linear mesoscale convective systems. *Wea. Forecasting*, **22**, 556-570.

Davis, C., N. Atkins, D. Bartels, L. Bosart, M. Coniglio, G. Bryan, W. Cotton, D. Dowell, B. Jewett, R. Johns, D. Jorgensen, J. Knievel, K. Knupp, W.-C. Lee, G. Mcfarquhar, J. Moore, R. Przybylinski, R. Rauber, B. Smull, R. Trapp, S. Trier, R. Wakimoto, M. Weisman, and C. Ziegler, 2004: The bow echo and MCV experiment: observations and opportunities. *Bull. Amer. Meteor. Soc.*, **85**, 1075–1093.

Doswell, C. A., H. E. Brooks, and M.P. Kay, 2005: Climatological estimates of daily local nontornadic severe thunderstorm probability for the United States. *Wea. Forecasting*, **20**, 577–595.

Duda, J. D., and W. A. Gallus Jr., 2010: Spring and Summer Midwestern severe weather reports in supercells compared to other morphologies. *Wea. Forecasting*, **25**, 190–206.

Ek, M. B., K. E. Mitchell, Y. Lin, E. Rogers, P. Grunmann, V. Koren, G. Gayno, and J. D. Tarpley, 2003: Implementation of Noah land surface model advances in the National Centers for Environmental Prediction operational mesoscale Eta model, *J. Geophys. Res.,* **108**, 8851, doi:10.1029/2002JD003296.

Evans, J. S., and C. A. Doswell III, 2001: Examination of derecho environments using proximity sounding. *Wea. Forecasting*, **16**, 329-342.

Farrell, R. J., and T. N. Carlson, 1989: Evidence for the role of the lid and underrunning in an outbreak of tornadic thunderstorms. *Mon. Wea. Rev.*, **117**, 857–871.

Ferrier, B. S., 1994: A double-moment multiple-phase four-class bulk ice scheme. Part I: Description. *J. Atmos. Sci.*, 51, 249–280.

Frame, J., and P. Markowski, 2006: The interaction of simulated squall lines with idealized mountain ridges. *Mon. Wea. Rev.*, **134**, 1919–1941.

Gallus, W. A., N.A. Snook, and E.V. Johnson, 2008: Spring and summer severe weather reports over the Midwest as a function of convective mode: A preliminary study. *Wea. Forecasting*, **23**, 101–113.

Gilmore, M. S., and L.J. Wicker, 1998: The influence of midtropospheric dryness on supercell morphology and evolution. *Mon. Wea. Rev.*, **126**, 943–958.

Giordano, L. A., and J. M., Fritsch, 1991: Strong tornadoes and flash-flood-producing rainstorms during the warm season in the Mid-Atlantic region. *Wea. Forecasting*, **6**, 437–455.

Hong, S.-Y., Y. Noh, and J. Dudhia, 2006: A new vertical diffusion package with an explicit treatment of entrainment processes. *Mon. Wea. Rev.*, **134**, 2318–2341.

Hong, S.-Y., and J.-O. J. Lim, 2006: The WRF single-moment microphysics scheme (WSM6). *J. Korean Meteor. Soc.*, 42, 129–151.

Hong, J. Dudhia, and S.-H. Chen, 2004: A revised approach to ice microphysical processes for the bulk parameterization of clouds and precipitation. *Mon. Wea. Rev.,* 132, 103–120.

James, R. P., P. M. Markowski, and J. M. Fritsch, 2006: Bow echo sensitivity to ambient moisture and cold pool strength. *Mon. Wea. Rev.*, **134**, 950–964.

Janjic, Z. I., 1990: The step-mountain coordinate: Physical Package. *Mon. Wea. Rev.*, **118**, 1429–1443.

Jirak, I. L., W. R. Cotton, and R.L. McAnelly, 2003: Satellite and radar survey of mesoscale convective system development. *Mon. Wea. Rev.*, **131**, 2428–2449.

Johns, R. H., 1982: A synoptic climatology of northwest flow severe weather outbreaks. Part I: Nature and significance. *Mon. Wea. Rev.*, **110**, 1653–1663.

Johns, R. H., 1984: A synoptic climatology of northwest-flow severe weather outbreaks. Part II: Meteorological parameters and synoptic patterns. *Mon. Wea. Rev.*, **112**, 449–464.

Johns, R. H., and R. A. Dorr Jr., 1996: Some meteorological aspects of strong and violent tornado episodes in New England and eastern New York. *Natl. Wea. Dig*., **20,** 2-12.

LaPenta, K. D., L. F. Bosart, T. J. Galarneau Jr., and M. J. Dickinson, 2005: A multiscale examination of the 31 May 1998 Mechanicville, New York tornado. *Wea. Forecasting*, **20**, 494–516.

Lericos, T. P., H. E. Fuelberg, M. L. Weisman, and A. I. Watson, 2007: Numerical simulations of the effects of coastlines on the evolution of strong, long-lived squall lines. *Mon. Wea. Rev.*, **135**, 1710–1731.

Letkewicz, C. E., and M. D. Parker, 2010: Forecasting the maintenance of mesoscale convective systems crossing the Appalachian mountains. *Wea. Forecasting*, **25**, 1179–1195.

Letkewicz, Casey E., and M. D. Parker, 2011: Impact of environmental variations on simulated squall lines interacting with terrain. *Mon. Wea. Rev. Early Online Release.*

Lin, Y. L., R. Farley, and H. D. Orville, 1983: Bulk parameterization of the snow field in a cloud model. J. Climate Appl. Meteor., 22,1065–1092.

Lombardo, K. A., and B. A. Colle, 2010: The spatial and temporal distribution of organized convective structures over the northeast U.S. and their ambient conditions. *Mon. Wea. Rev.*, **138**, 4456–4474.

Lombardo, K. A., and B. A. Colle, 2011: Convective storm structures and ambient conditions associated with severe weather over the northeast U.S. *Mon. Wea. Rev.*, *early online release.*

Koren, V., J. Schaake, K. Mitchell, Q. Y. Duan, F. Chen, and J. M. Baker, 1999: A parameterization of snowpack and frozen ground intended for NCEP weather and climate models. *J. Geophys. Res.,***104,** 19569-19585.

Kuo, Y.-H., and G. T.-J. Chen, 1990: The Taiwan area mesoscale experiments: An overview. *Bull. Amer. Meteor. Soc.,* **71,** 488–503.

Maddox, R.A., 1981: Satellite depiction of the life cycle of a mesoscale convective complex. *Mon. Wea. Rev.*, **109**, 1583–1586.

Maddox, R. A., and C. A. Doswell, 1982: An examination of jet stream configurations, 500 mb vorticity advection and low-level thermal patterns during extended periods of intense convection. *Mon. Wea. Rev.*, **110**, 184–197.

Mapes, B., E., T. T. Warner, M. Xu, and A. J. Negri, 2003: Diurnal patterns of rainfall in northwestern South America. Part I: Observation and context. *Mon. Wea. Rev.*, **131**, 799–811.

Mesinger, F., G. DiMego, E. Kalnay, K. Mitchell, P. C. Shafran, W. Ebisuzaki, D. Jović, J. Woollen, E. Rogers, E. H. Berbery, M. B. Ek, Y. Fan, R. Grumbine, W. Higgins, H. Li, Y. Lin, G. Manikin, D. Parrish, and W. Shi, 2006: North American Regional Reanalysis. *Bull. Amer. Meteor. Soc.*, **87**, 343–360.

Miglietta, M. Ma., and R. Rotunno, 2009: Numerical simulations of conditionally unstable flows over a mountain ridge. *J. Atmos. Sci.*, **66**, 1865–1885.

Miller, J.E., 1948: On the concept of frontogenesis. *J. Atmos. Sci.*, **5**, 169–171.

Moncrieff, M. W., and C. Liu, 1999: Convection initiation by density currents: Role of convergence, shear, and dynamical organization. *Mon. Wea. Rev.,* **127,** 2455–2464.

Morrison, H., G. Thompson, and V. Tatarskii, 2009: Impact of cloud microphysics on the development of trailing stratiform precipitation in a simulate squall line: Comparison of one- and two-moment schemes. *Mon. Wea. Rev.* **137**, 991–1007.

Murray, J. C., and B. A. Colle, 2011: The spatial and temporal variability of convection over the northeast U.S. during the warm season. *Mon. Wea. Rev.* **139**, 992–1012.

Nakanishi, M., 2001: Improvement of the Mellor-Yamada turbulence closure model based on large-eddy simulation data. *Bound.-Layer Meteor.*, **99**, 349-378.

Nakanishi M, Niino H. An improved Mellor-Yamada level-3 model: Its numerical stability and application to a regional prediction of advection fog. *Bound.-Layer Meteor.* 2006, 119, 397–407.

Nakanishi, M. and H. Niino, 2004: An improved Mellor-Yamada level-3 model with condensation physics: Its design and verification. *Bound.-Layer Meteor.*, **112**, 1-31.

Orville, R.E., and G.R. Huffines, 2001: Cloud-to-ground lightning in the United States: NLDN results in the first decade, 1989–98. *Mon. Wea. Rev.*, **129**, 1179–1193.

Parker, M.D., and R.H. Johnson, 2000: Organizational modes of midlatitude mesoscale convective systems. *Mon. Wea. Rev.*, **128**, 3413–3436.

Parker, M. D., S.A. Rutledge, and R.H. Johnson, 2001: Cloud-to-ground lightning in linear mesoscale convective systems. *Mon. Wea. Rev.*, **129**, 1232–1242.

Parker, M. D., and R. H. Johnson, 2004a: Simulated convective lines with leading precipitation. Part I: Governing dynamics. *J. Atmos. Sci.*, **61**, 1637–1655.

Parker, M. D., and R. H. Johnson, 2004a: Simulated convective lines with leading precipitation. Part I: Evolution and maintenance. *J. Atmos. Sci.*, **61**, 1656–1673.

Parker, M.D., and D.A. Ahijevych, 2007: Convective episodes in the east-central United States. *Mon. Wea. Rev.*, **135**, 3707–3727.

Parker, M. D., 2008: Response of simulated squall lines to low-level cooling. *J. Atmos. Sci.*, **65**, 1323–1341.

Pleim, J. E., and A. Xiu, 2003: Development of a land surface model. Part II: Data assimilation. *J. Appl. Meteor.,* 42, 1811–1822.

Pleim, J.E., 2006: A Simple, efficient solution of flux–profile relationships in the atmospheric surface layer. *J. Appl. Meteor. Clim.,* 45, 341–347.

Pleim, Jonathan E., 2007: A combined local and nonlocal closure model for the atmospheric boundary layer. part i: model description and testing. *J. Appl. Meteor. Climatol.*, **46**, 1383–1395.

Pleim, J. E., 2007: A combined local and nonlocal closure model for the atmospheric boundary layer. Part II: application and evaluation in a mesoscale meteorological model. *J. Appl. Meteor. Climatol.*, **46**, 1396–1409.

Reeves, H. D., Y.-L. Lin, 2007: The effects of a mountain on the propagation of a preexisting convective system for blocked and unblocked flow regimes. *J. Atmos. Sci.*, **64**, 2401–2421.

Rotunno, R., J.B. Klemp, and M.L. Weisman, 1988: A theory for strong, long-lived squall lines. *J. Atmos. Sci.*, **45**, 463–485.

Rutledge, S. A. and P. V. Hobbs, 1984: The mesoscale and microscale structure and organization of clouds and precipitation in midlatitude cyclones. XII: A diagnostic modeling study of precipitation development in narrow cold-frontal rainbands. *J. Atmos. Sci.,* 41, 2949–2972.

Schultz, D. M., and W. J. Steenburgh, 1999: The formation of a forward-tilting cold front with multiple cloud bands during Superstorm 1993. *Mon. Wea. Rev.*, **127**, 1108–1124.

Schultz, D. M., 2005: A review of cold fronts with prefrontal troughs and wind shifts. *Mon. Wea. Rev.*, **133**, 2449–2472.

Schuman, M.R., and P. J. Roebber, 2010: The influence of upper-tropospheric potential vorticity on convective morphology. *Mon. Wea. Rev.*, **138**, 463–474.

Shapiro, A., 1992: A hydrodynamical model of shear flow over semiinfinite barriers with application to density currents. *J. Atmos. Sci.,* **49,** 2293–2305.

Smull, B.F and R.A. Houze, 1985: A Midlatitude squall line with a trailing region of stratiform rain: Radar and satellite observations. *Mon. Wea. Rev.*, **113**, 117–133.

Stensrud, D. J., M. C. Coniglio, R. P. Davies-Jones, and J. S. Evans, 2005: Comments of "'A theory for strong ling-lived squall lines' revisited". *J. Atmos. Sci.*, **62**, 2989–2996.

Teng, J.-H., C.-S. Chen, T.-C. Chen Wang, Y.-L. Chen, 2000: Orographic effects on a squall line system over Taiwan. *Mon. Wea. Rev.*, **128**, 1123–1138.

Thompson, R. L., R. Edwards, J. A. Hart, K. L. Elmore, and P. Markowski, 2003: Close proximity soundings within supercell environments obtained from the Rapid Update Cycle. *Wea. Forecasting*, **18**, 1243–1261.

Thompson, G., R. M. Rasmussen, and K. Manning, 2004: Explicit forecasts of winter precipitation using an improved bulk microphysics scheme. Part I: Description and sensitivity analysis. *Mon. Wea. Rev.*, 132, 519−542.

Thompson, G., P. R. Field, R. M. Rasmussen, and W. D. Hall, 2008: Explicit forecasts of winter precipitation using an improved bulk microphysics scheme. Part II: implementation of a new snow parameterization. *Mon. Wea. Rev.*, **136**, 5095–5115.

Wakimoto, R. M., C. Liu, and H. Cai, 1998: The Garden City, Kansas, storm during VORTEX 95. Part I: Overview of the storm's life cycle and mesocyclogenesis. *Mon. Wea. Rev.*, **126**, 372–392.

Wasula, A. C., L. F. Bosart, and K.D. LaPenta, 2002: The Influence of terrain on the severe weather distribution across interior eastern New York and western New England. *Wea. Forecasting*, **17**, 1277–1289.

Weckwerth, T. M., and R. M. Wakimoto, 1992: The initiation and organization of convective cells atop a cold-air outflow boundary. *Mon. Wea. Rev.*, **120**, 2169–2187.

Weisman, M., and J. Klemp, 1982: The dependence of numerically simulated convective storms on vertical wind shear and buoyancy. *Mon. Wea. Rev.*, **110**, 504–520.

Weisman, M. L., and J. B. Klemp, 1984: The structure and classification of numerically simulated convective storms in directionally varying wind shears. *Mon. Wea. Rev.*, **112**, 2479–2498.

Weisman, M. L., J.B. Klemp, and R. Rotunno, 1988: Structure and evolution of numerically simulated squall lines. *J. Atmos. Sci.*, **45**, 1990–2013.

Weisman, M. L., 1992: The role of convectively generated rear-inflow jets in the evolution of long-lined mesoconvective systems. *J. Atmos. Sci.*, **49**, 1826–1847.

Weisman, M. L., and R. Rotunno, 2004: "A theory for strong long-lived squall lines" revisited. *J. Atmos. Sci.*, **61**, 361–382.

Weisman, M. L., and R. Rotunno, 2005: Reply. *J. Atmos. Sci.*, **62**, 2997–3002.

Workoff, T., 2010: A study of the effect of Lake Erie on deep convective systems. *Masters thesis, Univ. of Illinois at Urbana-Champaign.*

Zajac, B.A., and S.A. Rutledge, 2001: Cloud-to-ground lightning activity in the contiguous United States from 1995 to 1999. *Mon. Wea. Rev.*, **129**, 999–1019.

Zwiers, F. W., 1990: The effect of serial correlation on statistical inferences made with resampling procedures. *J. Clim.*,**12**, 1452-1460.

Appendix

ACARS: Aircraft Comminucations Addressing and Reporting Sytem
ARW: Advanced Research WRF
ASL: Above sea level
BE: Bow echo
BL: Broken line
CC: Clusters of cells
CO: Coastal ocean dimain
CP: Coastal plain domain
IC: Isolated cells
HT: High terrain domain
LFC: Level of free convection
LS: Linear system with leading stratiform precipitation
LSM: Land surface model
MCV: Mesoscale convectve vortex
MUCAPE: Most unstable CAPE
NARR: North American Regional Reanalysis
NOWrad: National Weather Operational Radar
NS: Linear system with no stratiform precipitation
NL: Nonlinear system
MYJ: Mellor-Yamada-Janjic PBL
MYNN2.5: Mellor-Yamada Nakanishi and Niino Level 2.5 PBL
PBL: Planetary boundary layer
PS: Linear system with parallel stratiform precipitation
RIJ: Rear inflow jet
RUC: Rapid Update Cycle
Q-G: Quasi-geostrophic
QLCS: Quasi-linear convective system
TS: Linear system with trailing stratiform precipitation
UP: Upslope domain
YSU: Yonsei University PBL